Fakultät für Physik
Physics of Energy Conversion and Storage

The Impact of the Electrode/Electrolyte Interface Status on the Activity, Stability, and Selectivity of Electrocatalytic Centers

Viktor Čolić

Vollständiger Abdruck der von der Fakultät für Physik der Technischen Universität München zur Erlangung des akademischen Grades eines

Doktors der Naturwissenschaften

genehmigten Dissertation.

Vorsitzende(r): Prof. Dr. Norbert Kaiser

Prüfer der Dissertation:

1. Prof. Dr. Aliaksandr Bandarenka
2. Prof. Dr. Julia Kunze-Liebhäuser
3. Prof. Dr. Radim Beranek
   (nur schriftliche Beurteilung)

Die Dissertation wurde am 10.08.2016 bei der Technischen Universität München eingereicht und durch die Fakultät für Physik am 06.09.2016. angenommen.

The Impact of the Electrode/Electrolyte Interface Status on the Activity, Stability, and Selectivity of Electrocatalytic Centers

Viktor Čolić

Physics of Energy Conversion and Storage

Physik-Department

Technische Universität München

Supervisor: Prof. Aliaksandr S. Bandarenka (Technische Universität München, Germany)

Referee: Prof. Dr. Julia Kunze-Liebhäuser (Leopold-Franzens-Universität Innsbruck, Austria)

Abstract

The status of the electrode/electrolyte interface determines the key properties of electrocatalytic systems: their activity, selectivity, and stability. In turn, the status of the interface itself is determined by numerous factors. They can be classified as *i*) effects due to the electrode material composition, *ii*) effects due to the surface morphology, and *iii*) the electrolyte effects. In order to develop methodologies for the rational design of electrocatalysts, complex dependencies between those factors should be better understood. The focus of this thesis is set on further understanding of factors governing the performance of electrocatalytic systems.

As the target and model processes for this work, reactions significant for energy conversion in so-called "hydrogen economy" were selected. Namely, the hydrogen evolution reaction, hydrogen oxidation, oxygen evolution reaction and oxygen electroreduction are considered. It should be noted that due to the complexity and interdisciplinary nature of the scientific questions selected for this work, some experiments and theoretical considerations were performed in collaboration with the groups of theoreticians from University of Leiden (The Netherlands) and University of Lyon (France), as well as teams of experimentalists from Ruhr-Universität Bochum (Germany) and Technische Universität München (Germany). The corresponding acknowledgments are given in the thesis, where necessary.

The main results of this work can be summarized as listed below.

– New methodologies for accurate electrocatalytic activity benchmarking have been elaborated, particularly addressing the iR-drop correction, issues related to the emerging gas phase at the electrode surface and accurate determinations of the electrode real surface area.

- The effects of the electrode composition have been specifically elucidated for Pt-alloy catalysts, both in the form of bulk alloys, as well as surface/near-surface alloys. It has been for the first time demonstrated that for bulk Pt-alloys with 3d-transition metals and lanthanides, where the lattice strain primarily determines the surface electronic structure, the radius of the solute element can be used as a simple activity descriptor. It is also shown that surface and near-surface alloying of Pt with Cu can efficiently change the binding of different species to the surface, and therefore influence not only the activity and stability of these systems, but also their susceptibility to certain catalytic poisons, such as the sulfonate groups present in Nafion.

- The effects of surface morphology, such as coordination and the presence of specific defects on the activity were elucidated for various Pt electrodes. It has been shown that the generalized coordination number can be used as an activity descriptor for the oxygen reduction reaction on Pt. This approach has been used to engineer Pt-electrocatalysts with high ORR activity.

- Finally, the electrolyte effects have been analyzed. It is demonstrated that alkali metal cations, which are often considered as "spectator species", can in fact influence the electrocatalytic activity, and sometimes exhibit trends that are difficult to explain based on the current state of understanding: this is demonstrated for the case of acidic sulfate-containing electrolytes. It is also shown that the presence of an ionic liquid in aqueous electrolytes can change the selectivity of metal-oxide electrocatalysts towards the anodic two-electron process at different pH-values during electrochemical water splitting.

These specific cases demonstrate multiple “degrees of freedom” for the design of the electrode/electrolyte interface towards new better electrocatalysts. Further challenges in the design of new generations of electrocatalysts for energy provision are also outlined. The main results of this work were presented in 11 articles published in peer-reviewed international scientific journals and in 5 contributions at dedicated international scientific conferences.

Zusammenfassung

Die Elektrode/Elektrolyt-Grenzfläche bestimmt die Eigenschaften eines elektrokatalytischen Systems: seine Aktivität, Selektivität und Stabilität. Die Eigenschaften der Grenzfläche wiederum werden von vielen Faktoren bestimmt, wie i) Komposition des Elektrodenmaterials, ii) Oberflächenmorphologie und iii) Einflüssen des Elektrolyten. Um eine Methodik für das rationale Design der Elektrokatalysatoren zu entwickeln, müssen die komplexen Wechselwirkungen dieser Faktoren besser verstanden werden. Im Rahmen dieser Dissertation soll ein tieferes Verständnis elektrokatalytischer Systeme erarbeitet werden.

Als Modelprozesse wurden die für die Energieumwandlung relevanten Reaktionen der Wasserstoffökonomie gewählt. Dies sind die elektrochemische Wasserstoffentwicklung (Reduktion), die Wasserstoffoxidation, die Sauerstoffentwicklung und die Sauerstoffreduktion. Aufgrund der Komplexität und der interdisziplinären Natur dieser wissenschaftlichen Arbeit wurden einige Experimente und theoretische Überlegungen in Kooperation mit Gruppen der Universität Leiden (Niederlande), der Universität Lyon (Frankreich), der Ruhr-Universität Bochum und der Technische Universität München durchgeführt. Die Beiträge werden an den entsprechenden Stellen gewürdigt.

Die zentralen Resultate dieser Arbeit lassen sich wie folgt zusammenfassen:

- Eine Methodik für akkurates elektrokatalytisches Aktivitäts-Benchmarking wurde ausgearbeitet. Insbesondere wurden der Potentialverlust, die Problematik durch eine zusätzliche Gasphase an der Elektrodenoberfläche und akkurate Bestimmungen der Elektrodenoberfläche thematisiert.

- Die Effekte der Elektrodenzusammensetzung wurden spezifisch für Platin in Form von Bulklegierungen, sowie als oberflächennahe und Oberflächenlegierungen untersucht. Für Pt-Bulklegierungen mit 3d-Übergangsmetallen und Lanthaniden, deren elektronische Oberflächenstruktur durch die Spannung des Kristallgitters bestimmt wird, wurde erstmalig gezeigt, dass der Radius der legierten Elemente als einfacher Aktivitätsdeskriptor verwendet werden kann. Weiterhin wurde gezeigt, dass die oberflächennahe und Oberflächenlegierung von Platin mit Kupfer die Chemisorption von unterschiedlichen Adsorbaten an die Oberfläche verändern kann. Dadurch wird die Aktivität und Stabilität dieser Systeme, sowie ihre Suszeptibilität für gewisse katalystische Gifte, wie z.B. die in Nafion vorkommenden Sulfonatgruppen, beeinflusst.

Die Auswirkungen der Oberflächenmorphologie, wie die Koordinationszahl und die Präsenz von bestimmten Defekten, auf die Aktivität wurden für mehrere Pt-Elektroden erläutert. Es wurde nachgewiesen, dass die „Erweiterte Koordinationszahl“ (generalized coordination number) als Aktivitätsdeskriptor für die Sauerstoffreduktion auf Platin genutzt werden kann. Diese Methodik wurde zur Entwicklung von Pt-Elektrokatalysatoren mit höherer Aktivität der Sauerstoff-Reduktionsreaktion (ORR) verwendet.

- Abschließend wurde der Einfluss des Elektrolyten analysiert. Es wurde gezeigt, dass Alkalimetallkationen, welche oft als unbeteiligte Spezies betrachtet werden, tatsächlich die elektrokatalytische Aktivität beeinflussen. Basierend auf dem aktuellen Stand der Forschung sind die beobachteten Trends schwer zu erklären. Dieser Einfluss wird für den Fall von sulphathaltigen sauren Elektrolyten demonstriert. Weiterhin wird gezeigt, dass die elektrochemische Wasserspaltung mit Hilfe eines Metalloxid-Elektrokatalysators in einer

Lösung bestehend aus einer ionischen Flüssigkeit und einem wässrigen Elektrolyten verstärkt mittels eines anodischen Zwei-Elektronen-Prozesses verläuft.

Diese Befunde zeigen mehrere Freiheitsgrade für das Design der Elektroden/Elektrolyt-Grenzfläche bei der Verbesserung von Elektrokatalysatoren auf. Weitere Herausforderungen bei der Entwicklung neuer Elektrokatalysatoren-Generationen zur Energieversorgung werden dargestellt. Die Hauptergebnisse dieser Arbeit wurden in 11 Artikeln veröffentlicht, die nach „peer-review"-Verfahren in internationalen wissenschaftlichen Zeitschriften erschienen sind. Zudem wurden fünf Beiträge auf internationalen Fachkonferenzen vorgestellt.

Contents:

1. Introduction

1.1 Energy: global consumption, current and future challenges

One of the most significant challenges humankind is facing currently is the steady and stable provision of energy without the radical degradation of the environment[1,2]. With the growing global population, deteriorating environment, and the depletion of fossil fuel reserves on which the current energy supply heavily relies on, it is expected that this challenge will require innovative and flexible solutions in the not-so-distant future.

The current global average consumption of energy is *ca* 17TW[3,4]. In the period of 1973-2013 the global electricity production increased from 6144TWh to 23391TWh, with an average annual growth rate of 3.4%[5]. This trend is expected to continue and the world's energy demands are projected to increase by 37% in the next 20 years [6], and reach *ca* 30TW[7] in the year 2050.

Most of the world's energy is still gained from fossil fuels, which still meet more than 80% of global primary energy demands. Unsurprisingly, 90% of all energy related CO_2-emissions are the result of fossil fuel combustion[8]. In 2013, 67.2% of the world's electricity was provided by fossil fuel powered plants, with geothermal, solar, and wind contributing only around 6% [5]. However, the contribution of renewables in the overall energy consumption is expected to increase from 3 to 8% by 2035, being the fastest growing energy source in the near future [6].

At the same time, it is estimated that 1.2 billion people (17% of the world population) live without electricity, while 2.7 billion (38% of the population) rely on the use of biomass for heat provision and thermal treatment of food[9]. Almost half of the primary energy is used by 10% of the population living in the most developed countries, while the lowest-consuming quarter of humanity uses only about 3% of global energy[10]. If their standards of living were to be raised to a level comparable to that of developed countries, the global energy demand would be greatly increased. As developing countries embark on the road of modernization and electrification, a new energy market will be necessary, which will pose an additional challenge for energy provision in addition to general population growth. The fact that fossil fuels will not be able to meet the energy demands at some point in the future is not an "if", but a "when". Some estimates suggest that this can happen as soon as *ca* 2030[11], while other state that fossil fuel production is currently at its peak, with expected future decrease[12].

Nuclear energy has been proposed as a substitute, and is widely exploited worldwide as it offers a steady and controllable supply of energy at an acceptable price. However, on one hand, nuclear fission power faces several serious problems: 1) it relies on finite stores of uranium 2) it produces 9-25 times more carbon per unit energy in comparison to renewables (uranium refining and transportation, reactor construction) 3) the ever-present possibility of incidents 4) increased chances of nuclear weapons proliferation 5) issues with radioactive waste disposal, etc.[13] Nuclear fusion, on the other hand, is still far from a stage of commercial implementation[14].

Renewables, on the other hand, suffer from limitations regarding upscaling. Nonetheless, from the overall capacity added in OECD (Organisation for Economic Co-operation and Development) countries in 2013, the biggest contributors were solar photovoltaics, *ca* 25%, and wind with *ca* 7%[5]. The fastest growing sectors of the energy industry in general are renewables (water, wind, sunlight - WWS) and nuclear.

In the year 2008, 12.9% of the world's overall energy consumption was provided by WWS sources[15]. The power capacity of renewable sources in the world is estimated to have increased by 128 GW in 2014 alone (of which *ca* 37% is wind, 33% solar, and 25% hydro), and contributed close to half of all the worlds energy additions[8]. In fact, as a result of growing energy demand, as well as concerns over local pollution issues, China, India, Brazil, and other developing countries account for about 2/3 of the expansion of renewable energy sources in 2015, with China alone contributing >40%[16].

The overall theoretical potential of wind and solar power far exceeds the projected future demands. It has been estimated that the overall deliverable wind power (wind speeds over 7 m/s and over land or near the shore) is about 72-170 TW, and deliverable solar is 240-340 TW[13].

Furthermore, as the impact of human activity on the climate system becomes increasingly pronounced[17], the need for cleaner energy grew into a pressing issue. CO_2 emissions from energy make up about 60% of all global greenhouse gas (GHG) emissions[18]. In 2014, the concentration of CO_2 was 397ppm (averaged marine surface annual mean value)[19], which is around 40% higher than in the mid-1800s with an average growth of 2ppm annually in the last decade[18]. In order to tackle the ongoing climate change, UN-member states have put forward the Paris Agreement[20], which aims to limit global warming to a maximum of 2°C by 2050. This means that industrialized countries must reduce their GHG emissions by 80-95% by 2050, compared to 1990, which entails a serious cutback in fossil-fuel consumption[21].

While CO_2 emissions in highly developed countries are not showing substantial growth due to significant efforts to reduce them, the emission rates in developing countries have been steadily increasing in the last decades because of their developing industries and increasing public use[18].

Urbanization provides a further incentive for the pursuit of clean energy provision at larger scales. The quality of life in large cities is becoming progressively more determined by the pollution. As the world is rapidly urbanizing (since 2008, for the first time in human history, more people lived in urban, than in rural environments[22]), this issue can be expected only to grow in importance in the future. It is clear that providing, e.g., alternatives to classical internal combustion engines for automotive applications is of paramount significance for the facilitation of a high quality of life in urban areas.

Moreover, the increasing demand for energy, combined with the limited and localized reserves of fossil fuels, is a source of continuous political instability. With the depleting reserves, such tensions are also expected to escalate in the future, and a failure to provide alternatives for fossil fuels could potentially lead to dire crises.

Finally, relying on only one or few sources of energy leaves economies vulnerable to various predicaments (market fluctuations, resource depletion, political issues, natural disasters, etc.). The diversification of energy sources generally results in an improved stability of energy provision and, consequently, economic and political stability as well.

The IEA projects that renewables will contribute over 2/3 of the global energy capacity expansion by 2020 and thus elevating the share of energy generation from 22% in 2013 to over 26% in 2020. The two main driving technologies behind this rise are onshore wind and solar

photovoltaics[15,23]. Some of the most ambitious estimates even state that it would be possible to achieve that all new additions to the global energy capacity until 2030 would be WWS sources, with a complete conversion by 2050, as no economic or technological, but only social and political obstacles exist to this goal[13].

1.2 The terawatt challenge and the hydrogen economy

For an energy source to make an impact on a global level, it must be possible to upscale it to the TW level. This notion has come to be known as the "The Terawatt Challenge"[24,25].

One of the major problems in the implementation of renewables, such as solar and wind power, on such scales is their varying performance. Their performance strongly depends on the weather conditions and production capacities do not "follow" demand. This means that under unfavorable weather conditions, their performance will be low; however, favorable conditions will result in a situation in which alternative sources may generate so much electricity that it is not possible to consume it all *via* grid distribution without proper storage. Additionally, it is considered that no more than 20% of the grid load can come from varying sources; otherwise, the functioning of the distribution is disturbed[26]. Figure 1.1, shows the power output of a single wind power station, and illustrates the output, which varies not only on a monthly, but on an hourly level as well.

In order to integrate greater capacities of renewables into the energy grid and for the wider implementation of these technologies, suitable energy storage is necessary[27,28] allowing these sources to be upscaled to the terawatt level. Chemical energy storage in particular has many desirable properties: high energy density, easy storage and transport, use of existing infrastructure, etc.

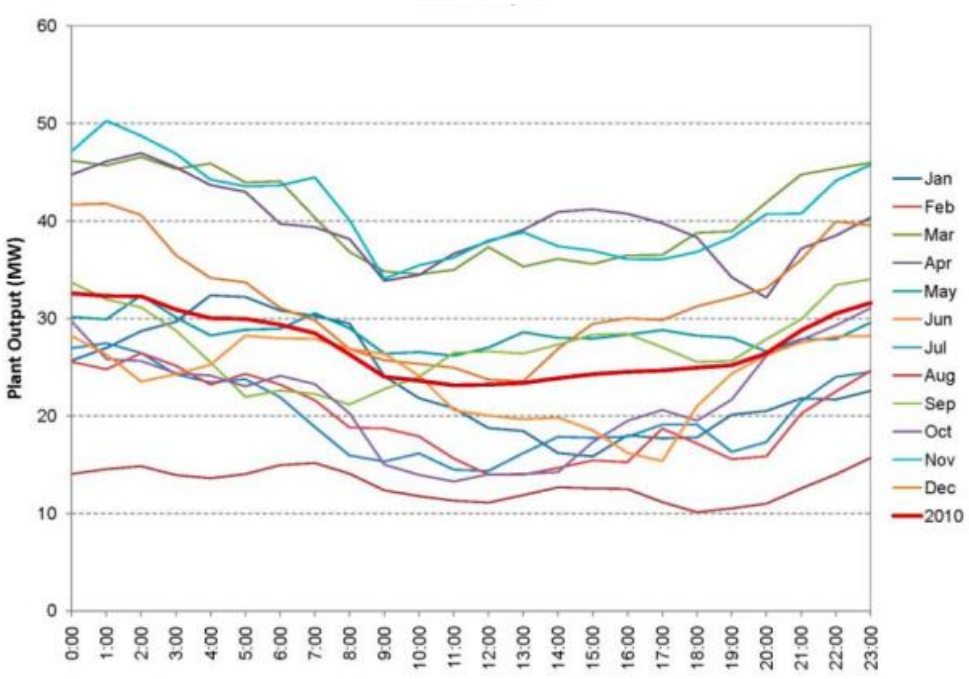

Figure 1.1: Variation of the energy output of the Blue Canyon Wind Farm, Oklahoma, USA. Figure taken from reference 29.

One of the proposed solutions to the aforementioned problems is the introduction of hydrogen as a wide-use fuel, as formulated, e.g., by John Bockris and John Appleby in their seminal 1972 paper "The Hydrogen Economy: An Ultimate Economy?"[30,31]. The hydrogen economy, in the simplest sense, is the idea of transporting and storing energy from renewables to the users in the form of hydrogen[32,33,34], as illustrated in Figure 1.2. The energy from renewable sources in this concept would be stored chemically - by the electrolysis of water to gain hydrogen. This hydrogen could be then used to generate electricity in fuel cells, or heat *via* combustion. Importantly, both of these processes are significantly less polluting than fossil fuel combustion[35] and they mainly result in the emission of water vapor.

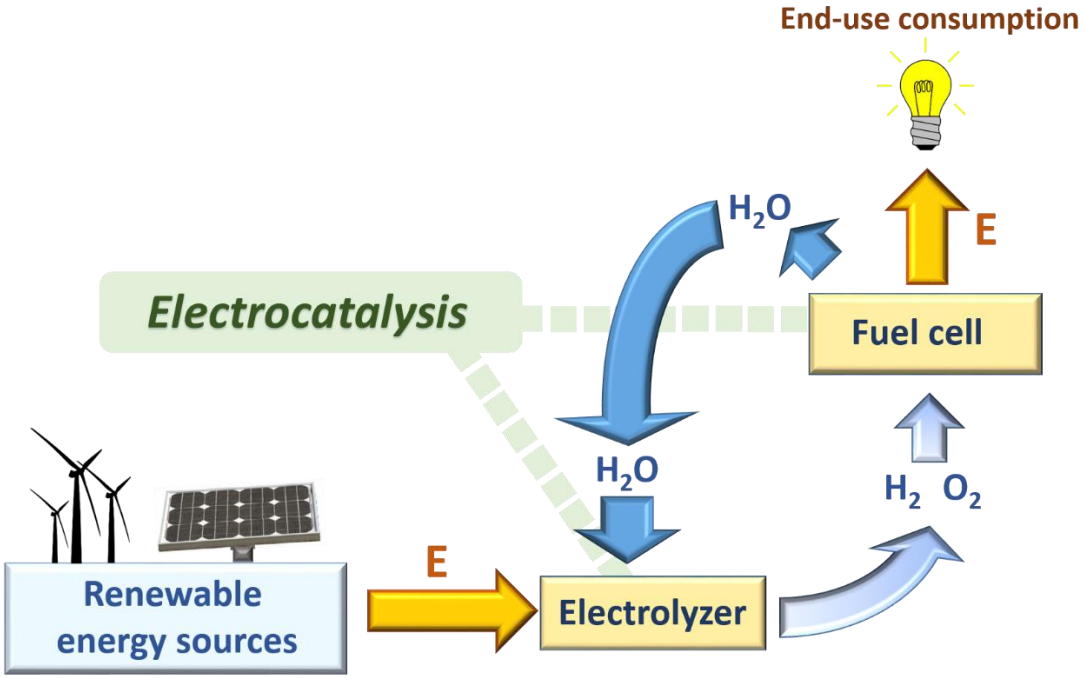

Figure 1.2: Schematic representation of the proposed "Hydrogen Economy". Renewables (WWS) are used to generate hydrogen at their peak production value, i.e., when they exceed the needs of immediate consumption. Hydrogen is then transported to users and converted to electricity in fuel cells. Electrocatalysis is crucial for the development of both types of energy conversion devices necessary for the implementation of hydrogen economy: electrolyzers and fuel cells.

In above-mentioned energy conversion stages, the electrolysis of water, and the use of hydrogen for electricity generation, electrocatalysis plays a crucial role. Besides the obvious technical difficulties in the transport and storage of hydrogen (new infrastructure, hydrogen leakage, economic viability, etc.[36]), there are several fundamental obstacles that need to be addressed in order to implement hydrogen as a widespread use fuel, among these, the most prominent are at least three, as indicated below[37,38,39]:

1. **The efficiency of electrolysis**. The production of hydrogen *via* water electrolysis is still a relatively expensive process. Most of H_2 is acquired from natural gas, as well as gasification of coal and heavy oil[40]. Less than 4% of the world hydrogen production is generated using

electrolysis nowadays[41,42,43]. Electrolysis is, for instance, applied when there are requirements for high purity hydrogen, since the electrolysis product contains virtually no contaminants. System efficiencies of modern commercial electrolyzers reach up to 73%[40,44]. For hydrogen generation to become competitive on the market, the energy efficiency of electrolyzers needs to be increased, as well as the stability of the implemented catalysts, thus lowering the cost of H_2-production[45].

2. **Hydrogen storage** is an issue that needs to be effectively solved in order for hydrogen to be implemented as a wide-use fuel particularly for automotive applications where it is considered one of the key "bottleneck" technologies[46,47]. The physical limitations of the compressed liquid hydrogen storage are a major restricting factor. However new approaches seek to store hydrogen in solids, as metal or complex hydrides[48]. The main properties of an ideal material should have near-ambient-condition operation, high H_2-storage density, and fast reaction kinetics.

3. **The efficiency of fuel cells** needs to be high enough to compete realistically with internal combustion engines, both in terms of price and performance[49]. It is estimated that the performance of the cathode electrocatalyst needs to be improved by 2-10 times[50,51,52] (according to different estimates) for this to be achieved, with improved catalyst durability as well[53]. At present, there is no FC technology fulfilling the technical requirements for vehicles with a range >750km with satisfying operational levels. The durability of fuel cell materials, particularly of proton-conducting membranes, also requires considerable improvements.

Some of the most fundamental among the above-mentioned problems are rooted in the lack of suitable catalysts for the reactions taking place during the operation of electrolyzers and fuel cells[54,55] regarding their efficiency, stability, and/or natural abundance.

The principal problem in the search for new catalysts is that, despite the vast amount of empirical data collected during the last century or so, there is not yet a comprehensive theory that can predict which material would be a good catalyst for a certain reaction. For this reason, the most common way to search for catalysts, often even nowadays, is the use of a trial-and-error approach. The drawback of this procedure is that it requires large amounts of experimental data and is therefore time- and resource-consuming.

The major goal of modern heterogeneous catalysis in general, and thus electrocatalysis as well, is to formulate a coherent theoretical framework that will allow the rational design of catalysts, i.e., provide *predictive power*. In order to advance towards the rational design of catalysts it is necessary to form a detailed understanding of the link between the interface status and electrocatalytic properties of the material[56]. In order to elucidate this link, first the basics of electrocatalysis will be laid out, followed by the statement of the state-of-the-art, and the formulation of the problem that will be addressed in this work.

1.3. The scope and the aims of this work

The understanding of the various effects that influence the electrocatalytic properties at a detailed and quantitative level needs to be substantially improved in order to enable the rational design of catalysts. The rational design should practically entail the identification of optimal surface sites, morphology, and electrolyte composition, and the subsequent design of systems with maximized desired properties. Additionally, the implementation of several of the aforementioned effects simultaneously can lead to better results, e.g. it has been suggested that changing electrolyte composition can change the nature of scaling[57].

The widely implemented, so-called "surface science approach" is to attempt to identify the active sites on the surface by using a number of well-defined single crystal surfaces for the catalysis of the reaction in question in standard ultrapure electrolytes. From the results of such experiments, the relations between the electrolytic interface status and electrocatalytic activity can be deduced (see, e.g., references 58, 59, and 60). Single crystals surfaces allow the separation of the various effects and the determination of the role of different crystal planes, steps, kinks, etc., as well as the effects of surface modifications, such as underpotential deposition (UPD), surface alloying (SA), near-surface alloying (NSA), creation of islands and cavities, etc. They also allow the elucidation of the influence of the electrolyte composition by enabling the testing the performance of particular well-defined surfaces in different electrolytes. The practical implementation of single crystals in operating devices is, however, not practical due to their high price, easy reconstruction, and difficult handling. The study of well-understood model single crystal surfaces, therefore, does not always fully elaborate the behavior of real-world catalysts, which are usually implemented as polycrystalline materials, in the form of nanoparticles or high surface-area thin films[6161,62,63,64] in order to minimize catalyst loading. The catalysts in these forms can display unique properties for which experiments with model surfaces are not sufficient to understand (e.g., the finite size effect, mass diffusion, substrate effect, cleanliness issues, etc.)[65,66,67,68,69]. Even though model surfaces provide invaluable information for the elucidation of fundamental phenomena at the interface, in order to develop applicable catalysts, the gap in the understanding between the well-defined model surfaces and practically applied catalysts must be surmounted.

Computational techniques can, of course indicate the optimal values of energetic descriptors[70,71]. However, this does not often provide sufficient information about the physical properties of the electrochemical interface that would exhibit such energetic factors. There is a significant gap in understanding between the desirable energetic properties and the ability to design a system with such properties. To overcome this, the development of easily assessable physical variables that can be logically linked to the energetics of the system is necessary.

The stability of the catalysts used in the "real-world" devices is extremely important as it determines the costs of their implementation and maintenance. Therefore, the creation of electrocatalysts stable under reaction conditions is important. Control over the selectivity of catalytic systems allows switching between different reaction pathways, which can be beneficial for a number of reasons. Selectivity is important not just because of energy efficiency, but also environmental and practical factors (generation of unwanted byproducts).

The aim of this work is to further elaborate the understanding of the factors that determine

the status of the electrode/electrolyte interface and, therefore, the electrocatalytic activity, selectivity and stability from the bulk of the electrodes to the electrolyte composition. Figure 1.3 shows a schematic illustration displaying the different factors that are subjects of this work and that are known to influence the electrocatalytic performance[72] regarding electrode design[73]: electrode material[74,75,76] and surface morphology[77]; and the influence of the electrolyte[78,79,80,81] including: non-covalent interactions at the interface[82,83], cation[84,85,86,87,88,89,90,91,92] and anion effects[93,94,95], concentration[96,97], pH effects[98,99], and presence of ionic liquids[100].

In order to elaborate the knowledge on the role of different factors that influence the status of the electrode/electrolyte interface, and consequently the catalytic activity, selectivity, and stability, several aspects of electrocatalytic system design are addressed in this work, as listed below.

1. The development of new methodologies for reliable and precise activity benchmarking.
2. Precise modification of the electrode material through bulk, as well as surface and subsurface alloying. New understanding of how to control and explain ligand and strain effects in different bi-metallic systems.
3. Further understanding of the influence of the surface morphology: what are the effects of defects and coordination governing the electrocatalytic activity?
4. Electrolyte composition: further steps in understanding of the cation, anion, pH, and ionic liquid effects.

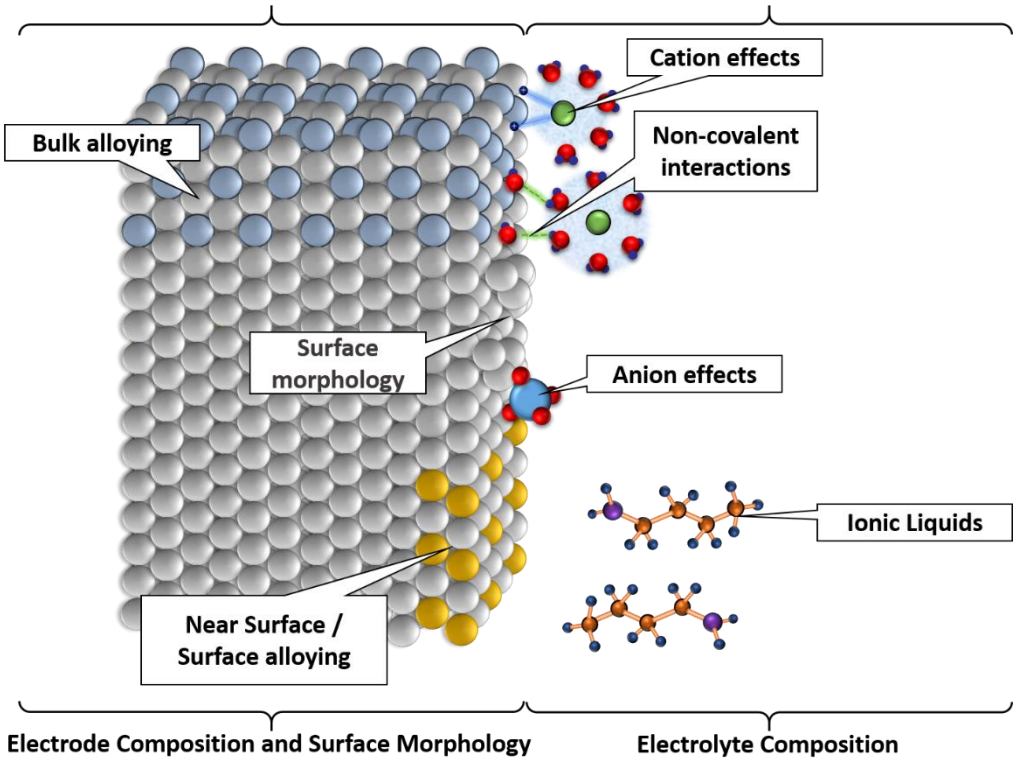

Figure 1.3: Illustration of the electrode/electrolyte interface and different effects that influence its status. Hence, by manipulating these factors, the activity, selectivity, and stability of electrocatalysts can be improved.

While all of the above-mentioned effects are known to influence the electrocatalytic properties, significant improvements in their understanding are necessary for their implementation in the rational design of catalysts. Further elucidation of these effects and possibilities of their implementation in the design of electrocatalytic systems are addressed in this work.

2. Theoretical considerations

2.1 Heterogeneous catalysis and electrocatalysis

A catalyst, by definition, is a substance that accelerates the rate of a chemical reaction, without taking part in the reactions itself[101]. This behavior of certain materials was first reported by Berzelius, as early as in 1836[102]. However, only after the formal definition of chemical thermodynamics by Clausius and Gibbs in the late 19th century, was an understanding of the role of the catalyst possible. While catalysts increase the rates of chemical reactions, they have no influence on the chemical equilibrium, i.e. "a catalyst is a substance that changes the rate but not the thermodynamics of a chemical reaction" as defined by F.W. Ostwald[103]. In a simplified sense, the reactant or reactants interact with the catalyst and form a complex, therefore opening a new pathway towards the reaction products.

If the catalyst and reactants exist in a common physical phase, then we consider that the reaction is homogeneously catalyzed. Conversely, if the reactants and the catalyst are in different phases – we deem it heterogeneous catalysis. Heterogeneous catalysis has many advantages in practical applications, among others the easy separation of the products from the catalyst, the easy replacement of the catalyst itself, and additional degrees of freedom in catalyst design (morphology, nanoparticulate implementation, alloying, etc.)

The ideal catalyst should have certain basic properties[70]:

1. *Activity*: high reaction turnover rate. In electrocatalysis, the activity can be expressed in several ways, usually it is represented as current density (as the current is indicative of the reaction rate at the electrode), but it can also be indicated as overpotential, activation barrier, halfwave potential, etc.

2. *Selectivity*: the catalyst should facilitate only the desired reaction(s). Selectivity describes the particular activities of specific reaction pathways. This is linked to the ability of a catalyst to favor particular reaction pathways, the optimization of which is usually not a trivial task, since it involves complicated assessments in the changes of energy barriers of particular pathways, further complicated by scaling relations. For practical purposes, side-reactions and unwanted reactions should be suppressed in order to maximize catalyst efficiency, and obtain a clean and more environmentally friendly product[104].

3. *Stability*: even though the catalyst itself does not participate in catalytic reactions that does not mean its state is unaffected by the ongoing processes. The state of the catalyst surface undergoes various changes during the catalytic cycle, which can render the catalyst inactive or lead to its destruction. Therefore, one of the main requirements for practical applications is that the catalyst should not degrade quickly.

Activity and selectivity are closely linked to another important catalytic property (especially for practical industrial applications) – energy efficiency. In general, the more active (higher production rate) and the more selective (energy is not wasted on undesired processes) a catalyst is, the more energy efficient the process is. Although in order to upscale to industrial levels, other factors, such as heat and mass transport in the reactor, need to be taken into account as well.

It should be noted that electrocatalysis, as a part of heterogeneous catalysis, is a special field in which chemical reactions are driven by electric current resulting in the oxidation/reduction of the reactant *via* electron transfer at the electrodes. While electrocatalysis and classical heterogeneous catalysis share many of the fundamental principles, a key difference that additionally complicates electrocatalytic systems is the fact that the processes occur at an electrified interface, where charges in the proximity of the active centers[105] must be taken into account.

The advantage of electrochemical over chemical reactions is in the additional degree of freedom offered by the adjustable potential (or current). This allows the variation of the energy of the active species in a continuous manner, opening up many new possibilities. What is achieved in classical catalysis by temperature changes can be in many cases also achieved in electrocatalysis by changing of the potential[106], sometimes with significantly higher energy efficiency and selectivity. In the following chapters, the basic principles of catalysis and electrocatalysis will be discussed.

2.2 The Sabatier principle

Paul Sabatier formulated this principle in 1902[107], and it is considered as one of the basic tenets of heterogeneous catalysis. It is based on the premise that the reaction intermediates bind to the catalysts surface, and it states that the binding energy between the surface sites and the reactant or intermediate should be strong enough to activate the reactant species, but not so strong that the surface is blocked by intermediates or the products for a significant amount of time. This means that for a reaction there is an ideal binding energy, which results in the most efficient facilitation of the reaction. The highest turnover rate is a result of efficient activation, in concord with catalytic centers being free for adsorption for the longest possible time.

The Sabatier principle is a purely qualitative rule that states general trends in heterogeneous catalysis. From the principle itself, one cannot state what the ideal bond strength is, or even what quantity should be used to quantify the value of "bond strength"[57]. While this general principal was known more than a century ago, its quantification was achieved more than six decades later (see section 2.4).

2.3 Active sites

The Sabatier principle does not state where the adsorption of the reactants and intermediates at the surface should take place[108]. However, their adsorption is not equally likely and differs in energetics on different sites on the surface, which is not homogeneous at the atomic level. This was first claimed by Langmuir in 1922, and further developed by Taylor in 1925[109]. Taylor recognized that not all surface atoms would be equally active towards the catalysis of a certain reaction, and introduced the idea of active sites. Active sites are specific parts of the surface, which bind intermediates and actively participate in the facilitation of the reaction in question. The active site can be an atom, a set of atoms, or an ensemble. A mandatory requirement is that they must be available for adsorption.

Depending whether a specific surface structure is necessary in order to promote a certain process, electrochemical reactions can be arbitrarily divided into two categories[110]:

1. Structure-insensitive reactions are reactions for which all surface sites seemingly exhibit equal activity. They usually involve some kind of surface restructuring or outer-sphere reactions[54] in which there is no strong interaction between the electrode and the reactant.

2. Structure-sensitive reactions are those for which adsorption of the reactant and/or reaction intermediates takes place at specific sites on the surface[65,111]. This implies a strong interaction between the surface and the substrate, i.e., chemisorption.

2.4 Volcano plots. Descriptors and activity indicators. Scaling relations.

In some cases the quantification of the Sabatier principle can be achieved by the construction of so-called "volcano plots", which take into account energy relations, such as the Bronsted-Evans-Polanyi equation[112]. For instance, Parsons and Gerischer[113,114] observed in the 50s that the hydrogen adsorption free energy is indicative of the HER activity on different catalysts. A.A. Balandin proposed to use the volcano plots, as summarized in the perspective paper dated 1969[115], as a representation of such activity trends in heterogeneous catalysis. Later Trasatti (1972) demonstrated that the concept of the volcano plots could be successfully used in electrocatalysis as well.

In order to construct the volcano plots, a variable descriptive of the electrocatalytic activity (such as the current density, halfwave potential, or overpotential) is plotted *versus* a "descriptor", which is a variable directly connected to the properties of the surface and interface[116]. While the interface is a very complicated system, the properties of which depend on many parameters, often it is possible to define a single variable, a "descriptor", which dominantly controls its properties and describes the catalyst at a level of detail relevant for its catalytic activity. Usually the descriptor is the surface binding energy, or a variable logically linked to it such as, e.g., the heat of adsorption (which is often easier to estimate), although historically other quantities were used as well, such as the heat of formation of an oxide or other suitable compounds.

A schematic representation of a volcano plot is shown as an example in Figure 2.1, where the current density is plotted as a function of the intermediate binding energy.

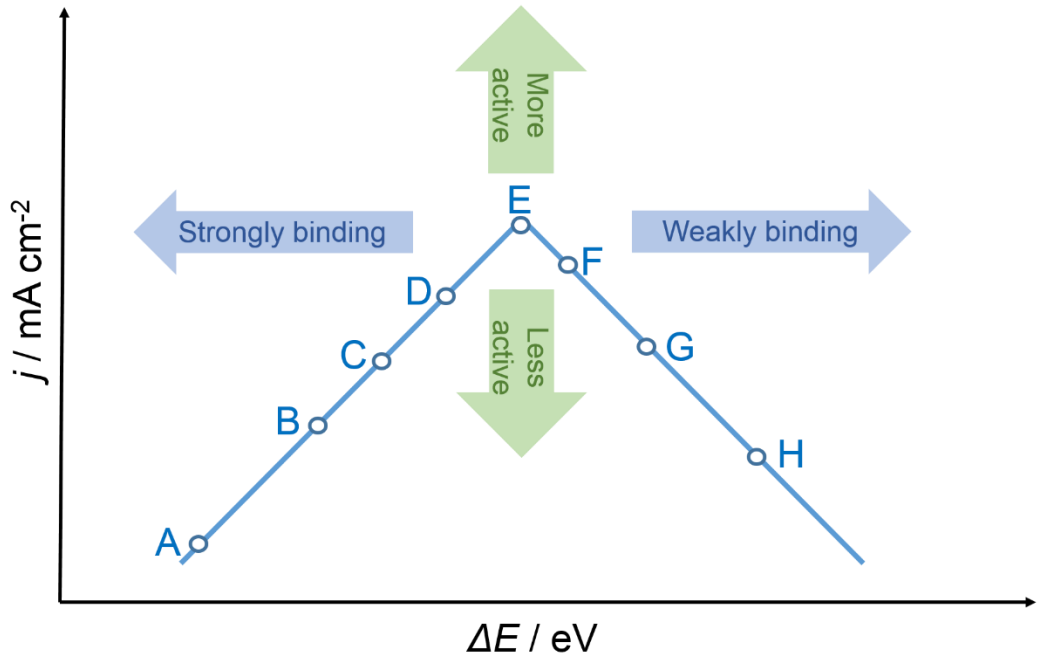

Figure 2.1: Schematic representation of a volcano plot. The activity defined in terms of current density is plotted versus the binding energy of the intermediate to the surface. The catalysts on the left (A, B, C, D) of the optimum (E) are binding too strongly, and their activity is thus generally limited by the desorption of the products. The catalysts on the right (F, G, H) are binding more weakly than optimal, and their activity is generally limited by the insufficient activation of the reactant.

The activity-binding energy plots take on a "volcano" shaped dependence with the ideal catalyst (in this case E) lying at the top, as higher current densities indicate higher catalytic activity. Materials lying to the left from the top bind the intermediate too strongly, which generally means that the removal of the product form the surface is the rate-determining step. Those on the right side bind more weakly than ideal.

Norskov et al.[117] pointed out that there would be a universal and reaction-independent relation connecting the activation energies and stabilities of important intermediates in a particular reaction, allowing the estimation of reaction barriers from thermodynamic data[118] and justifying the use of the heat of adsorption as an activity descriptor. Although the volcano plots provide a good overview of the catalytic properties of materials and allow the observation of trends, the fine-tuning of the catalytic properties requires a detailed understanding of the link between the electrocatalytic properties and the interface status.

For a reaction that involves the transfer of only one electron, without any intermediates, the reaction rate is determined primarily by the solvent and ligand reorganization around the species. For reactions with one intermediate (2 electron transfers), the binding energy of the single intermediate can be modified independently and an ideal catalyst might be identified with a zero thermodynamic potential. However, if there are several intermediates (which is often the case) their binding energies generally cannot be changed independently. They are often linked through scaling relations and the process of finding an ideal catalyst is a

multiparametric optimization problem that leads to a non-ideal catalyst, with a non-zero overpotential.[119,120]

Thus, thee binding energies often scale linearly with each other and the optimization of the intermediates' binding energies is difficult due to their interdependence[74,121,122]. This means that by changing the binding energy of one intermediate the binding energies of all other intermediates are changing as well, so the number of independent variables describing the surface is limited.

The scaling relation between two species 1 and 2 can be mathematically expressed as[121,123]:

$$\Delta E_1 = \gamma \Delta E_2 + \xi \qquad \text{(Eq. 1)}$$

where γ and ξ are constants of the given adsorbates on the given crystal facet (γ can often be linked to the ratio of the number of "unsaturated"† bonds for the adsorbates[74]) and ΔE_1 and ΔE_2 are the adsorption energies of species 1 and 2.

One of the simplified explanations of the origin of this phenomenon lies in the fact that, generally, in a reaction with several intermediates, all the intermediates are bound to the surface sites through the same atom. While the changes occurring in the rest of the species affect the binding properties, the difference they exhibit at different substrates will always change proportionally.

The limitations in activity improvement that appear due to the non-optimal scaling, i.e., the sub-optimal relations between the binding energies, could be theoretically addresse[57] if the active site would be capable of changing its geometry during the course of the reaction, thus breaking the linear dependences. Such specialized catalysts already exist in nature - enzymes, and they are widely used by living organisms to promote various reactions. However, enzymes are notoriously complex in comparison to practical catalysts and their rational design is not close to practical application. Additionally, natural enzymes are highly specialized and catalyze only specifically targeted reactions. The other potential possibility to break the constraints of scaling is that the intermediates could be very mobile on the surface, so they can "utilize" several active sites to achieve ideal activation. This makes multicomponent catalysts particularly attractive for reactions that require the adsorption of several molecules (e.g., CO hydrogenation, HOR, etc.), as dissimilar atoms at the surface can display optimal binding for different reactants simultaneously[57].

In a reaction which requires the dissociation of a bond in the reactant, the rate of dissociation will be determined by the activation barrier for dissociation E_a, while the rate of the product removal (after undergoing the transformation steps following dissociation) will be determined by the stability of the intermediates at the surface – ΔE. A good catalyst for such a reaction would have a high ΔE_a (lowering the activation barrier) and a low ΔE. However, since there is a linear Bronsted-Evans-Polanyi[116,124,125]-type relationship linking them together, there is an optimal "compromise" between the values of these two variables in accordance with the Sabatier principle. Therefore, the scaling relations are not merely an empirical finding, but they

† "Unsaturated" in this sense means the number of bonds the species lacks o reach a stable electron configuration, i.e., to reach its valence number.

are related to the fundamentals of chemical bonding and catalyst-substrate interactions, such as electron counting rules, bond-order conservation, configurational correlation, etc.[74]

The volcano plots, as a quantification of the Sabatier principle, sometimes coupled with theoretical procedures such as density functional theory (DFT) provide a powerful tool for the prediction of catalytic properties [126], and as such, they take a pivotal role in modern electrocatalysis.

2.5 The electrochemical interface and the electrocatalytic activity

A general definition of the interface is that it is the physical separation between two phases in a heterogeneous system, which cannot be described as a simple mathematical surface of discontinuity. The electrochemical interface is defined as the high heterogeneity zone, i.e., a narrow area (in the order of magnitude of nanometers) that lies between, e.g., materials of different conduction modes (electronic and ionic). Within the interface, parameters, such as concentration, have large gradients and show a discontinuity at the interface on macroscopic levels[127].

The properties of the interface, as such a complex multiparametric system, depend on many different variables and effects, most notably: the electrode material, surface morphology, the composition of the electrolyte, temperature, pressure (if the reactants or products are gaseous), etc. Since most electrode reactions involve the chemisorption of reactants and reaction intermediates to the electrode surface, the electrocatalytic properties of a material are highly sensitive to the status of the electrochemical interface. It has been shown that coordination plays a significant effect on the electrocatalytic properties of surface atoms[128,129]. Coordination affects the electronic structure, and therefore the electrocatalytic properties of the surface atoms as well.

Alloying presents a very common approach in designing catalytic materials, since bi- or multi- metallic catalysts possess an additional degree of freedom (the composition of the alloy) for the fine-tuning of their properties. This is important since metals neighboring in the periodic table can exhibit binding energies that differ as much as 1eV for the same intermediate[130]. Meaning that if one metal binds slightly too strongly, the closest "neighbor" in terms of binding energy can already bind too weekly, and vice-versa. By changing the composition of the alloy or the alloying element, one can create materials with different binding energies unlimited by the discontinuity of the properties of pure metals.

The electronic structure, and consequently the electrocatalytic activity of two (or more)-component catalysts is determined by a number of parameters, which are in general considered to be the result of several effects[60, 61,131,132]:

1. *Ensemble effects*, which arise due to the different functional roles ensembles of atoms, may take on the surface.

2. *Ligand effects,* which exist due to the presence of a dissimilar neighboring atom in the immediate vicinity of a surface atom, which influences its electronic structure.

3. *Strain effects*, which occur due to the difference in the lattice parameters between different phases, which introduces strain, either compressive or tensile, in the crystal lattice.

In most materials, these effects appear simultaneously and are, therefore, difficult to decouple and consider independently.

Other effects that can affect the number and properties of the catalytic centers are particle size (for powders and nanoparticles), catalyst-support interactions, poisoning by side-products, catalyst surface degradation, etc.

In order to investigate such complex systems, all the parameters must be carefully evaluated and varied, while others are kept constant, in order to isolate the specific influences. This requires the use of well-known systems: electrodes with well-defined crystal surfaces, high-purity electrolytes of well-known properties, ultrapure conditions, and careful probing of the system in question.

2.6 Electrochemical systems and reactions

In common definitions, electrolytes contain chemical compounds that can dissociate into ions in their solid, liquid, or dissolved state. Ions in aqueous solutions become surrounded by a sheath of solvent molecules, in a process called solvation (or if the solvent is water – hydration). When ions are subjected to an electric field, they are under the influence of a force F[133]:

$$F = ze_0E \qquad \text{(Eq. 2)}$$

where z is the charge of the ion, e_0 is the elementary charge, and E is the strength of the electric field. Under the influence of this field, the ions are set in motion. This leads to an organized movement of charged particles, i.e., the flow of electric current in the electrolyte.

An electric field in the electrolyte is applied to electrochemical systems by the introduction of at least two electronic conductors (usually metals, carbon, but also certain oxides, semiconductors, etc.) and applying a potential difference. The electronic conductors used for this purpose are called electrodes.

The ions migrate towards the electrode with the opposite signs: cations towards the negative electrode, and anions towards the positive one. When the ions arrive to the electrodes they will undergo electron exchange if the potential difference between the electrodes, i.e., the cell voltage exceeds a certain value – the decomposition potential, E_D. In this process, generally the more negative ions would "give away" electrons, i.e. they would oxidize, while the more positive ones would accept electrons, and become reduced. This whole process is termed *electrolysis*, and the system - an *electrolyzer*. If the reactions are reversed, and the reactants are brought to the electrodes where they similarly undergo redox reactions, as a result of which a current flows through the electronic conductor connecting the electrodes, the system is called a *galvanic cell*. Galvanic cells directly transform chemical into electrical energy. The two most important types of galvanic cells for energy provision are *batteries* and *fuel cells*. They differ in the fact that in batteries the fuel is an integral part of the device, while for fuel cells the fuel needs to be supplied externally.

Irrespective to the mode in which the electrochemical cell is operating, the electrode at which a reduction is taking place is referred to as the *cathode*, and the current at the cathode is flowing towards the electrode. Conversely, oxidation takes place at the *anode*, and the current is flowing towards the electrolyte.

The reactions taking place in an electrochemical cell can always be divided into two, spatially separated, so-called "half reactions" or "electrode reactions", which individually denote a process taking place at a single electrode. For the general reaction:

$A^a + B^b \leftrightarrows C^c + D^d$

The half-reactions can be written as:

Anode: $A^a \leftrightarrows C^c + (c-a)e^-$

Cathode: $B^b + (b-d)e^- \leftrightarrows D^d$

When written in this format the number of electrons that are exchanged in the anodic and cathodic reaction must be the same.

When examining electrochemical systems, the variables that are most often observed are a) the potential difference between the electrodes and b) the current flowing through the cell.

However, if one monitors the current and the potential simultaneously in such systems, one can observe that these two variables are not independent. In fact, in a cell operating as an electrolyzer the potential between the electrodes increases with the increasing current:

$$E = E_D + iR \qquad \text{(Eq. 3)}$$

where i is the current flowing through the system, and R are the internal resistances of the cell. Conversely, in a galvanic cell the potential decreases with the increasing current:

$$E = E_0 - iR \qquad \text{(Eq. 4)}$$

where E_0 is the rest potential, equal to the electromotive force (*EMF*) of the cell, which is observed in the galvanic cell when the external resistance is very high so no current flows between the electrodes. The potential current dependence for electrolyzers and galvanic cells is illustrated in Figure 2.2.

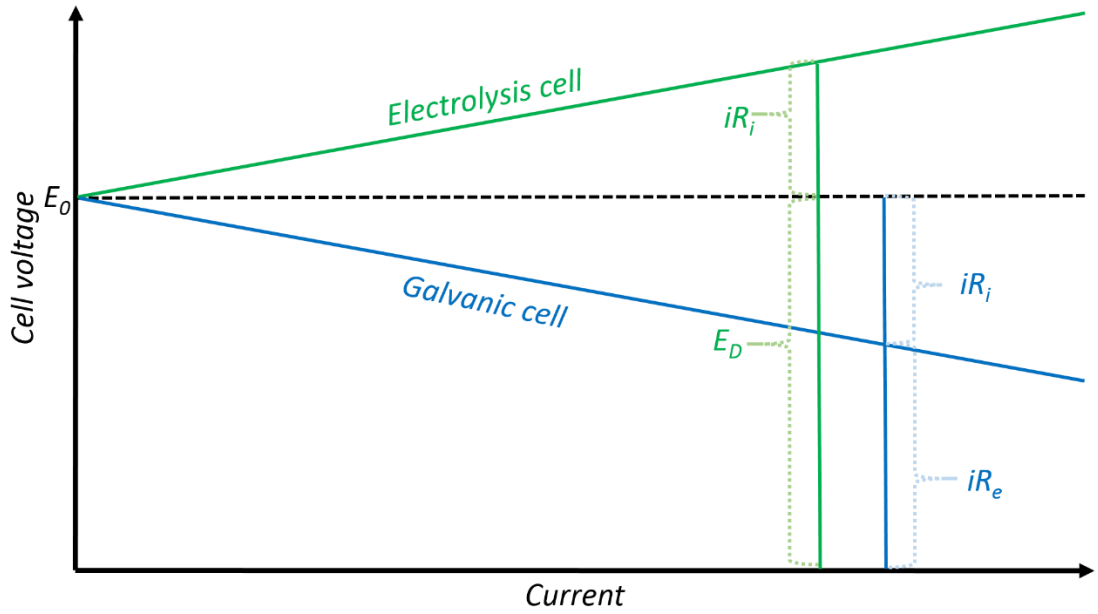

Figure 2.2: Schematic representation of the cell voltages in galvanic cells (—) and electrolyzers (—) in dependence of the current flowing through the system. E_0 – voltage at zero current, E_D – decomposition voltage, R_i – internal cell resistances, R_e – external resistances, *i*-current[133].

The amount of any substance developing at the electrode during electrolysis is closely related to the amount of charge (q) that passes through the interface, and, consequentially, to the current passing through the system (i_e). This means that the amount of substance (or its mass, m) obtained during the time of electrolysis t must be proportional to these values as well:

$$m = const \cdot q = const \cdot i_e \cdot t \qquad \text{(Eq. 5)}$$

This relation was first reported by Michael Faraday in 1833[133], who established it entirely empirically. As later the concepts of molarity and elementary charged were introduced, the full equation became better known in the form:

$$m = \frac{MQ}{ze_0N_A} = \frac{Q}{F}\frac{M}{z} = \frac{ItM}{Fz} \qquad \text{(Eq. 6)}$$

where M is molar mass, Q – charge, z – charge of the ion, e_0 – elementary charge, N_A – Avogadro's number, F – Faraday constant, I – the current, t – time.

However, as already mentioned, a certain reaction will take place at an electrode in an electrolyzer only if its potential has exceeded a certain value. Below that potential, the reaction does not occur and the current does not flow through the interface. In order to describe an electrochemical system, and predict its behavior, the potentials of the electrodes need to be defined.

While the absolute potentials cannot be measured, the potential difference between two phases at equilibrium (when no current flows) can be calculated theoretically. The chemical potential of the i^{th} component of a mixture is defined as[133]:

$$\mu_i = \mu_i^0 + RTlna_i \quad \text{(Eq. 7)}$$

where μ is the chemical potential, a – the activity, and μ_0 – the chemical potential for $a=1$, R – universal gas constant, T – temperature. μ_i^0 is the chemical potential when the value of the activity is 1. The condition for the existence of an equilibrium between two phases I and II is:

$$\mu(I) = \mu(II) \quad \text{(Eq. 8)}$$

At equilibrium conditions, Equation 8 is valid for every species within those phases. In electrochemical systems, at electrified interfaces, the potential difference needs to be taken into account in thermodynamic equations. For a component i at the boundary of two phases the equilibrium condition becomes:

$$\mu(I) + z_iF\varphi(I) = \mu(II) + z_iF\varphi(II) \quad \text{(Eq. 9)}$$

The expression $\mu(I) + z_iF\varphi(I)$ defines the *electrochemical potential*, $\tilde{\mu}$. The full expression for which is, therefore:

$$\tilde{\mu}_i = \mu_i^0 + RTlna_i + z_iF\varphi \quad \text{(Eq. 10)}$$

Hence, the condition for the general electrochemical equilibrium is:

$$\sum_i \nu_i \tilde{\mu}_i = 0 \quad \text{(Eq. 11)}$$

For a general redox reaction, of an electrode of element A immersed in solution and undergoing a redox reaction described by the equation:

$$A^0\,(M) \leftrightarrows A^{x+}(aq) + xe^-(M)$$

The equilibrium condition becomes:

$$\tilde{\mu}_A(M) = \tilde{\mu}_{A^{x+}(aq)} + x\tilde{\mu}_{e^-}(M) \quad \text{(Eq. 12)}$$

Given that the species A is assumed to be electroneutral, it is not influenced by the electric field, so in this case: $\tilde{\mu}_A = \mu_A$, so, considering Equations 10-12, the equilibrium condition becomes:

$$\mu_A^0(M) + RTlna_A(M) = \mu_{A^{x+}}^0(aq) + RTlna_{A^{x+}}(aq) + xF\varphi_{aq} + x\mu_{e^-}^0(M) + x\,RTlna_{e^-}(M) - xF\varphi_M \quad \text{(Eq. 13)}$$

From this equation, the Galvani potential difference between the electrode and the solution can be obtained, with the approximation that the concentrations of both atoms A in the electrode and electrons will be constant. The activities of solid substances are considered unity by convention. The potential difference between the electrode and the solution is, thus:

$$\Delta\varphi = \varphi_M - \varphi_{aq} = \frac{\mu_{A^{x+}}^0 + x\mu_{e^-}^0 + \mu_A^0}{xF} + \frac{RT}{xF} lna_{A^{x+}} = \Delta\varphi^0 + \frac{RT}{xF} lna_{A^{x+}} \quad \text{(Eq. 14)}$$

where $\Delta\varphi_0$ is the *standard Galvani potential difference*, which is the Galvani potential difference between the electrode and the solution in case $a_{A^{x+}} = 1$.

As it is not possible to define the absolute value of a potential, $\Delta\varphi$ and $\Delta\varphi_0$ are not experimentally measurable. Therefore, potentials are usually expressed in comparison to a

known reference point. If a third electrode with a constant Galvani potential difference $\Delta\varphi'=const$, is introduced into the solution, then the potential of the working electrode (WE), i.e., the electrode which is investigated, can be measured in respect to this electrode, which is referred to as the *reference electrode* (RE), $E = \Delta\varphi - \Delta\varphi'$. The standard electrode potentials at unit activity will allow the measurement of $E_0=\Delta\varphi_0 - \Delta\varphi'$, (since $\Delta\varphi'=const$):

$$E - E_0 = \Delta\varphi - \Delta\varphi' - (\Delta\varphi_0 - \Delta\varphi') = \Delta\varphi - \Delta\varphi_0$$

By measuring the potential difference between the RE with a constant potential and the WE, i.e., the electrode that is being investigated under different conditions, we are practically following the potential changes of the WE independently of the potential of the RE.

In electrochemistry, usually a well-defined redox couple of a known potential is implemented as a reference point (in physics the reference to the vacuum state is used as an "absolute scale", i.e., *versus* an electron at rest in vacuum). The standard hydrogen electrode (SHE)[134] is a widely accepted reference point as it establishes its equilibrium potential quickly and reproducibly, and maintains it well over time. In the SHE, the following reaction takes place:

$$H_2 + 2H_2O \leftrightarrows 2H_3O^+ + 2e^-$$

All components are assumed to be of unit activity, so the SHE can be generally represented as:

$$Pt/\ H_2(a=1,\ g)/H^+(a=1,\ aq)$$

The SHE is a rather theoretical electrode and contemporary devices can only approach its behavior. For practical applications in electrocatalysis the reversible hydrogen electrode (RHE) is often used, as this way the measured potential "does not depend" on the *pH*. The potential of the RHE is linked to the SHE potential through the following equation:

$$E_{RHE} = E_{SHE} + 0.0591 \cdot pH \qquad \text{(Eq. 16)}$$

Further considering Equation 15 gives:

$$E = E^0 + \frac{RT}{xF} ln a_{A^{x+}} \qquad \text{(Eq. 17)}$$

Alternatively, in the general case:

$$E = E^0 + \frac{RT}{zF} ln a_{M^z} \qquad \text{(Eq. 18)}$$

where *z* is the symbol for the overall charge of the ion.

This equation is called the Nernst equation, after Walther Nernst who first formulated it; but in this form, it applies only to the aforementioned special case. In case there are several species undergoing redox processes, such as for the general reaction:

$$\nu_1 S_1 + \nu_2 S_2 + \ldots + \nu_i S_i + ne^- \leftrightarrows \nu_j S_j + \ldots + \nu_k S_k$$

where ν are the stoichiometric coefficients, and *S* are the particular chemical species under consideration, the equation becomes[133]:

$$\sum_{ox} \nu_{ox}\tilde{\mu}_{ox} + n\tilde{\mu}_{e^-} = \sum_{red} \nu_{red}\tilde{\mu}_{red} \quad \text{(Eq. 19)}$$

$$\sum_{ox} \nu_{ox}\left(\mu_{0,ox} + RTlna_{ox} + z_{ox}F\varphi(I)\right) + n(\mu_{e^-} + RTlna_{e^-} - F\varphi(I)) \quad \text{(Eq. 20)}$$
$$= \sum_{red} \nu_{red}\left(\mu_{0,red} + RTlna_{red} + z_{red}F\varphi(II)\right)$$

$$E = E^0 + \frac{RT}{nF} ln\left(\frac{\prod_{ox} a_{ox}^{\upsilon_{ox}}}{\prod_{red} a_{red}^{\upsilon_{red}}}\right) \quad \text{(Eq. 21)}$$

Which is termed *the generalized Nernst equation for the half-cell.* This equation relates the potential of the half-cell to the activities of the species in the reaction, temperature and the standard electrode potential.

The electrochemical potential of the whole cell will be given as the difference of the half-cell potentials of the anode and the cathode:

$$\Delta E = E_a - E_c \quad \text{(Eq. 22)}$$

In practice, however, it is observable that even when these potentials are reached, e.g., in an electrolyzer, the desired reactions are not detected, due to the activation energy barrier, losses in electrochemical cell, or slow kinetics. The potential difference between the potential at which a certain electrochemical process is thermodynamically possible and the potential at which the given process is observed is called *overpotential*, and it is defined as[133]:

$$\eta = E - E_{eq} \quad \text{(Eq. 23)}$$

where E is the potential at which the particular process takes place, while E_{eq} is the equilibrium potential, at which it should take place according to thermodynamics.

There are several sources of overpotentials, and different ones will be the main contributors to the overall value under different conditions. At low current densities, the limiting rate of the electron transfer through the interface is the dominant cause, and is termed *transfer overpotential.* At higher current densities, limitations arise due to the sluggishness of mass transport – *diffusion overpotential,* or due to chemical changes associated with the electron transfer – *reaction overpotential*.

The rate of an electrode reaction depends on several parameters: the nature of the electrodes, the composition of the electrolyte (specifically, the composition of the electrolyte in the immediate vicinity of the electrodes), the electrode potential, and the overpotential of the reaction under the given conditions.

According to the activated complex theory, the forward, υ_f, and backwards, υ_b, rates of a reversible reaction of the type A + e^- → B are:

$$\upsilon_f = k_f^0 C_A e^{\frac{-\Delta G_f}{RT}} \quad \text{(Eq. 24)}$$

$$v_b = k_b^0 C_B e^{\frac{-\Delta G_f}{RT}} \quad \text{(Eq. 25)}$$

where k_f^0 and k_b^0 are the forward and backward reaction standard rate constant, C_A and C_B are the concentrations of the reactants, and ΔG_f is the free energy difference for the reaction in question.

If the potential of the electrode changes by $\Delta E = E - E^0$, the relative energy of an electron in the electrode will alter by $-F\Delta E$. If ΔE is positive, i.e., if the potential of the electrode is raised, the oxidation barrier ΔG_a will be lowered by a fraction of the electrode potential change. This fraction will be noted as $(1-\alpha)$, where α is the *transfer coefficient* ($0<\alpha<1$). Therefore, we have[133]:

$$\Delta G_a = \Delta G_{0,a} - (1-\alpha)F(E - E^0) \quad \text{(Eq. 26)}$$

At the same time, the height of the cathodic (reduction) barrier is increased by:

$$\Delta G_c = \Delta G_{0,c} + \alpha F(E - E^0) \quad \text{(Eq. 27)}$$

The rate constants k_f and k_b take on an Arrhenius-type form:

$$k_f = A_f e^{\frac{\Delta G_c}{RT}} \quad \text{(Eq. 28)}$$

$$k_b = A_b e^{\frac{\Delta G_a}{RT}} \quad \text{(Eq. 29)}$$

By inserting the activation energies (Equations 26 and 27) here, we get:

$$k_f = A_f e^{\frac{\Delta G_{0,c}}{RT}} e^{-\alpha f(E-E^0)} \quad \text{(Eq. 30)}$$

$$k_b = A_b e^{\frac{\Delta G_{0,a}}{RT}} e^{(1-\alpha) f(E-E^0)} \quad \text{(Eq. 31)}$$

where $f = F/RT = e/kT$. The first two factors in these expressions yield a product independent of the potential, which is equal to the rate constant for $E = E^0$.

If the interface is at equilibrium with the solution in which bulk concentrations of the oxidized and reduced species are equal $C_o^* = C_r^*$, the following statements are true:

$$E = E^0 \quad \text{(Eq. 32)}$$

$$k_f C_o^* = k_b C_r^* \quad \text{(Eq. 33)}$$

$$k_f = k_b \quad \text{(Eq. 34)}$$

This means that at the potential E_0 both rate constants have the same value $k_f = k_b = k_0$, so they can be expressed as:

$$k_f = k^0 e^{-\alpha f(E-E^0)} \quad \text{(Eq. 35)}$$

$$k_b = k^0 e^{(1-\alpha) f(E-E^0)} \quad \text{(Eq. 36)}$$

Combining these with the equation for the net cell current density ($j = j_c - j_a$) yields:

$$j = j_c - j_a = nF[k_f C_0(t,0) - k_b C_r(t,0)] \quad \text{(Eq. 37)}$$

where n is the number of electrons exchanged, $C_0(t,0)$and $C_r(t,0)$ are the concentrations of the oxidized and reduced species in the immediate vicinity of the electrodes in moment t, and A is the electrode surface. Taking into account the expression for the overpotential (Eq. 23), the following relationship between the overpotential and the current density is obtained[134]:

$$j = Fk^0(C_0(t,0)e^{-\alpha f(E-E^0)} - C_r(t,0)e^{(1-\alpha)f(E-E^0)}) \quad \text{(Eq. 38)}$$

Equation 38 is commonly known as the *Butler-Volmer equation*. If we define the exchange current density j_0 as the current flowing through the interface at zero net current and zero overpotential (which is strongly dependent on the electrode material, and is a good indicator of the activity of a material) as:

$$j_0 = Fk^0 C_R^{1-\alpha} C_O^{\alpha} \quad \text{(Eq. 39)}$$

Equation 38 becomes:

$$j = j_0 \left(e^{-\frac{\alpha F\eta}{RT}} - e^{\frac{(1-\alpha)f\eta}{RT}}\right) \quad \text{(Eq. 40)}$$

The Butler-Volmer equation is extremely important as it shows the relationship between the overpotential and the current density, which is indicative of the reaction rate. It is used (or some variation of it) in the treatment of most problems that require the consideration of electrode kinetics.

2.7 Important electrocatalytic reactions in energy conversion and storage

For energy conversion and storage in the hydrogen economy, the most significant processes are water splitting, where hydrogen gas is generated, and the reactions taking place in fuel cells, where hydrogen is used as a fuel.

Water splitting or "water electrolysis" is the generation of gaseous hydrogen and oxygen from aqueous electrolytes driven by the direct current. The reactions taking place are the hydrogen (HER) and oxygen evolution reaction (OER), at the cathode and anode, respectively. The formed gaseous products are then collected (oxygen can be also released to the atmosphere without significant negative environmental impact), and the generated hydrogen can be used as fuel.

A particularly attractive way to consume hydrogen fuel is the use of fuel cells (FCs), since they do not suffer from efficiency limitations like combustion engines. In these devices, oxygen electroreduction (ORR) takes place at the cathode, while hydrogen electrooxidation (HOR) occurs on the anode simultaneously. During these spontaneous processes, a potential difference is established between the electrodes and electric current flows through the external circuit, which can be used to perform work.

In this chapter an overview of these four reactions significant for energy conversion and storage will be given, outlining the challenges and current state of understanding.

2.7.1 Water splitting

Nicholson and Carlisle were among the first who discovered and investigated water electrolysis at the end of 18th and the beginning of 19th centuries[127]. While the phenomenon itself attracted substantial attention (although initially generating a lot of doubt as well), the practical applications were limited. In the 1920s probably the first large scale commercial electrolyzers of 100MW power have been introduced to the market in Canada[135]. Efforts to improve the technology were renewed in the 1970s, primarily for space exploration - PEM-electrolyzers, and military applications - high-pressure alkaline electrolyzers for submarines.[136]

The summary reaction of water electrolysis is as follows:

$2H_2O(l) \rightarrow 2H_2(g) + O_2(g)$

During this process, two reactions are taking place at the electrodes: the hydrogen evolution reaction (HER) on the cathode, and the oxygen evolution reaction (OER) on the anode of the electrolyzer. The half-reactions are:

1. In acidic media

Cathode: $2H^+ + e^- \rightarrow H_2$

Anode: $H_2O \rightarrow 1/2O_2 + 2e^- + 2H^+$

2. In alkaline media:

Cathode: $2H_2O + 2e- \rightarrow 2OH^- + H_2$

Anode: $4OH^- \rightarrow 2H_2O + O_2 + 4e^-$

An example electrolyzer (in this case alkaline) is shown in Figure 2.3. The basic elements of the electrolyzer are: the anode (where OER takes place), the cathode (HER), electrolyte, *dc* power source, and the diaphragm, which allows electrical contact while keeping the anolite and catholite separated. The diaphragm keeps the evolving gases divided as well, ensuring the purity of the electrolysis products.

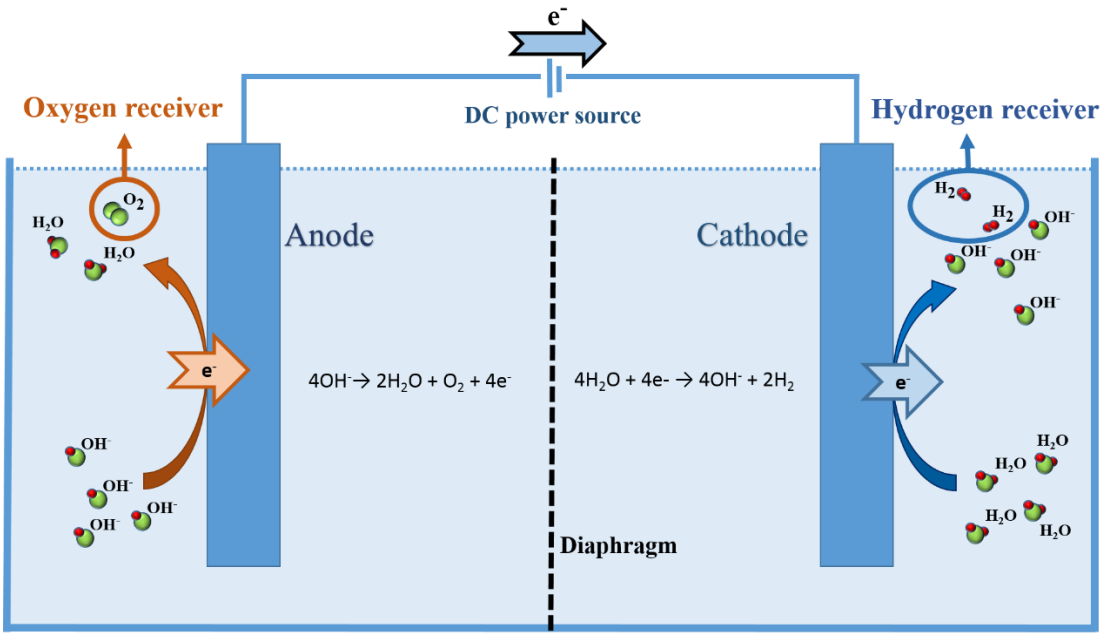

Figure 2.3: A schematic representation of an alkaline electrolyzer.

In order to generate hydrogen and oxygen from water, the minimum theoretical potential that needs to be applied is the equilibrium cell voltage, E^0, which is defined as:

$$E^0 = E^0_{anode} - E^0_{cathode} \quad \text{(Eq. 41)}$$

Which is linked to the Gibbs free energy of the electrochemical reaction by the expression:

$$\Delta G = -nFE^0 \quad \text{(Eq. 42)}$$

The equilibrium cell voltage for water splitting is 1.23V at 25°C, and ΔG=237.2kJ/mol. However, due to the overpotential the typical cell potentials in commercial electrolyzers is 1.8-2 V at the current density of 300-1000 Am^{-2}. [136]

Water electrolysis, while being still relatively costly, has been implemented on an industrial scale for around a century. Three distinct types of electrolyzers are currently in use today:

1. *Alkaline electrolyzers* are the most widely used electrolyzers nowadays[137]. An alkaline solution is used as an electrolyte (usually 20-40% NaOH or KOH), which offer high conductivity but does not cause corrosion issues like the use of acidic media. The electrodes are separated by a diaphragm that keeps the product gases from mixing to ensure the cleanliness of the final product, as well as safety of operation. The drawbacks are low partial load range, limited current density due to the high ohmic losses, and cross-diffusion.

2. *PEM electrolyzers*. A solid perfluorosulfonate polymer membrane is used as an electrolyte (e.g., Nafion®) as it allows the transfer of protons from the anode to the cathode, ensures very low gas crossover, compact design and high-pressure operation[138]. The harsh conditions in the PEM electrolyzers (pH=2, 2V vs. RHE) demand the use of stable, but scarce materials such as noble catalysts (Ir, Ru, Pt and Pt-group metals), titanium alloys, etc. The advantages include good energy efficiency, high current densities (>2 a cm^{-2}), high production rates, and compact design[139], while some of the drawbacks are expensive membranes and

porous electrodes[140]. Its relatively short service time also limits the use of PEM electrolyzers for general applications[136].

3. *Solid-oxide electrolyzers* conduct high temperature (820-1073K) water electrolysis with solid oxide as the working electrolyte. The steam passes through the cathode side where hydrogen is generated, releasing O^{2-}, which then migrates through the solid oxide towards the anode where it is oxidized and gaseous oxygen is released[136.] It generally consumes less electric power because of the more favorable thermodynamics of the reactions at higher temperatures. Challenges include expensive materials, durability issues with the ceramic materials at high temperature and long-term operation, safety problems, and requirements for temperature control.

The current state-of-the-art materials used to catalyze these reactions are Pt for the HER, and IrO_2 for OER in acidic media. However, due to the scarcity of these materials, significant efforts are being invested to reduce the catalyst loading of precious metals in electrolyzers, or to find non-precious alternatives that can offer a similar activity. In alkaline media, several catalysts can be used. For the cathode side, Ni and its alloys as well as some composite Ru-based electrocatalysts, while for the anode side, Co-, Ni- and Fe-based complex oxide materials are used. The majority of the overpotential in electrolyzers comes from the side of the OER, Figure 2.4, and improving the kinetics of this reaction is a key milestone towards the more widespread implementation of commercial electrolyzers. Nonetheless, the reduction of platinum loadings on the cathode side in PEM electrolyzers is also of great interest due to the high price of the catalyst, which significantly influences the cost-effectiveness of the device.

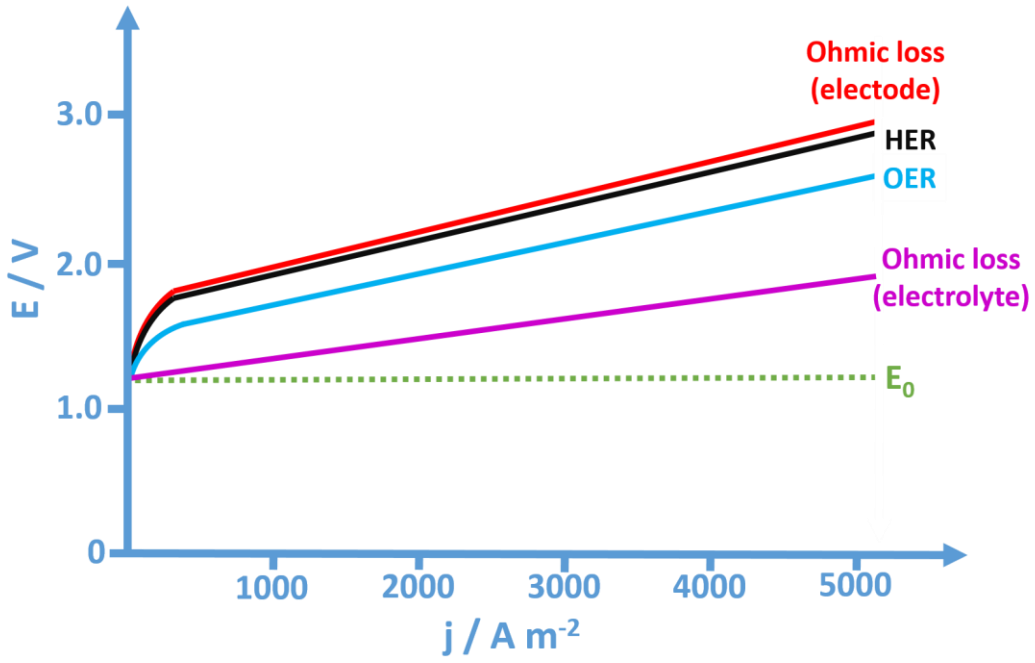

Figure 2.4: The sources of overpotential in an alkaline electrolyzer. Ohmic losses come mostly from the side of the electrolyte and they increase linearly with the current passing through the cell. Most of the overpotential at the electrodes comes from the side of the OER, although the HER side requires relatively high catalyst loadings as well.

In the following subsections, the electrode reactions taking place in water electrolyzers are discussed in detail.

2.7.1.1 Hydrogen evolution reaction

The hydrogen evolution reaction (HER) involves the reduction of protons to hydrogen at the electrode surface. The mechanism involves the transfer of two electrons and it is understood to go through the following steps[55,136]:

$H^+ + e^- + * \rightarrow *H$ Volmer reaction

$2*H \rightarrow H_2 + 2*$ Tafel reaction

$H^+ + e^- + *H \rightarrow H_2 + *$ Heyrovsky reaction

where the asterisk denotes a surface adsorption site. Since there is only one intermediate it should theoretically be possible to identify a catalyst with an ideal binding energy in accordance with the Sabatier principle that would exhibit zero thermodynamic overpotential and maximal current densities.

The volcano plot for HER is shown in Figure 2.5. The best known pure-metal catalyst for the HER is Pt. It is often implemented as nanoparticles supported on carbon black or carbon nanotubes (CNT) [138], however due to its scarcity Ni, or Ni-, Co- and Fe- based alloy electrodes are often used in commercial devices, as mentioned above.

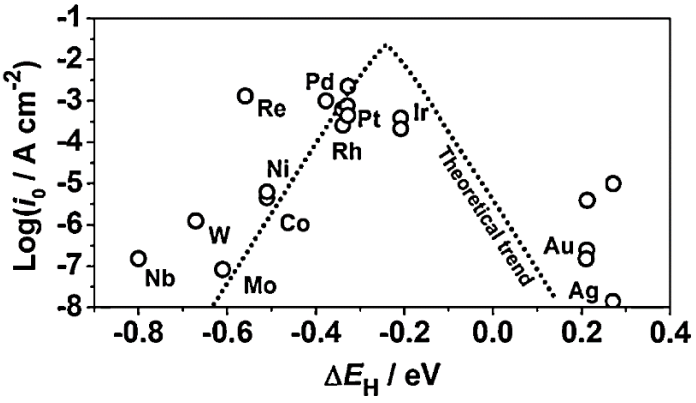

Figure 2.5: Volcano plot for HER. Original data from reference 141.

While the HER has a much lower overpotential in comparison to OER, still high loadings of Pt are used for electrolyzers (0.5-1 mg cm^{-2} [138]). Therefore, significant efforts are invested in the improvement of HER catalyst activity and reduction of noble catalysts loadings in electrolyzers.

The HER and the hydrogen oxidation reaction (HOR) activities are interconnected since they go through the same intermediates, basically, the HOR is HER's microscopic reverse. If a substance is a good catalyst for the HER, it can be expected that it will show considerable activity towards the HOR, and vice versa. It is important to note the same cannot be said about

OER and ORR, as they, among other things, take place under very different conditions (e.g. at OER potentials most metals are covered with an oxide layer).

2.7.1.2 Oxygen evolution reaction

The oxygen evolution reaction (OER) generally occurs at high overpotentials, on oxidized metal surfaces, which have complex structures and are difficult to characterize.

The mechanism of the OER is significantly more complex in comparison to that of HER. It has several reaction intermediates (*OOH, *OH, *O), the binding energies of which are interconnected through scaling relations, complicating catalyst optimization[142]. There are a number of proposed pathways for the reaction, but the most widely accepted ones are listed below:

In alkaline media[136]:

$*OH^- \rightarrow *OH + e^-$

$OH^- + *OH^- \rightarrow *O + H_2O + e^-$

$*O + *O \rightarrow O_2$

While in acidic media, the reaction mechanism is[143]:

$H_2O + * \rightarrow *OH + H^+ + e^-$

$*OH \rightarrow *O + H^+ + e^-$

$*O + *O \rightarrow O_2 + 2*$

The volcano plot for OER is shown in Figure 2.7A. The state-of-the-art catalysts for the OER (in acidic media) are IrO_2 and RuO_2[144,145] (MnO_2 catalysts have been reported to show high activity, see Section 4.4.3, but they are very unstable). RuO_2, while being more active suffers from instability issues that limit its practical applicability[145]. Therefore, the more stable, although slightly less active iridium-oxide catalysts are considered for real-world-applications[146].

2.7.2 Fuels cell reactions

The basis for fuel cells was laid in 1839 when Sir William Robert Grove discovered the reversibility of the water electrolysis. FCs offer the opportunity to close the proposed hydrogen cycle. However, they did not go through much technological improvement until the NASA space program in the 1960s. Because of the fact that they can provide several times more energy per unit mass and that they offer reasonably high efficiency even at 100°C in comparison to heat engines[147], they found their first application in the "Gemini" program in 1964.

The theoretical efficiency of FCs exceeds 80%, while practically it can be as high as *ca* 70%. PEMFCs are particularly interesting for the automotive industry[50] due to their low operating temperatures and short start-up times[50]. They have also been proposed for grid storage

technology, in which batteries would serve to stabilize the varying energy output of renewable sources on the hourly scale, while electrolyzer/fuel cell devices would serve for longer-scale energy storage/generation.

The working principle of these devices is that the fuel and an oxidant (oxygen or air) are brought to the electrodes where they undergo redox reactions and the chemical energy is transformed to electric. A schematic representation of an FC is shown in Figure 2.6. The fuel is oxidized at the anode (in the case of hydrogen fuel HOR takes place there), while the oxidant is brought to the cathode where the ORR takes place. Different fuels may be used (such as methanol, methane, etc.). However, in the sense of environmentalism the most attractive solution is H_2, as in hydrogen-FCs only water vapor would be generated during the operation.

However, their widespread application is hindered by the high loadings of noble metals needed to catalyze the reactions (HOR and ORR) at the electrodes at a rate sufficient to operate them at a satisfactory performance. The performance of these devices is limited by the cathode reaction, the ORR, because of its sluggish kinetics[51,76, 148 , 149] , which results in a high overpotential, e.g., *ca* 0.4V at a current density of 1 mA cm^{-2} [150] on Pt, a widely used catalyst.

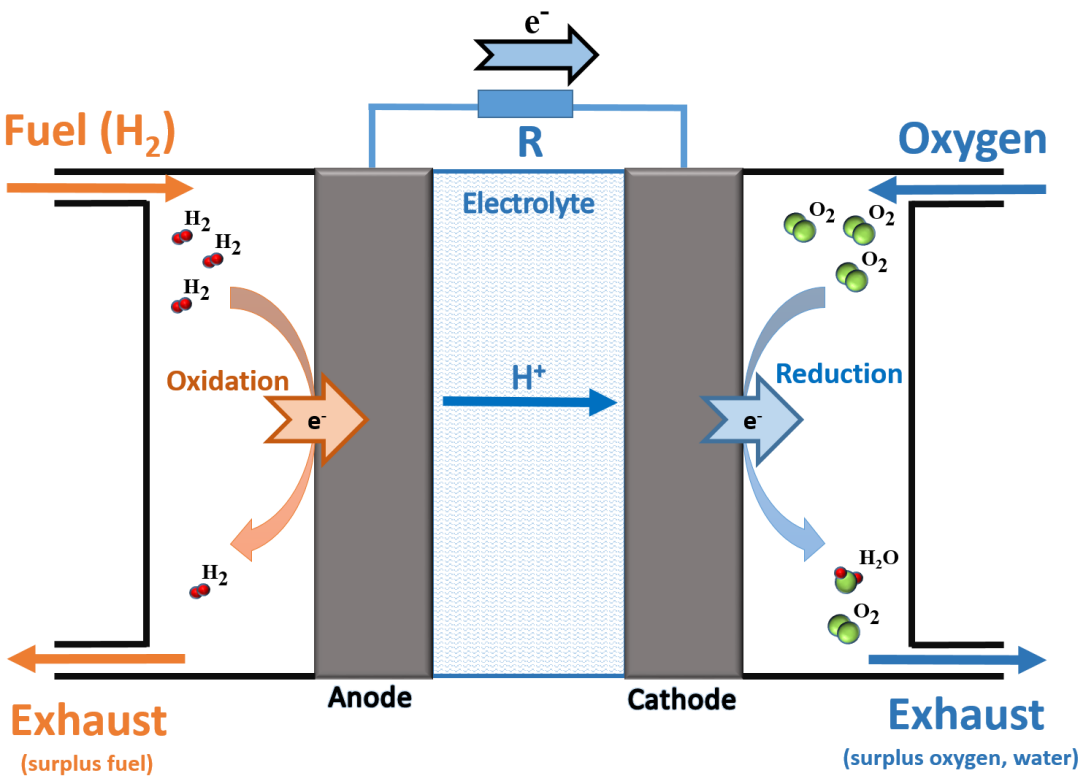

Figure 2.6: A schematic representation of a fuel cell, which uses H_2 fuel and an acidic electrolyte. The fuel is oxidized at the anode, while oxygen (practically, air is often used) is fed to the cathode where it is reduced to water. During the process, electric current flows through the external circuit.

The mechanisms of the reactions taking place in FCs differ in acidic and alkaline media and are as following:

In acidic media:

Cathode: $O_2 + 4H^+ + 4e^- \rightarrow 2H_2O$

Anode: $H_2 \rightarrow 2H^+ + 2e^-$

In alkaline media:

Cathode: $O_2 + 4e^- + 2H_2O \rightarrow 4OH^-$

Anode: $H_2 + 2OH^- \rightarrow 2H_2O + 2e^-$

There are several different types of FCs which use hydrogen fuel, as described below[51, 151]:

1. *Alkaline Fuel Cell (AFC)* is the simplest low-temperature fuel cell. It operates at *ca* 70°C, and it offers the great advantage that ORR is more facile in alkaline media. H_2 is used as a fuel and it utilizes concentrated KOH as an electrolyte. The corrosive alkaline environment places demanding requirements to the component stability. The electrodes are usually constructed from carbon and polytetrafluorethylene, which ensures macroporosity and hydrophobicity. Most of the cost in their construction comes from the electrode material, primarily on the cathode side, where usually Pt is implemented as a catalyst. The primary issue with AFCs is that the alkaline solution readily absorbs CO_2 from air (if air is used as an oxidant), and carbonates can deposit on the electrode passivating them, not discussing the dilution of the working electrolyte with the water generated in the cathodic reaction.

2. *Phosphoric Acid Fuel Cell (PAFC)* was the first commercially available FC. Due to the acidic electrolyte, they do not suffer from CO_2-related issues like AFCs. While phosphoric acid is not a strong electrolyte at room temperature, at temperatures above 150°C it polymerizes into pyrophosphoric acid, which is a strong acid with a high conductivity. The operating temperatures are 190-210°C, which make the use of active cooling systems mandatory.

3. *Molten Carbonate Fuel Cell (MCFC).* The electrolyte used is a 68% Li_2CO_3/ 32% K_2CO_3. The cathode is made from porous lithiated NiO ($Li_xNi_{1-x}O$; $0.022 \leq x \leq 0.04$), and the cathodic reaction is:

$\frac{1}{2}O_2 + CO_2 + 2e^- \rightarrow CO_3^{2-}$

At the, anode, made out of porous 10% Ni/Cr alloy, the reaction is:

$H_2 + CO_3^{2-} \rightarrow H_2O + CO_2 + 2e^-$

In real-world devices, the CO_2 must be mechanically transferred back to the cathode, which complicates the FC's design. The cell's higher operating temperature, coupled with its resistance to CO makes it suitable for combining with fuel reformers. However, the drawbacks are high ORR overpotentials, Ni^{2+} migration to the anode, and complicated electrolyte management.

4. *Solid-Oxide Fuel Cell (SOFC).* The FCs operate at sufficiently high temperatures that the cathode kinetic limitations become negligible and the use of solid ceramic oxide-ion conductors becomes possible (>900°C). The electrolyte is typically ZrO_2 stabilized with 8-10 mol% of Y_2O_3 (yttria-stabilized zirconia, YSZ), which, besides stability, also provides substantial ionic conductivity, due to the presence of mobile O^{2-} ions.

At the anode side, usually 36% $Ni/ZrO_2/Y_2O_3$ cermet is applied as a catalyst for the reaction:

$$H_2 + O^{2-} \rightarrow H_2O + 2e^-$$

The high temperature and the oxidizing atmosphere in these FCs set strict limitations for the cathode material due to stability requirements. In commercial devices, usually porous perovskite manganite is used, namely $La_{1-x}Sr_xMnO_3$, with $0.1>x>0.15$, for the cathode reaction:

$$\frac{1}{2}O_2 + 2e^- \rightarrow O^{2-}$$

The SOFCs, while being a very promising technology, still face numerous challenges for their widespread application, particularly related to the thermal stability and expansion of the materials, as well as relatively low cell voltage.

5. *Polymer Electrolyte Membrane Fuel Cells***,** or alternatively *Proton-Exchange Membrane Fuel Cells (PEMFCs)*, were the first fuel cells to find practical applications. They are currently considered promising devices for transport applications. A PEMFC is comprised of three main components[152]: The membrane-electrode assembly (MEA), two bipolar (flow field) plates, and the seals. The basic parts of the MEA are the proton-conducting membrane, the dispersed catalyst layers, and two gas diffusion layers - GDLs, (one for each electrode). The GDL ensures the steady and uniform flow of the fuel and the oxidant to the electrodes, which are made of or covered with the appropriate catalytic materials. The catalysts are used to facilitate the reactions[153,154]:

Anode (Pt): $2H_2 \rightarrow 4H^+ + 4e^-$

Cathode (Pt-alloy): $O_2 + 4H^+ + 4e^- \rightarrow 2H_2O$

The membrane separates the half-reactions taking place on the electrodes, while allowing the passage of protons from the anode to the cathode, thus maintaining the reaction. The membrane also prevents the reactants from mixing. The most widely used material for the membrane is perfluorosulfonic acid (PFSA)[152].

The bipolar plates have several functions, including the distribution of the fuel and oxidant within the cell, facilitation of water management, the separation individual cells in the stack, and carrying the current away from the cell.

PEMFCs possess many appealing features, such as high power density, rapid start-up, high efficiency, etc. However, still there are issues hindering its widespread use: the need for improved efficiency, inadequate water and heat management, intolerance for impurities, particularly CO, and high cost (which is linked to the high loadings of the precious metal catalysts on the electrodes) [155]. Improving the kinetics of the electrode reactions, as well as their durability, particularly in cycling operation mode[156], is of paramount significance to the commercialization of these devices.

2.7.2.1 Hydrogen oxidation reaction

The hydrogen oxidation reaction (HOR) takes place on the anode of FCs. Because of its facile kinetics the overpotential due to HOR in fuel cells is often negligible[157]. Since HOR has the same intermediates as HER, activities of materials towards this reaction follow the same trends, as already mentioned.

HOR is a structure-sensitive reaction whose activity on Pt *fcc* surfaces increases in the order Pt(111)<Pt(100)<Pt(110), i.e., with decreasing coordination of the surface atoms[158]. The dissociative adsorption of hydrogen is the first reaction step in HOR, and it can occur either with (Heyrovsky reaction), or without (Tafel-reaction) simultaneous electron transfer[157,159]. It has been found that the kinetics of HER/HOR are about an order of magnitude faster in acidic media, in comparison to alkaline. Moreover, in alkaline media the mechanism may be Heyrovsky (rds)-Volmer, while in acidic media the current densities simply follow a Nernstian hydrogen diffusion overpotential relationship, which indicates reversible and infinitely fast HOR/HER kinetics[160].

2.7.2.2 Oxygen reduction reaction

The oxygen reduction reaction (ORR) is a multielectron reaction with several elementary steps and reaction intermediates, which makes the finding of an optimal catalyst quite difficult[161]. Its complex mechanism includes the transfer of 4 (or 2) electrons and involves 4 protons. The ORR takes place under harsh reaction conditions, which limits the choice of materials for catalysis, since many materials do not exhibit the necessary stability under the circumstances.

The ORR is of great importance for fuel cells[147,162], as well as corrosion science[163] and metal-air batteries[164,165]. Since the adsorption energies of intermediates O*, OH*, and OOH*[166,167] are normally linearly interdependent[121,122] it is possible to use only a single variable (ΔG_{O*}; ΔG_{OH*}, ΔG_{OOH*}) as a descriptor[74] for the construction of the volcano plot, as discussed above.

The understanding of the ORR mechanism is still not complete due to its high complexity. The ORR can in fact go through several pathways, on Pt-surfaces. Under conditions relevant for catalysis in real-world devices, the four-electron path to water is believed to be dominant, at least on Pt and Pt-alloy surfaces. [168]

The first step is the adsorption of molecular oxygen, which can occur in two ways, either dissociatively or reductively (reactions shown are in acidic media)[169]:

$O_2 + * \leftrightarrows 2*O$

$O_2 + 2H^+ + 2e^- + 2* \leftrightarrows 2*OH$

where * denotes an adsorption site on the surface.

If the dissociative adsorption is the first step, the adsorbed oxygen species them undergoes a reductive transition to OH:

$*O + H^+ + e^- \leftrightarrows *OH$

Finally, the adsorbed hydroxyl is subject to the final reductive desorption step.

$*OH + H^+ + e^- \leftrightarrows H_2O + *$

The reaction can also follow a different pathway, the so-called "two-electron pathway", which results in the production of H_2O_2[170]:

$O_2 + * + H^+ + e^- \leftrightarrows HOO*$

$HOO* + (H^+ + e^-) \leftrightarrows H_2O_2 + *$

This pathway is particularly prominent on Hg and Au[168]. H_2O_2 is an important industrial chemical[171], and is considered to be a "green" reactant, as it usually decomposes to water and oxygen. It is produced by the anthraquinone process, which is quite energy consuming, complicated, non-eco-friendly itself because of the use of significant amounts of organic solvent, and it carries significant safety risks. Therefore, the production of H_2O_2 by electrochemical means is of increasing interest for the chemical industry. This reaction is also significant since the change in selectivity of the OER in electrolyzers could decrease the anode overvoltage. The Nernstian potential for H_2O_2 production by water splitting is 0.7V[170], significantly lower in comparison to that of H_2O – 1.23V.

The volcano plot for the ORR is shown in Figure 2.7B. The materials on the left side of the volcano plot bind the intermediates too strongly so the rate-limiting step is the hydroxyl desorption from the active sites. The materials on the right side, which bind the intermediates more weakly than ideal, the limiting step is the activation of O_2. DFT calculations indicate that the optimal ORR catalyst should bind the *OH intermediate *ca* 0.1eV [76,148,166] more weakly than Pt(111), or in the case of *O 0.2V weaker than Pt(111)[76]. The ideal binding energy for the two-electron process, which yields H_2O_2 as the reaction product is, however, different from the four-electron one, and it is *ca* 0.3eV weaker than Pt(111)[170].

Durability is, naturally, another important requirement for the operation of fuel cells, and therefore, the stability of Pt and Pt-alloy catalysts is an important factor that needs to be improved for the widespread implementation of FCs[172,173,174].

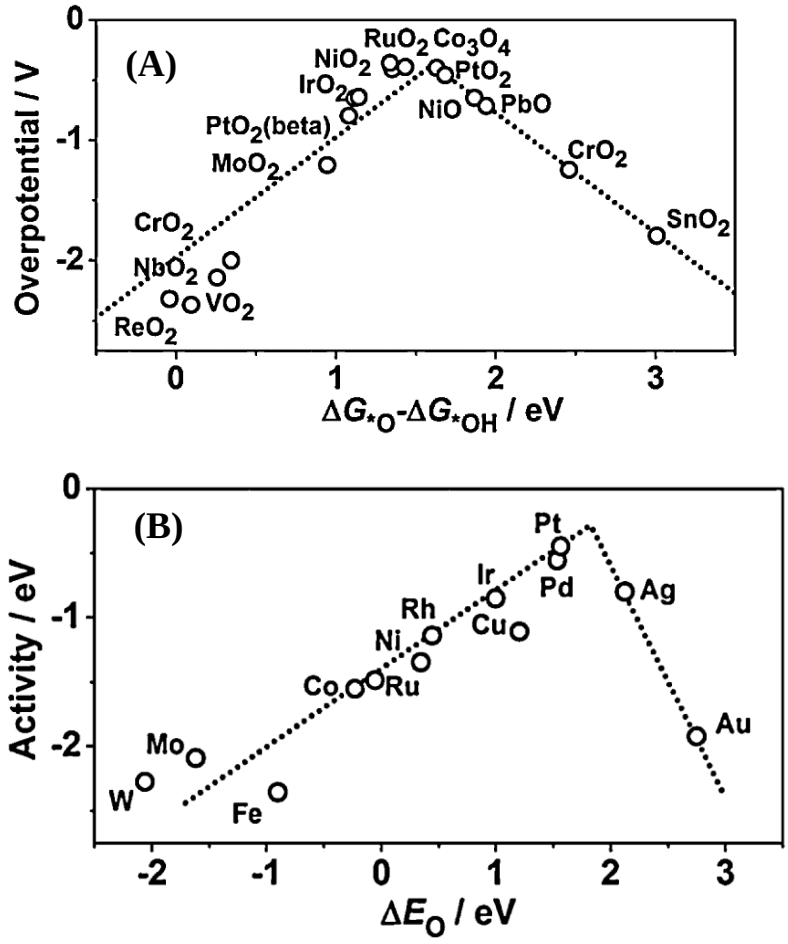

Figure 2.7: Volcano plots for the (A) OER. Adapted from reference 175 (B) ORR. Taken from reference 76.

3. Experimental part

3.1 Experimental setup

3.1.1 Electrochemical cells

In this work, three types of cells were used to perform electrochemical experiments. In all those cells, the standard three-electrode system was implemented. A mercury-mercurous sulfate (MMS) electrode was used as a reference electrode (RE), and a polycrystalline platinum wires (GoodFellow) as a counter (auxiliary) electrode (CE).

Before each experiment, the glassware was cleaned with a 3:1 mixture of concentrated 96% H_2SO_4 and 30% H_2O_2 ("Piranha solution"), followed by extensive rinsing with ultrapure water. After that, the glassware was boiled in ultrapure water for *ca* 5 hours, and the water changed at least 3 times.

The RE (MMS) was always kept in a separate compartment separated from the working electrolyte by an ionically conducting ceramic insert. The RE-compartment was filled with 0.1M $HClO_4$ (Merck, Suprapur) to ensure contact with the working solution.

All the electrode potentials in this work are referred to on an RHE scale.

Experiments were always performed using the hanging meniscus (HM) configuration.

3.1.1.1 Cell for single crystal electrochemistry

The schematic of the cell is shown in Figure 3.1. The cell allows the thermal treatment and surface modification of the working electrode (WE) and its subsequent electrochemical characterization[176,177].

(A)

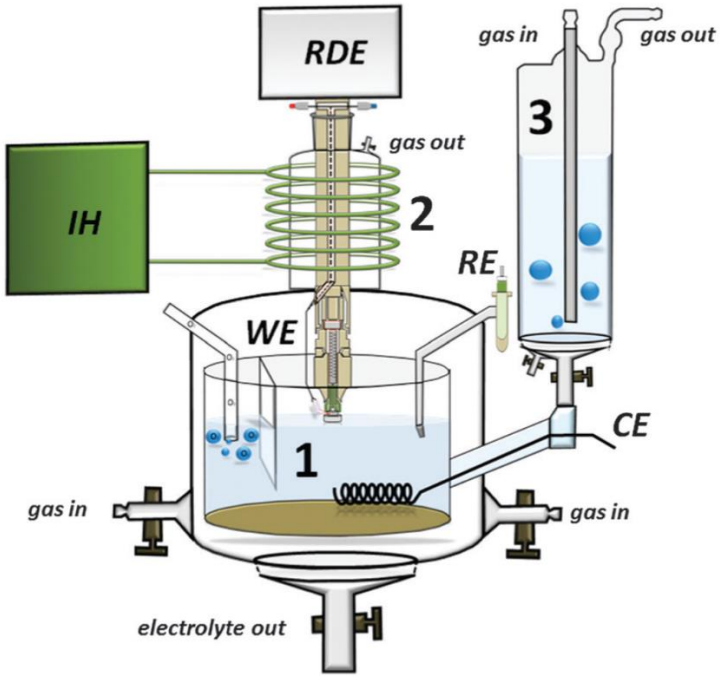

(B)

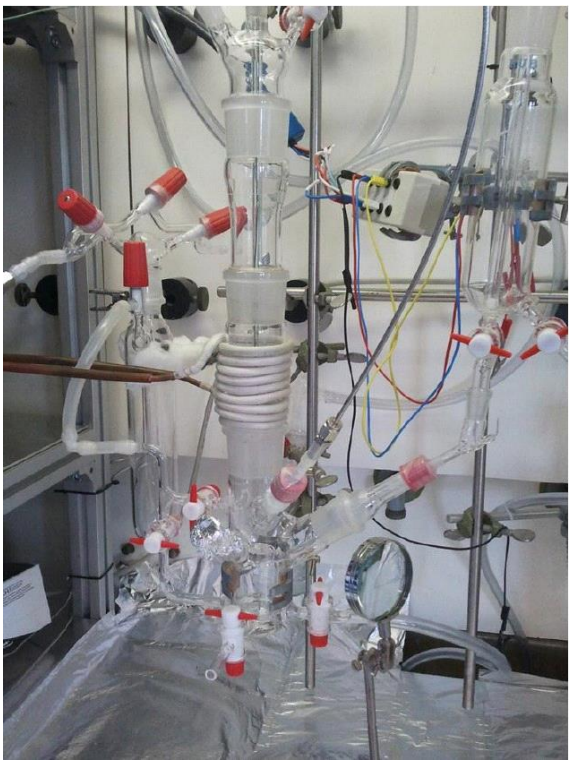

Figure 3.1: (A) A Schematic of the cell used for single crystal electrochemistry. RDE – rotating disk electrode, IH – inductive heater, WE – working electrode, CE- counter electrode, RE – reference electrode. Taken from reference 177. (B) A photograph of the cell.

It consists of compartments made of Pyrex™ or quartz glass. The WE can be vertically moved by means of a moveable shaft and thus brought into contact with the working electrolyte. The WE was introduced using the HM configuration, both in stationary and in R(R)DE configurations. The shaft provides an electrical connection. The shaft is sealed off using a Thermogreen LB-1 (Supelco) insert. The CE is introduced into the cell *via* a port as shown in the picture. This compartment allows the electrolyte to be purged of oxygen by Ar-saturation, or saturated with any gas introduced into it, prior to its introduction to the cell, as it is equipped with an independent gas inlet and outlet. The construction of the cell makes it possible to change the working electrolyte while maintaining potential control. A dummy electrode (Pt-wire, GoodFellow), is also included in the setup. The dummy electrode is connected in series to the WE, and it allows us to keep the WE under potential control during electrolyte replacement.[177]

The atmosphere in the cell is maintained by flushing the cell with a continuous stream of the designated gas or gas mixture (in this work: Ar, O_2, H_2, or Ar-CO mixture) through the assigned gas inlets and outlets. In order to reduce the disturbance of the electrolyte from the constant gas flow, a protecting inner glass wall is incorporated into the design. The volume of the inner working compartment was *ca* 50 cm^3. The outlets are connected to the "water locks" to prevent gas backflow. All the gases were supplied to the cell *via* Swagelok™ stainless steel tubes.

3.1.1.2 Cell for oxide thin-layer deposition and OER activity measurements

A special cell was used to deposit thin layers of oxide materials onto different substrates and to conduct the OER activity measurements. The cell is schematically shown in Figure 3.2 A.

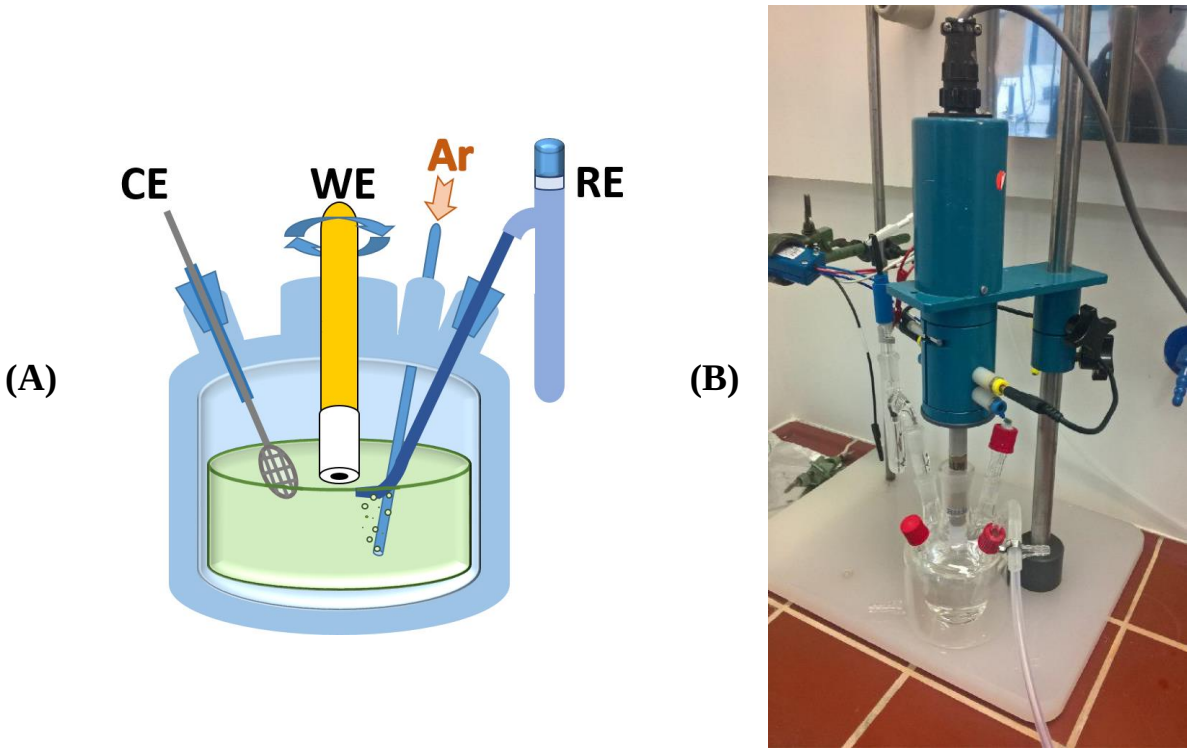

Figure 3.2: (A) A schematic representation of the cell used for OER activity measurements and the deposition thin films of oxide materials. (B) A photograph of the cell.

The cell used is a single compartment cell with a gas inlet allowing the degassing of the electrolyte by the introduction of Ar, or the saturation of the electrolyte with O_2. The counter electrode is a Pt-mesh, securing a large surface area of the CE. The RE is a MMS electrode in a separate compartment connected to the working electrolyte *via* an ionically conducting ceramic insert. The WE is introduced using a HM-RDE configuration, which allows the elimination of mass transport effects and the assessment of kinetic parameters in a wider range of potentials. A photograph of the cell is presented in Figure 3.2B.

3.1.2 Single crystal electrochemistry

Single crystals are important in electrochemistry as they offer the possibility to assess the properties of specific crystal planes and establish a link between the electrode surface structure and its electrocatalytic properties. However, no single crystal is ideal. There are always defects in the bulk (point or line defects, dislocations, etc.), and consequently also on the crystal surfaces.

In electrocatalytic research, monoatomic steps are often purposefully introduced to form surfaces with quasiperiodic step defects, so-called – stepped single crystals. The geometry of the steps themselves can be either (111) or (100), if relevant *fcc* metal electrocatalytic surfaces are used.

For the most of experiments in this study Pt crystals were utilized, namely polycrystalline (*pc*), *fcc*(111), and *fcc*(331). Au(pc) was used as a substrate for metal-oxide catalyst depositions,

while Ir(111) was used for iridium-oxide layer growth for OER catalysis studies. Pt, Au and Ir have a face-centered cubic (*fcc*) lattice, while Ru has a hexagonal close-packed (*hcp*) one.

The **Pt (111)** electrodes used in this work were purchased from Mateck (Jülich, Germany). The crystals had a diameter of 5mm, with a surface roughness of 30nm, oriented better than <0.1°. Before each experiment, the crystal was annealed in a buthane/oxygen flame at *ca* 1100°C, and subsequently cooled in an CO (1000 ppm; 4.7, Air Liquide, Germany)/Ar (5.0 Air Liquide, Germany) mixture. The crystal was subsequently characterized electrochemically by CV in the model electrolytes[166] to ensure the desired quality of the surface was achieved. This was done by inserting the freshly annealed and cooled electrode in 0.1M $HClO_4$ or 0.05M H_2SO_4 electrolyte under potential control at 0.05V vs. RHE and performing cyclic voltammetry in the potential range between 0.05 and 1.15V vs. RHE. An example CV of a well-defined Pt(111) in a 0.1M $HClO_4$ surface is shown in Figure 3.3. The sharp peaks at *ca* 0.78V are especially sensitive and indicative to the presence of defects on the surface and cleanliness of the system. The flame annealing or inductive heating procedures normally result in surfaces in which the terraces are atomically flat and wide enough (up to 1000 atoms) to consider the initial surface as a model Pt(111).

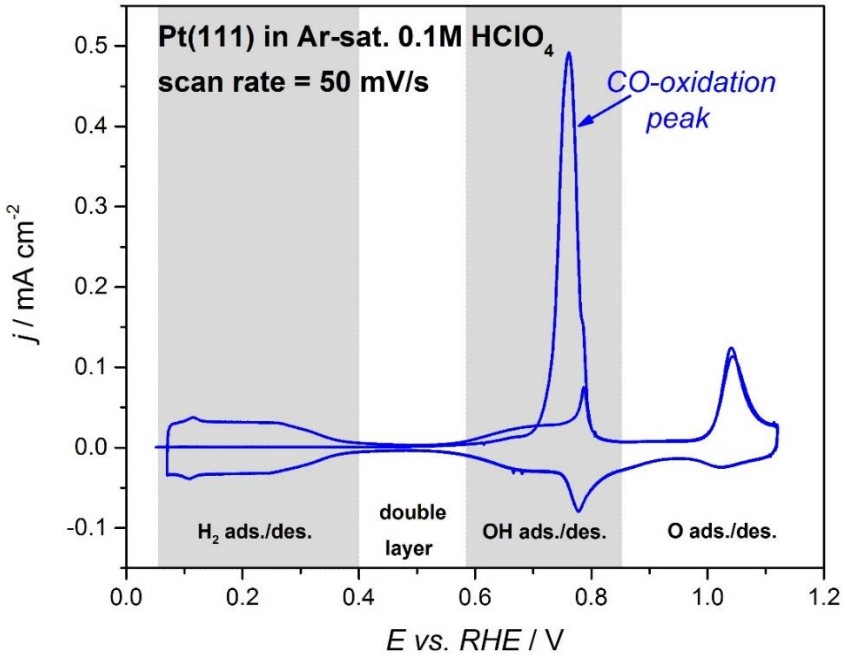

Figure 3.3: Pt(111) in Ar-saturated 0.1M $HClO_4$ electrolytes, at a scan rate of 50 mV/s. The CVs have well-defined features that can be used to characterize the electrode. In the first cycle, the CO adsorbed on the electrode surface during the annealing process is oxidized (CO-oxidation peak at *ca* 0.76V). "H_2 ads./des." denotes the hydrogen adsorption (UPD) and desorption region, "double layer" – the so-called double-layer region, "OH ads./des." – adsorption and desorption of hydroxyl species, "O ads./des." - adsorption and desorption of the oxygen species.

The CO that is adsorbed on the surface in the annealing process is oxidized in the first potential cycle at *ca* 0.76V, Figure 3.3. The reaction ensues as follows:

$$*CO + H_2O \rightarrow * + CO_2 + 2H^+ + e^-$$

The reaction is very sensitive to the structure and status of the Pt-surface[65]. As CO adsorbs strongly on Pt, the determining step is believed to be the formation of *OH at a free surface site[65]:

$$* + H_2O \rightarrow *OH + H^+ + e^-$$

Once formed, *OH reacts with *CO according to the Langmuir-Hinshelwood reaction:

$$*CO + *OH \rightarrow 2* + CO_2 + H^+ + e^-$$

Thus the adsorbed CO is stripped from the surface and the ordered Pt(111) surface is exposed.

Several processes can be distinguished in the CV in Figure 3.3: the adsorption/desorption of hydrogen (0.05-0.4V), the double layer region (0.4 – 0.6V), OH – adsorption desorption (0.6 – 0.85V), and finally the O-adsorption/desorption (>0.85V).[177] The "butterfly" peaks that appear at 0.8V indicate the completion of a 1/3ML OH-adsorbate layer[177], and the peak height correlates with the quality of the Pt(111) surface and the overall cleanliness of the system[178].

The **Pt(331)** crystal used was a bead-type crystal (Icryst, Jülich, Germany), with a 2.5mm diameter, oriented better than <0.5°, with a surface roughness of less than 50nm. The crystal was annealed in a butane/oxygen flame, and subsequently cooled in a CO (1000 ppm; 4.7, Air Liquide, Germany)/Ar (5.0 Air Liquide, Germany) mixture. The crystal was electrochemically characterized to ensure the desired quality of the surface using the same procedure as described for the Pt(111) electrode.

The **Ir(111)** (Mateck, Jülich, Germany) single crystal electrode (diameter of 5mm, surface roughness less than 30nm, and orientation better than 0.1°) was used for OER experiments. It was annealed at 1200±25°C for 10 minutes in a stream of H_2(10%) (6.0, Air Liquide, Germany)/Ar (5.0, Air Liquide, Germany) mixture and cooled in the same atmosphere. The thermal treatment was conducted using an inductive heater with an automatic time controller (20-80Hz, 15KW-EQ-SP-15A, MTI, USA). The quality of the surface was assessed its characteristic CV in Ar-saturated $HClO_4$ and H_2SO_4 solutions.

Ir is not stable at the OER conditions – it is normally covered by a layer of oxide and which catalyzes the reaction. In order to create reproducible oxide layers, Ir(111)/oxide surfaces were freshly prepared before each experiment by the oxidation of the surface in an anodic scan. Anodically formed iridium-oxide films (AIROF) were grown by cycling in the range between 0.7 and 1.575V until stable voltammograms were recorded.[82]

3.1.3 Modification of single crystal electrodes

3.1.3.1 Underpotential deposition (UPD)

Cu UPD on Pt(111) was carried out in a 0.1M $HClO_4$ solution containing 0.004M Cu^{2+}, prepared by dissolving CuO (99.99%, Sigma Aldrich, Germany) in the perchloric acid. The electrode was held at 0.33V vs. RHE for 3 minutes in order to form a pseudomorphic overlayer of Cu at the surface.

3.1.3.2 Surface and near-surface alloying (SA & NSA)

Pt/Cu NSA: Pseudomorphic Cu-overlayers were initially formed *via* UPD on the surface of a Pt(111) electrode. A Pt-wire serving as a ‘‘dummy’’ electrode was connected in parallel to the WE. Afterwards, the gas in the cell was replaced by Ar/H_2(5%) and the electrode was rinsed with ultrapure water under potential control in order to remove traces of the deposition solution. The electrode was dried in the Ar/H_2(5%) stream (still under potential control through the dummy electrode), and annealed for 2 min under in Ar/H_2(5%) atmosphere at 400ºC. This procedure results in the formation of the Cu–Pt(111) near surface alloy (NSA), where approximately 2/3 ML Cu is located in the second atomic layer of Pt, while the topmost layer (the surface itself) consists of only Pt atoms. The Pt/Cu NSAs obtained were characterized using CV.

Pt/Cu SAs: Pt/Cu NSAs were converted into SAs by annealing the samples in an Ar/0.1% CO mixture for 2 minutes. The adsorbed CO was removed by electrochemical oxidation at 0.57V vs. RHE in 0.1M $HClO_4$. The SAs were characterized using CV.

Figure 3.4 shows typical cyclic voltammograms of unmodified Pt(111), Pt(111)/Cu SA and Pt(111)/Cu NSA electrodes in Ar-saturated 0.1M $HClO_4$, in the range of their stability.

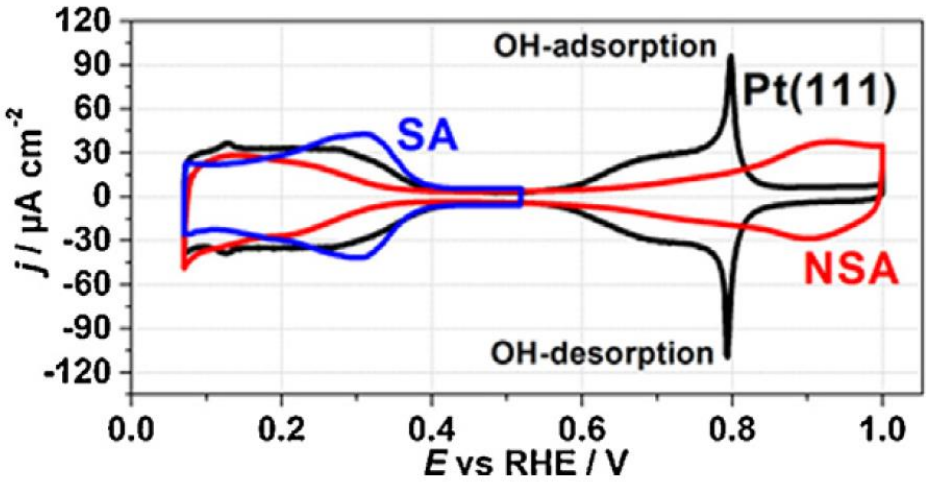

Figure 3.4: Pt(111), Pt(111)/Cu SA and Pt(111)/Cu NSA electrodes in Ar-saturated 0.1M $HClO_4$. Scan rate: 50mV/s. From ref. 179.

3.1.3.3 Introduction of defects

The introduction of defects through dealloying of a quasi-ordered Cu-Pt(111) SA produces relatively small cavities. The dealloying was achieved by a potential sweep up to 1V.

The maximum amount of Cu at the surface of SAs can be up to *ca* 2/3 of a monolayer. The rest of the copper atoms diffuse deep into the bulk of the crystal irreversibly during the first annealing. It is not possible to segregate the remaining 1/3ML Cu by additional annealing of the crystal in a CO-containing atmosphere: the repeated procedure does not result in a surface alloy, but in a Pt(111) surface.

The preparation of defective surfaces by galvanic displacement (GD) was achieved by underpotential deposition of Cu pseudomorphic overlayers and subsequent spontaneous displacement of Cu by Pt. For this purpose, the electrode was inserted at open-circuit in Ar-saturated 0.1M $HClO_4$ containing 1mM $K_2[PtCl_4]$ at room temperature for 10 min.

Electrochemical destruction was conducted by multiple cycling of the electrode up to 1.72 V. At this potential subsurface oxide is formed, which is reduced during the backwards scan with the loss of some Pt atoms, resulting in the formation of cavities on the Pt(111) surface.

3.1.3.4 Oxide deposition

Before the CoO_x film deposition, Au-electrodes were cycled in the potential range between 0.25 and 1.85V in Ar-saturated 0.05M H_2SO_4. Pt microelectrodes, Pt "macro" electrodes, and GC-electrodes were cycled in 0.5M H_2SO_4 from 0.05 to 1.4V vs RHE until reproducible voltammograms were obtained. CoO_x films were deposited from a solution prepared using 0.1M Na_2SO_4, 0.1M CH_3COONa, and 0.1M $CoSO_4$ *via* cyclic voltammetry conducted in the potential range between 1.23 and 1.83V, in an RDE configuration at 400 r.p.m. The thickness of the film was followed by recording a *charge=f(time)* curve.

It has been shown[180] that the activity of Co-oxide catalysts towards the OER depends on the substrate for thin films, and it reaches that of bulk CoO_x as the thickness of the film increases. The minimal thickness of the oxide film exhibiting bulk-like activity was determined by plotting the activity of electrodes with different CoO_x layer thicknesses versus the amount of charge associated with the deposition of the oxide layer. The charge was determined by the integration of the anodic parts of the cyclic voltammograms related to the oxidation of Co^{II} to Co^{III}. The resulting curve is shown in Figure 3.5 and it shows that at *ca* 15mC cm^{-2} of charge is necessary for the activity to reach a plateau and it is not affected by the nature of the substrate.

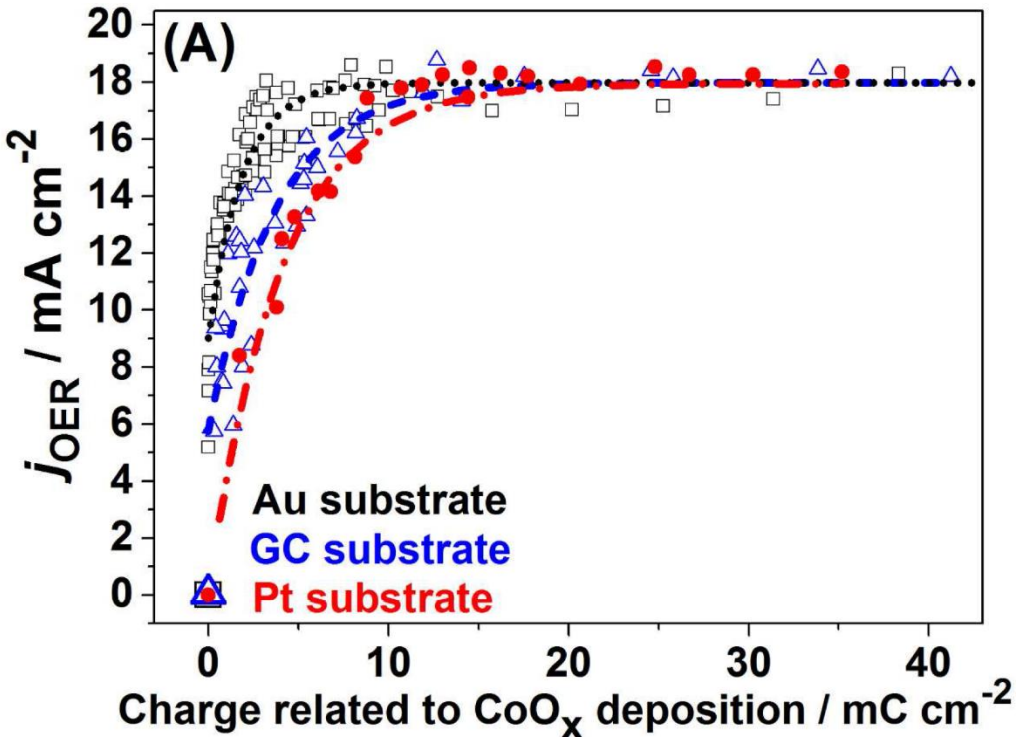

Figure 3.5: Activity of CoO_x thin films in 0.1M KOH (scan rate: 50mA s^{-1}, RDE, 400 r.p.m.) on different substrates, as a function of the charge related to the deposition process. Substrates: Au(pc) (□), glassy carbon (△), and Pt(pc) (●). The activity of the CoO_x thin films reaches a plateau after *ca* 15mC cm^{-2} of Co-associated charge on all substrates.

The thin film deposition process was conducted until a Co-associated charge >20 mC cm^{-2} was reached. For the experiments with electrodes prepared in this manner, the absence of the substrate effects was assumed.

Pt and GC-electrodes were cycled in 0.5M H_2SO_4 from to 1.05-1.55V vs RHE until reproducible voltammograms were obtained. Nickel-oxi-hydroxide (NiO_x) films were deposited from a solution prepared using 0.1M Na_2SO_4, 0.13M CH_3COONa, and 0.13M $NiSO_4$ *via* cyclic voltammetry conducted in the range between 0.23 and 2.13V vs RHE in an RDE configuration at 400 r.p.m. The thickness of the film was followed by recording a *charge=f(time)* curve, as described for CoO_x films.

Before $FeNiO_x$ deposition Pt polycrystalline electrodes and GC-electrodes were cycled in 0.5M H_2SO_4 from 0.05 to 1.4 V vs RHE until reproducible voltammograms were obtained. The deposition of was performed as described in reference 213, by cathodic deposition at −50 mA cm^{-2} for 50 s, in an RDE configuration at 1200 r.p.m. The deposition solution contained 0.09M of $NiSO_4$, 0.009M of $FeSO_4$, and 0.022M of $(NH_4)_2SO_4$.

3.1.3.5 Fabrication of microelectrodes

Needle-type disk shaped Pt-microelectrodes have been fabricated by simultaneous pulling of Pt-wire inserted in a quartz-glass capillary using a laser puller. Microelectrodes with the diameter of Pt surface of ~25μm were obtained. The preparation of microelectrodes is described in detail in reference 181.

3.1.3.6 Nafion coating

Nafion® is an ionomer developed and produced by the DuPont company. The chemical structure is as follows[182]:

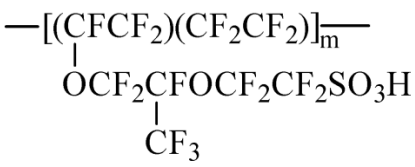

As a proton conductor, it is important for applications in PEMFCs. It is of general interest in electrochemistry as well.

Nafion-coated electrodes were prepared by dropping 10 μL of Nafion solution on the electrode. The solution was prepared by diluting a 5 wt % Nafion 117 suspension in a mixture of lower aliphatic alcohols and water (Sigma-Aldrich) with ultrapure water (1mL Nafion: 100 mL H_2O). The drying was performed overnight at room temperature in an Ar-atmosphere.

3.1.4 Determination of binding energies

The binding energies of the reaction intermediates can be estimated from experimental data CV data. The adsorption isotherms for the ORR intermediates can be constructed by determining the electrode potentials at which a certain adsorbate coverage is reached. The surface coverage of a particular species can be calculated by the integration of the corresponding peaks in the CVs for the electrode in question in standard electrolytes, such as oxygen-free 0.1M $HClO_4$, and by correlating the attained charge to the amount of adsorbed species. For this analysis, the surface of the electrode needs to be well-defined and the voltammetric features have to be clearly interpretable. The difference in potentials required to reach the fractional surface coverage of $\Theta=0.5\Theta_{max}$ theoretically corresponds to the shift in the binding energy at t=0K. This approach is valid if one can neglect[183] the heterogeneity of adsorption sites, changes in the adsorbate-adsorbate interactions, and the effective change of the real surface area with step-density. The isotherms constructed by this method are illustrated in Figure 3.6.

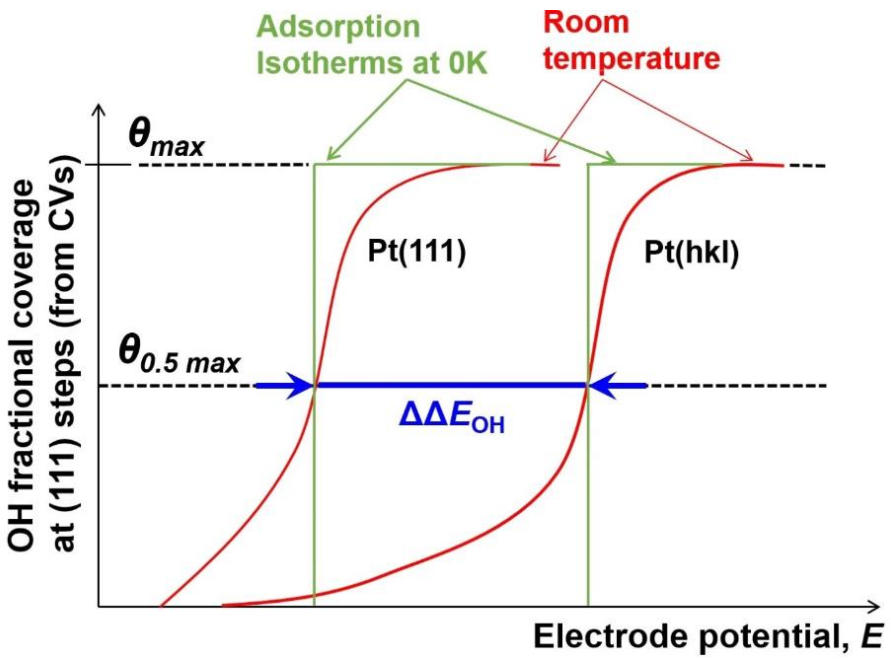

Figure 3.6: Schematic illustration of the procedure used for the determination of the difference in the OH-binding energies on different surfaces, $\Delta\Delta E_{OH,}$ for a Pt(hkl) electrode with respect to Pt(111). The isotherms were constructed by the integration of the corresponding CV-curves. The difference in potential required to reach θ=0.5θ_{max} reflects the difference in the binding energies of *OH[184].

3.1.5 Rotating-disk and rotating ring-disk electrodes

The rotating disk electrode (RDE) is a convective electrode technique, and one of the few for which there is a rigorous solution for the convective-diffusion at a steady state.

The device contains a disk of the conductive electrode material enclosed in insulating material (Teflon, epoxy-resin, etc.), as shown in Figure 3.7A. The rod is attached to the motor directly or by a chuck and is rotated at a certain frequency *f* (rotations per second/minute), also expressed as angular velocity ω (s^{-1}). Electrical connection to the electrode is provided by graphite or carbon-silver brushes in contact with the shaft. The noise level in the RDE is strongly dependent on the quality of this contact.[134]

Because of the rotation of the disk, the fluid in the immediate vicinity flows outward in a radial direction due to the centrifugal force. The fluid at the surface is continuously replaced by the flow normal to the surface. This allows a constant flow of fresh electrolyte and the reduction of mass transport limitations.

Additional information about the system equivalent to reversal techniques at stationary electrodes can be acquired by adding an independent ring electrode around the disk. This configuration is known as the rotating ring-disk electrode (RRDE), and the one used in this work is shown in Figure 3.7B. By measuring the current at the ring electrode, further information about the processes taking place at the disk can be collected. Since RRDE experiments involve the application of two potentials (the disk, E_D, and the ring potential, E_R)

and the recording of two currents (i_D, i_R), a bipotentiostat is necessary. The use of an RRDE allows the application of several different types of experiments, of which the most commonly used ones are collection experiments (where the species generated at the disk are detected at the ring), and shielding experiments (the flow of bulk electroactive species to the ring is perturbed by the disk reaction).

(A)  (B) 

Figure 3.7: Photographs of (A): glassy carbon rotating-disk (RDE), and (B) Pt(pc) rotating ring-disk (RRDE) tips with electrodes that were used in this work. Both electrodes are produced by Pine Research Instruments (USA).

In this work, Pine Research Instruments (USA) instruments were used to perform all RDE and RRDE experiments. A Pine RDE 710 RDE with MSR electrode rotator with CE and ETL marks with compatible shafts for RDE and RRDE tips were purchased from the same producer.

3.2 Electrochemical techniques

In order to manipulate, characterize, and test various electrochemical systems different electrochemical techniques were implemented. Since no single technique can produce a complete description of the system, the correct choice of techniques is an important step on the path to the elucidation of the problem at hand. In this chapter, the techniques used in this work are briefly explained. This includes electrochemical techniques such as cyclic voltammetry, impedance spectroscopy, quartz-crystal microbalance, and others, which were combined with electrochemical approaches to ensure a more detailed understanding of the investigated systems, such as atomic force microscopy, scanning tunneling microscopy, and x-ray photoelectron scattering.

3.2.1. Cyclic voltammetry

Cyclic voltammetry is a reversal potential-scan technique in which the current flowing through the system is recorded as a function of the applied potential. CV is widely used for initial electrochemical studies of new systems due to its simple application and quick implementation.[134]

In cyclic voltammetry, a so-called forward scan is applied first up to a vertex potential E_1, where the direction of the scan is reversed and proceeds to E_2, the second vertex potential. The cycling between the potential vertices E_1 and E_2 can be repeated as many times as necessary. The changing of the potential with time is shown in Figure 3.8A. The rate at which the potential is changed during CV is important as it significantly affects the characteristics of the voltammograms. The rate of change, or "scan rate" is always emphasized when considering voltammetry.

The response to the potential sweep is the current flowing through the system. Since the electrode/electrolyte interface is a boundary between two kinds of conductors (electronic and ionic), there are two main types of processes that allow the current to flow through the interface[134], as described below:

1. The charging of the double layer, which acts as a non-ideal capacitor. These are called capacitive processes.

2. Due to the transfer of electrons between the electrode and species in the electrolyte, i.e., due to redox reactions taking place. These are termed as "faradaic processes".

The results of CV are usually represented as $i=f(E)$, which are often referred to as *I-E* curves. Frequently, instead of current (*I*) the current density (*j*) is plotted. A typical *j-E* curve for a reversible electrochemical reaction is schematically shown in Figure 3.8B.

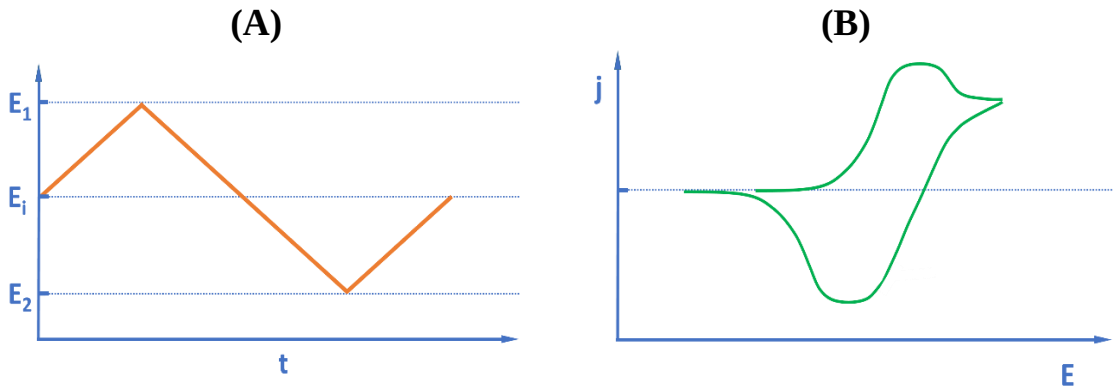

Figure 3.8: (A) The change of potential during CV E_i – initial potential, E_1 & E_2 – vertex potentials, *t* – time (B) A schematic representation of a CV for a reversible electrochemical reaction, where *j* – current density, *E* - potential.

All cyclic voltammetry experiments were carried out by Bio-Logic SP-300 and VSP-300 devices.

3.2.2. Chronocoulometry

Chronocoulometry (CA) is a technique in which the current passing through the system is measured as a function of time. Using the Faraday law (Eq. 6) the amount or mass of the product generated in the electrochemical reaction can be calculated, assuming 100% current efficiency. Chronocoulometry produces the same information as chronoamperometry, as it is just an

integrated form of the current-time response, but it offers several experimental advantages: better signal to noise ratio and the possibility to distinguish between the electrochemical double layer charge/discharge and the part due to the diffusion of electroreactants.[185]

All chronoamperometry experiments were carried out in this work using a Bio-Logic VSP-300 potentiostat.

3.2.3. Electrochemical impedance spectroscopy

Electrochemical impedance spectroscopy (EIS) is a technique in which the electrochemical system is probed by an alternating current (*ac*) signal of a small magnitude and the response of the system to this perturbation is observed. In contrast to other electrochemical techniques where the system is driven far from equilibrium, EIS offers the advantage distinguish many constituents of complex electrochemical processes, such as the interfacial charge transfer, diffusion adsorption, double layer charging, etc.[134]

The perturbing voltage can be expressed as:

$$e = E \sin \omega t \qquad \text{(Eq. 43)}$$

where ω is the angular frequency ($\omega=2\pi\nu$), t is time, E - the voltage wave amplitude, while e - the voltage observed at the moment t. The current response of the system will follow at the same frequency, but at a different phase, which is shifted by a phase angle φ:

$$i = I \sin(\omega t + \varphi) \qquad \text{(Eq. 44)}$$

where I is the current amplitude, and i - the current measured at time t. The angle between the two phasors (the current and the voltage) remains constant.

The ratio of the amplitudes of the perturbing signal and the response is measured, which produces the absolute value of the overall system impedance, $|Z| = E/I$, and the phase shift φ at different frequencies, which expresses the balance of capacitive, inductive, and resistive components. These values in general depend on the overall impedance of the system, which is given as:

$$Z(\omega) = Z_{Re} - jZ_{Im} \qquad \text{(Eq. 45)}$$

where $Z(\omega)$ is the overall (frequency dependent) impedance, while $Z_{Re} = |Z|\cos\varphi$ and $Z_{Im} = |Z|\sin\varphi$ are its real and imaginary components, respectively. The real part is associated with the classical ohmic resistances, while the imaginary part depends on the capacitive and inductive properties of the system.

The dependence of the impedance on the probing frequency can be expressed in different ways. In a Bode plot, $\log(|Z|)$ and φ are simultaneously plotted against $\log(\omega)$. Alternatively, the Nyquist plot, plots Z_{Re} vs. Z_{Im} ($Re[Z]$ vs. $Im[Z]$) for different values of ω. An example of an impedance spectrum is displayed using the Nyquist plot in Figure 3.9.

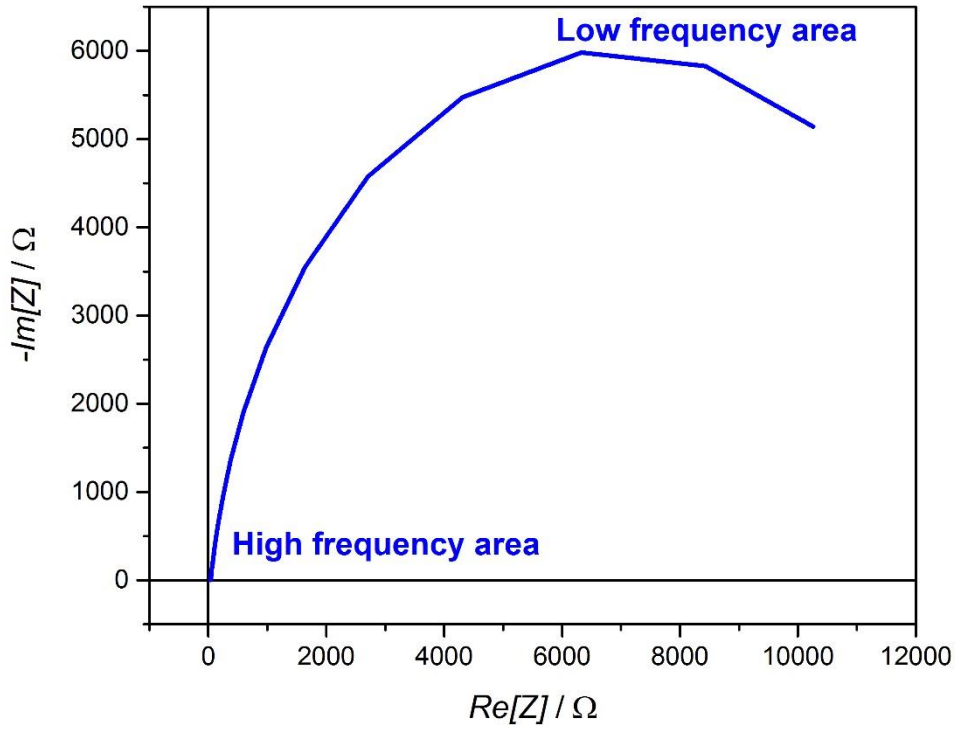

Figure 3.9: A Nyquist plot of an EIS spectrum obtained in 0.1M KOH for a $FeNiO_x$ thin film deposited on Pt(pc). Frequencies: 30kHz – 1Hz. Probing signal amplitude is 10mV. E_{WE}= 1.42V.

In order to verify the validity of the spectra before the modelling, certain conditions are required[186]:

i. causality - that the response is only due to the applied perturbation

ii. linearity - principle of superposition holds

iii. stability - the system should not change its properties during data acquisition

The validity of the results is usually checked by Kramers-Kronig transformations. They allow the calculation of one component of the impedance from another, the phase angle from the magnitude of the impedance, or the real part of the impedance from the imaginary part. For some Kramers-Kronig procedures, the impedance must have finite values for $\omega \rightarrow \infty$ and $\omega \rightarrow 0$ and must be continuous and finite-valued for all intermediate values.[187]

In order to analyze impedance spectra, an equivalent electric circuits (EECs) can be constructed. An EEC is an equivalent representation of physico-chemical equations describing the system under investigation. The circuits are normally made out of (quasi)linear passive elements. An EEC is normally elucidated for each individual system. However, sometimes EECs can be purely formal and their individual components do not correspond to specific physical processes (formal EECs). In order to gain information on electrochemical systems, however, the construction of "physical" EECs is necessary [186].

After an appropriate EEC is elucidated, the impedance spectrum is fitted to the circuit and various physico-chemical parameters describing the system can be obtained.[188]

Potentiodynamic electrochemical impedance spectroscopy (PDEIS) is a modification of EIS which uses an additional variable – the electrode potential, to help disambiguate the equivalent circuit analysis. PDEIS uses a common potentiostat and virtual instruments for electrochemical system probing with streams of mutually coordinated wavelets and a real-time analysis of the response.[189]

In the following, the description of one of the special EEC elements, the constant phase element, frequently used in EIS is briefly given.

The constant phase element (CPE) describes the response of the double electric layer, and it accounts for the so-called frequency dispersion. The frequency dispersion is the phenomenon when the value of the measured capacitance depends on the frequency of the applied *ac* signal. It is defined as:

$$CPE = \frac{1}{C'_{dl}(j\omega)^n} \qquad \text{(Eq. 46)}$$

where j is the imaginary unit, ω – the angular frequency, C'_{dl} – a factor related to the double-layer capacitance, and n – a dimensionless exponent formally taking values between 0.5 and 1, directly related to the dispersive behavior. When n=1 CPE becomes the pure capacitance C_{dl}. The CPE cannot be represented by any finite number of elements such as R, C, and L.

There are several suggestions how to explain the origin of the frequency dispersion[190]: roughness effect, fractal nature effect, distortion of the double-layer by faradaic processes, etc. However, none of these can account fully for all of the reported experimental observations.

Findings obtained from single-crystal EIS spectra suggest that[191]:

1. C'_{dl} and n are strongly dependent on the applied potential
2. There is a strong relation between frequency dispersion and phase transition processes at the interface
3. Values of n can be significantly lower than 1 if ordering in the adsorbate layer occurs
4. At potentials where such processes don't take place n is close to one and the interface displays a close-to-pure capacitive behavior

Therefore, the dependences of C'_{dl} and n on the electrode potential and can be used as a sensitive tool to examine the status and behavior of the electrode/electrolyte interface.

All EIS experiments were carried out by Bio-Logic SP-300 and VSP-300 potentiostats.

3.2.4. Electrochemical quartz-crystal microbalance

The electrochemical quartz-crystal microbalance (EQCM) is an application of a quartz crystal microbalance (QCM) to perform electrochemical measurements normally using a three-electrode configuration. One crystal face of the oscillator electrode is in contact with the

electrolyte. The quartz crystal microbalance is a piezoelectric sensing device. It consists of an oscillator circuit and a piezoelectric crystal incorporated into its feedback loop. Due to the reverse piezoelectric effect, alternating voltage induces mechanical oscillations in the crystal. These oscillations are stable only at the natural resonant frequency of the given crystal. This resonant frequency changes if mass (such as a thin film) is deposited on the surface of the crystal. If the deposited film is uniform, the Sauerbrey equation can be applied[192]:

$$\Delta f = -\frac{2f_0^2 \Delta m}{A(p_c \mu_c)^{\frac{1}{2}}} = -C_f \Delta m \qquad \text{(Eq. 47)}$$

where Δf is the frequency shift, f_0 is the natural resonant frequency of the crystal; Δm is the mass change, while p_c and μ_c are the density and the sheer modulus of the crystal. The *ac* excitation current used for the crystal oscillation can be easily distinguished from the *dc* current used for the perturbation of the electrochemical system. This allows electrochemical experiments to be carried out in parallel with the surface mass change measurements. This allows the electrochemical data (e.g. charge passed through the interface) to be correlated with mass changes at the electrode.[193]

3.2.5 Atomic force microscopy

The electrochemical methods mentioned above all deliver macroscopic information about the surface. In order to obtain morphological information about the electrode surface microscopic techniques are necessary. Such techniques supplement "purely" electrochemical methods and provide invaluable information about the interface.

Atomic force microscopy (AFM) is a kind of scanning probe microscopy relying on the measurements of the changes in the deflections of a small cantilever holding a sharp tip (usually made of Si_3N_3 or SiO_2). It provides complementary information about the electrode surface topography and surface forces[134]. Since its introduction by Binnig and Quate[194] in the 1980s, it has grown to become one of the most widely used techniques for surface characterization. As the tip is scanned across the surface, deflections are caused by the changes in the short-range interatomic forces between the tip and the surface, usually in the range of μN or nN[195]. The sample is held on a scanner, which is moved in all three directions by the means of the piezoelectric crystals, alternatively, the tip is scanned across the surface (depending on the type of device). The measurement of the movements of the tip is usually carried out by a laser beam that is reflected off the cantilever. The beam is reflected to a photocell array, which registers small movements due to the deflections of the tip. From the amount if deflection and the cantilever spring constant the repulsive force between the tip and the surface can be estimated.

The surface imaging can be carried out in several different modes, which all have their advantages and drawbacks. In the "contact" mode the tip is held as close to the surface as possible. In this mode, the beam deflection is held constant and the tip is moved up and down while the piezo voltage is recorded as a function of position. Since the local forces are large, only stable, mechanically hard samples can be imaged this way. However, this technique allows the parallel measurement of friction force acting on the moving tip. The "non-contact mode" entails the driving of the cantilever close to its resonant frequency. The interactions of the tip

with the surface cause changes in this frequency resulting in changes in the oscillation amplitude, which provides the feedback signal. The tip remains in the range of attractive forces for the entire oscillation period. The problem with this mode is its rather low imaging. In the "tapping mode", the tip position is modulated throughout the scan and recorded. The tip comes into contact with the surface for brief periods at the outermost oscillation point. This results in a better resolution in comparison to the noncontact mode, without the exertion of large lateral forces on the surface.

It is possible to obtain atomic resolution with AFM[196], however single atom defects are difficult to image. AFM is widely used for the microscopic characterization of electrode surfaces, ranging from atomic resolution images to studies of the surface morphology.[195]

AFM used in this work: a.) AFM; Digital-Instruments b.) Nanowizard 3. JPK Instruments. c.) Multimode VI (Multimode version 5), EC-STM/AFM with Nanoscope IIID controller, Veeco.

3.2.6 X-ray photoelectron spectroscopy

X-ray photoelectron spectroscopy (XPS) is a surface analysis technique that involves the irradiation of the sample in ultrahigh vacuum (UHV) conditions with an x-ray source of low energy. Ejected photoelectrons from the deep core levels (requiring photon energies is in the range of 150 - 2000 eV[197]) are detected and sorted as a function of energy by an electrostatical spherical sector analyzer. The XPS spectrum is the electron count plotted versus the kinetic or binding energy of the electrons.

Soft X-rays are obtained from Al or Mg targets, which are used due to their narrow characteristic K_α lines, are used to irradiate the sample. If the energy of the inbound photon is larger than the sum of the binding energy E_b and the work function ϕ_w, $h\upsilon > E_b+\phi_w$, photoelectrons are ejected from the surface. The kinetic energy E_k of the ejected electron is given by the equation:

$$E_k = h\upsilon - E_b - \phi_w \qquad \text{(Eq. 48)}$$

where h is the Planck constant, υ is the frequency of the exciting radiation. This means that a characteristic X-ray will produce a series of photoelectron peaks reflecting the binding energies of the electrons present in the sample. Due to the strong interaction between electrons and solid-state objects, the electrons penetrate the sample in the nanometer range. This means that the signal collected during XPS is linked only to the surface or the region immediately beneath it. This makes XPS particularly suitable for the study of solid surfaces and thin films. XPS is capable of assessing not just the composition of a surface, but can also indicate the chemical environment and bonding state of molecular species on single crystal surfaces[198].

The XPS measurements were carried out in a UHV set-up equipped with Specs X-ray Source XR 50 and Specs Hemispherical Energy Analyzer PHOIBOS 150. Base pressure in the measurement chamber: $< 2\times10^{-9}$mbar. Incident radiation from an unmonochromatic Al Kα (1486.6eV; 13kV; 23mA) source was used. Pass energy: 70eV resulting in an energy resolution better than 0.5eV. Binding energies were calibrated based on positioning the main C1s peak at 284.5eV. Measurement conditions: 4×10^{-9}mbar at room temperature.

Before each measurement, the samples were kept in an exchange chamber at a pressure $<5\times10^{-6}$mbar for 17-20h to remove physisorbed water. The CASA XPS program with a Gaussian–Lorentzian mix function and Shirley background was used to analyze the XP spectra quantitatively.

3.3 List of equipment, materials, and chemicals

A list of all the equipment materials, and chemicals used in this work are alphabetically given in the lists below. Since experiments were performed partially at Ruhr-Universität Bochum (RUB), and partially at the Technical University of Munich (TUM), the locations of particular pieces of equipment and materials are given where appropriate.

3.3.1 Equipment

AFM/STM: a.) multi-mode atomic force microscope, Digital-Instruments (RUB) b.) Nanowizard 3. JPK Instruments. (RUB). b.) Multimode V EC-STM/AFM with Nanoscope IIIa controller, Veeco. (TUM)

EQCM: QCM 200. Stanford Research Systems, USA. (RUB&TUM)

Inductive heater: 20-80kHz, 15KW-EQ-SP-15A, MT, USA. (RUB)

Potentiostats: a.) VSP-300. Bio-logic, France. (RUB & TUM) b.) SP300. Bio-logic, France. (RUB)

RDE/RRDE: Pine RDE 710 RDE with MSR electrode rotator with CE and ETL marks. Pine Research Instruments, USA. (RUB & TUM)

Reference electrode: MMS. a.) Schott, Germany (RUB) b.) SI Analytics, Germany. (TUM)

Thermometer: TMD90A dual input. Amprobe, USA.

Water purification systems: a.) Evoqua Ultra Clear 10 TWF 30 UV. Evoqua, Germany. (TUM) b.) Siemens Ultrapure. Siemens, Germany (RUB).

XPS: SPECS Surface Nano Analysis GmbH using a focused monochromatized Al-K\alpha radiation (1486.6 eV), equipped with Specs X-ray Source XR 50 and Specs Hemispherical Energy Analyzer PHOIBOS 150. (TUM)

3.3.2 Materials

Ar – 5.0. Air Liquide, Germany.

Ar/CO – 5.0 / 4.7, Air Liquide, Germany.

Ar/H_2 (5%) – 6.0, Air Liquide, Germany.

Au(pc) – 99.99%, Diameter: 3mm, CH Instruments, USA.

FTO – NSG TEC 8 A, Pilkington, UK.

Glassy Carbon Electrode – Diameter: 5mm, Pine Research Instruments, USA.

HOPG - HOPG/ZYB/DS/1, Spread 0.8º±0.2 º, MikroMasch, Germany.

H_2– 6.0, Air Liquide, Germany.

Ir(111) - 99.99%. Diameter: 5mm, oriented better than 0.1°, roughness: 30nm. Mateck, Jülich, Germany.

O_2 – 5.0. Air Liquide, Germany.

Pt(pc) - 99.99%, Diameter: 5mm. roughness: 30nm. Mateck, Jülich, Germany.

Pt-wire – 99.99%, Diameter: 0.3mm. GoodFellow, Germany.

Pt(111) –99.99%, Diameter: 5mm, oriented better than 0.1°, roughness: 30nm. Mateck, Jülich, Germany.

Pt(331) - 99.99%, Diameter: 2.5mm, oriented better than 0.5°, roughness: 50nm. Icryst, Jülich, Germany.

3.3.3 Chemicals

Butylamine – 99.5%. Sigma Aldrich, Germany.

Butylammonium-sulfate (BAS) - was prepared from mixing butylamine and H_2SO_4 in a 2:1 molar ratio

CH_3COONa – a.) ≥99% J.T. Baker, USA b.) ≥99% Sigma Aldrich, Germany.

$CoSO_4 \cdot 7H_2O$ - ≥99%, ACS Reagent. Merck, Germany.

Cs_2SO_4 - 99.99%, Sigma Aldrich, Germany.

CuO - 99.99% Sigma Aldrich, Germany.

$FeSO_4 \cdot 7H_2O$- ≥99%, ACS Reagent. Merck, Germany .

$HClO_4$ – 70%. Suprapur. Merck, Germany.

H_2O_2 – 30%, Suprapur. Merck, Germany.

H_2SO_4 – 96%, Suprapur. Merck, Germany.

KOH – a.) ≥85%, ACS reagent, Sigma Aldrich, Germany. b.) 85% Grüssing, Germany.

K_2PtCl_4 - Sigma Aldrich, Germany.

K_2SO_4 – 99.99%. Sigma Aldrich, Germany.

Li_2SO_4 - 99.99%, Sigma Aldrich, Germany.

Nafion® 5 wt. % in lower aliphatic alcohols, contains 15-20% water - Sigma Aldrich, Germany.

NaOH - ≥98%. Sigma Aldrich, Germany.

$NiSO_4 \cdot 6H_2O$- ≥99%, ACS Reagent. Merck, Germany.

Na_2SO_4- a.) 99.99%, Sigma Aldrich, Germany b.) ≥99% AppliChem, Germany.

Rb_2SO_4- 99.98%, Sigma Aldrich, Germany.

3.3.4 Software

EC-LAB V 10.40 – for the control and data acquisition from the potentiostats.

EIS Data Analysis 1.0 - for the fitting of EIS spectra.

GetData – for the digitalization of graphs from literature

Nanoscope 5.31r1 - AFM data acquisition

OriginPro 2015G – for data analysis, graphing, and processing

SpecsLab Prodigy 4.8.3-r48573 - for obtaining XPS spectra

SRS QCM200 - EQCM data acquisition

TM-SWA– temperature control with inductive heater

4. Results and discussion

4.1 Experimental aspects of activity benchmarking

A prerequisite for the identification and optimization of electrocatalysts is the accurate and meticulous assessment of their activity. This is particularly important for the evaluation of newly developed catalyst materials. Nevertheless, with the growing number of reports published, such evaluations and comparisons of different materials become increasingly difficult. This is, to a large degree, due to the lack of widely accepted protocols for precise activity measurements. An additional source of difficulties is the fact that modern electrochemical equipment, despite great improvements in its construction and application, is not ideal and measurements can be affected by hardware-related issues.

Three particularly important aspects for electrochemical activity benchmarking that are often underestimated or even ignored in modern electrocatalysis are discussed in this chapter[199]: compensation of the iR-drop, issues related to the evolution of a non-conducting gas phase, and careful determination of the real surface are using surface-limited reactions. In particular, a new methodology for benchmarking the catalytic activity of gas evolving electrodes at high current densities is presented.

4.1.1 Determination of the uncompensated resistance (iR-drop)

The uncompensated resistance in an electrochemical system is the sum of all the resistances in the path of the current to the working electrode. The sources of these resistances can be generally divided into three groups:

1. ion migration in the electrolyte
2. electron transport
3. contact resistances

The dominant source of the uncompensated resistance depends on the type of electrochemical system. In common three-electrode electrochemical cells which use liquid electrolytes, the uncompensated resistance is usually dominated by the resistance of the electrolyte between the WE and the tip of Luggin capillary of the RE[200]. In the case of solid electrolytes, the situation can be even much more complicated as pseudo reference electrodes are used, and the position of RE can drastically change the EIS response.

As the value of the Ohmic drop in the electrolyte is itself dependent on several parameters (temperature, current density, concentration and hydration state of the ions, etc.), it must be accounted for when comparing data collected under different conditions. Several approaches have been developed for the measurement of the ohmic resistance: current interrupt, AC resistance, high frequency resistance, and electrochemical impedance spectroscopy (EIS). The main advantage of EIS is the fact that it can provide more accurate and reproducible data because it introduces only very small perturbations to the measured system.[201]

EIS has been commonly implemented for the determination of the value of the uncompensated resistance since the 1970s[202,203,204]. This is achieved by recording the impedance spectra in a wide frequency range, including high frequencies (~ kHz, MHz, depending on the system). The high-frequency part of the impedance spectrum above a certain value is entirely due to the bulk ionic and electronic resistances. This means that an EI spectrum in a Nyquist plot would intersect the real-number axis (*Re[Z]*) in the high-frequency area. The point of intersection corresponds to the value of the uncompensated resistance[201]. In order to analyze EIS data a physical model for the system under investigation should be elucidated. By fitting the EIS data, the uncompensated resistance can be estimated. One should however note that the values of the uncompensated resistance determined this way should not be influenced by additional processes taking place during the polarization of the electrode (gas evolution, chemisorption, etc.).

Figure 4.1A shows Nyquist plots of simulated impedance spectra for two cases, with and without a "virtual" charge transfer, with the corresponding equivalent electric circuits (EECs) used to perform the simulations in the insets. The double layer is represented by a CPE. The uncompensated resistance is denoted as R_U. From Figure 4.1A one can straightforwardly see that the value of the determined uncompensated resistance does not depend on the occurrence of charge transfer processes.

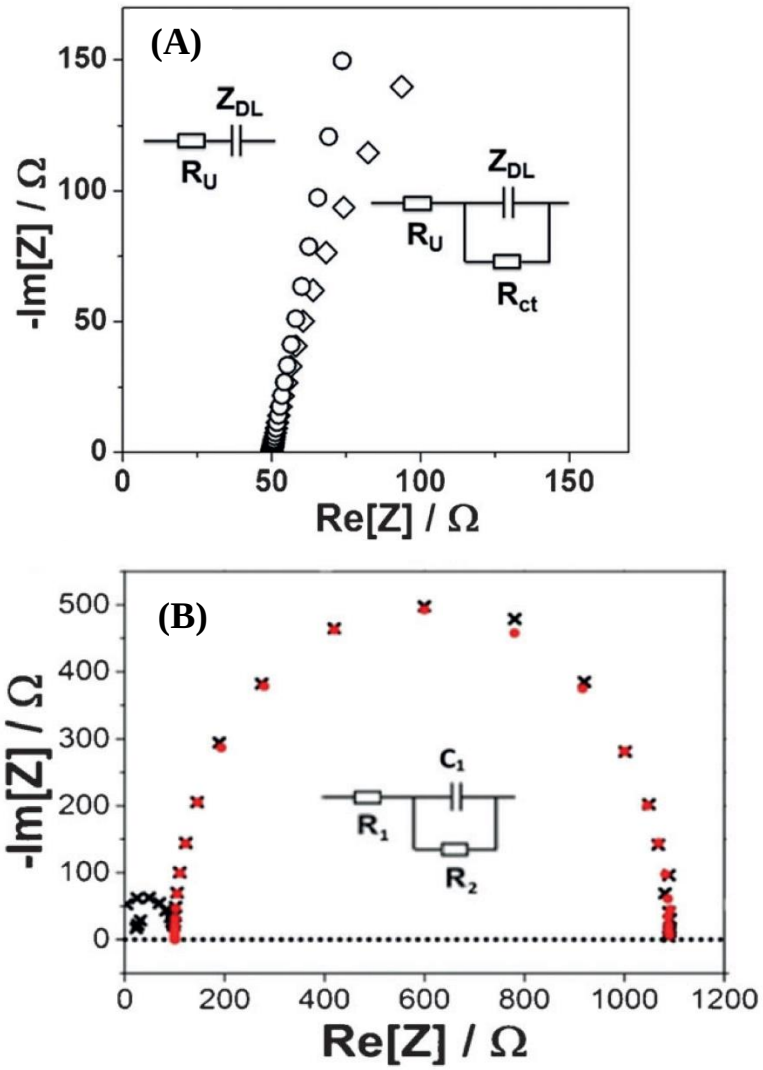

Figure 4.1: Nyquist plots of EIS spectra. (A): Simulated spectra for two different cases with (◇) and without (○) faradaic processes (charge transfer through the interface). R_U is the uncompensated resistance, Z_{DL} – impedance of the double layer, and R_{ct} is the charge transfer resistance. The high-frequency parts of both spectra intersect the real-number axis at the value of the uncompensated ohmic resistance (in this case at *ca* 50Ω). (B): EIS spectra taken in a dummy cell, with a circuit shown in the inset, without (✕) and with (●) the shunt capacitance connected. Frequencies: 1MHz – 100Hz. Values of the equivalent electric circuit elements: R_1=100Ω, R_2=1kΩ, and C_1=2μF.[199]

Figure 4.1B displays a simple example. The EIS spectrum recorded in a dummy cell unexpectedly displays two semi-circles instead of one, showing artifacts due to the limitations of the real-world operational amplifiers. To compensate this non-ideal behavior, a so-called "shunt capacitance" or the "capacitor bridge" needs to be connected between the CE and RE. The optimal value of the shunt capacitance depends on the properties of the system, and it is generally determined experimentally. The above-mentioned effect is demonstrated in Figure 4.1B where a shunt capacitance of 2 μF is connected. Without the shunt capacitance the high frequency part of the spectrum is distorted and it does not intersect the real-number (*Re[Z]*) axis. Surprisingly, an apparent rise is observed in the absolute value of *Im[Z]* due to the fact

that the high-frequency sine waves are filtered out by the low-pass resistor-capacitor (*RC*) filter formed by the RE electrode resistance with the stray capacitance of the reference circuit[205]. The shunt capacitor allows the high-frequency part to bypass the cell, and in the impedance spectrum the graph intersects the real-number axis, as expected[206].

The determination of the exact point of intersection with the *Re[Z]* axis is important for the accurate determination of the uncompensated resistance in real electrocatalytic systems. Figure 4.2 shows impedance spectra taken using Pt(111) electrodes in a Ar-saturated solution containing 0.05M H_2SO_4 and 0.05M Rb_2SO_4. Without the shunt capacitance, the spectra do not intersect the real-number axis. If the uncompensated resistance would be estimated without the shunt capacitor connected, based on the distorted graph, as for instance mistakenly recommended in a recent paper by van der Vliet et al[207]., an error of *ca* 20% would be introduced.

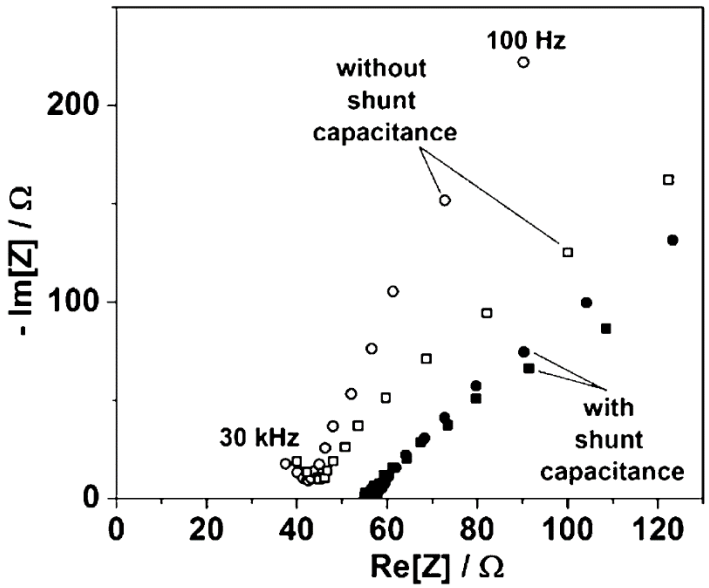

Figure 4.2: EIS spectra of Pt(111) in Ar-saturated 0.05M H_2SO_4 + 0.05M Rb_2SO_4, with (●,■) and without (○,□) the shunt capacitance connected between the RE and CE, at OCP. Frequency range: 30kHz – 100Hz. RDE configuration, 1600 r.p.m.[199]

When performing the iR-drop compensation, it is very important to perform the EIS measurements under conditions as close as possible to the conditions that take place in the system under investigation. Changes in experimental conditions can introduce significant errors in the values of the measured uncompensated resistance. Figure 4.3 illustrates that the introduction of hydrogen, instead of argon gas to the solution can lead to significant changes in the recorded EIS spectra. H_2 adsorbs on the surface of the Pt(111) electrode and changes the open-circuit potential (OCP) of the system. If the EIS is performed at OCP, it is actually performed at different potentials in the two different cases, which leads to significant shifts in the spectra, introducing an error of *ca* 20%.

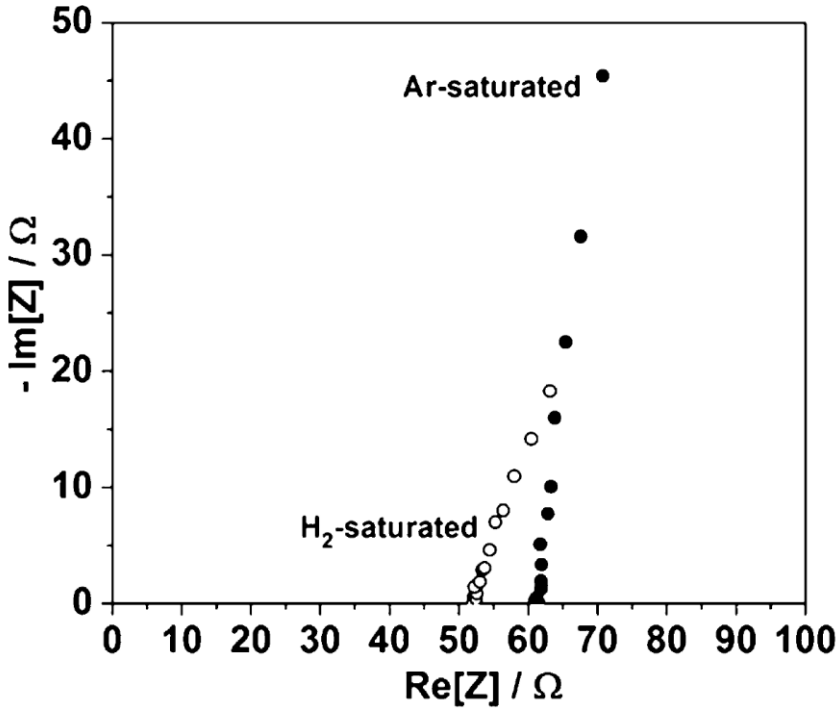

Figure 4.3: EIS spectra of Pt(111) in 0.05M H_2SO_4 saturated with H_2 (○) or Ar (●), at OCP. Both spectra are recorded with a connected shunt capacitance. Frequency range: 30kHz – 100Hz. RDE configuration, 1600 r.p.m.[199]

Alterations in the electrolyte composition, like the introduction of a new ion, or dissolution of a different gas in the electrolyte can lead to significant changes in the properties of the interface, even at the same pH-value. The fact that the uncompensated resistance is sensitive to numerous factors, the effects of which are often not easy to foresee, further reiterates the importance of recording the spectra under circumstances as close to reaction conditions as possible.

Even with the use of the shunt capacitance, there are instances in which, due to hardware or other limitations, the EIS spectrum does not intersect the real-number axis, or the high-frequency part is too noisy to determine accurately the intersection point. This is illustrated in Figure 4.4, where a *ca* 1.1Ω uncertainty is introduced to the determination of the iR-drop, due to the noisy high-frequency part of the spectrum.

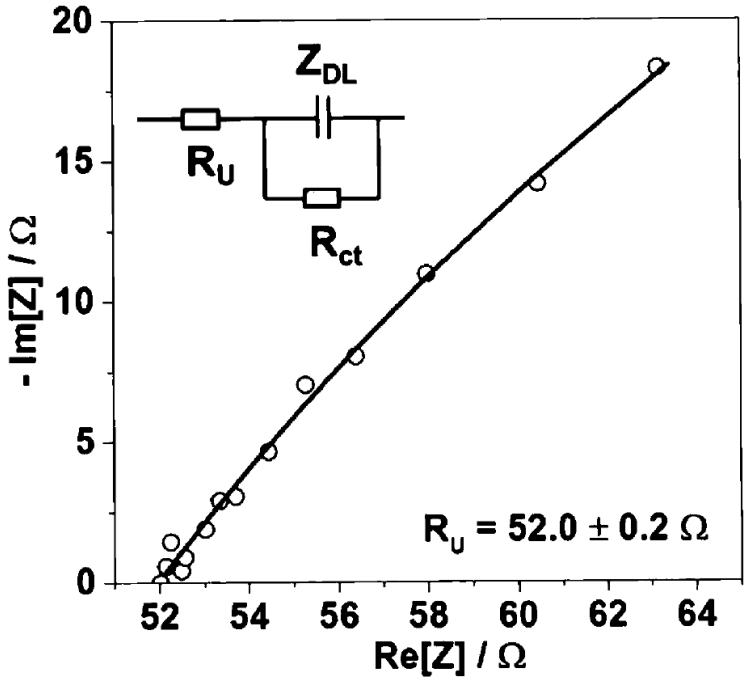

Figure 4.4: Example of an EIS spectrum with significant noise in the high-frequency area, rendering the determination of the intersect real-number axis unreliable. Inset shows the EEC used for fitting.[199]

While this error is not significant for small currents, at higher current values it would cause significant problems in the evaluation of the ohmic drop in the system. The magnitude of the error introduced this way is particularly significant if the potential sweep introduces large current[162], such as for the HER. For instance, at a current of 10mA, the 1.1 Ω uncertainty could lead to an error in the estimation of the uncompensated resistance up to 11mV, which is in many cases not acceptable for the activity benchmarking.

In this case the simple determination of the intersection point is not sufficient to correctly asses the uncompensated resistance. This issue can be solved by fitting the EIS spectrum to the appropriate EEC. By applying this approach, the fitting of the spectrum in the case presented in Figure 4.4 reduced the measurement error to *ca* 0.2Ω.

To further illustrate the importance of the accurate determination of the uncompensated resistance, the activity measurements of the HER and HOR at polycrystalline Pt surfaces are considered, Figure 4.5.

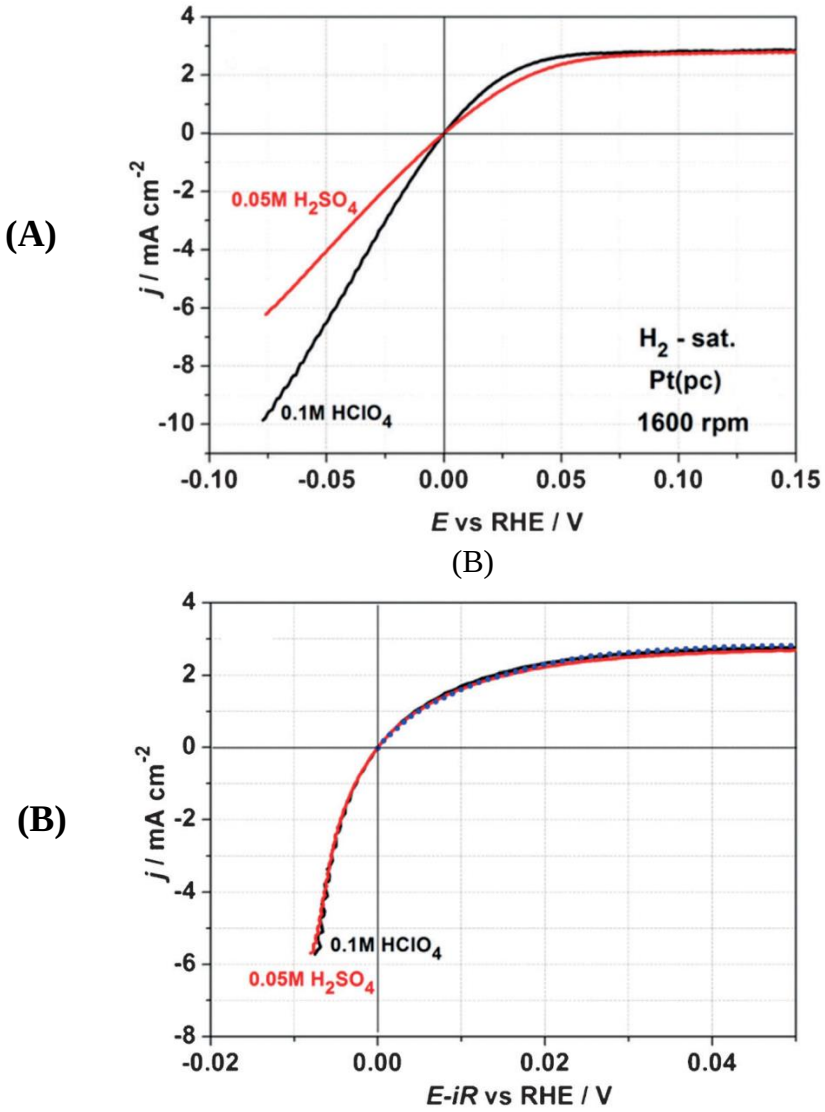

Figure 4.5: CVs of Pt(pc) in H_2-saturated 0.05M H_2SO_4(—) and 0.1M $HClO_4$(▬). RDE, 1600 r.p.m. (A) without iR-drop correction (B) with iR-drop correction. The dashed line (▪▪▪▪) represents the theoretical curve (only the HOR part) derived from the Butler-Volmer equation. After the correction for the iR-drop, the voltammograms in the two electrolytes align with each other as well as with the theoretical curve.[199]

Without iR-drop correction it appears as if both reactions were significantly faster in perchloric acid, at the same pH-value (pH=1), as shown in Figure 4.5A. It should be noted here that significantly different HER exchange current densities are often cited for benchmarking purposes in perchloric and sulfuric acids[71,138,157,158,208,209,210, 211,212].

If one performs the iR-drop correction according to the described procedure, the two voltammograms line up with each other and with the curve based on theoretical predictions, as illustrated in Figure 4.5B. This is in good agreement with the classical theory of HER. Note that Figure 4.5B shows only the low-overpotential part of the HER voltammogram. The evaluation of the iR-drop at higher overpotentials where the gas phase starts evolving (i.e., gas bubbles appear and partially block the electrode surface) requires the consideration of the influence of the non-conducting gas-phase, which will be discussed in Section 4.1.2.

4.1.2 Effects due to the emergence of a non-conducting gas phase

If a new gaseous phase is formed during an electrocatalytic reaction, the measured uncompensated resistance will be further affected by the emergence of the gas phase bubbles periodically or stochastically leaving the surface. The bubble formation influences the uncompensated solution resistance in two ways:

1. The bubbles reduce the active electrode surface. This effect is diminished, but not completely eliminated in an RDE setup. While the bubbles leave the surface relatively quickly using the RDE configuration, the developing gas phase still blocks the active sites on the surface, decreasing the effective electrode surface area.

2. The non-conducting gas phase reduces the bulk conductivity of the electrolyte, according to the Bruggeman equation:

$$R_b = R_e(1-\varepsilon)^{-\frac{3}{2}} \qquad \text{(Eq. 49)}$$

   where R_b is the electrolyte resistance in the presence of the non-conducting gas phase, R_e is the electrolyte resistance without the gas phase, and ε is the gas phase fraction.

The iR-drop correction is particularly important in these systems and it should be performed with great care and under real experimental conditions. Otherwise, the error introduced to the results increases with the increasing electrolyte resistance due to the gas phase emergence.

To illustrate the significance of the gas-phase evolution issues, a well-known OER catalyst, cobalt-oxi-hydroxide (further denoted as CoO_x) thin film, in 0.1M KOH was used as a model system, Figure 4.6. In systems with gas-phase evolution, the speed of bubble formation is dependent on the speed of the reaction, and, thus, the electrode potential. More rapid bubble formation at higher potentials increases the uncompensated resistance.

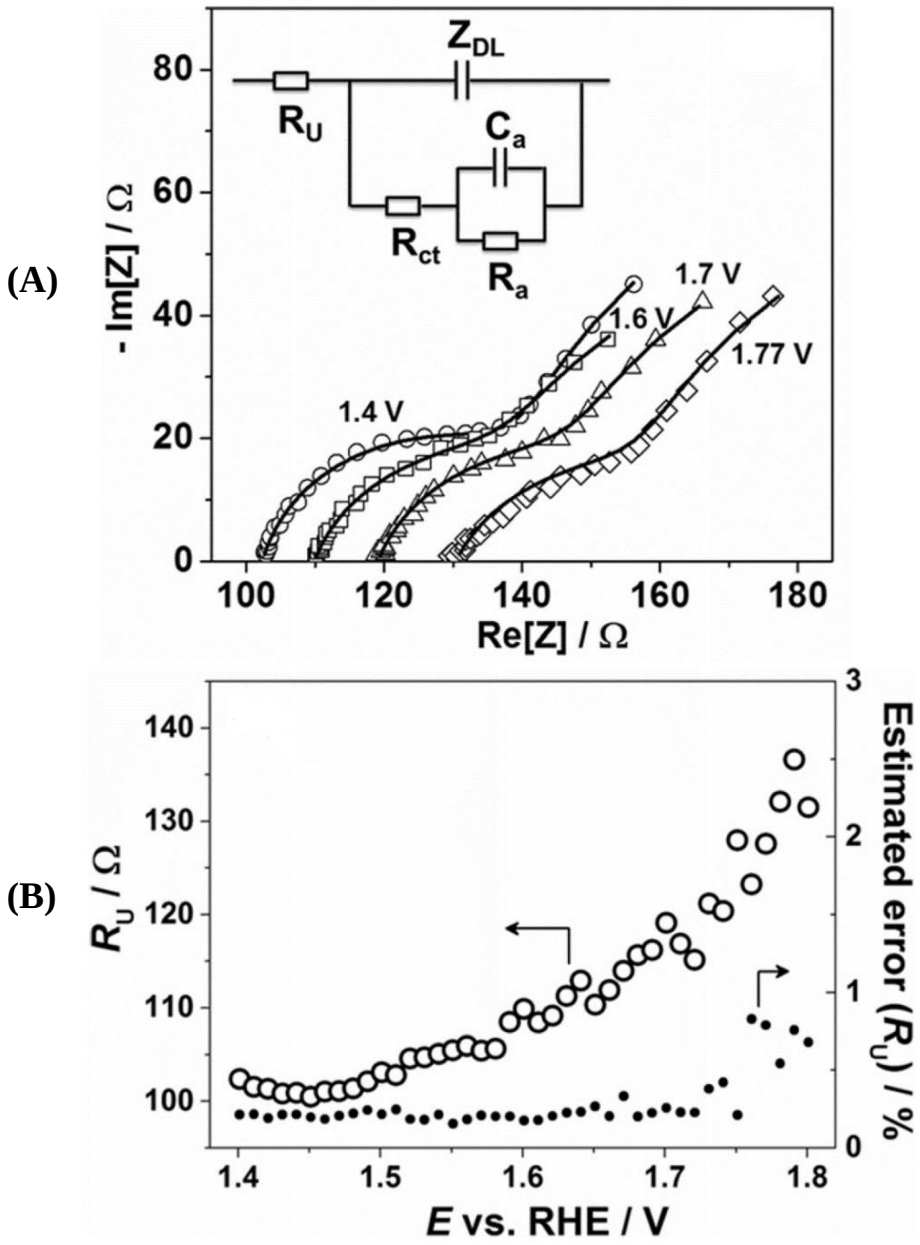

Figure 4.6: Electrodeposited CoO_x thin film in 0.1M KOH (A) EIS spectra during OER 1.4 – 1.77V vs. RHE. Inset shows the EEC used for fitting. R_u – uncompensated resistance, R_{ct} – charge transfer resistance, Z_{dl} – double layer impedance. Additionally, the EEC contains a parallel connection of an adsorption resistance, R_a, and capacitance, C_a, connected in series to the R_{ct} to account for the behavior of the reversibly adsorbed reaction intermediates. (B) Estimated uncompensated resistances (○) and their corresponding uncertainties (●), as a function of the applied electrode potential.[198]

In Figure 4.6A one can see that the value of the R_U increases from *ca* 102Ω to *ca* 130Ω during the increase of the applied electrode potential from 1.4V to 1.77V. This can lead to at least two significant errors in activity benchmarking if the iR-drop correction is not correctly performed:

1. The Tafel slope will be significantly influenced changing the estimated kinetic parameters.

2. The error introduced to the determined activity will be different at different potentials, reaching *ca* 30% difference in the example in Figure 4.6B, making the comparison of data for different electrocatalysts very difficult.

This is essential since the current densities used in, e.g., OER in industry, are about an order of magnitude higher than those used in laboratory environments, which are performed up to *ca* 10mA cm^{-2} [213,214,215] as the noise at higher current densities becomes too large. These current densities are insufficient to be considered for real-world devices, and they should be increased by one order of magnitude in order to obtain relevant data[44,216]. Misinterpretation of RDE data for partially covered or non-planar geometries is also a potential source of error[134].

State-of-the-art OER catalysts are usually oxide films (such as CoO_x), which are deposited on different substrates. The surface morphology is particularly significant in this kind of catalysts as it largely influences the blockage of the surface by gas bubbles. Sites where the local morphology allows a faster nucleation and release of the bubbles will be active for longer periods of time. The electrocatalytic properties of a material, however, are evaluated over the entire surface, including sites where bubble release is slow.

In order to assess the activities of such catalysts, mass transport needs to be greatly increased. This can be achieved by using a rotating microelectrode (RME), where spherical and linear diffusion are combined, resulting in a significantly enhancement in the mass transport. The dimeter of the microelectrodes is often smaller than the critical size of the bubble. This reduces the blockage effect at the surface, enabling a more accurate evaluation the catalyst activity, as demonstrated in Figure 4.7. Additionally, the use of RME allows close-to-iR-drop-free measurements, as the measured electrode potential is close to the real one with 1-2mV difference at most, (Figure 4.7B).

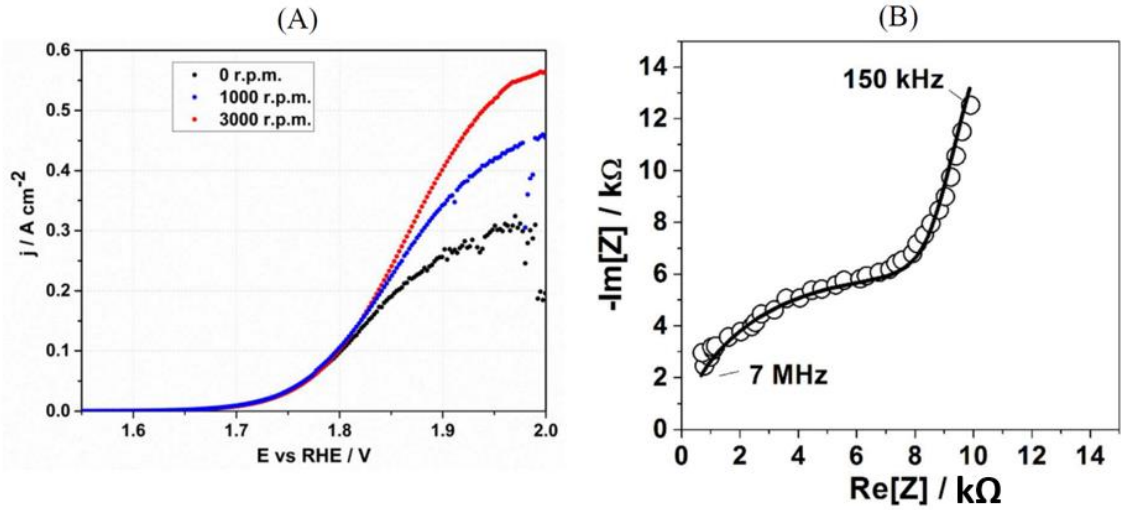

Figure 4.7: (A) CVs taken with an RME for CoO_x films on Pt(pc) in O_2-saturated 0.1M KOH, for rotation rates of 0, i.e., static conditions (●), 1000 r.p.m. (●), and 3000 r.p.m (●). Scan rate: 1mV/s. (B) Typical impedance spectrum (○) of a Pt microelectrode in 0.1M KOH. The fitting (black line (—)) was performed according to the procedure described previously.

Figure 4.7A clearly shows that the hydrodynamic conditions remove the effects of the emerging gas bubbles (and possibly changes in the local pH) effectively. This allows a more accurate determination of the electrocatalytic properties of the catalyst film at industrially relevant current densities (≥200mA cm^{-2} [138]).

4.1.3 Estimation of the real electrode surface area

In order to assess the activities of catalysts they need to be expressed as an intensive quantity. They are usually represented as current densities, i.e., current per electrode surface area. Considering this, it is clear that the determination of the real electrode surface area is a crucial procedure for accurate activity benchmarking. An error in the determined surface area value will result in a serious error in the evaluation of the electrocatalytic activity as well.

Several techniques for the determination of the real electrode surface area exist, however, none of them is ideal. For metal electrodes (particularly noble metal), the most widely used method utilizes the integration of voltammetric peaks related to specific surface-limited reactions. This approach assumes there is a strong, well-defined link between the structures of the electrode surface and the formed overlayer, resulting in a well-established surface charge density[217,218]. Nevertheless, the surface coverage of certain species, and the associated charge, strongly depends on the status of the electrode/electrolyte interface. Any change at the interface (e.g., alloying, morphology, electrolyte composition, etc.) may result in the alteration of the surface coverage of specific species. In such a case, the value of the real electrode surface area acquired *via* the aforementioned method cannot be used to assess the activity after such a change has been implemented. Therefore, the reaction by the means of which the surface area is evaluated must be chosen with great care, keeping in mind the specific properties of the system in question.

This issue is illustrated with model single-crystal systems, Figure 4.8.

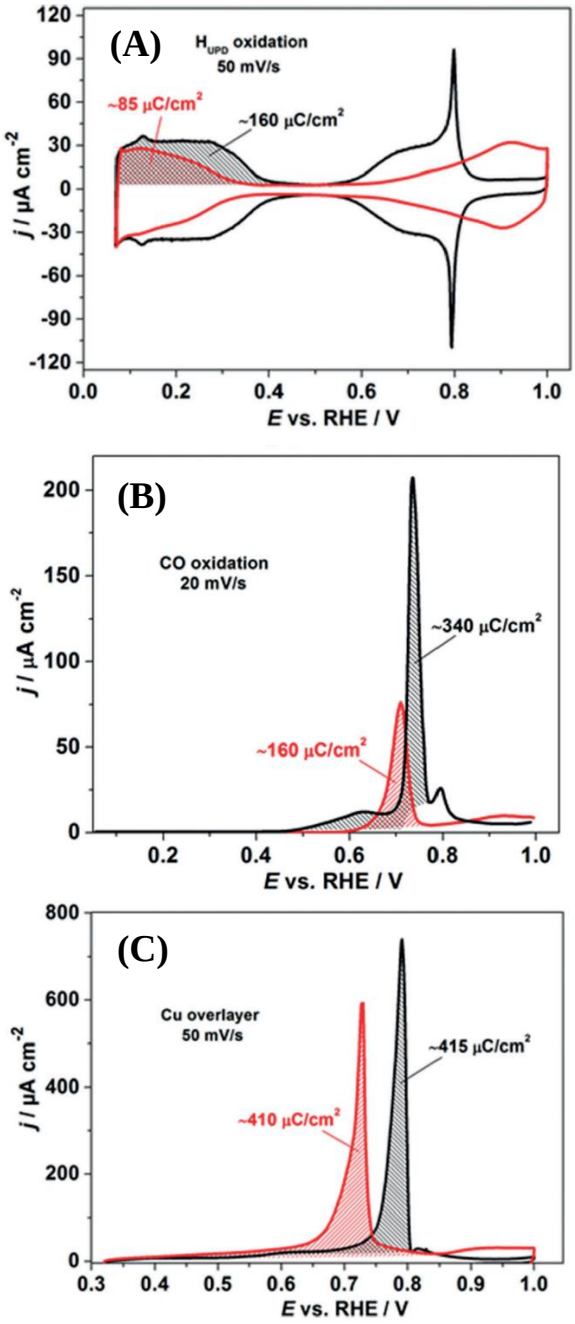

Figure 4.8: CVs with integrated peaks for surface-limited reactions on Pt(111) (—) and Cu-NSA (—). The charges calculated this way are shown in each image. CVs were taken in Ar-saturated 0.1M $HClO_4$. Integrated (A) hydrogen adsorption/desorption region. (B) oxidation of adsorbed CO. (C) oxidation of Cu overlayers.[199]

Figure 4.8 shows CVs of Pt(111) and Pt(111)/Cu NSA in Ar-saturated $HClO_4$. If the real surface would be estimated by the integration of the hydrogen adsorption/desorption region (0.05-0.4V), the procedure for the two electrodes would yield very different results. This reaction is frequently used to determine the real surface area of electrodes, however, referring to the area of unmodified Pt(111) is not justified. The Figure clearly demonstrates that changes in the electrode/electrolyte interfaces drastically influence the hydrogen adsorption properties

of the electrode. Thus, using the value known for Pt(111) as a reference for the NSA would introduce a *ca* 2-fold error in the real surface area determination.

The same is true for another widely used reaction – CO adsorption and subsequent oxidation of the surface-bound CO. Figure 4.8B shows that the charge calculated for the CO-oxidation is different on Pt(111) and the Cu-NSA. This technique is often applied for the estimation of the real surface area of Pt, Ir and Rh electrocatalysts. However, this approach has been shown to be problematic when applied to certain Pt-alloys[219] and nanoparticles[220].

On the contrary, the oxidation of the underpotentially deposited Cu-overlayers shows similar charge densities for both kinds of surfaces, Figure 4.8C. In this sense, Cu overlayer oxidation is more reliable since the Cu-atoms are deposited in a 1:1 ratio to the Pt-substrate[221]. This surface-limited reaction is suitable for the determination of the real-surface area of Pt and Pt-alloy catalysts. However, it has been shown that Cu-atoms form only a partial monolayer on the surface of Au-nanoparticles, where they preferentially deposit on defects. This is in contrast to the behavior reported on Au single crystals on which a complete monolayer is formed at 0.42V *vs.* RHE[222].

The estimation of the real surface area is particularly problematic for oxide materials. It is generally difficult to immobilize these materials on the electrode surface and, consequently, the real electrode surface is drastically different from the geometric area. Common methods used for the estimation of the real surface area, such as the Brunauer-Emmett-Teller (BET) method are often unreliable[217]. In addition, since oxide materials are often used as catalysts for gas-evolution reactions such as the OER the pores are often blocked by adsorbed H_2O or OH^- [223]. EIS is also often problematic for this application due to the insufficiently understood frequency dispersion of the double-layer response, in which multiple parameters that are difficult to predict and can lead to high errors in the determination of the real surface area[224,225,226].

An approach to overcome these issues is the use of microelectrodes, as proposed recently in collaboration with the group of Prof. Schuhmann (Ruhr-Universität Bochum)[227]. The small diameter of microelectrodes, typically *ca* 25µm, enables the visualization of the entire electrode surface *via* AFM, Figure 4.9, from which the "real" roughness can be estimated. The accurate assessment of the surface morphology enables a more accurate evaluation of the real surface area, and consequently more accurate benchmarking of the catalytic activity.

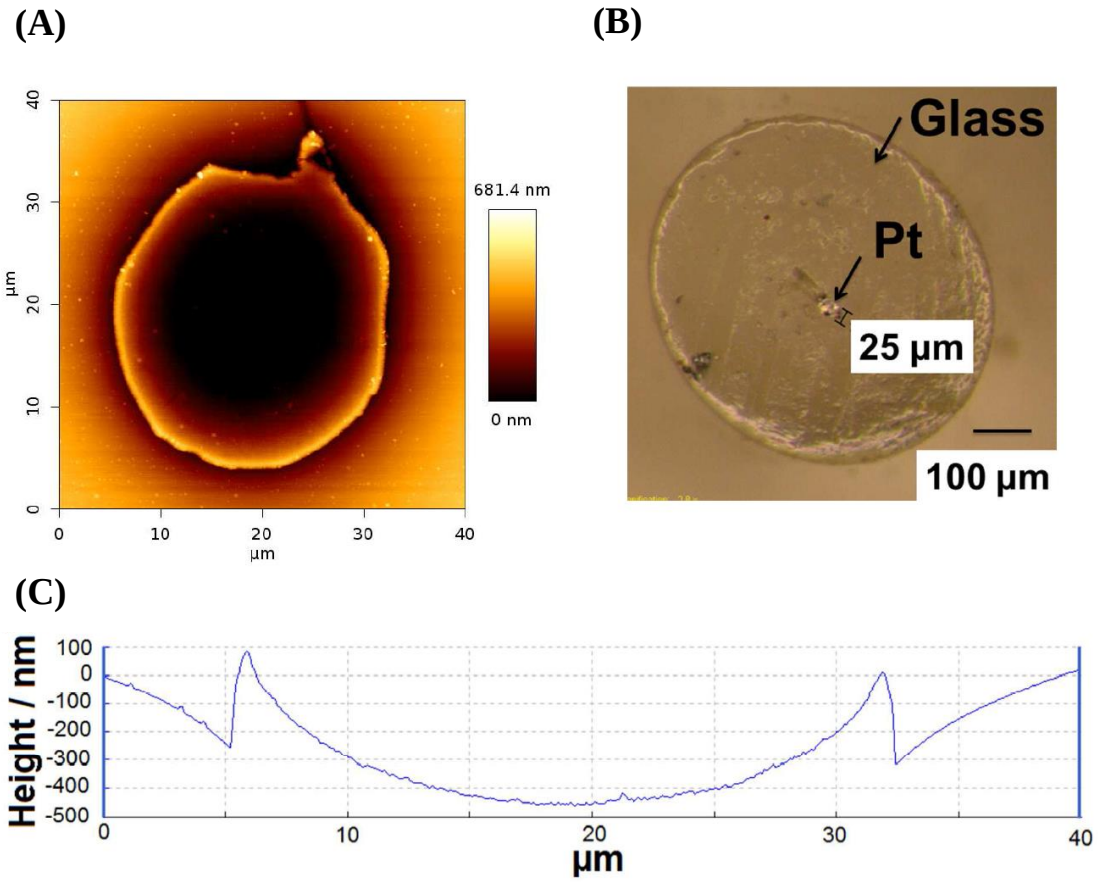

Figure 4.9: AFM images of the deposited CoO_x layer on a Pt-microelectrode. (A) 2D image of the surface. (B) Photograph of the microelectrode tip showing the inert glass housing and the 25µm diameter active Pt surface. (C) A typical AFM line profile passing through the center of the microelectrode with a CoO_x layer.[227]

Another advantage of this approach is that the imaging of the entire surface enables the investigation of the connection between the electrocatalytic activity and surface morphology. Profiles, such as the one shown in Figure 4.9C can be used to determine the real surface area of microelectrodes with high accuracy. Despite the slightly concave shape of the electrode, one-dimensional diffusion models are still applicable.

4.2 Modification of the electrode material for better electrocatalytic performance

4.2.1 Metal electrodes

The fact that the electrode material influences the electrocatalytic activity was well known since the earliest days of electrochemistry. Changing the material of the electrode is a straightforward way to manipulate the electrocatalytic activity. However, as it was mentioned before, even metals neighboring in the periodic table can exhibit binding energies that differ as much as 1eV for the same intermediate[130]. This fact means that more sophisticated ways of manipulating the binding energies had to be developed for the fine-tuning of the surface properties.

However, pure metal electrodes are used today for a variety of applications. The most significant ones are Pt-electrodes, which are used for the hydrogen oxidation (FCs) and evolution reactions (electrolyzers), as well as for the oxygen reduction reaction in FCs. As it was shown in Figure 2.5, Pt lies close to the tip of the volcano for HER and HOR. It offers reasonably high activity and selectivity, with good stability. Even though it possesses numerous desirable properties, Pt is expensive, and the catalyst contributes greatly to the price of devices in which it is used. Reducing the loadings in real-world devices is, therefore, a significant objective of modern electrocatalysis[228].

4.2.2. Bulk alloys

Alloying provides an opportunity to overcome the discontinuity of properties, which is prominent for pure metals. Metal alloys have a wide range of applications in modern electrocatalysis. Creating bulk alloy electrodes is probably the most straightforward way to implement such materials in electrochemistry.

In this chapter, the focus will be set on new understanding of the origin of the experimental activity trends for alloys of Pt with 3d transition metals and lanthanides with respect to the oxygen reduction reaction[229]. These alloys have been widely investigated as ORR catalysts for fuel cell applications[61,148,230,231,232,233,234,235] at least since the 1970s[236]. They offer high activity, with reasonably high stability under ORR conditions[148,174,237]. An additional advantage of bimetallic catalysts is that they offer additional degrees of freedom in their design– their composition.

In bimetallic alloys the electronic structure of the surface, and consequently the electrocatalytic properties as well, is determined by a number of parameters, which are generally considered to be the result of ligand and strain effects[61,131,132]. These effects appear simultaneously and it is not easy to decouple their influence and consider them independently. These alloys are, however, complex systems, the behavior of which often cannot be straightforwardly explained based on experiments with model surfaces. Catalysts in fuel cells are often implemented in the form of nanoparticles or nanostructured thin films. In this form, their surface structure and composition are not stable under PEMFC operating conditions. The more reactive alloy component dissolves from the surface and near-surface layers. In order to understand the behavior of real-world catalysts the gap in understanding between model surfaces on one side, and polycrystalline and nanoparticulate materials on the other, must be surmounted.

4.2.2.1 ORR at model surfaces of Pt-alloys with 3d-transition metals and lanthanides

The simplest model surfaces to consider are the basal low-index single crystals. When assessing the properties of these electrodes both the ligand and the strain effects need to be taken into account.

Using the binding energy differences determined according to the procedure in Section 3.1.4 and the activities reported for the given electrocatalysts the volcano plot shown in Figure

4.10 was constructed. The Figure shows the activities of Pt-alloys *fcc*(111) single crystals towards the ORR in O_2-free 0.1M $HClO_4$ plotted versus the binding energy of *OH. The binding energies were estimated using data from references: 238, 239, 240, 241, 242, 243, and 244.

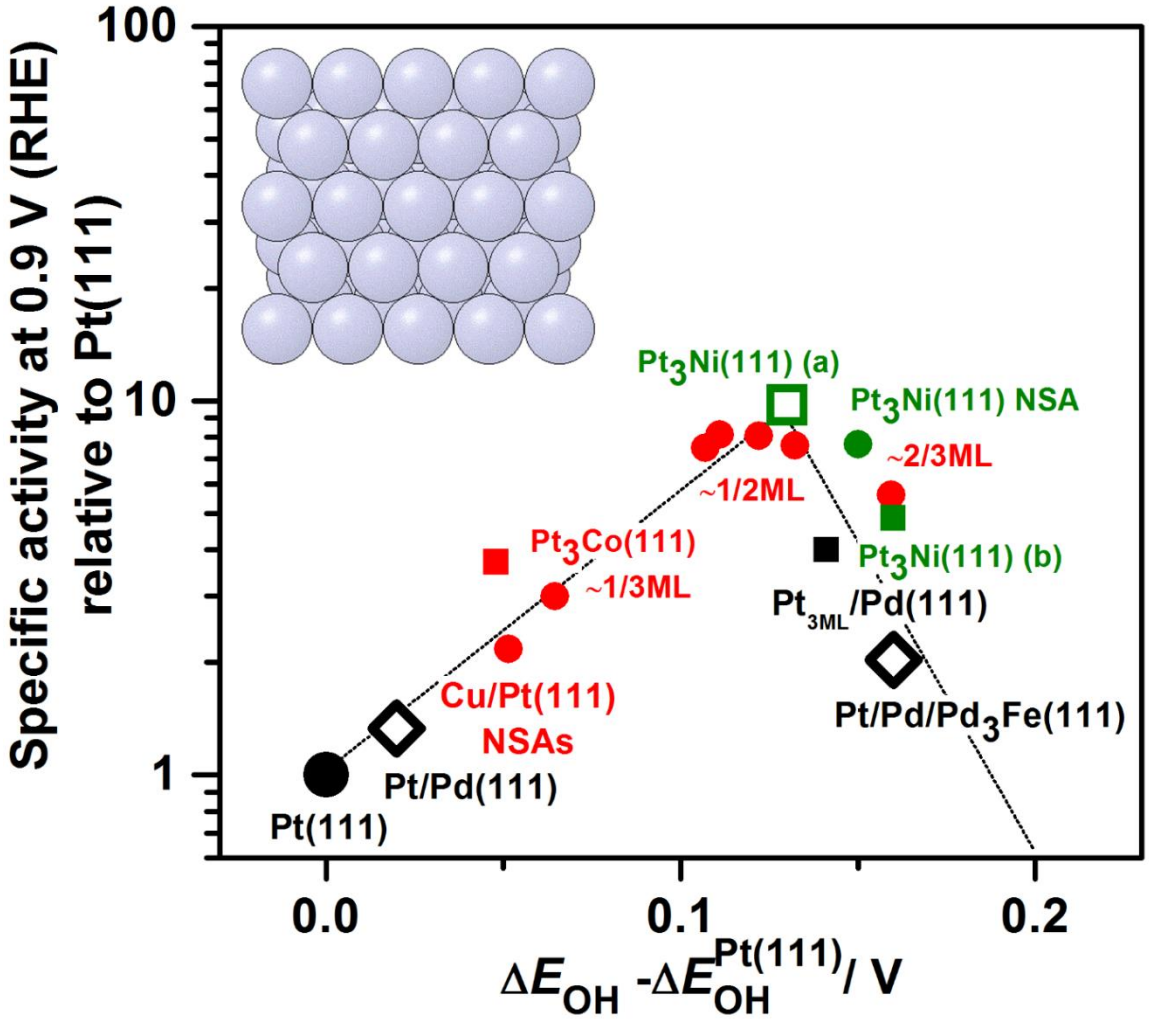

Figure 4.10: The relative activity of various *fcc* (111) single crystal Pt-alloy electrodes in comparison to Pt(pc) towards the ORR in 0.1M $HClO_4$ at the potential of 0.9V, plotted versus the *OH-binding energies. ● – Cu/Pt(111) NSAs, ● – Pt_3Ni(111) NSAs, ■ – bulk Pt_3Co(111), ■ – bulk Pt_3Ni(111), □ - Pt_3Ni(111) from reference 242, ■ – 3 monolayer of Pt on Pd, ◇ – monolayer of Pt on Pd(111), and Pt monolayer on an annealed Pd_3Fe(111) electrode with a segregated Pd-layer, ● – Pt(111). The inset shows a schematic representation of an *fcc*(111) surface. All the binding energies were estimated using original data from references: 238, 239, 240, 241, 242, 243, and 244.

The homogeneity of the adsorption sites on an *fcc*(111) surface allows the estimation of the binding energies of the reaction intermediates from experimental data with good accuracy. In this regard, the understanding of these systems is quite good: the plot shows a typical "volcano" relation, and it is possible to assess the activities of these surfaces both by the means of experimental data and *ab initio* calculations.

$Pt_3Ni(111)$ shows the highest activity from this group of catalysts, with a reported activity improvement of *ca* 10 times in comparison to Pt(111). The binding energy of *OH with respect to $Pt_3Ni(111)$ is about 0.13eV weaker than on Pt(111), showing good agreement with the theoretical expectations. The near-surface alloys exhibit a strong dependence of the activity on the fraction of the alloying metal in the subsurface layer. Figure 4.10 shows that alloying Pt with less noble metal decreases the *OH binding energy and is, therefore, an applicable approach for the improvement of the electrocatalytic activity of Pt-catalysts towards the ORR. In order to explain the behavior of real-world catalysts, however, one must consider surfaces that are more complex.

The surface of stepped single crystals is well defined but it contains quasi-periodic defects – steps and terraces of different lengths. Undercoordinated sites are expected to bind the reaction intermediates stronger than Pt(111), which already binds too strongly, so it is expected that the stepped single crystal surfaces would show a decrease in activity, as they should "move away" from the tip of the volcano in Figure 4.10. However, if a similar volcano plot is constructed for stepped single crystals, it shows that the trends are not as clear-cut as expected based on these straightforward assumptions. Figure 4.11 (constructed from data from references: 240, 241, 242, 245, and 246) shows the ORR activity data for Pt, Pt_3Co and Pt_3Ni [(111)×(111)] and [(111)×(100)] surfaces.

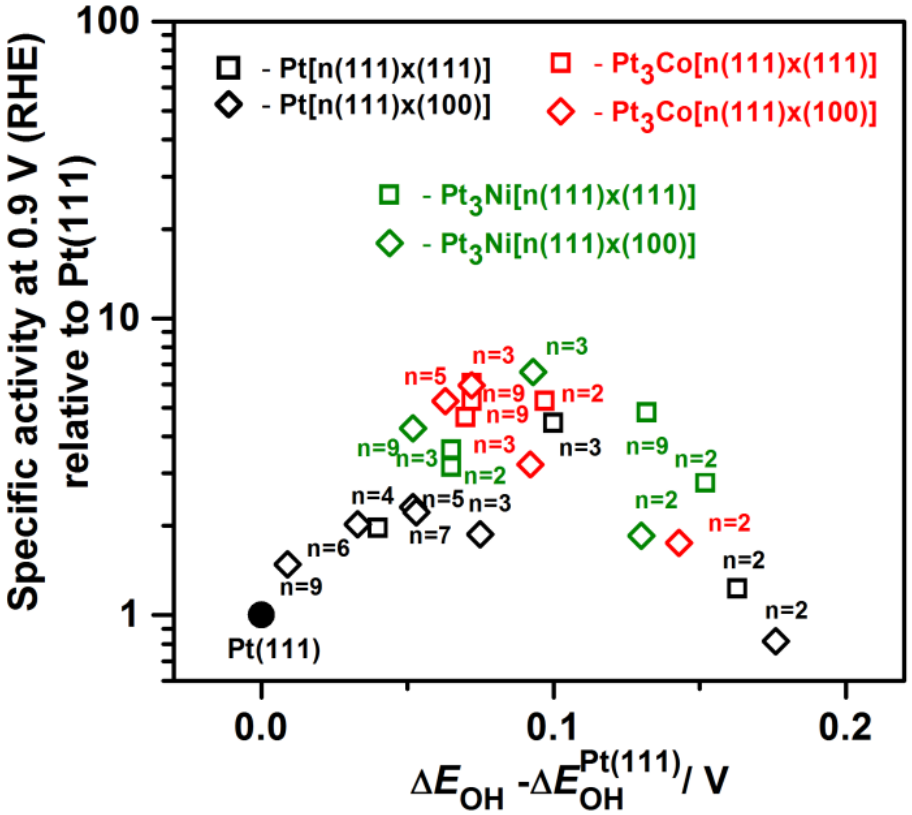

Figure 4.11: Relative activities of various Pt-alloy n(111)x(111) and n(111)x(100) stepped single crystal electrodes towards the ORR in 0.1M $HClO_4$ at the potential of 0.9V *vs* RHE, plotted as a function of the experimentally determined *OH-binding energies. Black squares – Pt-stepped crystals, red squares – Pt_3Co-stepped crystals, green squares - Pt_3Ni stepped crystals. *n* denotes the atomic width on the terraces. The binding energies were estimated using original data from references: 240, 241, 242, 245, and 246.

As there are more different adsorption sites on this type of surfaces in comparison to basal low-index single crystals, and because the position of the active sites is still under debate, the accurate theoretical calculation of binding energies here is not possible. To date, no theoretical calculations of binding energies have been reported that explain the experimentally observed activity trends, only experimentally determined binding energies are available. It should also be noted that as a first approximation, dealloying in these surfaces can be neglected, as (111) terraces have been shown to have considerable stability[74,244].

It should be pointed out that stepped single crystals show higher activities than basal low-index ones in general[245,247], e.g., it has been a well-known fact for more than two decades that the activities of Pt-single crystals towards the ORR in acidic media increase in the order Pt(100)<Pt(111)<Pt(110)[247,248]. Considering this, it may seem rather counter-intuitive that in Figure 4.11 no simple proportional dependence between the step density and the ORR activity can be observed. As the step density is decreasing, the ORR activity initially increases, then it reaches a maximum, and with further increase of the step density, the ORR-activity decreases.

The highest ORR-activity is reported for Pt_3Ni[(111)×(100)] electrodes. Interestingly, among Pt[(111)×(100)] surfaces, which are generally less active than Pt[(111)×(111)], the highest activity is exhibited by the surface with terrace length n=5, while for the even less active Pt surfaces with (100) terraces the effects of step density on ORR activity is comparatively small[249].

In order to explain the observed trends, it is necessary to consider the location of the active sites on these surfaces. However, this is still under strong debate. It has been suggested that the active sites lie on the (111) terraces[166]. Since the steps bind *OH and *O much more readily than terrace sites[250,251], under ORR conditions the step sites are blocked by strongly bound oxygen. It has been proposed that the presence of oxygen on the steps interrupts the existing network of *OH and *OOH and destabilizes the interactions with the *OH-adlayer, thus influencing the binding of the *OH on terrace sites adjacent to the steps[184]. However, the exact origin of the activity change is difficult to pinpoint in the case of these alloys, since the strain and ligand effects are both present and they simultaneously contribute to the changes in the surface electronic structure, consequently, their impacts are difficult to decouple.

Figure 4.11 shows that the maximum of the relative ORR activity lies close to 0.1eV lower than that of Pt(111), in agreement with the theory. The improvements in the activity in comparison to the benchmark Pt-alloys are only about 6.5 times in comparison to Pt(111). Still, the volcano like dependence is observed, and with the use of experimentally obtained binding energies, a good description of these systems is possible.

4.2.2.2 ORR at polycrystalline and nanostructured Pt-alloy electrocatalysts

The explanation and the prediction of the behavior of these even more complex, but practically more significant, surfaces is more difficult. Figure 4.12 shows the dependence of the experimentally measured ORR activities of polycrystalline Pt-alloys as a function of the calculated binding energies.

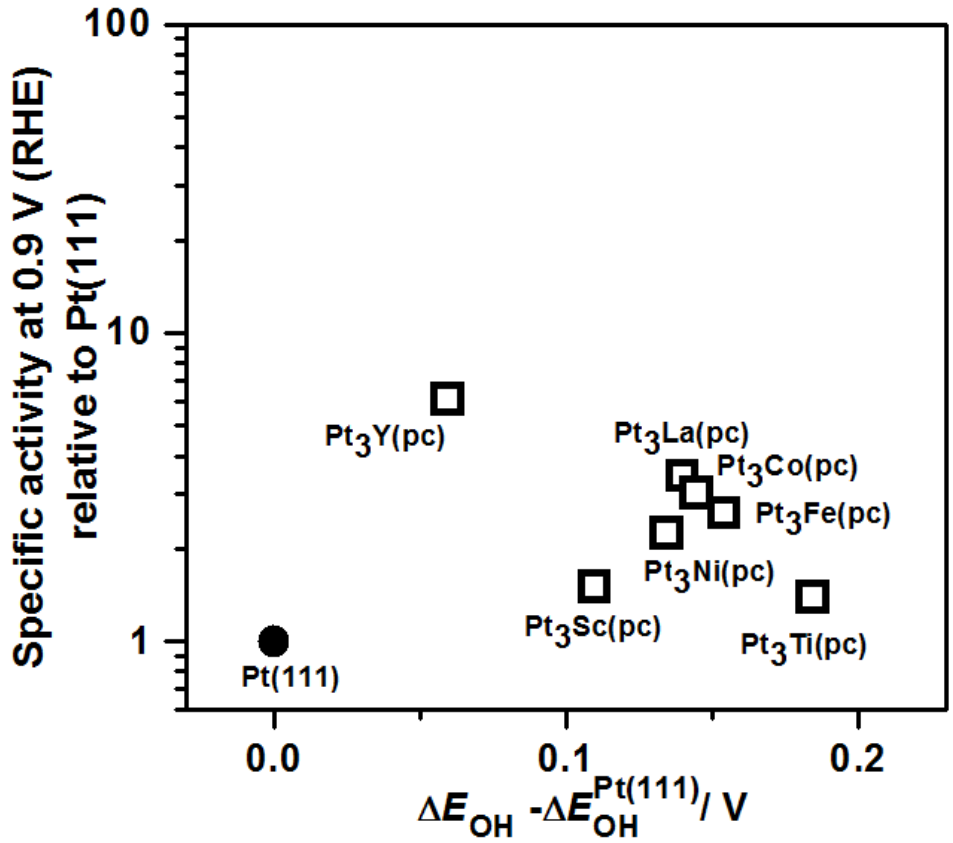

Figure 4.12: Relative activities of polycrystalline Pt-alloys in comparison to Pt(pc) towards the ORR in 0.1M $HClO_4$ at 0.9V plotted as a function of the difference in *OH binding energy in comparison to Pt(111). The binding energies were calculated assuming *fcc*(111) facets for all alloys. The original data are from references: 61, 148, 166, and 252.

The agreement with the theoretical predictions in this case is somewhat dubious. It is interesting to note that the Pt_3Ni(pc) electrode exhibits 5-fold lower activity than its *fcc*(111) counterpart, while the activities of polycrystalline and *fcc*(111) Pt_3Co electrodes are similar. Pt_3Sc should have a binding energy close to optimum and should be one of the best ORR catalysts according to theoretical predictions, yet its activity is merely *ca* 1.5 times higher than Pt[148].

These discrepancies most probably result from the complexity of polycrystalline surfaces, which contain random (111) and (100) facets, steps, kinks, grain boundaries, etc. The evaluation of binding energies on such a complex surface is very problematic. The binding energies in Figure 4.12 were calculated assuming only *fcc*(111) facets, which are assumed to dominate the surface. Aaronson et al.[253] have shown, however, that the assumption of a uniform surface is not a reasonable approximation for the calculation of binding energies on polycrystalline Pt. Considering this it is evident why the volcano-type dependence is not observed. The assumption that *fcc*(111) facets govern the activity of the polycrystalline alloys is probably not a reasonable approximation for the theoretical assessment of the intermediate binding energies. The ambiguous determination of the binding energy values means that the exact positions of particular alloys in the volcano plot in Figure 4.12 are uncertain.

The complexity of the surface also renders the experimental assessment of the binding energies challenging, as different processes are difficult to distinguish in the voltammograms and their interpretation is problematic. The description of the ORR activity is complicated for nanoparticulate Pt-alloy catalysts. Notably, they display behaviors that are difficult to explain for the point of purely energetic descriptors. For instance, it is expected that the activities of Pt-alloy nanoparticles would decrease with decreasing nanoparticle size. The reason for this is that with the decreasing NP size the number of undercoordinated surface atoms, which bind *OH more strongly, is increasing, so one would expect an activity decrease. This behavior has been indeed observed for a number of systems[254]. However, while this is the case for Pt and, for instance, Pt-Y alloys, Pt-Ni alloy nanoparticles display a different behavior. The activity of these alloys goes through a maximum with decreasing particle size, as shown in Figure 4.13.

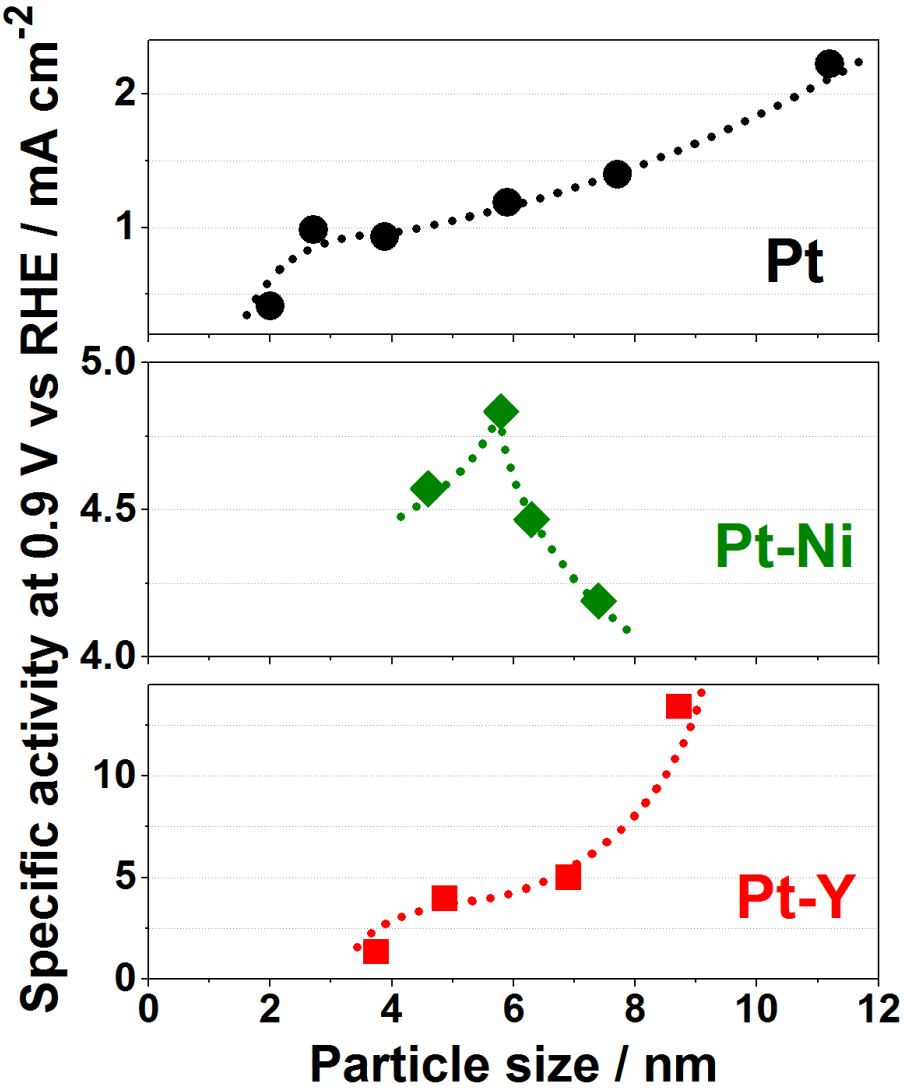

Figure 4.13: The specific activities of nanoparticulate Pt, Pt-Ni, and Pt-Y-alloy catalysts towards the ORR in 0.1M $HClO_4$ at 0.9V, plotted versus the nanoparticle size. Original data are from references: 254,255, and 256.

In order to explain and predict the electrocatalytic properties of polycrystalline and nanoparticulate catalysts, a descriptor which is more suitable for these materials should be

introduced. This descriptor should be logically linked to the surface binding energies, but more easily assessable and preferably structural in nature.

To achieve this, the status of the catalytic surface under operational conditions should be carefully examined. Pt_nX-type alloys (where X stands for 3d elements and lanthanides) in their polycrystalline form owe their stability to the fact that the less noble metal often dissolves from the surface layers under ORR conditions[257] (in contrast to single crystals) forming a Pt-rich protective layer. This process is called "dealloying"[258,259]. Dealloying is much more prominent on polycrystalline surfaces, as the process primarily takes place at defect sites[258,260]. Therefore, polycrystalline surfaces will show much lower stability towards it, in contrast to, e.g., *fcc*(111) surfaces[179]. The resulting structure consists, therefore, of a Pt-rich shell, which covers an alloy core[61,256,261,262,263], as schematically illustrated in Figure 4.14. Most Pt alloys will exhibit this type of behavior. The exceptions include only certain noble metals, such as Au and Pd[264].

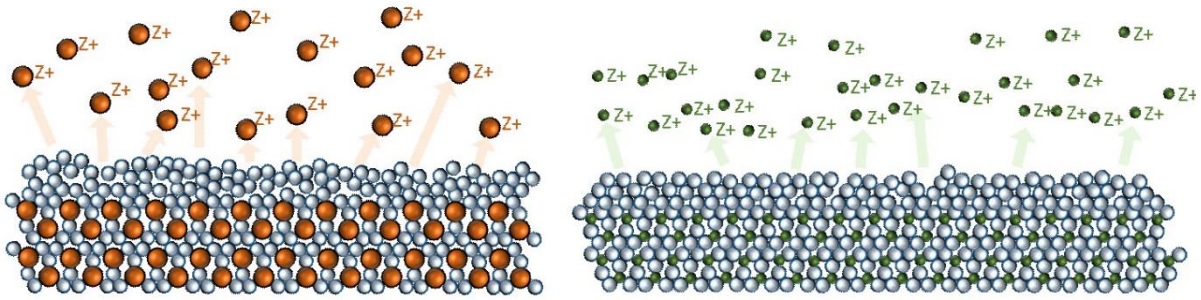

Figure 4.14: Schematic representation of the structure resulting from the dissolution of the less noble element from the surface of polycrystalline Pt_nX-type alloys with 3d- and lanthanide elements. The dissolution of atoms with radii larger (orange) or smaller (green spheres) than Pt from the alloy surface is shown.

As the lattice parameters of the alloy core and the Pt-shell are different, a significant amount of compressive strain is introduced to the shell, which results in the weaker binding of the ORR intermediates[61]. Since the Pt-rich shell is several atomic layers thick[61,265,266], the influence of the ligand effect can be neglected[61,256,267,268], since the it is negligible after 3 atomic layers. On the other hand, the strain effect gradually decreases only after ≥5 atomic layers[269] so it is likely the main factor influencing the electronic structure of the surface.

Since the surface electronic structure of these materials is determined mainly by the strain effect, it is possible to tune the binding energies and, consequently, the electrocatalytic activity by manipulating the lattice strain. The lattice strain in the shell in the simplest case would be determined by the radius and the content of the alloying metal, thus forming a 3D *activity=f(atomic radius, metal content)* surface. Such a surface is schematically represented in Figure 4.15. The construction of an exact *activity=f(atomic radius, metal content)* surface would be exceptionally difficult, not just because of the vast amount of data that would be necessary, but also due to the fact that the variables, the atomic radius and the alloy composition in particular, cannot be varied continuously.

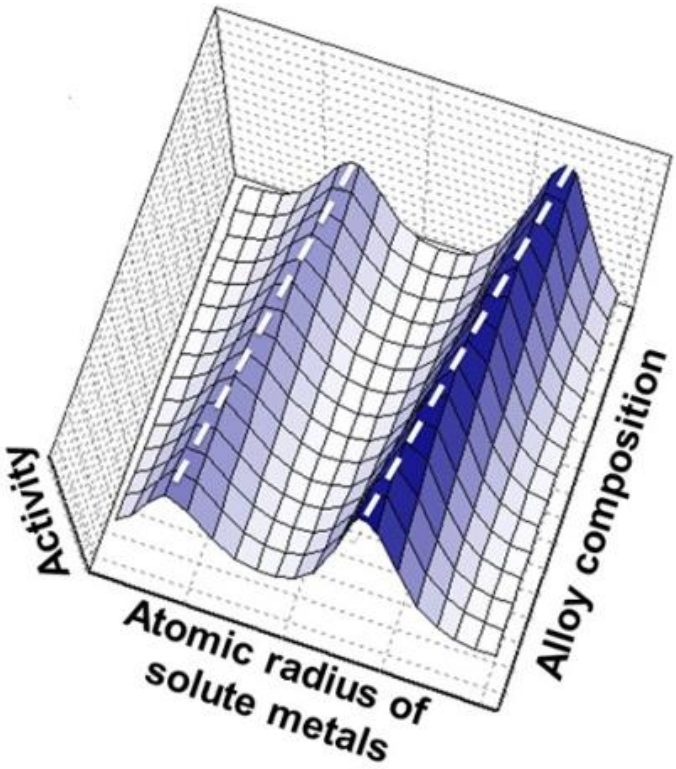

Figure 4.15: Schematic representation of the 3D surface illustrating the dependence of the activity of Pt_nX-type alloys on the composition of the alloy and the empirical radius of the "solute" metal. The white dashed lines connect the points of the highest activity.

However, the projection of the 2D surface that would intersect the points of highest activity to the activity-atomic radius plain could be constructed if the highest reported activities for the Pt-alloys with different metals were plotted against the radius of the alloying metal. To construct such a graph, systematic errors due to the comparison of data collected from different groups that were acquired under different conditions need to be eliminated. This requires the careful consideration and elimination of effects that are irrelevant for the intended analysis, such as, e.g., nanoparticle size, electrolyte effects, etc.

For these reasons, the activities of catalysts were evaluated by comparing their activity to the activity to the corresponding Pt-catalysts, which were taken as benchmarks. This means that the activities of polycrystalline Pt-alloys were expressed in comparison to Pt(pc), nanoparticles were compared to Pt-nanoparticles of the same size, etc. Only nanoparticles of "conventional" shapes were considered – hollow, open-structure, or convex NPs were not taken into consideration. All activities that were taken into account refer to the activity in 0.1M $HClO_4$ (pH=1). The highest reported activities of Pt-alloy catalysts in comparison to the activity of the corresponding Pt benchmark catalysts were, therefore, plotted versus the radius of the "solute" metal and the resulting plot is shown in Figure 4.16.

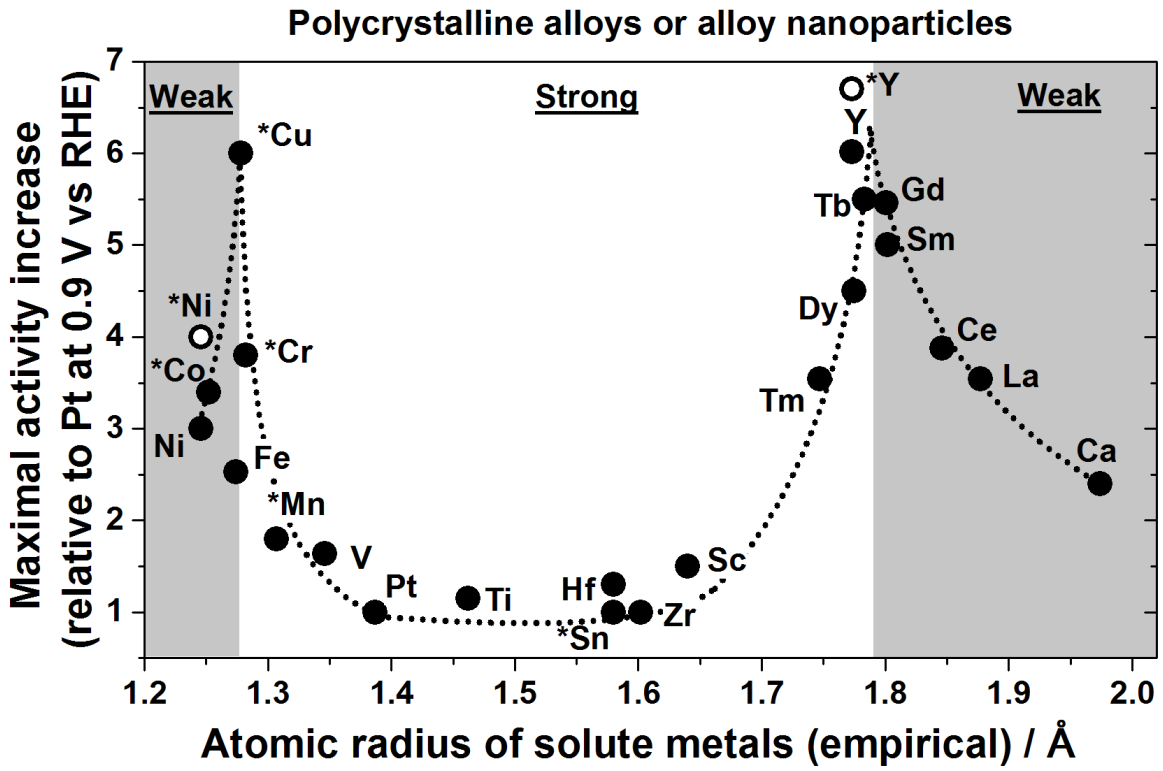

Figure 4.16: The highest reported relative activities of Pt-alloy catalysts towards the ORR, in comparison to the corresponding Pt-benchmark catalysts (at 0.9V vs. RHE 0.1M $HClO_4$), plotted *versus* the empirical atomic radius of the solute metal. The white area on the graph denotes the region where the binding of the intermediates is stronger, while the gray area marks the region where the binding is expected to be weaker than ideal. The asterisks denote nanoparticles. Original activity data are from references: 148, 166, 252, 257, 270, 271, 272, 273, 274, 275, 276, and 277. The specific activity of Pt_5Ca was taken from 257 and normalized according to the real electroactive surface area estimated from the hydrogen underpotential deposition peaks available in reference 257 supporting information. The empirical atomic radii are taken from ref. 278.

While this representation relies on empirical data, the trend observable in Figure 4.16 can be explained in terms of the strain introduced to the lattice of the Pt-shell. When Pt is alloyed with metal atoms of different radii, there is a difference in the lattice parameters between the core and the shell formed by dealloying. This means that strain will be introduced to the lattice of the Pt-rich shell, and the bigger the difference in radii - the more strain is likely to be introduced.

When Pt is alloyed with metal atoms of smaller radii (i.e., moving to the left from Pt in Figure 4.16), the smaller the atom of the solute element, the greater the compressive strain in the Pt-rich shell. This entails weaker binding of the intermediates. Since Pt binds the intermediates too strongly, with the weakening of the bonds the values of the binding energies reach the “ideal value”, and the activity reaches a maximum. With the further decrease of the atomic radii of the solute element, “too much strain” is introduced, and the alloy binds weaker

than ideal. Consequently, the activity starts to decrease. The same is true if Pt is alloyed with metals with larger empirical radii. While at first glance it might seem intuitive that alloying with metals of greater radii would introduce tensile strain, it has been shown[257] that alloying Pt with lanthanides in fact results in compressive strain in the Pt-shell and the weakening of the *OH-binding. It should be noted here that in Pt-alloy catalysts with solute metals with larger atomic radii, the resulting Pt-shells are probably not epitaxial to the alloy cores. This infers that the shell does not merely "stretch" to fit the outline of the core, but rather forms a distinct structure in which atoms are, on average, positioned closer to each other than in the unstrained *fcc*-crystal. The exact mechanism of surface relaxation, which occurs in order to minimize the surface energy after dealloying, and results in the introduction of compressive strain to the shell, is currently not known. Further research regarding the mechanism of surface relaxation after the dealloying process is needed in order to elucidate the processes that lead to the formation of the compressively strained Pt-rich shell.

It is also interesting to note that the positions of polycrystalline surfaces and nanoparticles of the same alloys are slightly different in Figure 4.16. This is possibly due to the partial delocalization[279] of the d-electrons in Pt-alloy nanoparticles, e.g., Pt-Y and Pt-Ni.

Figure 4.16 besides providing an overview of the introduced strain effects from different alloying elements, can also offer a phenomenological explanation for the "anomalous" dependency of the ORR activity of nanoparticles observed in Figure 4.13. As Pt binds the ORR intermediates too strongly, the decrease in size will lead to stronger binding and decrease in activity in Pt nanoparticles, which is indeed observed. Pt-Y lies quite close to the maximum of the "double-volcano" plot on the side of metals with radii larger than Pt; so an increase in the binding energies will lead to a decrease in activity, as is observed. In Pt-Ni NPs, however, the introduced strain is too high and the alloy binds the ORR intermediates too weakly. With the decrease of NP size, the *OH-binding energy increases, it reaches and optimal value, and with further size decrease the activity starts decreasing.

The trend shown in Figure 4.16 can also explain why polycrystalline Pt_3Sc is only marginally more active than Pt(pc): Sc-atoms in this catalyst are likely dissolved very quickly from the surface and near-surface layers in aqueous environment. However, the strain introduced in this process is insufficient to weaken the binding energy enough to induce a more notable increase in activity. The plot in Figure 4.16 can similarly explain why polycrystalline and nanoparticulate Pt-Ni alloys never reach the activity of $Pt_3Ni(111)$[‡].

Overall, Figure 4.16 allows a qualitative evaluation of the catalytic activity of complex surfaces (polycrystalline and nanoparticles) where currently used activity descriptors, such as the binding energies of intermediates and the d-band center are not easily applicable.

4.2.3. Surface alloys and near-surface alloys

Another approach to modify the electrocatalytic properties of material implements the formation of an alloy with another metal only at the surface or immediate subsurface regions

[‡] Here NPs of "conventional" shape are being considered, as it was already pointed out.

of the electrode[244,280]. This approach has certain advantages over bulk alloying, such as the possibility of modifying the electrode material *in situ* in the electrochemical cell, smaller amounts of alloying material, and the possibility of manipulating the position of the alloy layer with respect to the electrode surface.

It has been shown that the positioning of monolayer amounts of foreign metals at the surface and subsurface areas[60,273], of electrodes is a feasible way to optimize the properties of electrocatalytic surfaces. Near-surface alloys (NSAs) of Pt with various metal, where sub-monolayer amount of other metals are located in the second atomic layer from the surface of the electrode are also convenient model electrochemical systems[74,244,281]. In such structures, the atoms of the "solute" metal are protected from dissolution by the surface monolayer of Pt, while they directly influence the electronic structure of the surface Pt atoms through the ligand effect.

4.2.3.1 ORR at Cu-modified electrodes in presence of Nafion

The membrane electrode assembly (MEA) is a key element of PEMFCs, and it consists of an ion-conducting solid polymer electrolyte (Nafion) which is in contact with the electrocatalytic surface[282]. Subbaraman et al.[283] showed that Nafion electrolyte components, such as sulfonate groups adsorb specifically on Pt(111). These sulfonate groups compete with the *OH-species at 0.8V in 0.1M $HClO_4$ for the available adsorption sites on Pt(111) and Pt_3Ni(111) surfaces, and their electrocatalytic performance is significantly diminished (ca 25%[284]). This urges the investigation of the activity of ORR catalysts under conditions as close to those in real-world devices as possible, i.e., in the presence of Nafion. The effects of Nafion need to be evaluated for any catalyst that is to be implemented in FCs and the development of methods to minimize the negative impacts of the adsorption of sulfonate groups would be advantageous.

It has been shown that by modifying the position of Cu-atoms in alloyed Pt(111) electrodes the adsorption energies of (bi)sulfate anions change drastically[94]. Taking this into account, the evaluation of the impact of near surface alloying with Cu on the adsorption of sulfonate groups is of particular interest. Therefore, adsorption of anionic species on the Pt(111) and Pt(111)/Cu NSA and their influence on the ORR activity of these electrodes was investigated in the presence of Nafion[285].

Figure 4.17 shows CVs of Pt(111) and Nafion-modified Pt(111) (prepared according to the procedure described in Section 3.1.3.6) in Ar- and O_2-saturated 0.1M $HClO_4$ and 0.05M H_2SO_4.

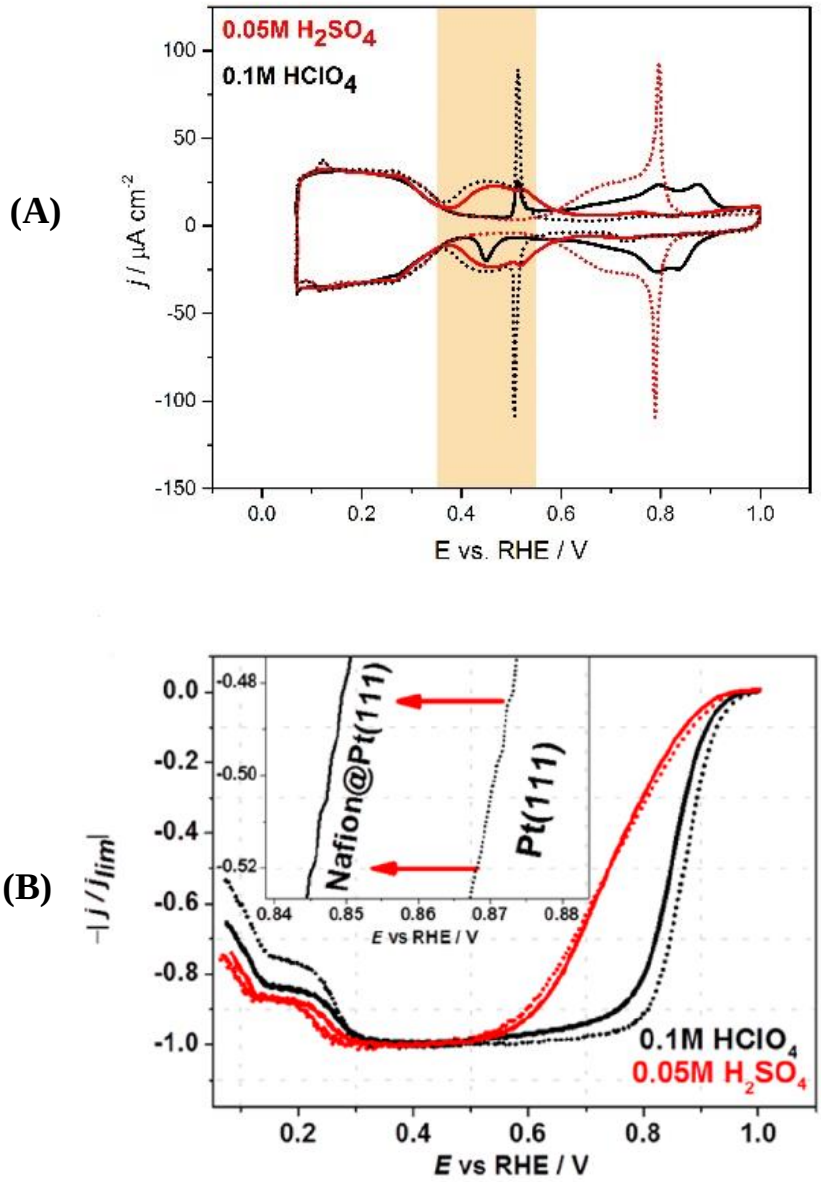

Figure 4.17: CV of Pt(111) - dashed lines, and Nafion-modified Pt(111) - full lines, in an RDE configuration (1600 r.p.m.) in (A) Ar-saturated (B) O_2-saturated 0.1M $HClO_4$ and 0.05M H_2SO_4 electrolytes. Pt(111) in $HClO_4$ (▪▪▪▪▪) and H_2SO_4 (▪▪▪▪▪), Nafion-modified Pt(111) in $HClO_4$ (—) and H_2SO_4 (—). Scan rate: 50mV/s. The data were obtained in collaboration with Dr. Jakub Tymoczko, Ruhr-Universität Bochum.

On the Nafion-free Pt (111) surface, certain distinctions between the voltammograms taken in perchloric and sulfuric acid solutions can be observed. While the hydrogen adsorption/desorption region is generally similar in both electrolytes, there are considerable differences in other parts of the voltammograms. The adsorption of sulfates occurs in the potential region of 0.35-0.55V and it manifests itself as a reversible feature in the voltammograms, i.e., a pair of sharp peaks at *ca* 0.52V indicating an order/disorder transition in the (bi)sulfate adlayer[286]. A $(\sqrt{3}\times\sqrt{7})R19.1^{o}$ superstructure with co-adsorbed H_2O molecules exists between 0.52V and 0.8V, with a surface coverage of *ca* 0.2 monolayers. Several smaller

peaks can be observed in the CV in the region 0.7-0.8V, which are associated with additional rearrangements in the adsorbate layer[286].

CVs of the Nafion-modified Pt(111) electrodes reveal significantly different behavior in the same electrolytes. The voltammogram recorded in 0.1M $HClO_4$ shows features that indicate the adsorption of sulfonate groups from Nafion on the Pt(111) electrode surface. The hydrogen adsorption/desorption region shows almost no changes in comparison to the Nafion-free electrode. However, in the region of 0.4-0.6V peaks ascribed to sulfonate adsorption are observed[286]. These peaks show considerable irreversibility, and their interaction of the adsorbates with the electrochemical interface is described by the so-called "spring model"[284]. The adsorption of sulfonates strongly affects the adsorption of *OH (observed in the potential region 0.6-1V) and, consequently, the ORR activity, Figure 4.17B.

In 0.05M H_2SO_4 the features characterizing the adsorption of sulfonates from the Nafion are masked by the adsorption of sulfates from the electrolyte, so the CVs are similar to those taken with Nafion-free Pt(111). However, even here differences were observed. The sharp peaks linked to the order/disorder transitions in the sulfate adlayer are absent, suggesting that the adsorbing sulfonate may be interfering with the 2D ordering in the sulfate adsorbate layer.

Figure 4.17B shows the ORR curves for Pt(111) and Nafion-modified Pt(111) in O_2-saturated 0.1M $HClO_4$ and 0.05M H_2SO_4. The negative effect of sulfate ions on the ORR activity, associated with the reduction of available active sites for the ORR due to the competitive adsorption of sulfates is well-known, and will be discussed in more detail in Section 4.4.2. The ORR curves for the unmodified and Nafion-modified Pt(111) in the sulfuric electrolyte are quite similar, again, probably due to the masking of the sulfonate effect by the sulfates adsorbing from the solution[284,287]. In contrast to this, in the 0.1 $HClO_4$ electrolyte, a *ca* 23 mV negative shift in the halfwave potential for the Nafion-modified Pt(111), in comparison to "bare" Pt(111), is observed. The surface- or near-surface alloying of platinum electrodes with copper significantly changes their electrocatalytic properties. Figure 4.18 compares the voltammograms of Pt(111) and Pt(111)/Cu NSA electrodes in Ar- and O_2-saturated 0.1M $HClO_4$ and 0.05M H_2SO_4.

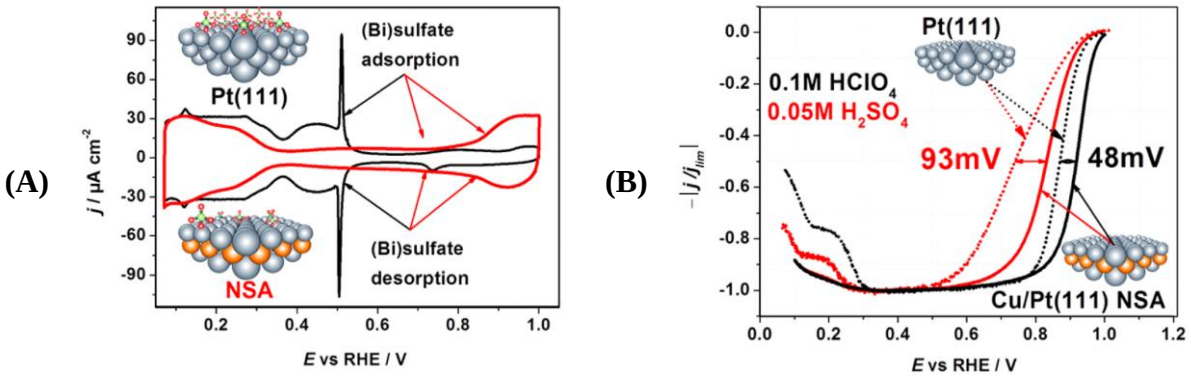

Figure 4.18: (A) CVs of Pt(111) (—) and Pt(111)/Cu NSA (—) electrodes in Ar-saturated 0.05M H_2SO_4 electrolyte. (B) Polarization curves of Pt(111) and Pt(111)/Cu NSA electrodes in O_2-saturated 0.1M $HClO_4$ and 0.05M H_2SO_4; RDE, 1600 r.p.m. Pt(111) with Nafion in $HClO_4$ (▪▪▪▪▪▪) and H_2SO_4 (▪▪▪▪▪▪), Nafion-modified Pt(111)/Cu NSA in $HClO_4$ (—) and H_2SO_4 (—). Scan rate: 50 mV/s. The data were obtained in collaboration with Dr. Jakub Tymoczko, Ruhr-Universität Bochum.

Figure 4.18A shows that the presence of Cu-atoms in the subsurface layers significantly affects the $H_{ads./des.}$ region. The hydrogen adsorption starts at significantly lower potentials on the Pt(111)/Cu NSA surface, in agreement with previously reported findings[244]. The "butterfly" peaks at *ca* 0.5V, which correspond to the sulfate adsorption/desorption process, are not present in the voltammograms of Pt(111)/Cu NSA surfaces, indicating that the adsorption process is shifted to more positive potentials (as shown in Figure 4.18A).

Figure 4.18B reveals the impact of the changes in the (bi)sulfate adsorption properties on the electrocatalytic activity towards the ORR. The Pt(111)/Cu NSA shows higher activity towards the ORR than Pt(111) in both electrolytes. In 0.1M $HClO_4$ a positive potential shift of *ca* 48mV in the pseudo-halfwave potential is observed, while in 0.05M H_2SO_4 the shift is *ca* 93mV, being one of the best activities reported towards the ORR in sulfuric media (see, e.g., references 245 and 288). DFT calculations showed that although the gradual addition of Cu decreases the adsorption enthalpies for both *OH and *SO_4, the effect is stronger for the adsorbed sulfates. The results are presented in Figure 4.19.

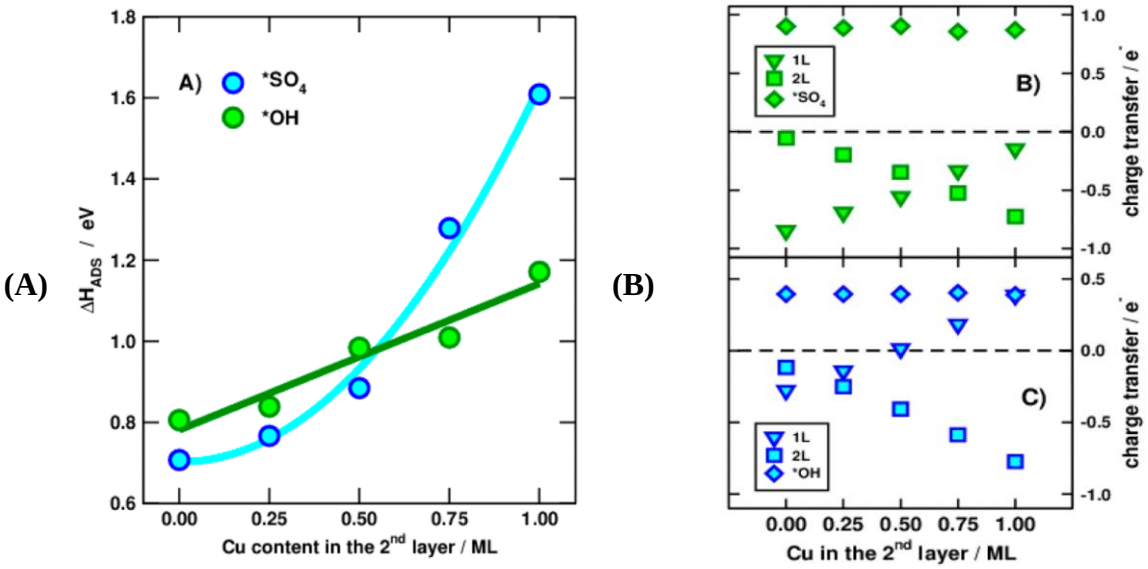

Figure 4.19: Adsorption energies of $*SO_4$ (blue circles) and *OH (green circles) on Pt(111) and Pt(111)/Cu NSA surfaces plotted against the content of Cu in the subsurface layer. (B) and (C) Transfer of charge between the first and second layers of the catalyst and the adsorbate for (B) $*SO_4$ and (C) *OH. Negative and positive values indicate charge donation and withdrawal, respectively. Calculations were made by Dr. F. Calle-Vallejo, University of Leiden, the Netherlands.

Figure 4.19 shows that the adsorption enthalpies decrease with the increasing of Cu-content in the subsurface layer in both cases. The effect is, however, qualitatively and quantitatively different for these two adsorbates. The trend is approximately linear for *OH, while $*SO_4$ adsorption enthalpies show a much more pronounced decrease with an approximately parabolic trend. The change in the enthalpy values from 0 to 1ML of Cu for *OH is merely *ca* 0.37eV, while for $*SO_4$ it is *ca* 0.9eV. It is also important to note that while the Cu content is under *ca* 0.5ML the adsorption enthalpies of the two adsorbates under consideration are similar, with slightly stronger binding for sulfates, indicating that the adsorption processes are competitive. However, if the Cu content in the subsurface layer exceeds 0.5ML, the sulfate adsorption is significantly more strongly suppressed for $*SO_4$ in comparison to *OH. This indicates that the high subsurface Cu-content causes the weakening of $*SO_4$ binding on the NSA surface.

Figures 4.19B and C characterize the electron density shift between the adsorbates and the surface and subsurface layers of the Pt(111) and Pt(111)/Cu NSA electrodes. The Figure shows that the electron density shift associated with the adsorption of *OH and $*SO_4$ is constant on all surfaces, but different for the two considered adsorbates. For *OH the transferred charge equals to $0.4e^-$, while for $*SO_4$ it is $0.9e^-$. The relative charge distribution is dependent on the Cu-content in the subsurface layer and the nature of the adsorbate. A simplified explanation for this fact can be that since Cu has more valence electrons than Pt, it "gives away" these more easily. This means that the higher the amount of Cu in the subsurface layer is, the more electron-rich in comparison to that of Pt(111) it becomes, which causes the weaker binding of the adsorbates. The adsorption of SO_4^{2-} generally involves the transfer of a higher amount of charge than the adsorption of OH^-. Therefore, increasing the amount of Cu in the second layer decreases the affinity of the surface for sulfates more than for the hydroxide.

Figure 4.20A compares the CVs of Pt(111) and Pt(111)/Cu NSA surfaces coated with Nafion, in 0.1M $HClO_4$. The hydrogen adsorption/desorption region remains almost unaffected in this case as well. The voltammetric features associated with sulfonate adsorption (0.4-0.6V) are suppressed on Pt(111)/Cu NSA, which suggests that the influence of the sulfonate ions is much less pronounced for this surface. This is also supported by DFT calculations which showed that the adsorption energy of $CF_3CF_2SO_3$* (used to approximate Nafion sulfonate groups) on Pt(111)/1ML Cu is *ca* 0.3eV weaker than on pure Pt(111).

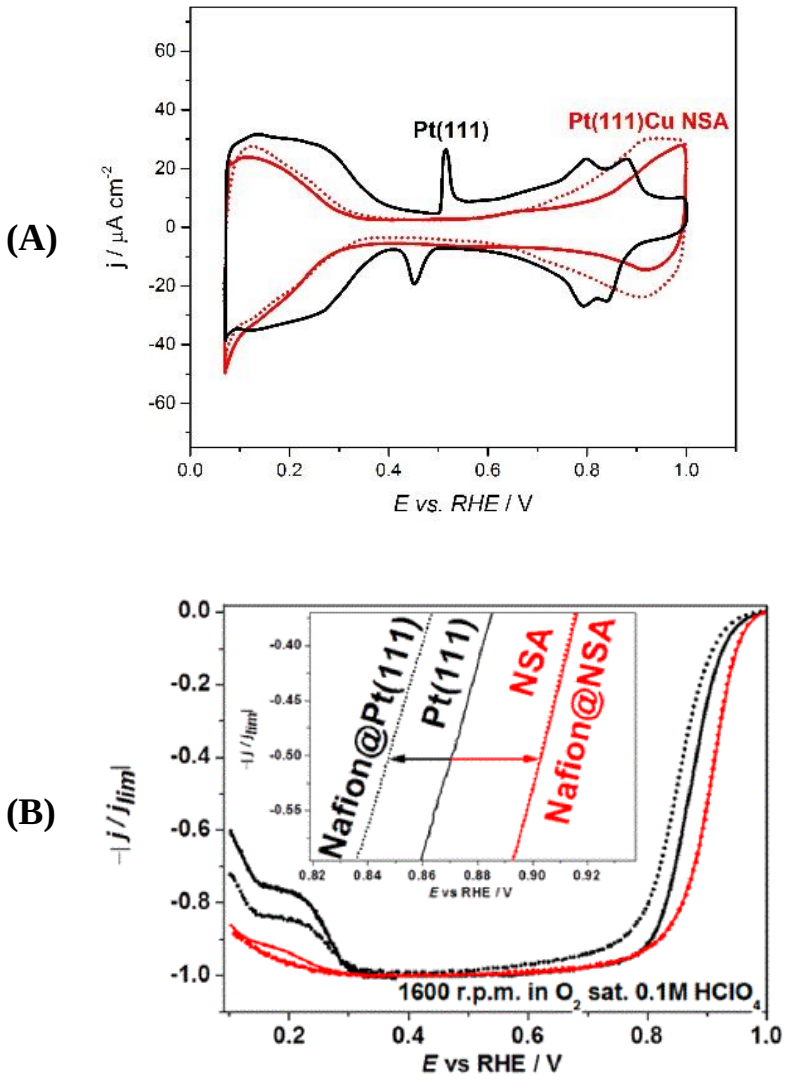

Figure 4.20: (A) CVs of Nafion-coated Pt(111) (—), Pt(111)/Cu NSA (•••••) and Nafion-coated Pt(111)/Cu NSA (—) in Ar-saturated 0.1M $HClO_4$. (B) Pt(111) (—), Pt(111)/Cu NSA (—), Nafion-coated Pt(111) (•••••), and Nafion-coated Pt(111)/Cu NSA (•••••) in O_2-saturated 0.1M $HClO_4$. RDE, 1600 r.p.m. Scan rate: 50 mV/s. The data were obtained in collaboration with Dr. Jakub Tymoczko, Ruhr-Universität Bochum, Germany.

Figure 4.20B shows the ORR on Nafion-covered Pt(111) and Pt(111)/Cu NSA electrodes in O_2-saturated 0.1M $HClO_4$. As already discussed, the adsorption of sulfonates from the Nafion polymer on Pt(111) surfaces decreases the ORR activity by blocking some of the active sites,

causing a negative potential shift of *ca* 23 mV in the pseudo-halfwave potential. The activity of the Pt(111)/Cu NSA electrodes in 0.1M $HClO_4$ is higher than Pt(111), due to the desirable weakening of the *OH adsorption energies caused by the near-surface alloying. Additionally, the voltammograms for the bare and Nafion-coated NSA electrodes are almost identical, indicating that the presence of Nafion has no considerable adverse effects on the ORR activity of these electrodes. This shows that the destabilization of the adsorbates by the presence of the Pt-Cu NSA has a beneficial effect due to the weakening of the binding of adsorbates. This shows that near-surface alloying is a viable tool for the improvement of PEMFC catalysts. The decrease of the poisoning effects from sulfates and sulfonate groups is important for the performance improvement of real-world devices. Near surface alloying of Pt-electrodes with Cu can not only increase the ORR activity, but also reduce the poisoning effects by the weakening of the binding of these species, due to specific charge-transfer phenomena.

4.2.3.2 Stability of model Pt(111)/Cu near-surface alloy catalysts

In order to assess the performance of catalysts for future practical applications, their stability under operating conditions is one of the key properties that need to be evaluated. However, the effect of the solute metal in the stability of these materials is not well understood, despite recent efforts (e.g., references 289, 290, 291, and 292).

Real-world electrocatalysts can form a variety of surface facets and various defects such as steps, kinks and adatoms. On such sites, the intermediate adsorption energies will be different and the surface cannot be represented by a single descriptor, such as the adsorption energy on Pt(111) (as already discussed in Section 4.2.2). Since undercoordinated sites bind *O stronger, i.e., they have higher affinity towards oxygen, it is expected that corrosion will start with *O adsorption at such sites. Considering this, it is clear that it is necessary to elucidate the influence of the subsurface Cu, known to influence the adsorption of oxygenated species, on the *O binding at NSA surfaces in order to assess the stability of these catalysts[179]. Figure 4.21 shows the binding energies of *O at the step edge of 3(111)×(100) surface as a function of the Cu-content in the subsurface layer.

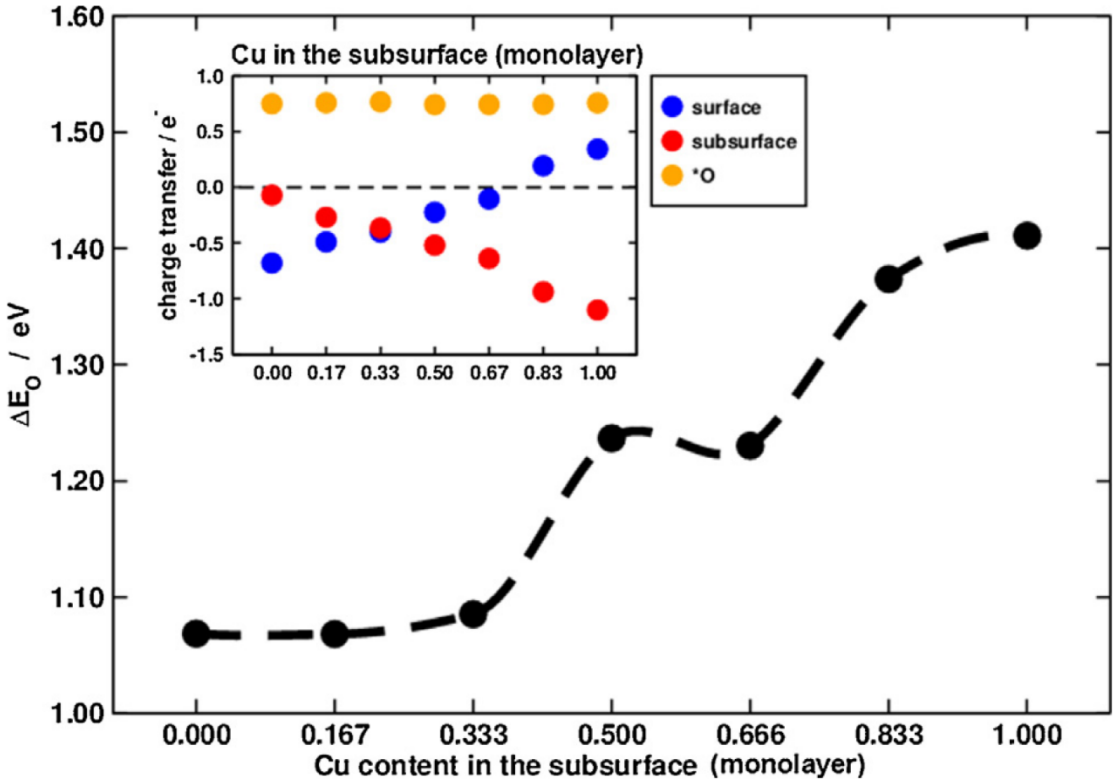

Figure 4.21: The *O binding energy on a Pt(211)/Cu NSA surface as a function of the Cu-content in the subsurface layer. The inset shows the charge transfer between the subsurface (●), surface (●) and the adsorbate (●). Calculations were made by Dr. F. Calle-Vallejo, University of Leiden, the Netherlands.

Figure 4.21 shows that the binding energy of *O decreases with the increase of the amount of subsurface Cu. The difference between Pt-Cu NSA with 1ML of copper, and pure Pt is *ca* 0.35 eV. A similar trend is observed for Pt(111)/Cu NSAs (Section 4.2.3.1). This decrease in the binding energy will generally not result in an activity increase because the adsorption energies of *O on the step edges are far from the tip of the volcano plot for the ORR (Figure 2.7B). Nevertheless, the decreased affinity towards oxygen will likely improve the catalyst stability.

From the inset in Figure 4.21, one can also see that the *O adsorbate exchanges a charge of *ca* 0.75e^- regardless of the type of surface (i.e., Cu-content in the NSA). The amount of charge exchanged by the surface and subsurface layers, however, show a strong and almost linear dependence on the Cu-content.

The performed stability tests entailed the cycling of the electrode potential in the range 0.05-1V *vs.* RHE, with the number of cycles for independent measurements being: 5, 500, 1600, 200, and 5000. The state of the electrode surface was evaluated by subsequent cyclic voltammetry measurements. The maximal value of subsurface Cu-content was taken to be *ca* 2/3 ML, since earlier studies showed that this amount could be stabilized by thermal annealing[281,293,294].

Figure 4.22A shows the CVs of Pt(111)/Cu NSAs in the potential range of 0.05-1V, after stability tests consisting of 500, 2000, and 5000 cycles in Ar-saturated 0.1M $HClO_4$.

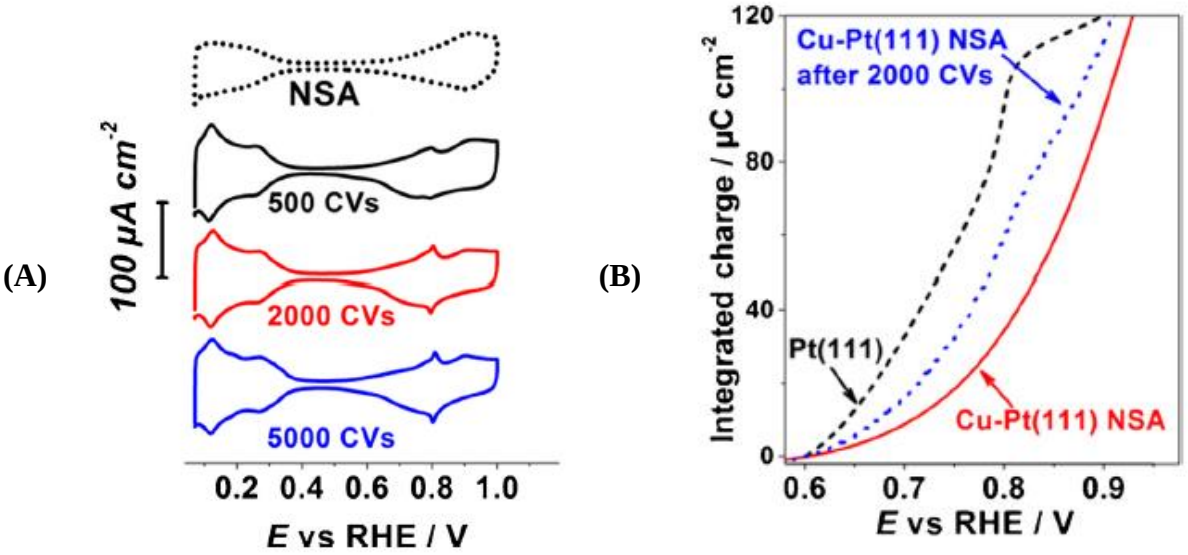

Figure 4.22: (A) CVs of Pt(111)/Cu NSA taken in Ar-saturated after 500, 2000, and 5000 cycles 0.05-1V in the same electrolyte. Scan rate: 50 mV/s. (B) Charge associated with *OH adsorption as a function of the applied potential for Pt(111), Pt(111)/Cu NSA, and Pt(111)/Cu NSA after 2000 cycles. The data were obtained in collaboration with Dr. J. Tymoczko, Ruhr-Universität Bochum, Germany.

The changes in the CVs indicate that a significant amount of defects is introduced to the electrode surface during potential cycling. After 500 cycles a pair of peaks in observed in the $H_{ads/des}$ region at the potential of approximately 0.12V, the height and position of which does not change significantly after further cycling, indicating that initial imperfections of the Pt surface layer likely undergo reconstruction in a relatively short period of time. At *ca* 0.8V a pair of sharp peaks appears gradually, indicating the order-disorder phase transition observed on bare Pt(111). The appearance of these peaks during the stability tests indicates the appearance of ordered Pt(111) facets.

In Figure 4.22B the charge associated with *OH adsorption is shown as a function of the applied potential. The presence of Cu-atoms in the subsurface layer weakens the binding of *OH. However, after 2000 cycles, this positive shift is less pronounced, indicating the possible dissolution of Cu. The CVs of Pt(111)/Cu NSA after 5000 cycles and SA after the complete dissolution of Cu from the surface are compared in Figure 4.23. The Figure reveals that while the SA after Cu-dissolution displays features similar for Pt(pc), the same is not true for the NSA sample, where the small pair of sharp peaks at *ca* 0.8V appears.

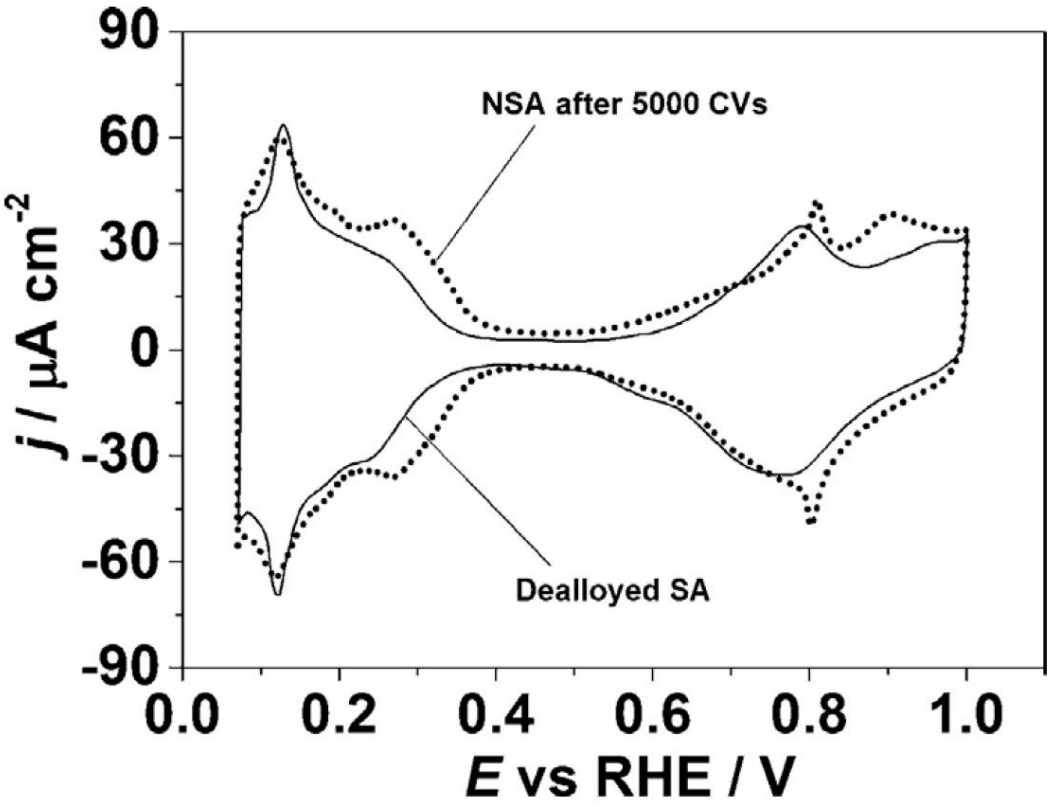

Figure 4.23: CVs of Pt(111)/Cu NSA after 5000 cycles and SA after the complete dissolution of Cu from the surface 0.05-1V in 0.1M $HClO_4$. Scan rate: 50mV/s. The data were obtained in collaboration with Dr. J. Tymoczko, Ruhr-Universität Bochum, Germany.

This suggests that the dealloying of the NSA goes through a different mechanism in comparison to the dealloying of SAs. Likely, in the case of NSAs, Cu does not dissolve simultaneously from all sites on the surface, but it rather dissolves preferentially from defects. This mechanism leads to the formation of different surface domains: Pt(111)/Cu-like and Pt(111)-like. This is a distinctive property of Pt(111)/Cu NSAs, not observable for dealloyed bulk alloys[295] or SAs.

In order to quantify the amount of Cu after the stability tests, the NSAs were converted to SAs. After the conversion to SAs, the Cu in the surface layer was anodically oxidized *via* CV and the anodic parts of the voltammograms characteristic for Cu-oxidation were integrated. The amount of Cu was calculated from the charge associated with the oxidation process.

The NSAs that were cycled only 5 times displayed an anodic Cu-stripping charge of *ca* 300µC cm^{-2}, corresponding to *ca* 0.68ML of Cu, in good agreement with the expected value (2/3ML). Meanwhile, the sample cycled 5000 times reproducibly displayed a value of 175µC cm^{-2}, which corresponds to *ca* 59% of the initially present Cu. Figure 4.24 presents an overview of the thus determined Cu-amount in the NSAs depending on the number of cycles performed during the stability tests.

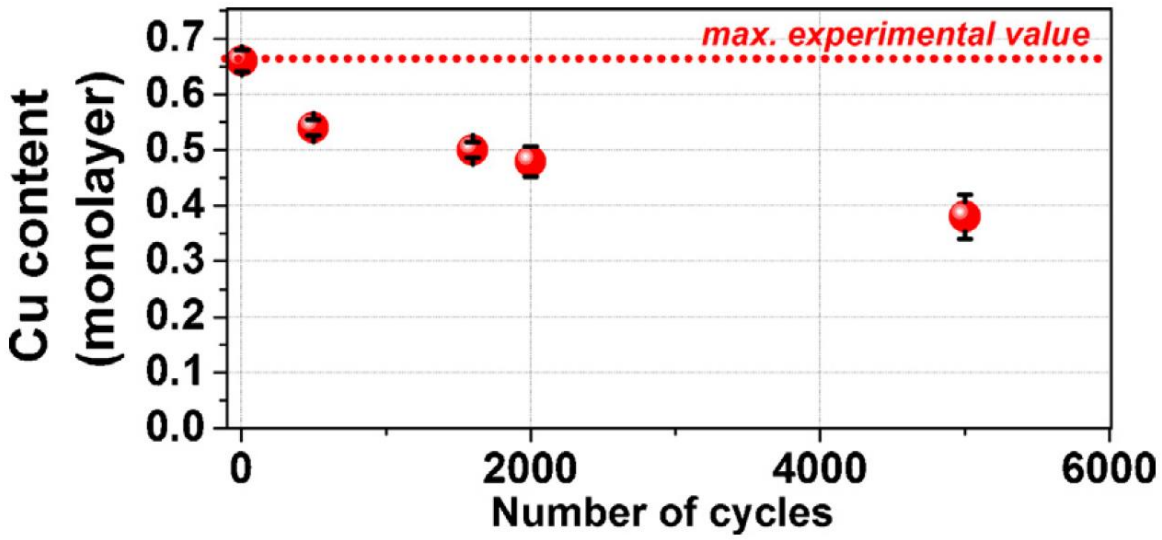

Figure 4.24: The amount of Cu in the subsurface layer (fraction of ML) versus the number of potential cycles in the range of 0.05-1V the Pt(111)/Cu NSA sample was submitted to in Ar-saturated 0.1M $HClO_4$ during the stability testing. Scan rate: 50 mV/s. The data were obtained in collaboration with Dr. J. Tymoczko, Ruhr-Universität Bochum, Germany.

The amount of Cu retained in the subsurface layer is surprisingly high considering the fact that the electrodes were cycled in the potential region were metallic Cu itself is not stable. While potentials of 0.9-1V are sufficient to dealloy bulk Cu-Pt polycrystalline[295] and Cu-Pt nanoparticles[61,292], only 0.3ML Cu is lost during 50 hour stability tests with Pt(111)/Cu NSAs. Despite the fact that the presence of Cu lowers the affinity towards oxygenated species, surface defects are still the main cause of the degradation of NSAs.

4.3 The effects of surface morphology

In this chapter, the link between the morphology of the surface and the electrocatalytic properties of the system is discussed. Pt is often considered a benchmark electrocatalysts for energy applications. Therefore, in this chapter it was used as a model material.

4.3.1 Active sites and coordination

Even small changes in the surface structure of a catalyst can induce drastic changes in the surface electronic structure. These changes have often been linked to the changes in the coordination number of the surface atoms. For instance, trends in adsorption energies for small intermediate species on extended surfaces of transition metals have been described by the coordination number (CN) of the surface sites[74,129]. However, CN is no longer an accurate tool for activity assessment for nanoparticles due to the so-called "finite size effects"[296,297]. For these surfaces, more advanced descriptors need to be developed[298]. Figure 4.25 illustrates this point: all sites shown in blue color have nine neighbors and CN=9, however, their *OH binding energies differ by up to almost 0.5 eV.

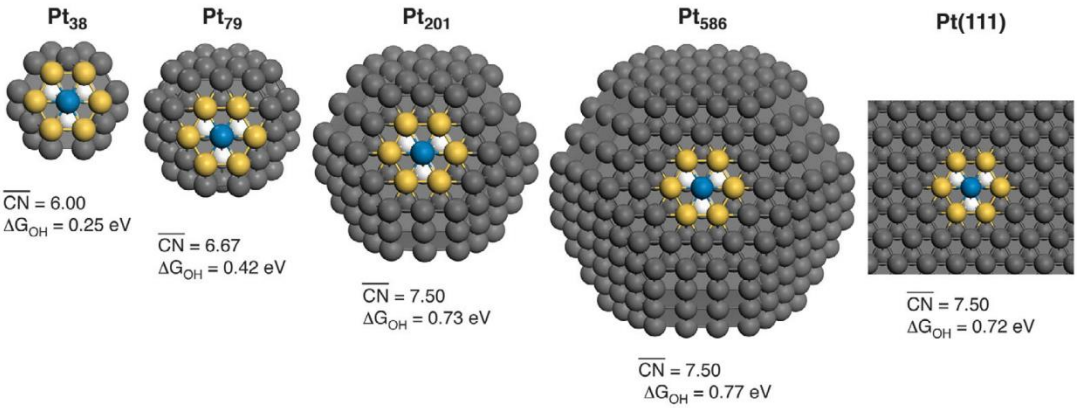

Figure 4.25: Sites with a coordination number CN=9 (blue) on nanoparticles of different sizes and on a Pt(111) extended surface. The nearest neighbors on the surface are marked in yellow, and the subsurface ones in white. While all the atoms marked blue have the same coordination number the *OH binding energies differ by *ca* 0.5 eV. The generalized coordination number, however, is a suitable descriptor in this case. Adapted from: 128.

This issue can be overcome by the use of "generalized" coordination numbers ($\overline{CN}$)[299], which introduces a "weight" to each first-nearest atom *j*, corresponding to its own coordination number, *cn(j)*. Generalized coordination numbers are a first-order extension of conventional coordination numbers. The formula for the calculation of the generalized coordination number is as follows[299]:

$$\overline{CN} = \sum_{j=1}^{n_i} \frac{cn(j)}{CN_{max}} \qquad \text{(Eq. 50)}$$

The sum includes all the first-nearest neighbors and the division is by the maximum number of first –nearest neighbors in the bulk (CN_{max}). This means that the $\overline{CN}$ is in the range of 0-12 in *fcc* crystal lattices, just as *cn*. The equation shows that the first neighbors are accounted for and they determine the largest part of the $\overline{CN}$ value. The second –nearest neighbor have a smaller, but non-negligible contribution. If all second-nearest neighbors would have full coordination, $\overline{CN}$ and *cn* would be of the same value. This implies that while *cn* treats all first-neighbors as if they were identical bulk atoms, $\overline{CN}$ assigns a "weight" to every first-nearest neighbor represented by its own coordination number.

The generalized coordination number can be calculated for any site on an extended surface or nanoparticle[76,300]. The way Equation 50 is applied is as follows:

1. The site *i* for which the $\overline{CN}$ will be calculated is identified.
2. The number of first-nearest neighbors *j* is determined, the overall number of which is n_i. In a model Pt crystalline structure, the interatomic distances are 2.81 Å. Due to strain distances at surfaces are often shorter, or sometimes larger. A reasonable confidence interval is 2.81±0.30 Å, i.e., bulk distance with *ca* ±10% tolerance.
3. When the nearest neighbors are identified, the number of their first-nearest neighbors must be determined to obtain *cn(j)*

4. The values are fed into Equation 50 and the generalized coordination number is calculated.

For instance, in Figure 4.25 the site marked by the blue sphere on Pt_{38} has six neighbors with cn=6 (yellow spheres), and three with cn=12 (white spheres), which leads to:

$$\overline{CN_{Pt_{38}}} = \frac{6 \cdot 6 + 12 \cdot 3}{12} = 6$$

The value of the $\overline{CN}$ rises with the increasing particle size reaching 7.5 for the extended *fcc*(111) surface. This simple extension explains the changes in the binding energy seen in Figure 4.26: the contribution of second-nearest neighbors, while smaller than the first-nearest, is not negligible.

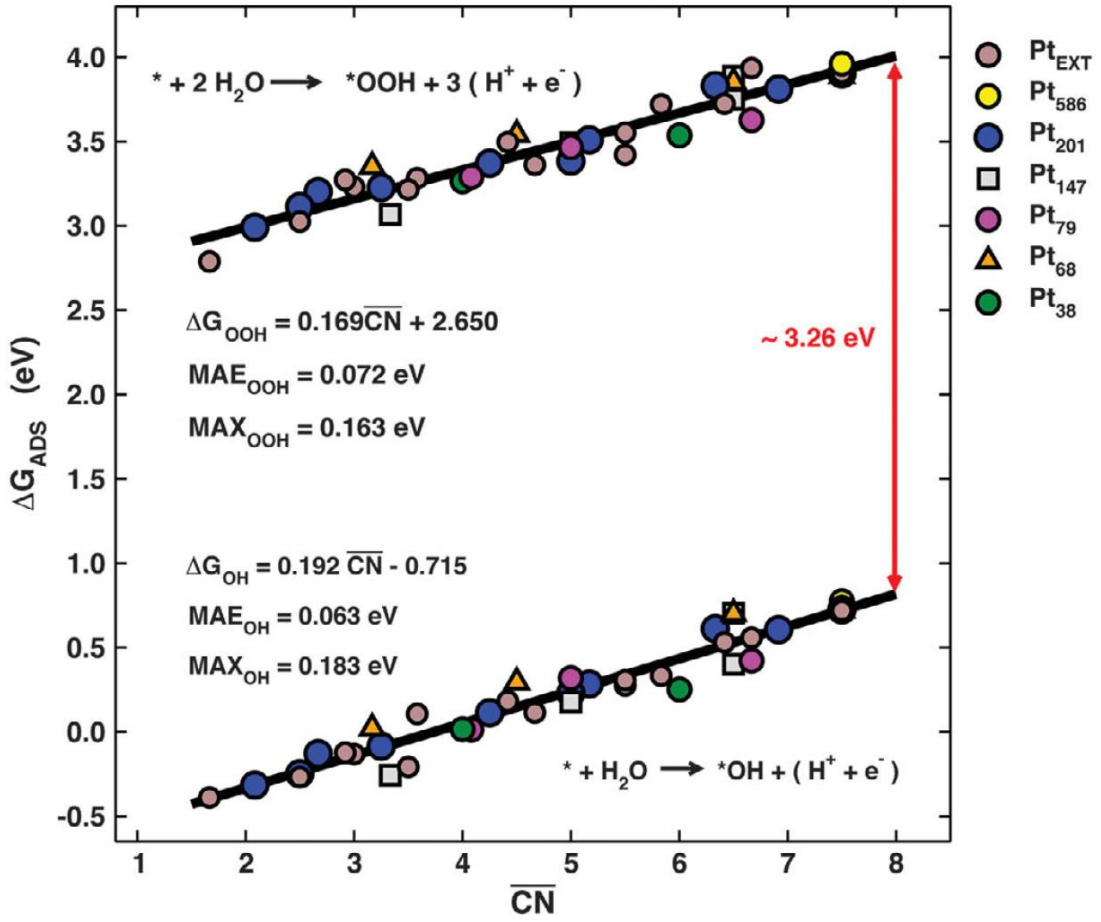

Figure 4.26: Values of ΔG_{OH} and ΔG_{OOH} as a function of the generalized coordination number $\overline{CN}$. Values shown for: extended surfaces (brown) as well as, truncated octahedron (symbol shape: ○), cuboctahedron (□), and tetrahedron-shaped (△) nanoparticles of sizes: Pt_{586} (symbol color: yellow), Pt_{201} (blue), Pt_{147} (gray), Pt_{79} (magenta), Pt_{68} (orange), and Pt_{38} (green). Insets show the reactions that were used to calculate the adsorption energies. Least-squares fits are provided together with mean (MAE) and maximum (MAX) absolute errors and as well. Calculations were made by Dr. F. Calle-Vallejo, University of Leiden, the Netherlands.

The generalized coordination number can be calculated for “bridge” (two-atom) and “hollow” (2- and 4-atom) sites as well. Depending on the type of site in question cn_{max} will be different. In *fcc* metals, top sites have maximal number of bulk neighbors of 12. Bridge site have 18, threefold, such as *fcc* and *hcp* hollow, have 22, and fourfold, such as hollows on *fcc*(100) terraces have 26. The $\overline{CN}$ for all these sites can be calculated by Equation 50, regardless of the type or shape of the particles.

Figure 4.27 shows that $\overline{CN}$ describes the binding energy trends better than *cn* (henceforth the generalized coordination number will be implied under “coordination” in the further text). As $\overline{CN}$ is purely arithmetical, it offers the significant advantage that its assessment does not require numerous DFT c ons.

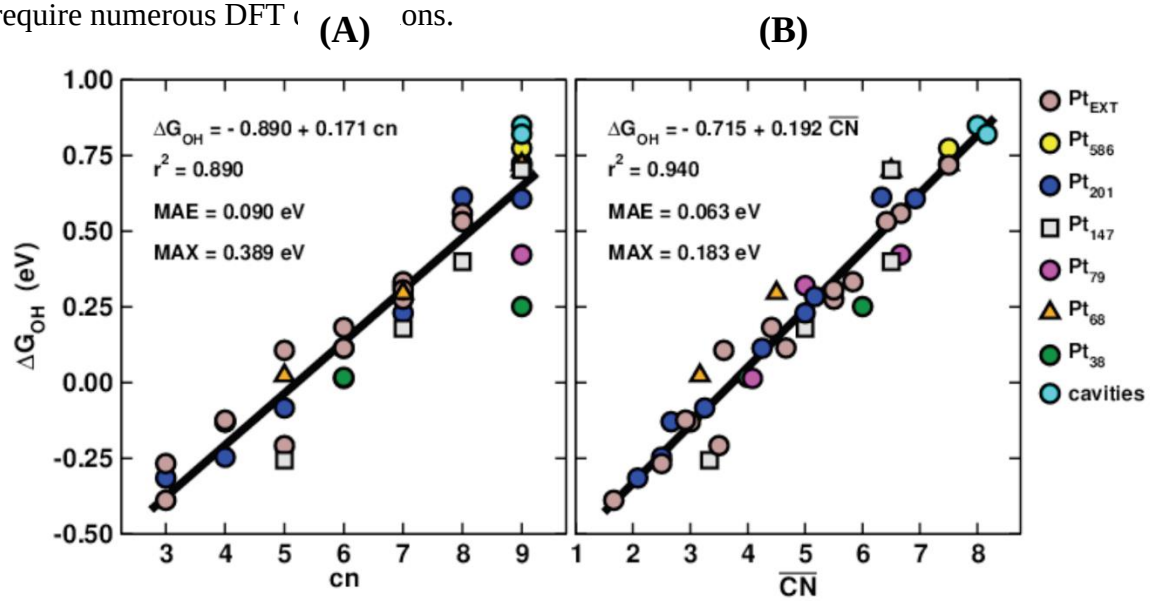

Figure 4.27: The adsorption energies of *OH on various sites on: Pt extended surfaces, Pt_{EXT}, (brown circle), Pt_{586} (yellow), Pt_{201} (blue), Pt_{147} (gray), Pt_{79} (magenta), Pt_{68} (orange), Pt_{38} (green), and cavities (cyan) plotted versus the (A) conventional coordination numbers (B) generalized coordination numbers of the given sites. The insets show the linear regressions and related statistical data. Calculations were made by Dr. F. Calle-Vallejo, University of Leiden, the Netherlands.

Since the rate determining steps for the ORR are the first and the last proton-electron transfers, the activity depends on the adsorption energies of *OH, and * OOH: ΔG_{OH} and -ΔG_{OOH}. However, if adsorption energies are used as descriptors, only optimal adsorption energies will be identified. These particular adsorption properties are difficult to link to the properties of the catalysts and could theoretically be met by many different materials. In order for the volcano plots to provide information on the ideal structural properties of a given materials, the use of structural activity descriptors is necessary.

Such a coordination activity plot is presented in Figure 4.28, which indicates that the optimal Pt surface sites for ORR catalysis have a $\overline{CN}\approx$ 8.3

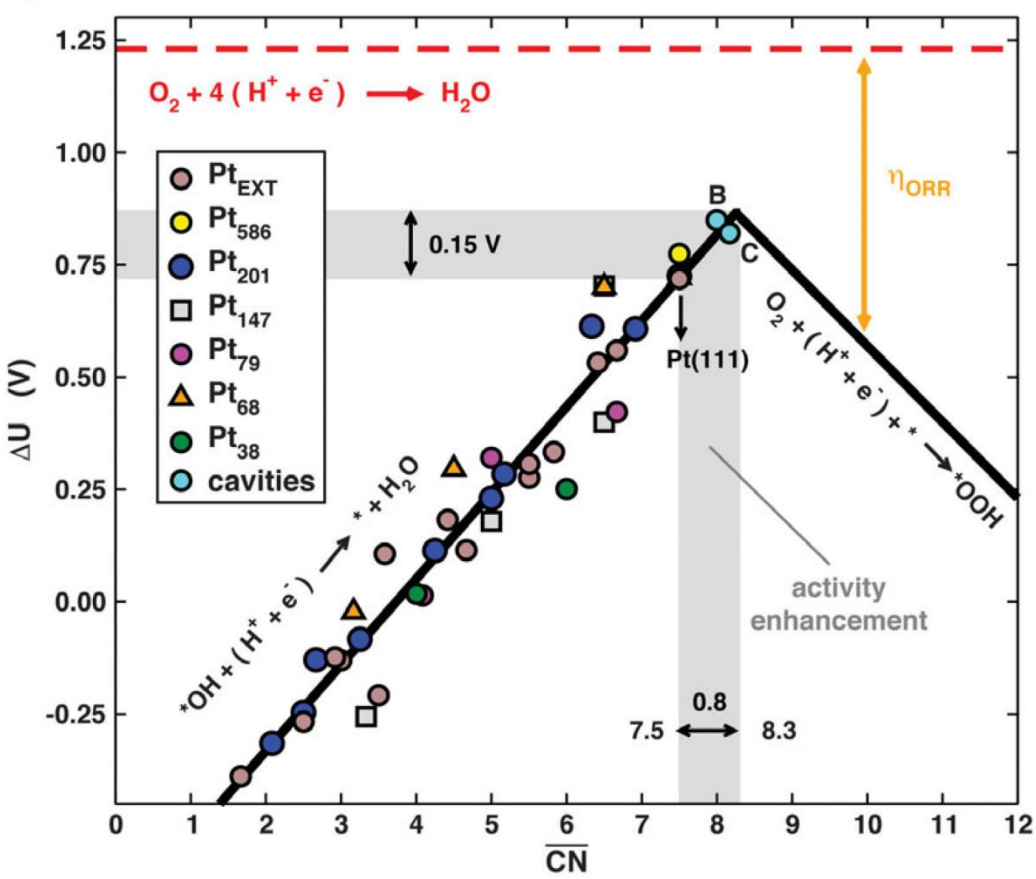

Figure 4.28: Potentials of the two rate-limiting steps on extended Pt-surfaces and nanoparticles. Points B and C (light blue) are given for two types of cavity sites on Pt(111) that are a result of the removal of six (A) and five (B) surface atoms. The potential-determining step on the left low, stronger, and right, weaker than ideal binding, sides of the volcano are indicated in the image. The theoretical overpotentials (η_{ORR}) are the vertical difference between the points and the equilibrium potential (red dashed line). Optimal catalysts have CN ≈ 8:3 and *OH adsorption energies ~0.15 eV weaker than Pt(111) (gray area). Calculations were made by Dr. F. Calle-Vallejo, university of Leiden, the Netherlands.

An optimal ORR catalyst binds *OH *ca* 0.15eV weaker than Pt(111), in agreement with previously reported findings[148,166]. The obtained ideal value of the generalized coordination number can be used to guide the experimental design of ORR catalysts.

To achieve this one must first identify the type of sites that would achieve ideal coordination. (111) terraces on extended surfaces (or large enough NPs) have $\overline{CN}$=7.5. In order to possess the optimal coordination of 8.3, the catalytic sites should have more neighbors than the (111) terraces. Sites with cn=10 such as bottom of (100) step sites, or cn=11, such as (110) facets or bottom (111) step sites, have $\overline{CN}$ values between 8.75 and 9.5, meaning they bind too weakly, while also experiencing other drawbacks like steric hindrance and proximity to strongly binding undercoordinated sites with high affinity for oxygenated species.

Since increasing the number of first-nearest neighbors does not result in sites with the optimal $\overline{CN}$, one must turn to manipulating the number of second-nearest neighbors. Figure

4.29, shows two one atomic layer deep cavities on a Pt(111) surface that are a result of the removal of six (A) and five (B) surface atoms.

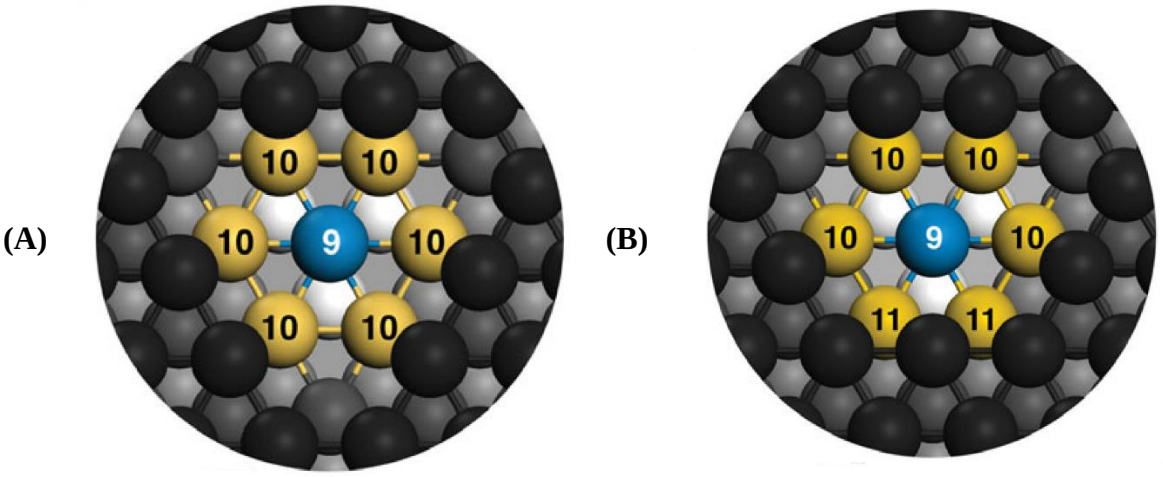

Figure 4.29: Illustrations of one atomic-layer deep cavities on a Pt(111) surface that are a result of the removal of (A) and six surface atoms $\overline{CN}$=8 (B) five surface atoms $\overline{CN}$=8.17. These surface defects provide sites with $\overline{CN}$ values close to the ideal. Adapted from: 128.

The configuration in Figure 4.29A effectively means that each first neighbor (yellow) of the active site (marked blue) has an additional neighbor in comparison to that on Pt(111) surface atoms. The active site has *cn*=9, each surface neighbor has *cn*=10, while the three subsurface neighbors (white) have the maximal *cn*=12, resulting in a $\overline{CN}$=8 for the active site in Figure 4.29A. Correspondingly, the active site in Figure 4.29B has $\overline{CN} = \frac{4 \cdot 10 + 2 \cdot 11 + 3 \cdot 12}{12}$=8.17. The overpotentials of these sites are *ca* 0.1 V and *ca* 0.13 V lower than on Pt(111), respectively.

Other configurations might also exist which offer $\overline{CN}$ values close to optimum. The active site design strategy is quite straightforward: it must have an increased number of second-nearest neighbors, so that *cn* > 9 for the first-nearest neighbors of the active site. This design principle could not have been reached with the simple coordination number, *cn*, since it does not account for the influence of second-nearest neighbors.

These theoretical guidelines can be used to create the desired active sites close-to-ideal with a close-to-ideal GCN on Pt(111) surfaces. In order to introduce the defects to the surface of Pt(111) electrodes several approaches were implemented (as illustrated in Figure 4.30):

1. Stripping away the surface Cu-atoms of an ordered Pt(111)/Cu SA[280].
2. Galvanic displacement (GD) of a Cu-overlayer with Pt resulting in the formation of "surface islands"[292]. Figure 4.32 shows an AFM image of the surface where such islands are visible. The active sites for the ORR with higher generalized coordination numbers should be located between the deposited "islands" as indicated by the blue circles.
3. Electrochemical destruction, i.e., formation and subsequent reduction of subsurface Pt-oxide which causes partial dissolution of Pt from the surface[172,301]. This results in both

small (desirable) and big (undesirable) cavities, as shown on the AFM image in Figure 4.33.

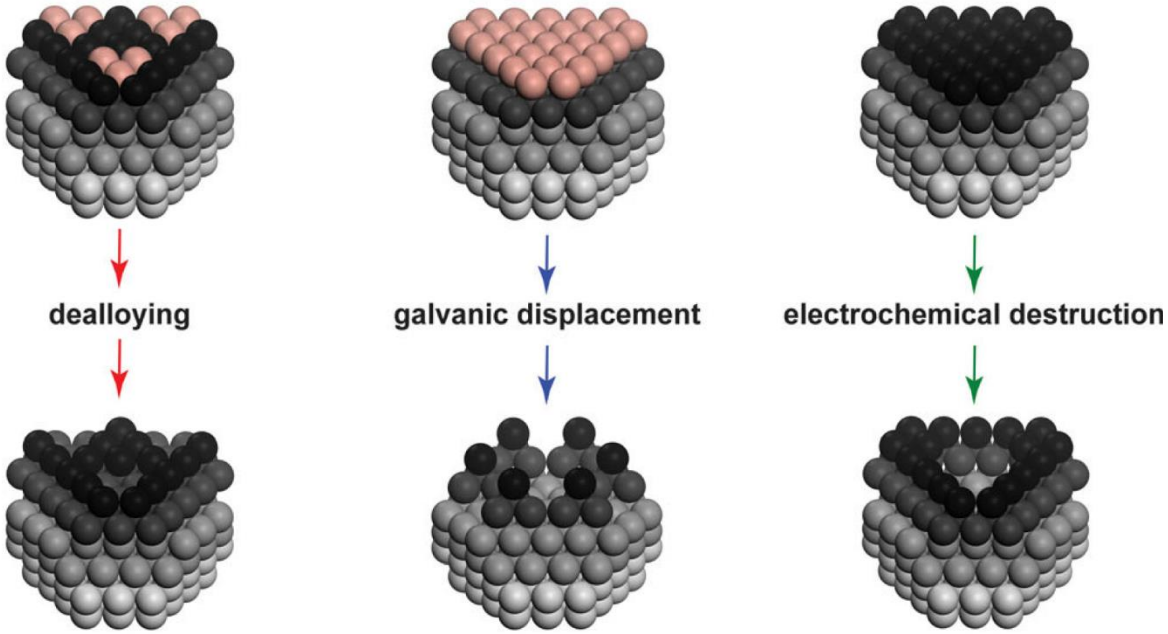

Figure 4.30: Schematic representation of the different approaches used to create defects on Pt(111) surfaces. Cu atoms are shown in red. Pt atoms are represented by gray or black spheres, depending on the depth they are located at with respect to the surface layer. Adapted from: 128.

The CVs of Pt(111) and dealloyed Pt(111)/Cu SA are shown in Figure 4.31. The changes in the adsorption/desorption properties of *H and *OH reveal that, while the number of adsorption sites remains approximately the same, the dealloyed surface binds *H and *OH adsorbates weaker than Pt(111).

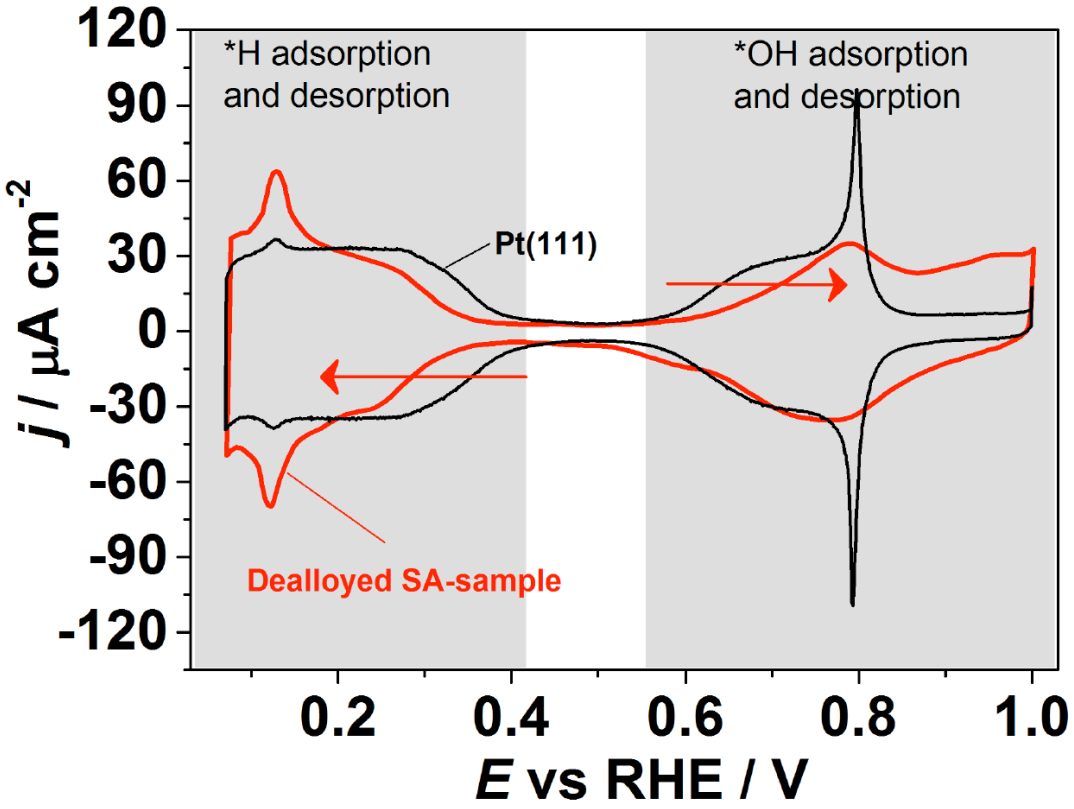

Figure 4.31: Typical cyclic voltammograms of freshly annealed Pt(111) and dealloyed SA electrodes. Scan rate: = 50mV s^{-1}, Ar-saturated 0.1M $HClO_4$. The data were obtained in collaboration with Dr. J. Tymoczko, Ruhr-Universität Bochum, Germany.

Taking into the account that the defects at the surface of the dealloyed SA electrodes are presumably 1 atomic layer deep, and only ~1/3ML of Pt atoms form the first surface layer, the theoretical prediction that active defect sites at 1-atom-deep cavities should bind *OH slightly weaker than Pt(111) terraces is confirmed.

Figure 4.32 shows an AFM image of the surface of a Pt(111) electrode after the galvanic displacement treatment. The surface is covered with platinum "islands" (protruding defects) with a uniform density of approximately 25 islands per μm^2. The islands seem to be quasi-rhombic in shape. However, this shape corresponds to the form of the used tip, suggesting that the islands are too small for their exact shape to be determined. Their height and area distributions are shown in the insets *i* and *ii* in Figure 4.32. Apart from few islands with heights larger than 2.5nm, most defects show a value of *ca* 1.1nm with a mean of (1.3 ±0.4) nm, which is about 3-4 Pt atomic diameters. The lateral dimension is even more uniform with a mean of (34.9 ± 5.6) nm with the median at 35.1nm. This indicates that an island consists of around 30-100.000 Pt-atoms.

Generally, the creation of sites with Pt atoms with $\overline{CN}$ as close to 8.3 as possible is desirable. Such sites could form in the narrow space between the islands on these surfaces. A single GD procedure forms only a limited number of such sites. The implementation of several GD procedures would increase the chance of generating such sites with atoms with close-to-ideal $\overline{CN}$. Therefore, several consecutive GD procedures were implemented to create defects on the investigated surface.

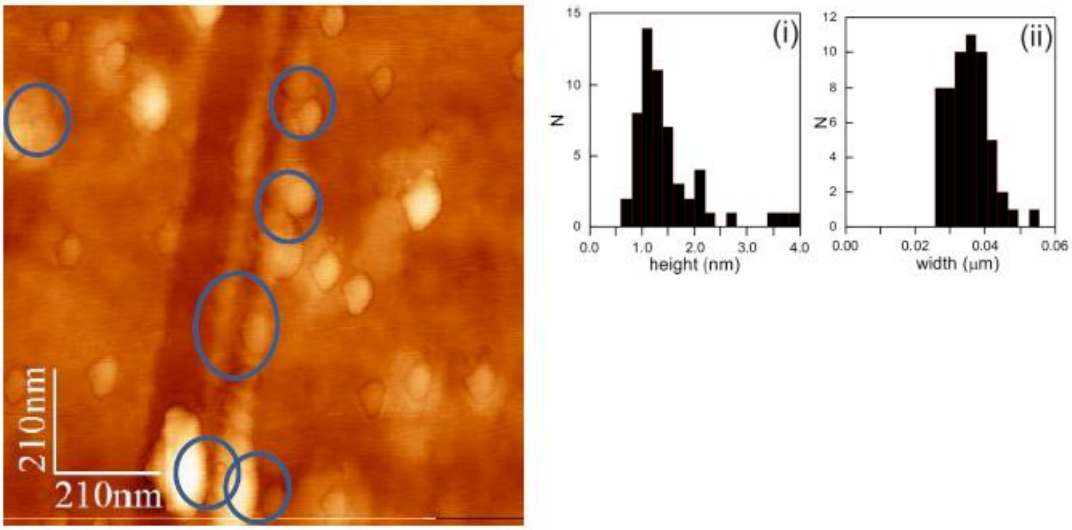

Figure 4.32: A typical AFM image of the Pt(111) surface after one galvanic displacement procedure (measured in contact mode) and distributions of defect dimensions (insets *i*, *ii*). The blue circles indicate active sites for the ORR with higher generalized coordination numbers. The data were obtained in collaboration with Dr. J. Tymoczko and Prof. K. Morgenstern, Ruhr-Universität Bochum, Germany

Figure 4.33 shows the AFM image of a Pt(111) surface after electrochemical destruction, i.e., cycling the electrode 10 times up to 1.72V. The resulting surface is covered with relatively large "holes". The concentration of defects is *ca* 0.08 defects per μm^2, which is significantly smaller than the one provided by the galvanic displacement procedures.

Due to the larger size of the holes, their shape can be determined in the AFM images, being mostly round or elliptical, only rare straight edges reflecting the surface symmetry are observed. The hole defects are an order of magnitude deeper than the protruding islands created by galvanic displacement and show a preference for depths that are separated by around 20nm. In contrast, the width shows only a small spread with a mean at (1.06 ± 0.41) μm. The single larger defect visible in Figure 4.33 is attributed to the coalescence of two holes. The hole defects correspond to $1 - 3 \cdot 10^9$ of missing atoms.

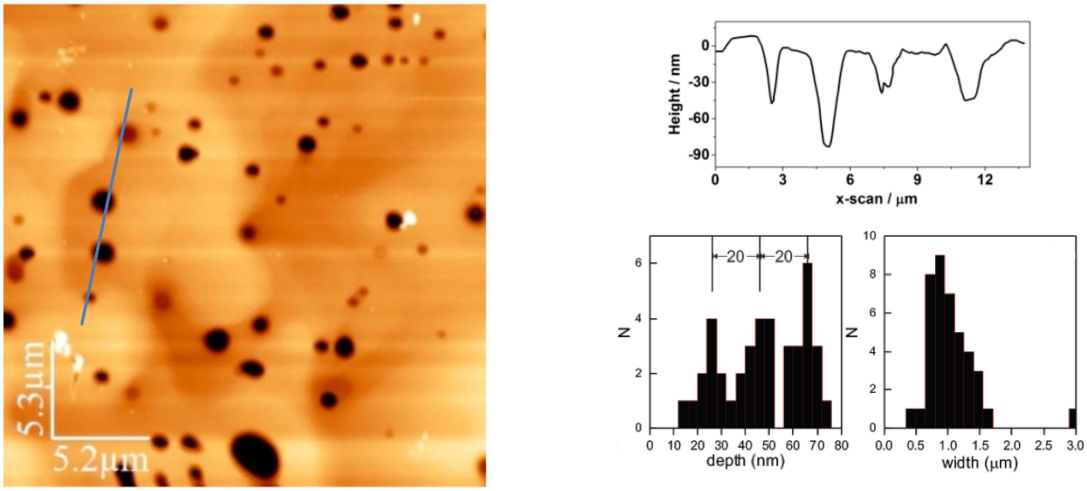

Figure 4.33: Left: AFM image of the Pt(111) surface after electrochemical destruction. Upper right: Line scan of the path indicated in the image on the right. Lower right: corresponding AFM-statistics of the dimensions of the defects. The data were obtained in collaboration with Dr. J. Tymoczko and Prof. K. Morgenstern, Ruhr-Universität Bochum, Germany

It is of particular interest to determine whether small cavities are also formed on the terraces and their surface density, as they should be responsible for the high electrocatalytic activity of these surfaces. However, this is not a trivial task since there is a large distribution of cavity sizes.

Figure 4.34 shows fragments of the surface of a freshly prepared Pt(111) electrode (A), and one subjected to electrochemical destruction (C). The surface of the electrode modified by electrochemical destruction contains a large and relatively shallow cavity and an adjacent terrace. The three line scans provided (D, E, F) suggest that the amount and depths of the surface defects on the terraces and inside extended "holes" is larger than in the case of the model Pt(111) surfaces (4.34B). These surfaces possess an ORR activity *ca* 3.5 times larger than Pt(111). The number of surface adsorption sites is increased by merely *ca* 15% compared to Pt(111), so the activity increase cannot be attributed to this fact.

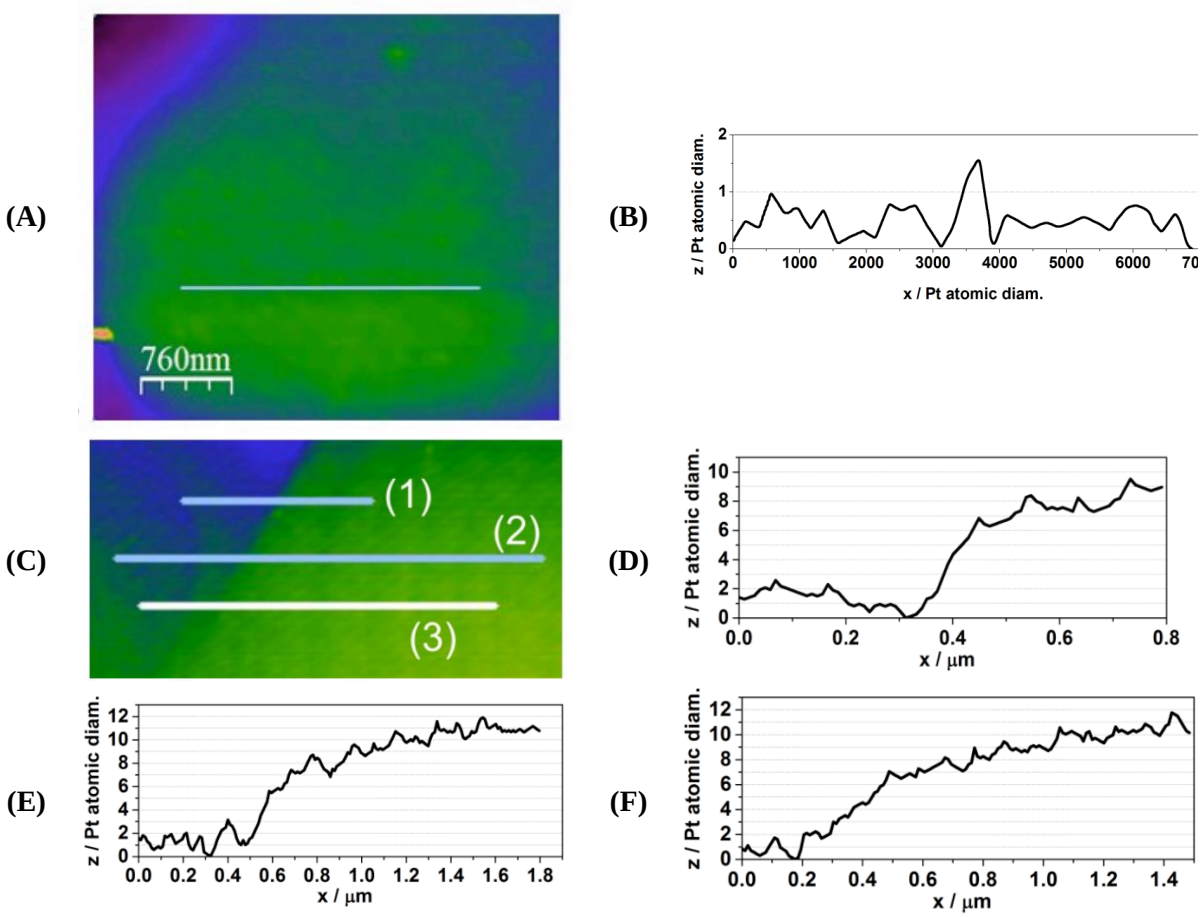

Figure 4.34: (A) Fragment of a freshly prepared Pt(111) surface (B) the line scan indicated in Figure (A), Note that the terraces are almost atomically flat (C) A fragment (2μm x 1 μm) of a Pt(111) surface subjected to electrochemical destruction showing a cavity with at a terrace (B-D) The three line scans indicated in Figure (C): (D)-line 1, (E) – 2, and (F) – 3. The data were obtained in collaboration with Dr. J. Tymoczko and Prof. K. Morgenstern, Ruhr-Universität Bochum, Germany

These techniques all result in the weakening of the adsorption energies of *OH in comparison to that on Pt(111), as Figure 4.35 shows.

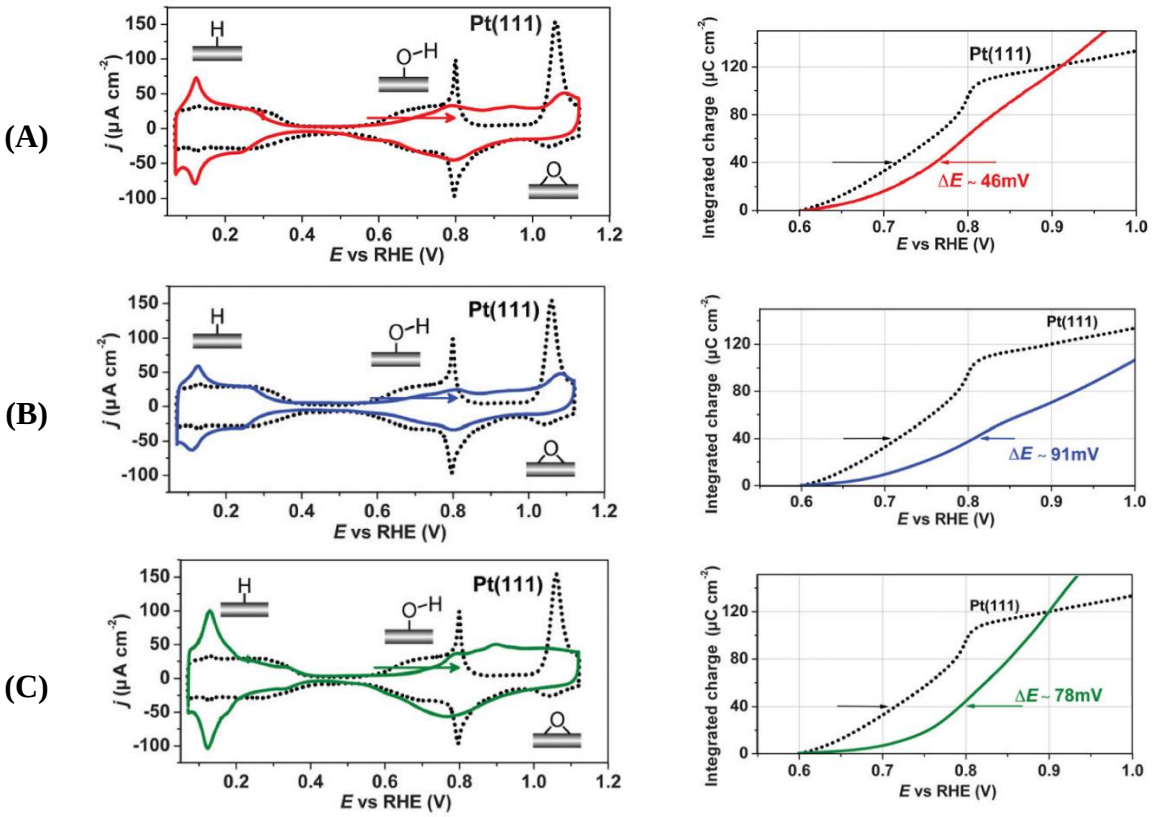

Figure 4.35: On the left: CVs of Pt(111) with the following modifications: (A) dealloying (B) galvanic displacement (C) electrochemical destruction, in Ar-saturated 0.1M $HClO_4$. Scan rate: 50 mV/s. Right: integrated anodic parts of the corresponding CVs. The data were obtained in collaboration with Dr. J. Tymoczko, Ruhr-Universität Bochum, Germany

The positive shifts in the integrated anodic parts of the voltammograms in the OH-adsorption region (0.6-1V), observed on Figure 4.35, indicate weaker *OH binding which should result in an increase in the ORR electrocatalytic activity, in accordance with the Sabatier principle. The shifts observed are *ca* 46mC for dealloyed Pt(111)Cu SA, *ca* 91mV for Pt(111) modified by galvanic displacement, and *ca* 78mV for the electrodes subjected to electrochemical destruction. The sharp "butterfly" peaks that appear in the CVs of Pt(111) attributed to the order/disorder phase transitions decrease in magnitude. This is in agreement with the AFM images that show high site heterogeneity of the defective surfaces, which possibly impedes the formation of the *OH-*H_2O adlayer.

The *OH adsorption potentials predicted from volcano plots generally compare well to experimentally determined onset potentials for *OH adsorption[166,244]. The experimental shifts in the *OH adsorption peaks in comparison to Pt(111) in Figure 4.35 are also in agreement with those in Figure 4.28.

The kinetic currents for the ORR of the modified electrodes in comparison to Pt(111) and similarly treated Pt(pc) are shown in Figure 4.36A. Figure 4.36B shows the activities of some of the state-of-the-art ORR catalysts and the activities of the Pt(111) electrodes created with the aforementioned defect-introduction methods, as well as Pt(pc). Pt(111) surfaces with cavities exceed the ORR activities of several well-known active alloys.

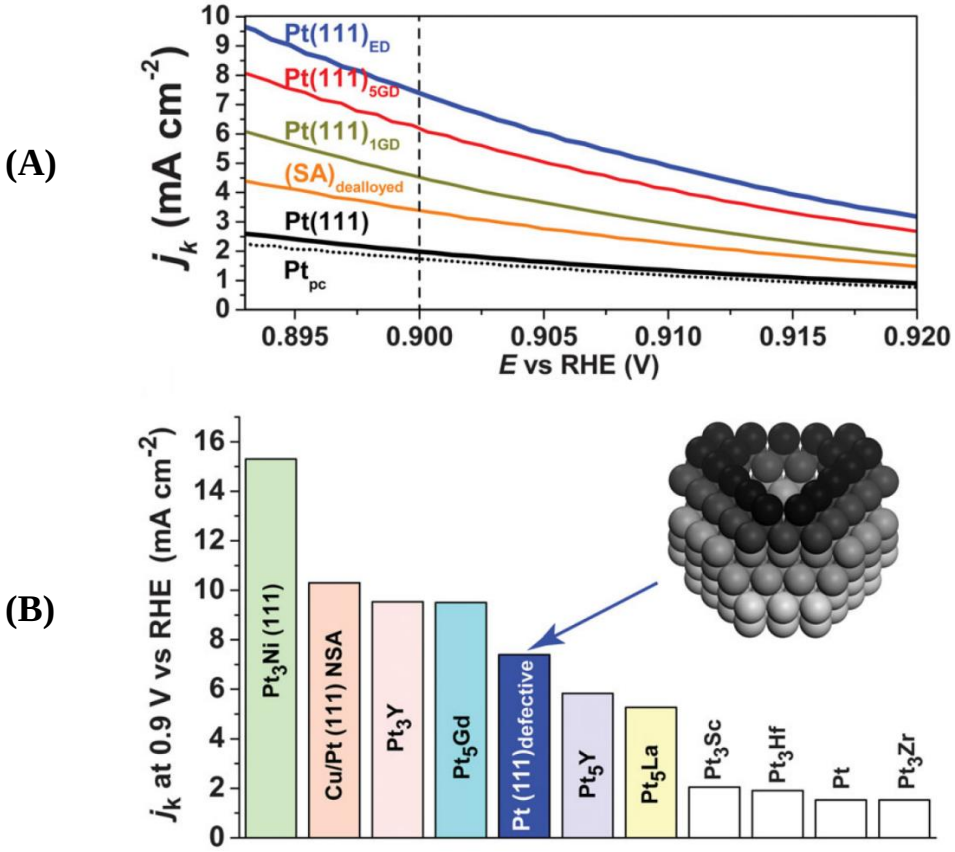

Figure 4.36: (A) Kinetic current densities in O_2-saturated 0.1M $HClO_4$ for defective Pt(pc) (•••••); Pt(111) (—); dealloyed Cu-Pt(111) SA, $(SA)_{dealloyed}$ (—); Pt(111) electrodes modified *via* galvanic displacement, $Pt(111)_{1GD}$ (1 Cu ML displaced) (—) and $Pt(111)_{5GD}$ (5ML Cu displaced) (—); and electrochemical destruction -10 cycles, $Pt(111)_{ED}$ (—). (B) ORR activities for defective $Pt(111)_{ED}$ and: Pt_3Ni[242]; Cu-Pt(111) NSA[244]; Pt_3Y and Pt_3Sc[148]; Pt_5Gd[277]; Pt_5Y; and Pt_3Zr, Pt_3Hf, and Pt_5La[166]. The current densities are compared at the potential of 0.9V. The data were obtained in collaboration with Dr. J. Tymoczko, Ruhr-Universität Bochum, Germany.

The Figure shows that the introduction of specific defects can increase the activity of Pt(111) electrodes towards the ORR by *ca* 3.5 times. This increase cannot be explained by the moderate increase in the number of accessible surface adsorption sites, which should be *ca* 15% at most. Therefore, alloying or changing the coordination have similar beneficial effects. However, such introduction of defects does not enhance the activity of any type of platinum surface. For instance, from Figure 4.36 one can see that the same anodic treatment did not enhance the activity of Pt(pc) electrodes. Figure 4.37A and B show that electrochemical destruction of polycrystalline platinum electrodes does not result in changes in the CVs in 0.1M $HClO_4$. Figure 4.37C shows that while electrochemical destruction of Pt(pc) causes an slight initial rise in the activity (indicated by the halfwave potential in Figure 4.7C), it quickly reaches a constant value and stays below that of Pt(111). This shows that only the introduction of specific types of defects will result in an increased ORR activity.

(A)

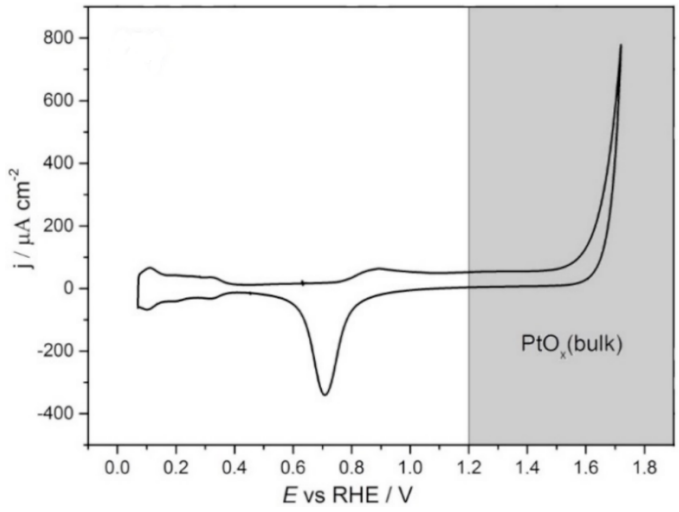

(B)

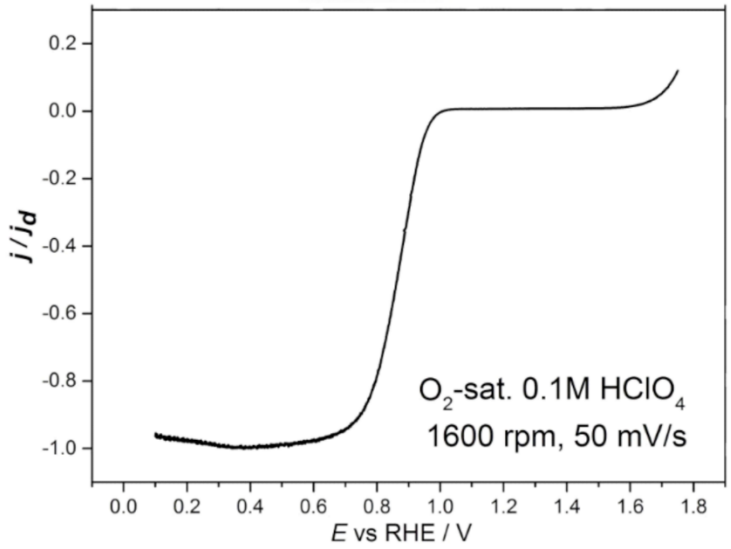

(C)

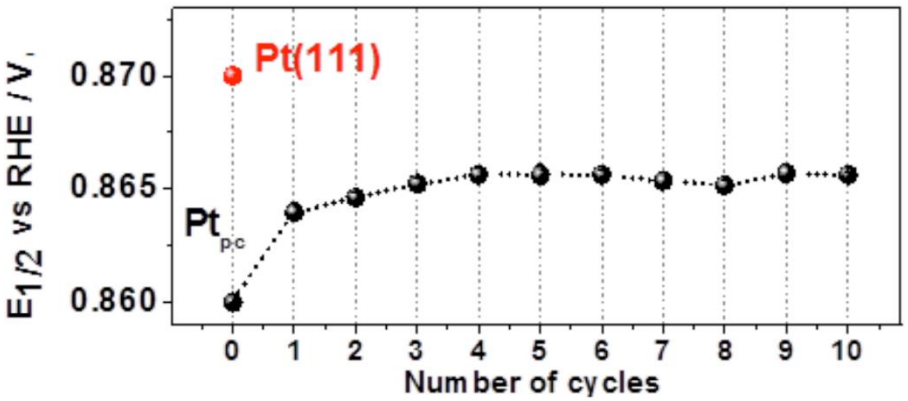

Figure 4.37: (A) A typical CV of a Pt(pc) electrode in Ar-saturated 0.1M $HClO_4$. The shape of the voltammograms remains stable during potential cycling. (B) Typical RDE-voltammogram of the Pt(pc) electrode in O_2-saturated 0.1M $HClO_4$ (C) halfwave potential for the ORR in O_2-saturated 0.1M $HClO_4$ plotted as a function of the number of oxidizing cycles (until the upper vertex potential of 1.72V). Scan rate: 50mV/s. Dotted lines are provided as a guide for the eyes. The data were obtained in collaboration with Dr. J. Tymoczko, Ruhr-Universität Bochum, Germany.

This difference in behavior is attributed to different corrosion mechanisms on facets that of Pt(pc) that lead to the formation of dissimilar defects[253]. Low-index sites or grain boundaries with high affinity for oxygenated species are likely the locations to initiate corrosion. Contrarily, on Pt(111) surfaces the formation of "holes" during corrosion is inevitable. This implies that the dominant types of defects on Pt(pc) and Pt(111) would be significantly different after ED treatment.

Further proof that the activity increase is due to the introduction of defects, and not the increase in the number of available sites is provided in Figure 4.38, which shows the activities of electrodes treated by the electrochemical destruction protocol for a different number of potential cycles, in different electrolytes: 0.1M $HClO_4$ and 0.05M H_2SO_4.

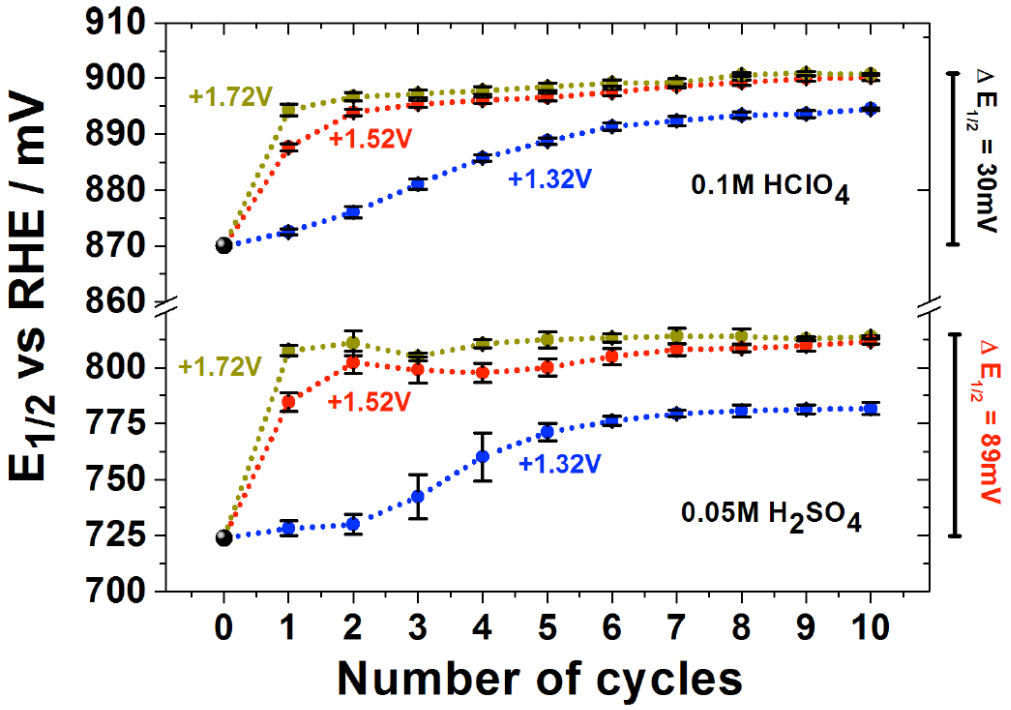

Figure 4.38: The effect of electrochemical destruction on the ORR activity of Pt(111) expressed as a shift in the halfwave potential ($\Delta E_{1/2}$ / mV), plotted versus the number of oxidizing cycles (upper vertex potential: 1.32 V (●), 1.52 V (●) and 1.72V (●)) in O_2-saturated 0.1M $HClO_4$ and O_2-saturated 0.05M H_2SO_4. RDE, 1600r.p.m. Scan rate: 50mV/s. Dotted lines are provided as a guide for the eyes. The data were obtained in collaboration with Dr. J. Tymoczko, Ruhr-Universität Bochum, Germany.

From Figure 4.38 one can see that while the trends in the activities in both electrolytes are similar, the differences in the halfwave potentials are different: *ca* 30mV for perchloric, and *ca* 89mV for sulfuric acid. The more pronounce improvement in 0.05M H_2SO_4 is likely the result of the weakening of both the OH^- and SO_4^{2-} binding. In order to further investigate the nature of the defects at the Pt(111) surfaces treated with electrochemical destruction, the electrooxidation of the adsorbed *CO in 0.1M $HClO_4$ was conducted. Since *OH binds strongly to undercoordinated sites, being a key intermediate for the reaction, the CO electrooxidation reaction will proceed most rapidly at step sites, kinks, and metal adatoms.

Taking this into account, three different surfaces were considered: freshly annealed Pt(111), Pt(331), and Pt(111) subjected to electrochemical destruction. For Pt(331) it is expected that *CO will cover the terraces, while *OH will cover the step edges and oxidize the *CO molecules adsorbed at the same terrace. The Pt(111), conversely, lacks suitable sites for *OH adsorption and the CO oxidation occurs at much higher potentials than Pt(331), Figure 4.39B. The Pt(111) surface with the cavities created by electrochemical destruction should produce voltammograms with significantly different features to the previous two electrodes. If the surface structure is indeed as it is assumed, i.e., there are abundant few-atom scale cavities at wide Pt(111) terraces, the *CO-oxidation CV should display features corresponding to both Pt(111) terraces and the bottoms of cavities with high coordination numbers at more positive potentials than Pt(111) or Pt(331). This is because *CO inside the cavities would not have *OH available for the oxidation process.

The CVs of CO-oxidation on these three surfaces are presented in Figure 4.39.

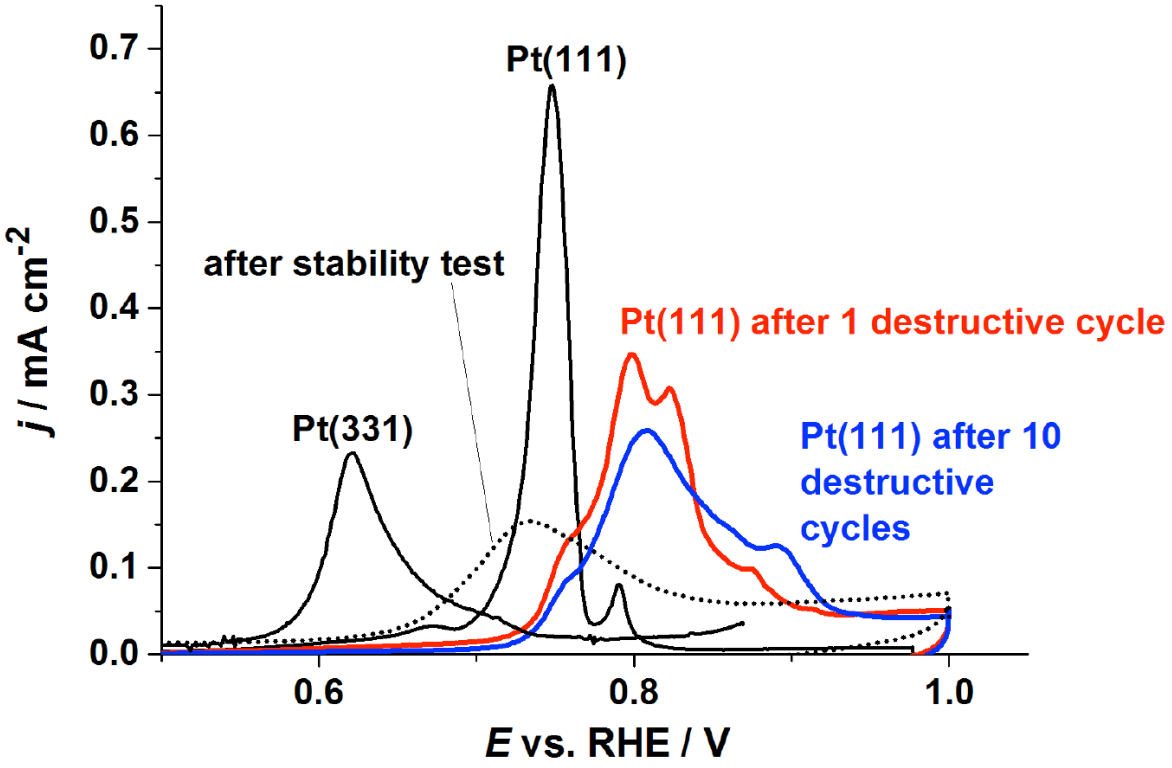

Figure 4.39: *CO-electrooxidation in Ar-saturated 0.1M $HClO_4$ on Pt(111), Pt(331) and Pt(111) treated with 1 or 10 electrochemical destruction cycles, and after the stability test. Scan rate: 50mV/s. The data were obtained in collaboration with Dr. J. Tymoczko, Ruhr-Universität Bochum, Germany and Mr. Marcus Pohl, Technische Universität München, Germany.

As expected, the CO-oxidation peak on Pt(331) (0.55-0.75V) appears at much lower potentials than on Pt(111) (0.7-0.78V). The peaks on Pt(111) after 1 and 10 electrochemical destruction cycles are shifted towards even more positive potentials (0.7-0.95V) in accordance with the aforementioned assumptions. The onset potential for CO-oxidation on these surfaces is similar to that observed on Pt(111) and the "shoulder" at *ca* 0.76V is likely due to the reaction

occurring on the Pt(111) terraces. This “shoulder” becomes smaller after 10 ED cycles, which indicates the reduction of the number of undisturbed Pt(111) surfaces after further treatment. The broad oxidation peaks in the potential region of 0.78-0.95V show that a site distribution exists among cavity sites. These all have, however, different adsorption properties from Pt(111). This *CO-electrooxidation voltammograms confirm the formation of sites with weaker *OH binding energies in comparison to Pt(111) with the electrochemical destruction treatment.

The above presented conclusions are further supported by the stability tests. The tests were performed using a Pt(111) surface subjected to electrochemical destruction by cycling the potential between 0.05 and 1.1V at a scan rate of 500 mV/s. After 500 cycles, the halfwave potential of the defective sample drops only 3-7mV. Even this small apparent degradation of activity can be potentially ascribed to the decrease in the meniscus surface area (the tests were done in HM-RDE configuration) during time due to electrolyte evaporation. AFM pictures of the electrode surface after the stability test are shown in Figure 4.40. From the AFM images, it can be observed that steps, hills and other defects appear during the testing. In Figure 4.39, one can see that the CO oxidation peak for these surfaces (dotted line) becomes broad, which indicates that several types of defects are present on the surface due to the normal-rate Pt-corrosion, such as steps, terraces, cavities, etc. While such cavities would cause an increase in activity, the appearance of undercoordinated sites (steps) would have an adverse effect on the electrocatalytic activity.

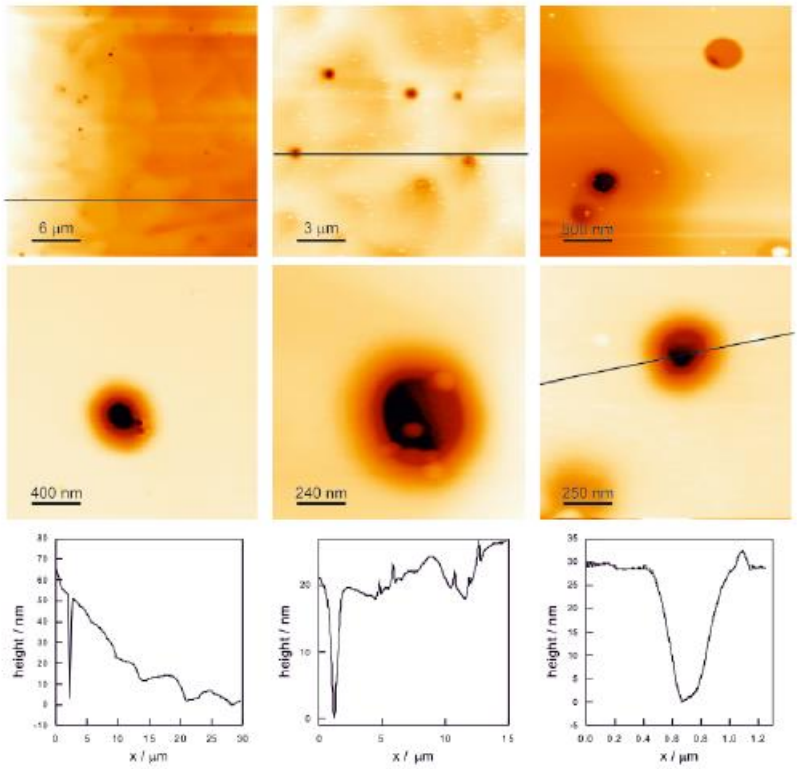

Figure 4.40: AFM pictures of the Pt(111) treated with electrochemical destruction after 500 cycles of a stability test performed by cycling the electrode in potential 0.05 - 1.1 V . Scan rate: 500 mV/s. The line scans indicated in the images are also presented. The data were obtained in collaboration with Dr. J. Tymoczko and Prof. K. Morgenstern, Ruhr-Universität Bochum.

The XPS measurements, Figure 4.41, did not show any presence of foreign metals at the electrode surface and shows that the Pt peaks in Figure 4.41 remain in nearly identical positions meaning that the average oxidation degree of Pt remains the same after the stability tests. Thus, the XPS data do not reveal any further obvious reasons for the activity increase besides the introduction of defects.

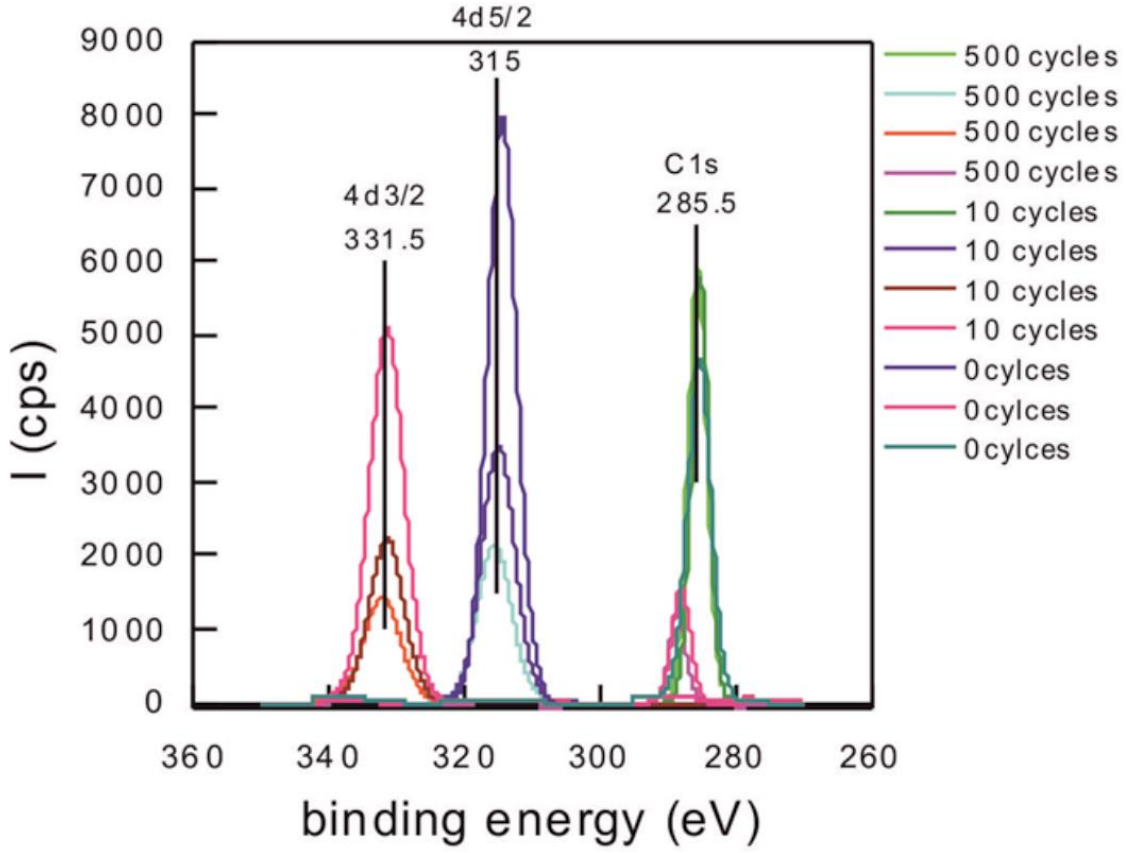

Figure 4.41: XPS spectrum showing the positions of Pt 4d peaks for the Pt(111) samples after different numbers of potential cycles as indicated in the picture. The data were obtained in collaboration with Dr. J. Tymoczko and Prof. K. Morgenstern, Ruhr-Universität Bochum.

In conclusion, the introduction of specific types of defects resulting in the creation of sites with suitable coordination is a feasible way to improve the electrocatalytic activity. Given the fact that only specific defects result in activity improvement, the development of "template" methods generating uniform surfaces with a high density of target defects is desirable. This is especially significant for the design of nanoparticulate catalysts. Convex NPs have a high number of undercoordinated sites that are not active towards the ORR, and only sites on large NPs are sufficiently similar to Pt(111). Therefore, based on the previous considerations, it can be concluded that concave NP geometries are recommendable to create sites with $\overline{CN}$=8.3[302].

4.4 The effects of the electrolyte composition

While the contribution of various "spectator species" to the electrocatalytic properties of the system is often considered negligible, a significant amount recent findings suggests that their role has been underestimated in electrocatalysis[79,93,303,304,305,306]. In addition, certain effects of electrolyte composition cannot be straightforwardly explained within the existing theories.

Experimental and theoretical investigations of the interactions between species in the electrolyte and active sites are generally not easy to conduct, due to their intrinsic dynamicity. Classical surface science techniques (such as AFM, STM, etc.) frequently fail to provide *in situ* information that is straightforward to interpret. On the other hand, theoretical quantum chemistry calculations often prove to be "too fast" (molecular dynamic) or "too static" (thermodynamic simulations) to provide deeper insight into these phenomena.

Nonetheless, experimental findings and theoretical models suggest that the composition of the electrolyte can be utilized as an additional degree of freedom in the design of electrocatalytic systems[80,81,96,97].

4.4.1 Alkali metal cations

Alkali metals are present in electrolyte solutions used for various purposes in electrochemistry, and electrocatalysis in particular (for instance pure H_2[43] and large scale Cl_2 production[307], etc.). The influence of the cations on electrochemical processes has been reported as early as in the 1930s. For instance, Herasymenko and Slednyk stated that the hydrogen overpotential on Hg electrodes depends on the nature of the cations in the electrolyte[308]. Shortly after that, Tokuoka[309] observed that the rates of the electroreduction of XO_3^- type anions were substantially influenced by (what was hypothesized to be) the adsorption of cations on the electrode surface. The subject has, however, drawn moderate interest ever since, despite the fact that it was investigated by some remarkable individuals, such as Heyrovsky and Frumkin[310,311,312,313].

Due to further advances in experimental methods and better understanding of electrocatalytic processes, the influence of alkaline cations has once again attracted a significant amount of attention in a wide range of experimental conditions[33,84,85, 86,87,88,89,90,91].

It is now accepted, that the properties of the electrode surface alone are not enough to describe fully the performance of electrocatalytic systems. Figure 4.42 presents an illustrative example for such systems: Pt and Pt/PtO_x electrodes have been widely used for ORR and chlorine evolution reaction (CER), respectively.

(A)

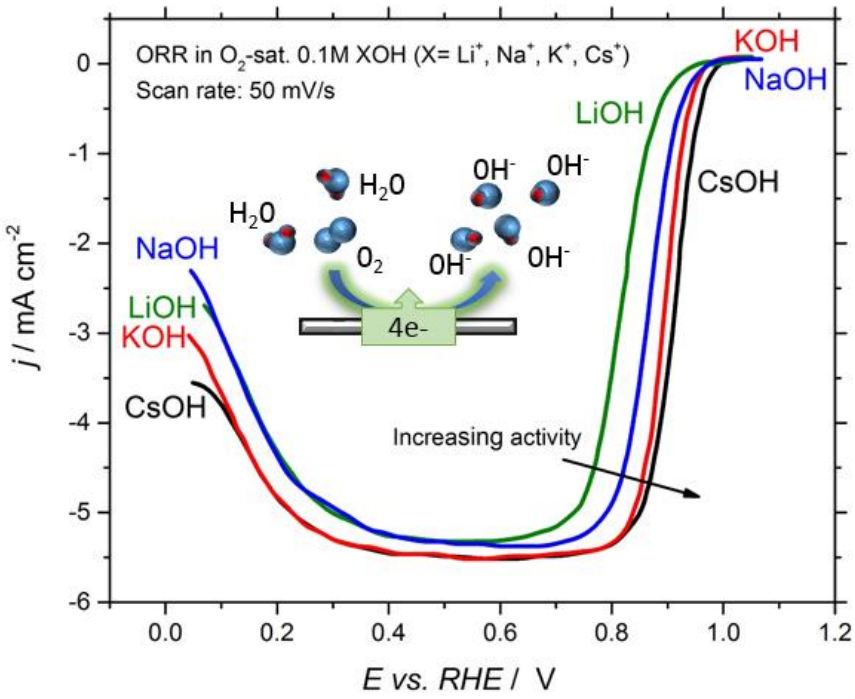

(B)

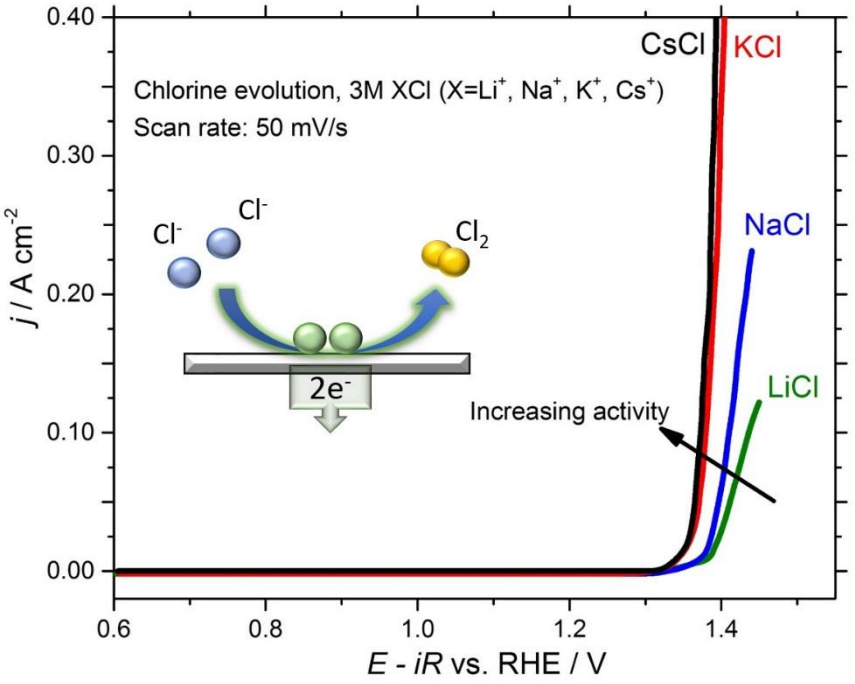

Figure 4.42: The effect of the presence of alkali metal cations on the activity of Pt-electrode (with different states of the surface) (A) CVs for the ORR on Pt(111) in O_2-saturated 0.1M XOH (X=Li, Na, K, Cs), original data are from ref. 86. (B) CVs of the chlorine evolution reaction on Pt(pc)/PtO_x in 3M XCl (X=Li, Na, K, Cs) electrolyte in HCl, pH=2. Original data are from ref. 87.

Figure 4.42, presents examples where one can clearly see that the presence of alkaline cations has a substantial impact on the electrocatalytic activity of these electrodes.

Specifically, Figure 4.42A shows that the activity of Pt(111) electrodes towards the ORR increases in the presence of alkali metal cations in alkaline media in the order: $Li^+ < Na^+ < K^+ < Cs^+$. The same trend is observed for the anodic CER at a very different pH and drastically different state of the electrode surface (under CER conditions a PtO_x layer is formed at the Pt-electrode surface), Figure 4.42B. A possible explanation of this phenomenon could be based on the proposed formation of dynamic $X(H_2O)$-adsorbate structures at the electrode surface. Since the hydration energy of the alkali metal cations increases in the order: $Cs^+<K^+<Na^+<Li^+$[314], the stability of those complexes could follow consistent trends in the same order[86,88,315].

In the case of the ORR, a possible explanation accounts for the Pt-*OH interaction, which is mainly determined by the high charge density between the surface and the OH-group. Ions such as Li^+ can likely polarize the adsorbed hydroxyl to a higher degree, thus stabilizing the envisaged complexes more in comparison to other alkali metals. The stabilized *OH can, in turn, act as a bystander and block the active sites on the surface[315]. This hypothesis can qualitatively explain why the activity towards the ORR is lowest in the presence of Li^+, and highest in the presence of Cs^+. The different stabilities of the aforementioned complexes result in different effective ion concentrations in the outer Helmholtz plane (OHP), with the highest being that of Li^+, and the lowest of Cs^+[86]. This means that the alkali cations remain in the close proximity of the electrode surface even at positive electrode potentials, consequently affecting the electrocatalytic activity.

X-ray scattering experiments have shown that the cations are located *ca* 3.5 Å from the electrode surface. This is more than their ionic radii, but less than the radii of the hydration shell, suggesting than they are only partially hydrated, in accordance with the suggested model.[316]

The trend in the case of CER can be explained accordingly. Figure 4.42B indicates that trends are similar to those observed for the ORR. In the potential region where CER takes place, the Pt-electrode is covered with a layer of non-stoichiometric Pt-oxides and hydroxides. The transition from *OH to *O covered surface is possible in this potential range as well[87]. The activity of catalysts towards CER has been linked to surface oxygenated species through the so-called Deacon process[317,318,319.320,321]. It has been indicated that the *OH-*O equilibrium needs to be reached under CER conditions[322], as these two adsorbates likely play a crucial role in the reaction mechanism[323]. The cation stabilization effect at the catalytic sites prevents the *OH groups from participating in further reactions. According to the proposed model, then, in the sequence from Cs^+ to Li^+ the cations hinder *O generation more pronouncedly, leading to the activity increase in the sequence from Li^+ to Cs^+.

Additionally, as the Cl^- ion adsorbs on the surface, one could expect similar interactions with the cations to take place in the case of this species as well. The intensity of the interactions between cations and certain surface-adsorbed species, like sulfates[324,325] and phosphates[326], has been shown to increase in the order from Li^+ to Cs^+. It is reasonable to assume that chlorides follow the same trend, in which case the stabilization of the surface-bound chloride may additionally contribute to the observed trend.

The analysis of CVs of Pt(111) in different alkali cation containing electrolytes supports the notion that the cations significantly affect the adsorption of *OH to *O on model electrodes, Figure 4.43.

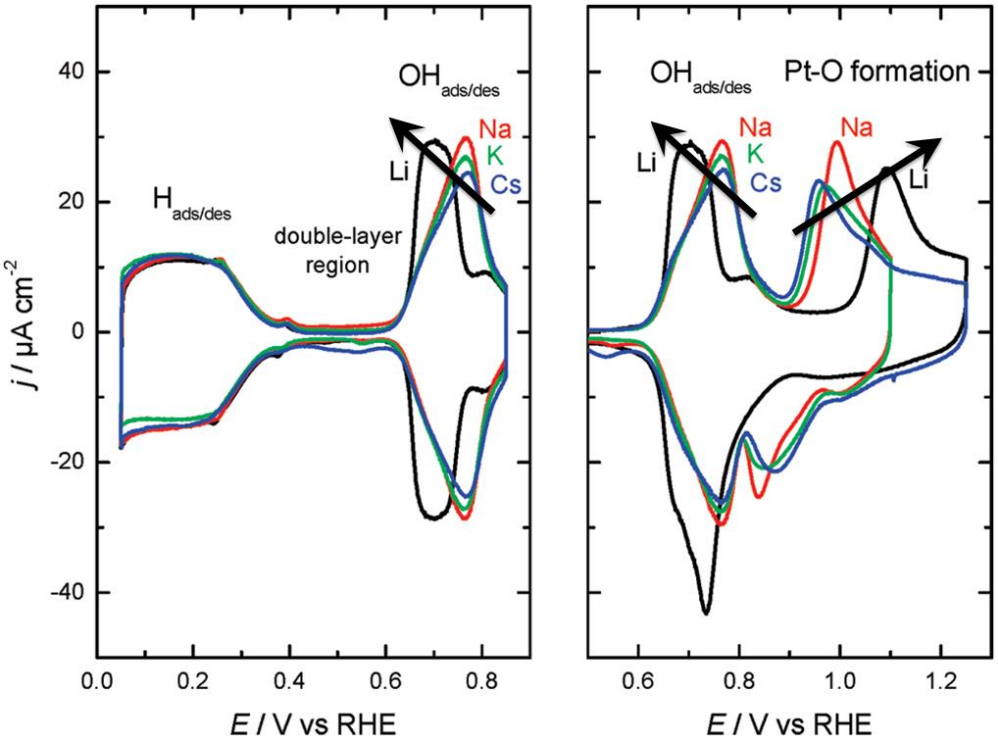

Figure 4.43: CVs of Pt(111) electrodes in Ar-saturated 0.1M XOH (X=Li, Na, K, Cs). Arrows mark the peak shifts indicating the stabilization of *OH. Scan rate: 20mV s^{-1}. Reproduced from reference 88.

The peaks in the CVs at *ca* 0.7V in Figure 4.43 are associated with OH-adsorption, while the ones at *ca* 1V with the formation of *O at the electrode surface. It is also notable, that the presence of cations affects the CV only above *ca* 0.6V, i.e., in the OH- and O-adsorption regions, while the $H_{ads/des}$ region remains largely unaffected. In the case of all four cations, the charges associated with O- and OH-adsorption are similar, showing that the amounts of oxygenated species at the surface are similar. Even though the onset potential for the OH-adsorption seems to be unaffected, the peaks of the OH-adsorption (ca 0.6V) and *O (>0.9V)[327] formation are shifted.

The OH-adsorption peaks shift towards more positive potentials, while the peaks for the formation of surface-bound oxygen shift in the opposite direction, to lower potentials, both more pronouncedly in the series from Li^+ to Cs^+. The stabilizing effect of Li^+ is particularly pronounced, resulting in a wide potential range in which the *OH adlayer exists in the presence of this cation in comparison to others, Figure 4.43, in accordance with the surface-cluster stabilization model.

DFT calculations have shown that the most favorable positions for the cations near the surface are the ones where they simultaneously interact with two distinct surface-bound OH-groups[86]. Figure 4.44 shows a schematic representation of such interactions, as well as direct

interaction with species on the surface (such as *H), though the intensity and significance of such interactions may be different.

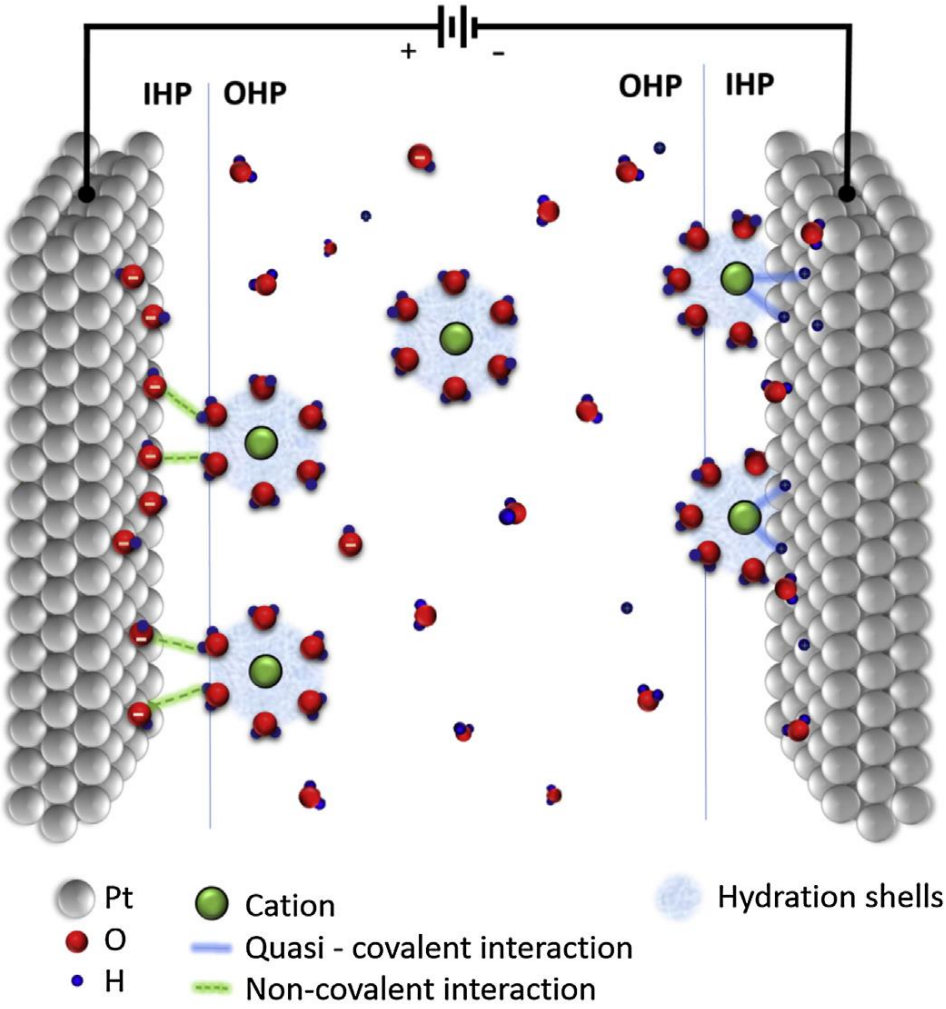

Figure 4.44: Schematic representation the proposed quasi-covalent and non-covalent interactions taking place at the electrode/electrolyte interface, according to the model suggested in reference 86. *OH-$(H_2O)_nX^+$ clusters are bound by hydrogen bonds between the water molecules in the hydration shells of the ions and two surface-bound *OH species (green dashed lines) (the left-hand side of the picture). *H-$X^+(H_2O)_n^{-1}$ clusters portraying direct interactions between the cation and two surface-bound *H (full blue lines) as shown in ref. 92, for Cs^+-specific adsorption on Pt-electrodes, and water and *H, as suggested in ref. 328. OHP – outer Helmholtz plane, containing fully hydrated ions. IHP – Inner Helmholtz plane, which contains ions with partial hydration shells. Only the first hydration shells are shown in the Figure for simplicity.

The effect of the alkali metal cations can be observed for other reaction as well. The methanol oxidation reaction (MOR) is another example of the electrode activity is impeded in the presence of Li^+, somewhat less by Na^+, and it proceeds most rapidly in KOH[86]. It is known, that in the presence of strongly adsorbing anions, the reaction may go through a different pathway in which CO is generated as an intermediate[329], meaning that the selectivity may also be altered by the electrolyte components.

CO-oxidation is known to be controlled by the *OH species; however, for this reaction *OH has a promoting effect. This implies that the activity should be proportional to the degree of *OH stabilization at the surface. Figure 4.45 shows that the expected trend is indeed observed experimentally.

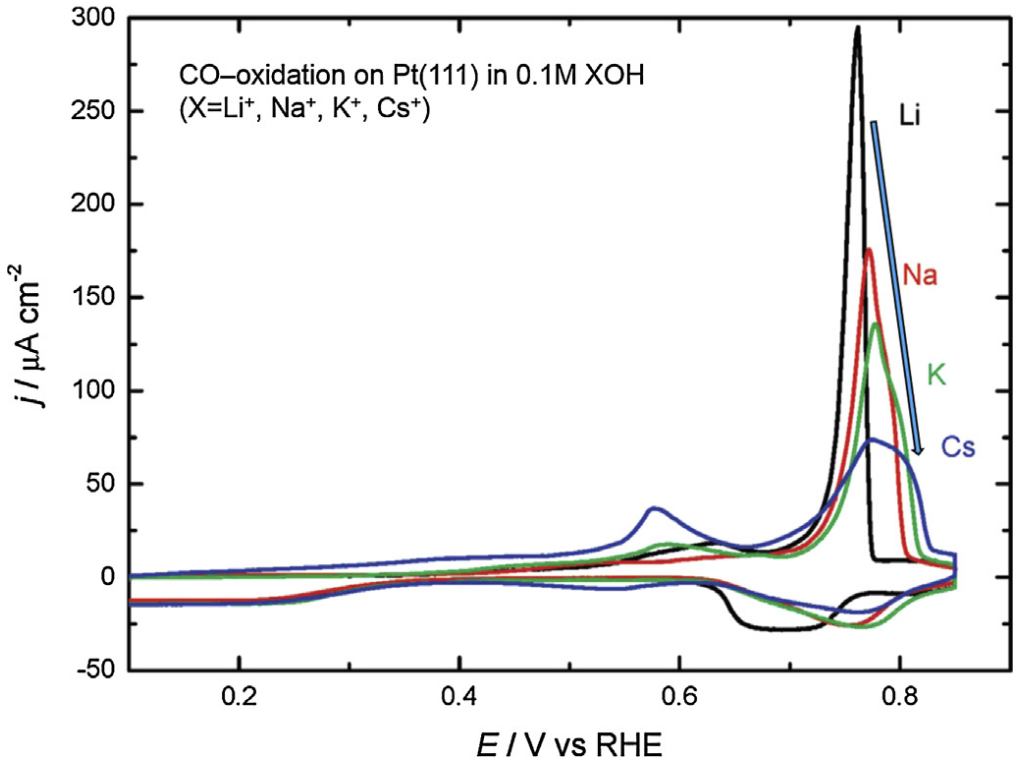

Figure 4.45: CVs of CO–oxidation on Pt(111) in 0.1M XOH (X=Li, Na, K, Cs). The potential for CO-adsorption was 0.1V. Scan rate: 20mV s^{-1}. The arrow points in the direction of decreasing CO-oxidation activity, in the sequence $Li^+ > Na^+ > K^+ > Cs^+$. Reproduced from reference 88.

While the CO stripping peak corresponding to the CO-oxidation at (111) terraces[330] appears at approximately the same potential in the presence of all four alkali cations, the broadness of the peak varies substantially. It is much narrower in the presence of Li^+ than the other ions and the CO-oxidation is indeed the fastest in the presence of this cation. It should be noted that Stoffelsma et al.[88] found that the effect of Be^{2+} on the adsorption processes on Pt is similar to that of Li^+: without any noticeable effect on hydrogen adsorption and a negative shift in the *OH-formation peak both on the steps and on (111) terraces. However, Be^{2+} introduces certain irreversibility to the *O formation process at the terraces. Both the terrace and the step-bound CO-oxidation are promoted, however, the latter less so than in the case of Li^+.

In order to quantify the influence of the cations on the electrocatalytic activity, their hydration energies have been proposed as an additional activity descriptor by several authors[86,90]. However, despite this straightforward approach, it is not trivial to elucidate the exact activity trend in a variety of cases. Figure 4.46A demonstrates that the activities of Pt(111) electrodes towards ORR, HER, and MOR in alkaline media display a quasi-linear dependency on the hydration energy of the cations. It is notable, nonetheless, that the Cs^+-containing electrolytes fall slightly off this trend for MOR.

(A)

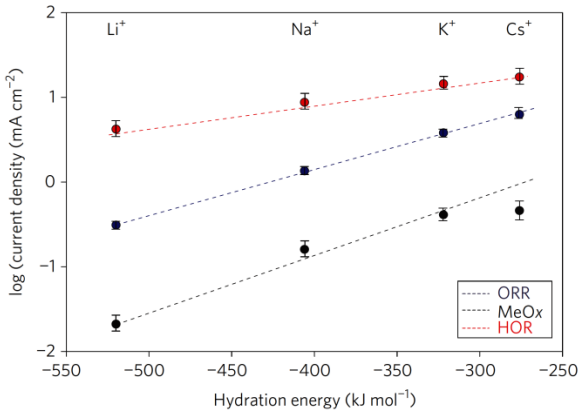

(B)

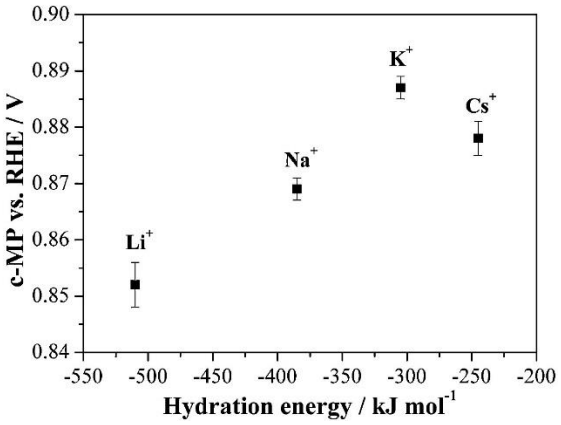

(C)

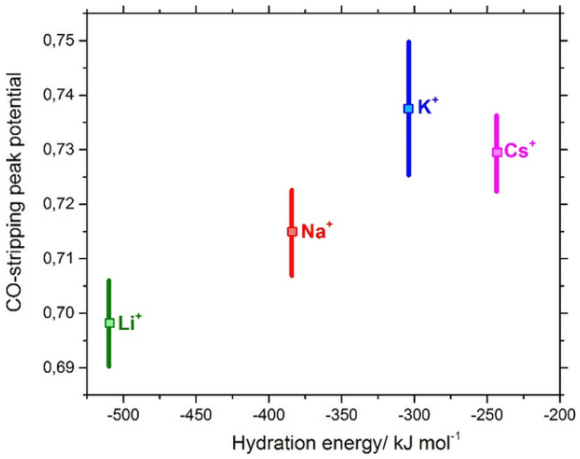

Figure 4.46: (A) The activity of Pt(111) towards the ORR (●, blue), the hydrogen oxidation (HOR) (●, red), and the methanol oxidation reaction (MOR) (●, black) in alkaline electrolytes plotted versus the cation hydration energy for the on (reproduced from reference 86). (B) ORR-corrected mixed potential (c-MP) of H_2O_2 oxidation/reduction reaction on Pt(pc) plotted versus the hydration energy of the alkali metal cations in the supporting alkaline electrolyte (reproduced from reference 90) (C) The potentials of the CO-oxidation peaks for Pt(100) electrodes plotted vs. the hydration energy of the alkali cations (adapted from reference 331).

Similar off-trend behavior of the Cs^+-containing electrolyte can be observed in Figure 4.46B as well, where the ORR corrected mixed potentials (c-MPs) for the H_2O_2 oxidation/reduction as a function of the cation hydration energy are presented. The c-MP is the potential at which the oxidation and the reduction of H_2O_2 are equally likely and it can be viewed as a measure of the intrinsic activity of the surface towards oxygenated species under the given conditions. It is generally determined as the crossing point between linear potential sweeps in the positive and negative directions at different electrode rotation speeds [332]. Remarkably, such off-trend behavior of Cs^+-containing electrolytes has been observed for cyanide-modified Pt(111) electrodes as well[85].

Van der Vliet and Koper[331] reported that in alkaline media the binding energies of the adsorbates on Pt(100) depend on the nature of cation present in the solution. However, it should be noted that in these systems the H- and the OH-adsorption cannot be easily distinguished[333]. Nonetheless, the CO-stripping activity trends shown in Figure 4.46C once again show a deviation of the Cs^+-containing electrolytes from the suggested linear dependence in a manner similar to that observed on Pt(111) electrodes.

The interpretation of activity trend is significantly less clear-cut in acidic media, especially when Rb^+-containing electrolytes are taken into account, which are otherwise often overlooked. One example of such systems is shown in Figure 4.47, in which voltammograms of HER/HOR on Pt(111) are presented in sulfuric media in the presence of alkali metal cations.

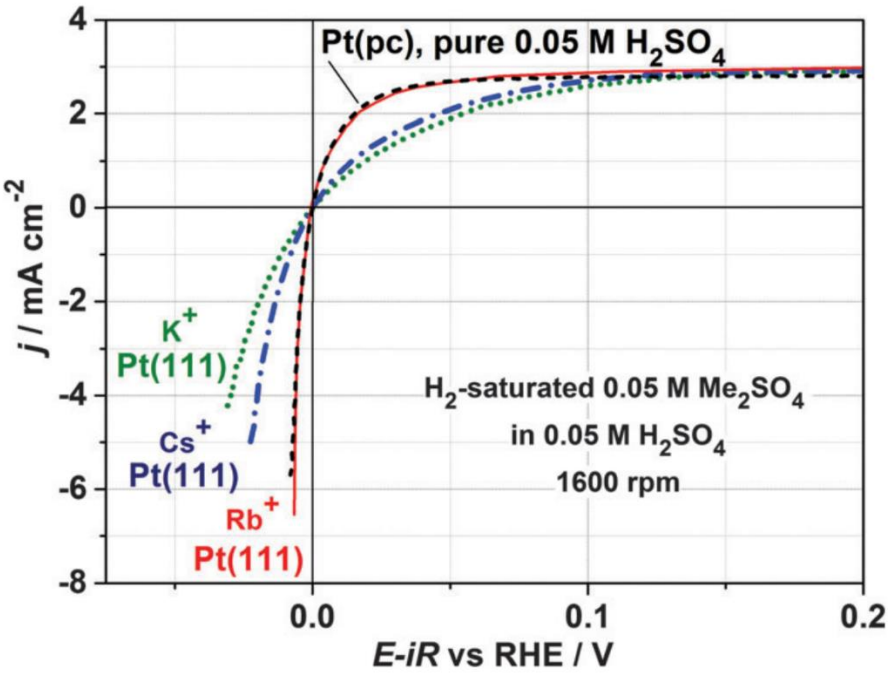

Figure 4.47: iR-corrected RDE-voltammograms characterizing HER/HOR on Pt(111) and polycrystalline Pt in H_2 saturated 0.05M H_2SO_4 and in 0.05M H_2SO_4 + 0.05M Me_2SO_4, (Me = K^+, Rb^+, Cs^+), as indicated in the figure. Scan rate 50 mV s^{-1}. The data were obtained in collaboration with Dr. J. Tymoczko and Mr. A. Ganassin, Ruhr-Universität Bochum, Germany.

The HER activity trend does not follow the increasing atomic radius nor the hydration energy trends. Despite the similar properties of the alkali elements, the Rb^+-containing electrolyte shows a distinctively high activity for the reaction.

The activity trends in acidic media are often not easily distinguishable, Figure 4.48[89] provides an overview of activity trend in alkaline metal ion containing acidic electrolytes. The adsorption of anions, e.g. sulfates, further complicates the interactions at the interface and the model illustrated in Figure 4.44 is not straightforwardly applicable. Indeed, it can be seen that the adsorption of cations can be linked to surface-specific adsorption processes[334,335].

Figures 4.48 A-C provide further evidence that the link between the alkali metal ion hydration energies and the electrocatalytic activity are not as straightforward in acidic media.

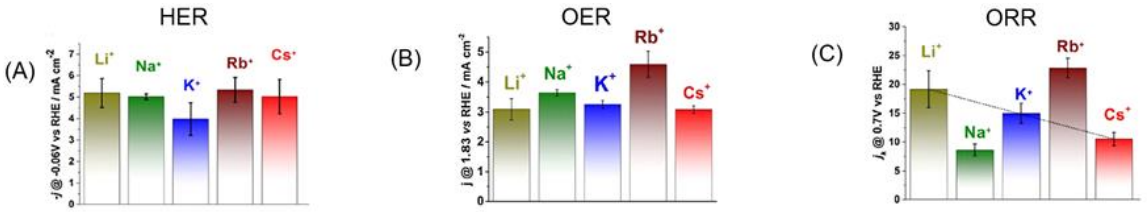

Figure 4.48: The activities of Pt(111) electrodes towards the (A) HER, (B) OER, (C) ORR in solutions containing 0.05M H_2SO_4 and 0.05M X_2SO_4 (X=Li, Na, K, Rb, Cs), saturated with H_2 (A) and O_2 ((B) and (C)). The data were obtained in collaboration with Dr. J. Tymoczko and Mr. A. Ganassin, Ruhr-Universität Bochum, Germany.

Figure 4.49A-F shows CVs of Pt(111) in Ar-saturated sulfate-containing electrolytes. The voltammograms change significantly indicating distinct tendencies for the adsorption of electrolyte components; however, it is not easy to link these tendencies to the electrocatalytic activities observed in Figures 4.48A-C. This might be at least partially due to the differences in the effects alkali metal cations exhibit on different adsorbates, e.g., sulfates and hydroxides.

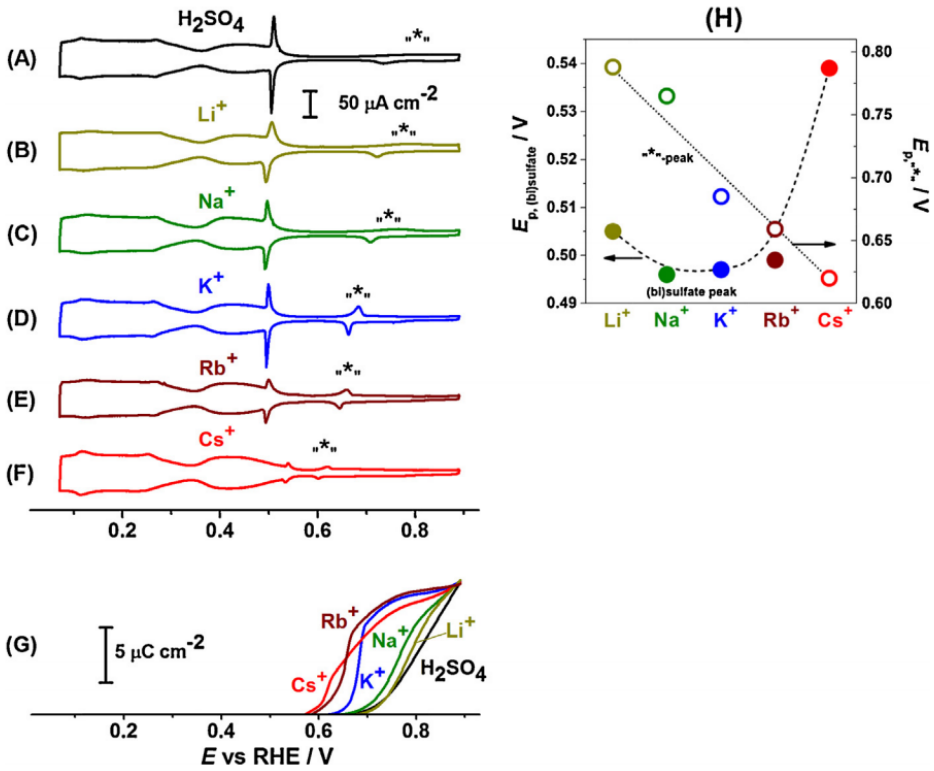

Figure 4.49: (A) CVs of Pt(111) electrodes in Ar-saturated (A) 0.05M H_2SO_4 and (B–F) 0.05M H_2SO_4 + 0.05M X_2SO_4 (X = Li+, Na^+, K^+, Rb^+, Cs^+). (G) Integrated anodic parts of the corresponding voltammograms in the potential range of 0.55V - 0.89V, corrected for the double layer charging. (H) Dependences of the positions of the anodic peaks corresponding to the "(bi)sulfate" disorder/order phase transition and further rearrangements in the adsorbate layer, "*", on the nature of the alkali cations present in the electrolyte. The data were obtained in collaboration with Dr. J. Tymoczko and Mr. A. Ganassin, Ruhr-Universität Bochum, Germany.

The hydrogen adsorption/desorption and double-layer regions seem to be only slightly affected by the presence of different cations, similarly like in alkaline media (Figure 4.49A-F). The onset potential for the phase transition in the adsorbed sulfate layer, appearing at *ca* 0.5V shifts to higher potentials and decrease in intensity in the sequence: $Li^+ > Na^+ > K^+ > Rb^+ > Cs^+$. The "hump" appearing in the potential range 0.6-0.8V, revealing further rearrangements in the adsorbate layer, shifts to more negative potentials (Figure 4.49G), indicating an increasing destabilization of the $(\sqrt{3}\times\sqrt{9})R19.1^o$ sulfate adlayer, by the alkali cations in the electrolyte with increasing ion radius.

The positions of the peaks attributed to the phase transitions represent indirect evidence about the stability of the corresponding adsorbate structures on the surface. Figure 4.49H shows the positions of these peaks in different electrolytes as a function of the potential. As the "hump" shifts gradually to lower, the "butterfly" peaks shift to higher potential from Li^+ to Cs^+, indicating that the sulfate, or alternatively the *OH[286] at the surface becomes more stabilized in this series.

Interestingly, even in the case of the HER, which takes place at potentials at which OH-adsorption is not expected, the effects of the alkali metal cations can still be observed. The "blank" voltammograms (in Ar-saturated electrolytes) also reveal marginal effects on the $H_{ads/des}$ region. However, the trend observed for HER activity is very different from that observed in the "blank" voltammograms.

The electrolytes containing Rb^+ show surprisingly high activities in comparison to those containing other alkali metal cations for several of the investigated reactions in acidic media, as demonstrated in Figure 4.48. The reason for this surprising effect of Rb^+ is yet to be explained[89]. The Rb^+ ion could possibly influence not only the activity, but also the selectivity of the system and facilitate the production of H_2O_2 in both OER and ORR.

Figure 4.50 shows a comparison of the anodic parts of the CVs characterizing the Pt(111) activity towards the ORR in O_2-saturated sulfuric media containing alkali metal cations.

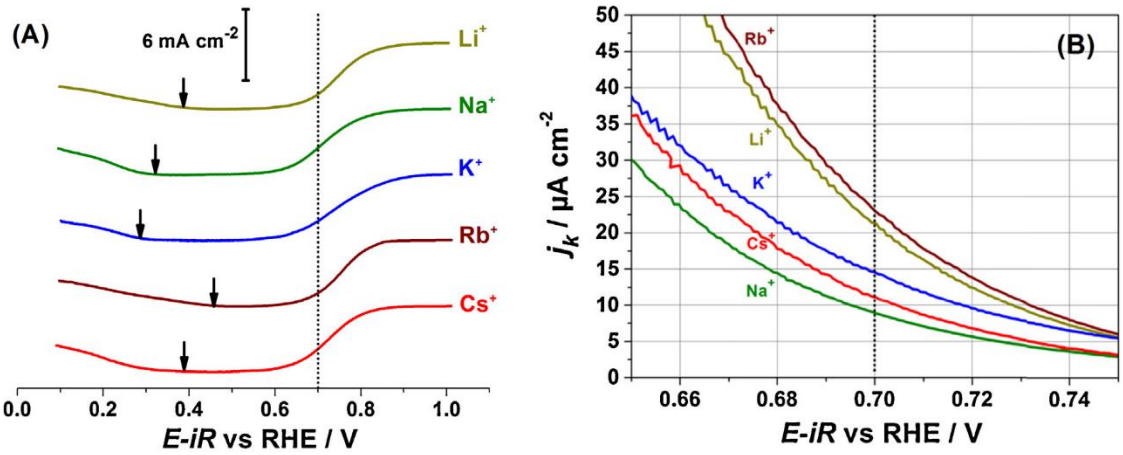

Figure 4.50: (A) Voltammograms of Pt(111) electrodes in O_2-saturated 0.05M H_2SO_4 + 0.05M Me_2SO_4 (Me = Li^+, Na^+, K^+, Rb^+, Cs^+). RDE, 1600 r.p.m. The black arrows indicate the approximate onset potentials for H_2O_2 formation. (B) The corresponding kinetic currents as a function of the applied (iR-drop corrected) potential. The data were obtained in collaboration with Dr. J. Tymoczko and Mr. A. Ganassin, Ruhr-Universität Bochum, Germany.

Comparisons of the pseudo-halfwave potentials for ORR show that the Rb^+-containing electrolytes exhibit the highest activity. Qualitatively, the onset potential for the H_2O_2 generation by the 2-electron process starts at the most positive potential in the Rb^+-containing electrolyte as well, as indicated by the black arrows in Figure 4.50A. Figure 4.50B further shows that the corresponding kinetic currents for the ORR depend on the nature of the alkali metal cations. Unexpectedly, the activity does not correlate linearly with the shift of the "hump" (Figure 4.49). While the activity drops significantly from Li^+ to Cs^+, Na^+ and Rb^+ lie outside the linear trend (Figure 4.48). In general, Rb^+ promotes ORR both to H_2O and to H_2O_2, i.e., both the four- and the two-electron process. The exact origin of this effect is not clear. Rb^+ likely induces complex interactions at the interface making straightforward interpretations difficult.

It should be noted here that the observed electrolyte effects are not easily observed on Au(100) and Au(111) electrodes[316], which is attributed to the low *OH coverage on these surfaces, and consequently lower surface concentration of the proposed complexes as well. This further reiterates the point that the electrolyte effect must always be considered together with the intrinsic properties of the electrode surface.

4.4.2 Anion and pH-effects

It is generally easier to account for anion effects in electrocatalysis, as their effects are in many cases straightforward and well understood, as they are frequently recognized as poisons of catalytic centers[95,336, 337,338,339, 340].

It is, for example, well-known that the activities of Pt surfaces towards numerous reactions decrease in the presence of sulfates, due to their specific adsorption to the active sites on the surface[75,94,341]. These, relatively straightforward cases are demonstrated in Figure 4.51.

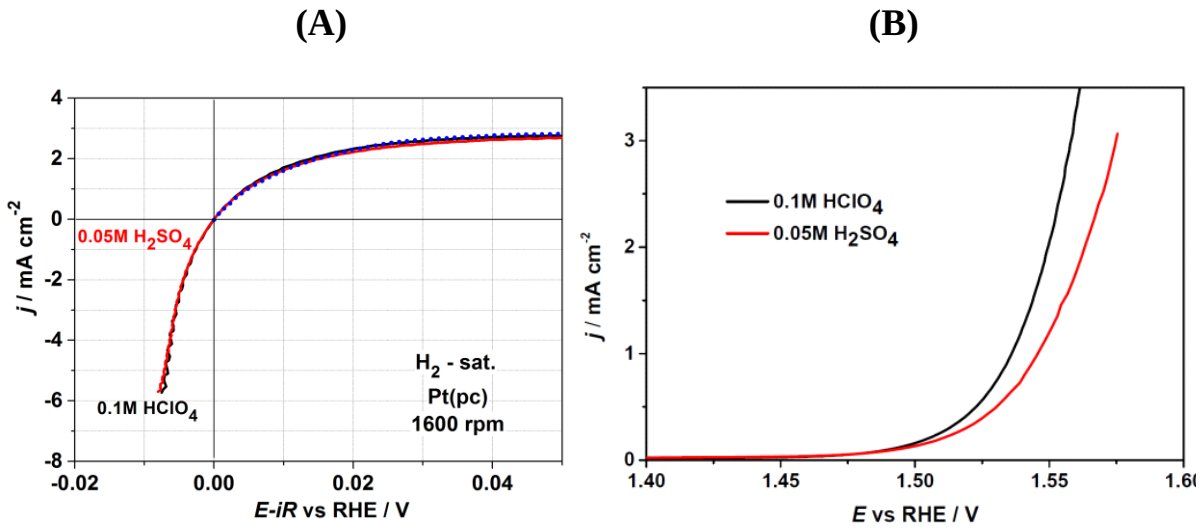

Figure 4.51: (A) RDE cyclic voltammograms of Pt(pc) electrodes in H_2-saturated 0.05M H_2SO_4 (—) and 0.1M $HClO_4$ (—) electrolytes. The dotted line (▪▪▪▪) represents the theoretical curve for the HOR under diffusion control according to the Butler-Volmer equation. Reproduced from reference 199. (B) The OER activities of Ir-oxide thin films in 0.1M $HClO_4$ (—) and 0.05M H_2SO_4 (—).The data were obtained in collaboration with Mr. A. Ganassin, Ruhr-Universität Bochum, Germany.

While the negatively charged ClO_4^- and SO_4^{2-} ions do not influence the cathodic HER taking place at negative potentials at Pt-electrodes in acidic media[199], they influence the electrode activity towards to the OER[82]. Strongly adsorbing sulfates suppress the anodic process, while weakly adsorbing perchlorates allow better activities of the iridium-oxide catalyst, Figure 4.51B. Even though two different surfaces were considered in this analysis, the anion effects were predictable by taking into account adsorption phenomena and the strength of the interactions at the surface in particular. However, a variety of pH effects are known the explanation for which is not trivial[98,99]. Reactions involving H^+ or OH^- species, as either

reactants or products, are generally expected to follow simply pH-rules in accordance with the Nernst equation[342]. For instance, this is the case for the HER and ORR: it is expected that the activities for the same electrode plotted versus the pH-indifferent RHE scale will be very similar, if not the same[343]. However, it was shown that for many processes significant for energy applications these simple rules do not apply[100,344].

Wildi et al.[345] suggested that taking into account the fact that OH-adsorption/desorption in alkaline solutions takes place at more negative potentials than it was predicted, other cations present in the electrolyte, including H^+, can easily non-covalently interact with *OH. Thus, a proton has to "remove" the cation layer before it is able to access the plane at which hydrogenation can take place. This results in an additional negative shift of the OH adsorption/desorption process. The cations will separate the reaction plane from the OHP altering the magnitude of the observed potential shift.

The pH effect can also be observed as an anion effect exhibited through the changing OH^- concentration[346]. In the following, examples are presented which illustrate the direct influence of the pH-value on reactions related to energy conversion and storage. One of the best-known examples is the non-trivial dependences are the HOR and HER activity dependences on the pH-value[157,347,348,349,350]. Expectations were that H^+-conducting membranes would be replaced by OH^--conducting membranes in PEMFCs allowing the use of more affordable catalysts, however it turned out H_2-oxidation was hindered at high pH-values. This also applies to the HER for various aqueous buffer solutions, Figure 4.52.

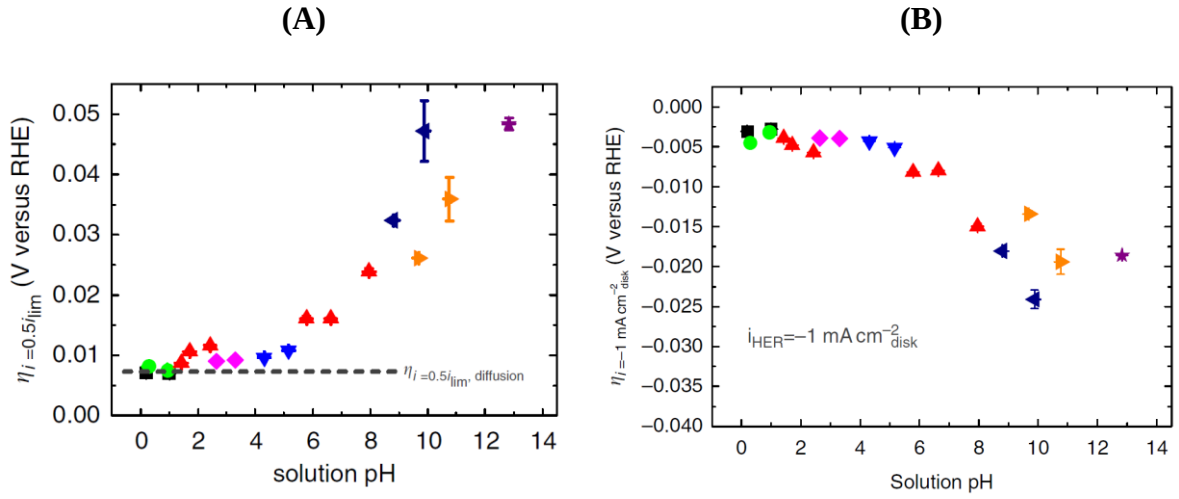

Figure 4.52: The overpotentials for (A) HOR (B) HER at Pt(pc) electrodes as a function of pH. ■ - perchloric acid (0.1M and 1M); ● - 0.1M and 1M sulfuric acid; ▲- 0.1M phosphoric acid and phosphate buffers; ▼- acetate buffers; ♦ citrate buffers; ◄ - borate buffers; ►- (bi)carbonate buffers; ★ - 0.1M potassium hydroxide solution. Reproduced from reference 351.

Some of these pH-dependences possibly involve OH-adsorption[352,353,354], which can in fact offer a qualitative explanation of the observed effects. The exact mechanism of such hydroxyl involvement is still purely hypothetical and has not been proven experimentally. An alternative explanation is based on the fact that the $H_{ads/des}$ region is affected on non-uniform Pt-surfaces,

such as Pt(pc). It has been suggested that the hydrogen binding energy is affected by the pH[351]. However, it is clear that further theoretical and experimental work is required to offer a suitable descriptor for the HER and HOR.

Certain pH effects on the ORR activities of certain non-uniform metal surfaces are arguably even more surprising. For instance, the Pt(331) surface, while being one of the most active ones in acidic media, demonstrates one of the lowest activities in alkaline solutions[59]. The OH-binding energy, which is a straightforwardly applicable activity descriptor in acidic solutions, is not easily applicable in an alkaline electrolyte. One of the suggested descriptors is the angle of the surface normal with respect to Pt(111) electrodes, i.e., "crystal orientation", which indeed allows the construction of a volcano plot[59]. The problem of *OH or *O and competition for the active sites, it appears, is not the only problem appearing in the ORR mechanism. The nature of the species adsorbed at the electrode surface or the charge at the interface can modify the electrode activity as well. The oxidation of peroxide, a potential intermediate in the ORR, could be a bottleneck in the process[184,355]. Unfortunately, there are currently no definite explanations for these pH-effects within the current theoretical framework.

It is of course, not always possible to decouple pH effects from those originating from alkali metal cations, e.g., in order to develop high-pH media one inevitably introduces alkali metal cations to the system as well. In such cases, it may be difficult to pinpoint the origin of certain effects. Nonetheless, the development of models explaining these phenomena is of great importance for the more detailed understanding of electrocatalytic systems.

4.4.3 Overcoming the limitations of aqueous electrolytes

Aqueous electrolytes are widely used in electrocatalysis (and chemistry in general) due to their affordability, but also for historic reasons. Nonetheless, aqueous electrolytes, while being by far the most common reaction media, can be disadvantageous in certain cases. Among these disadvantages, one can count the unwanted pH-effects and specifically adsorbing ions, as discussed previously.

Among the alternative solvents gaining esteem in modern electrocatalysis, ionic liquids are of special interest. Ionic liquids were discovered by Paul Walden in 1914[356]. Typically, they consist of an organic anion and a cation, and the resulting compound remains liquid at room temperatures due to charge delocalization in their constituent ions and steric effects that make it easy to overcome the lattice energy[357]. These compounds possess good ionic conductivity, enabling their application in electrochemistry. The behavior of ionic liquids near the electrode/electrolyze interface is still under debate with numerous papers published on the topic, as reviewed recently by Fedorov and Kornyshev[358].

The use of ionic liquids (ILs) in electrocatalysis, of course, has its advantages and disadvantages. Importantly, they allow the operation of electrocatalytic systems at higher temperatures, which often leads to enhanced reaction rates. Their ionic conductivity can be controlled as well as they usually exhibit a linear dependence of conductivity on temperature. Importantly, it is possible to widen the electrochemical stability window by several volts[359]. This makes it possible to run reactions that are not possible in aqueous media due to the

domination of HER or OER. Additionally, due to the variety of anions and cations capable of building ionic liquids, the choice of electrolyte is significantly broadened. This allows the choice of the anions and cations in a way to minimize their effects on the educts, intermediates, or products[360,361]. The latter, unfortunately, cannot be always achieved; instead, the poisoning of the catalytic sites can occur[362].

This allows the use of the composition of the IL as an additional degree of freedom in the design of the electrocatalytic system. For instance, it has been reported that ILs can change the selectivity of a system, even when mixed with aqueous electrolytes. Figure 4.53 shows an example of such a case for the OER in aqueous NaOH and butylammonium sulfate (BAS).

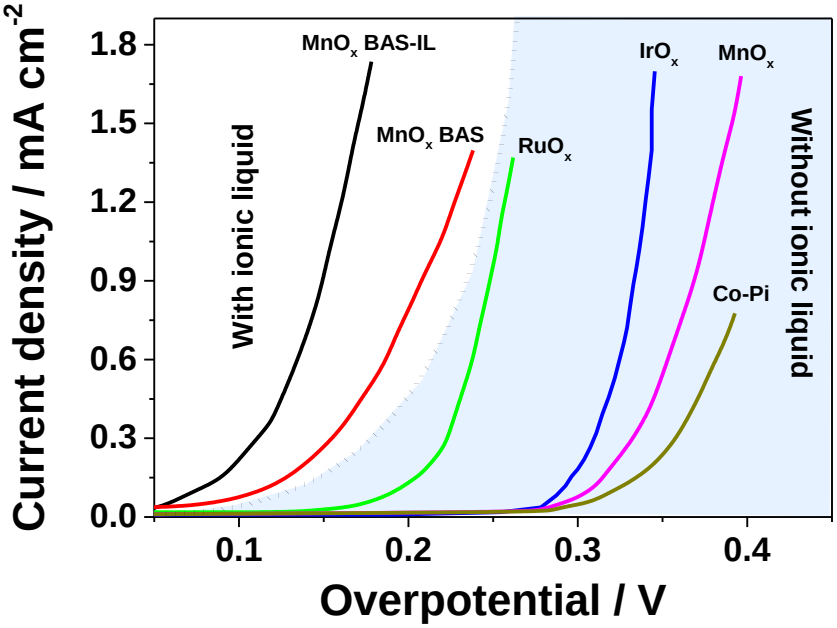

Figure 4.53: Anodic parts of CVs characterizing the activity of various metal-oxide catalysts towards the OER in 1M NaOH (RuO_x (—), IrO_x (—), MnO_x (—), and Co-Pi cobalt-phosphate (—)) and in ionic liquid - 0.4 M di(butylammonium) sulfate (BAS / pH=10) (—) (MnO_x BAS) and 2M BAS (MnO_x BAS-IL) (—). Adapted from reference 363.

The main product of the OER in aqueous electrolytes is gaseous O_2. However, if butylammonium-sulfate (BAS) is present in the electrolyte, it possibly changes the reaction selectivity towards the generation of H_2O_2. Importantly, this change in selectivity results in the reduction of the overpotential, as seen in Figure 4.53, and it is promising strategy for the reduction of energy losses in, e.g., alkaline electrolyzers. At a given overpotential, the electrolytes containing the hydrated ionic liquid display the highest currents. The formation of solvated H_2O_2 seems to be the rate-determining step in this medium. It has been shown that ethylamine molecules can stabilize H_2O_2 at the electrode surface. The suggested H_2O_2-ethylamine complexes are *ca* 13 kJ mol^{-1} more stable than the hydrated hydrogen peroxide. In general, one H_2O_2 molecule can be stabilized by four individual ethylamine molecules. Therefore, the high concentration of IL should promote hydrogen-peroxide formation.

Somewhat lower yields of H_2O_2 have been observed experimentally (64%), which may be caused by the loss of H_2O_2 through the standard disproportionation reaction[364].

In order to investigate the origin of the reduction of the overpotential in the IL electrolyte observed in Figure 4.53, the MnO_x catalyst was replaced with CoO_x and NiO_x, which are catalysts relevant for industrial applications. Figure 4.54 shows the CVs of NiO_x (A) and CoO_x, (B) in K_2SO_4 or BAS, at pH=10.

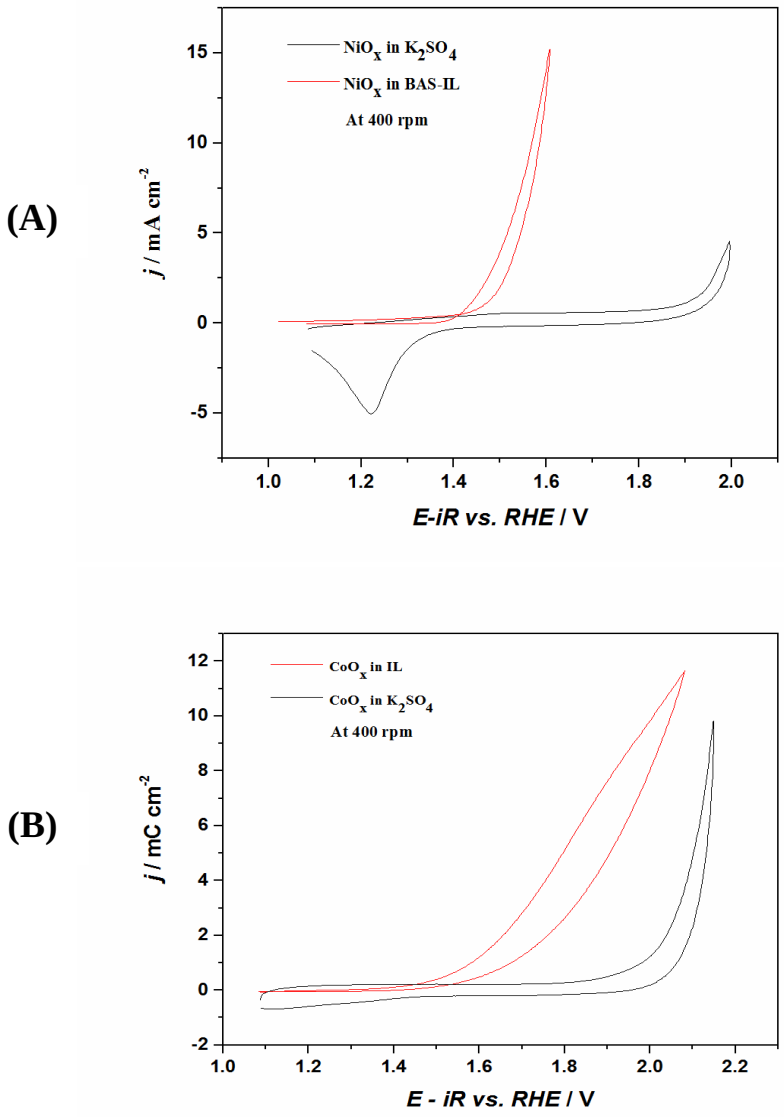

Figure 4.54: The comparison of the activities of (A) NiO_x and (B) CoO_x towards the OER at 400 rpm in 0.4M BAS (BAS-IL) and aqueous solution of K_2SO_4 at pH=10.

The fact that the effect is reproducible with other metal-oxide catalysts as well indicates that it is the electrolyte composition that allows the reduction of the overpotential, possibly by changing the selectivity towards the formation of H_2O_2. In order to further elucidate the processes taking place in BAS, RRDE measurements were conducted by cycling the potential

of the disk-electrode in the potential range of 1.05-1.55V, while keeping the ring Pt(pc) at 1.3V, where H_2O_2 oxidation takes place. The preliminary results are shown in Figure 4.55.

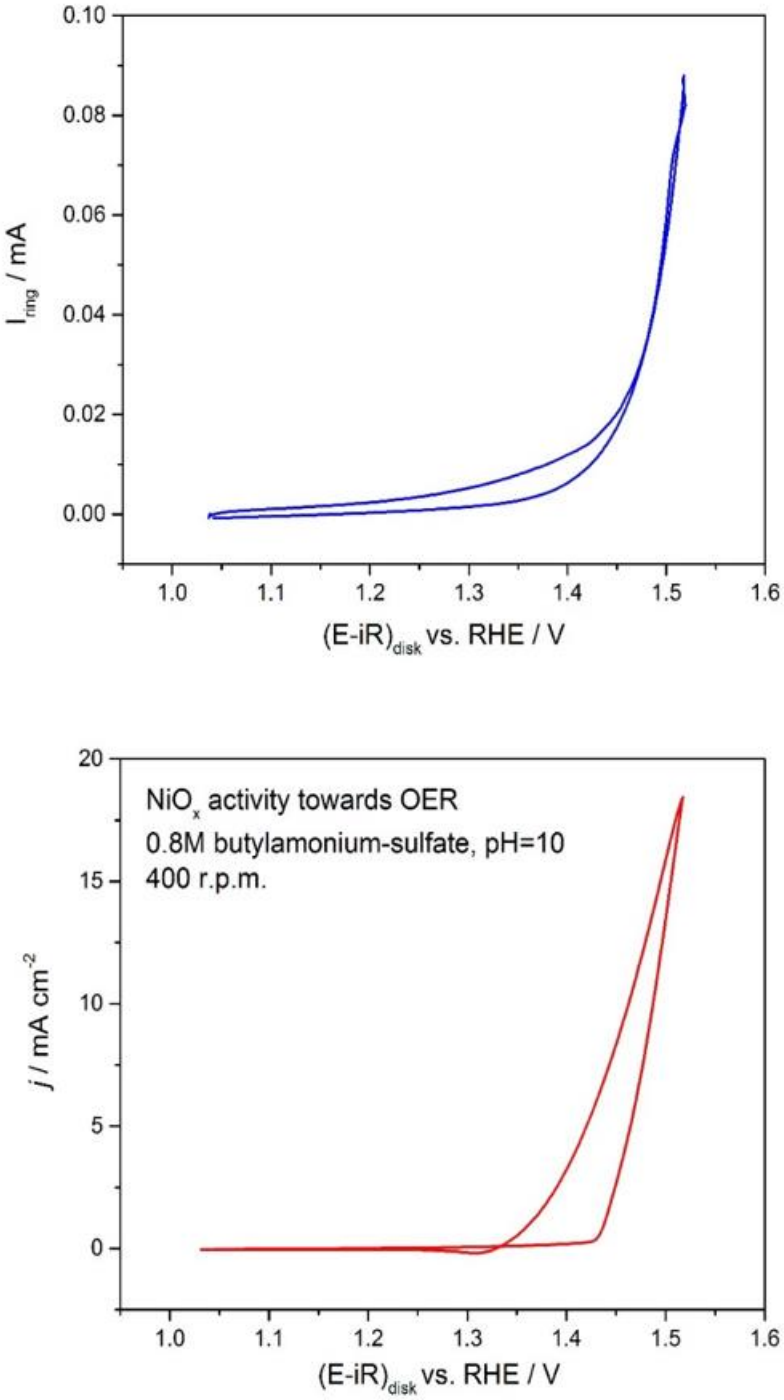

Figure 4.55: RRDE CV of NiO_x (disk) in 0.8M BAS, pH=10 (below) with the ring current on the Pt(pc) ring (above). CV scan rate on disk: 50 mV s^{-1}. RDE, 400 r.p.m. E_{ring}=1.3V.

The emergence of the ring current at disk potentials at which water splitting occurs on the disk offers further indication that H_2O_2 is generated. However, further experimental verification is required to clarify the nature and the source of this effect, and prove that H_2O_2 is generated

at the NiO_x disk electrode, and the currents do not appear due to unwanted side effects, e.g. chemical changes of the IL itself.

While the exact origin of these effects remains elusive for the time being, the presence of the IL has major impact on the activity trends of metal-oxide electrodes towards the OER, as illustrated in Figure 4.56.

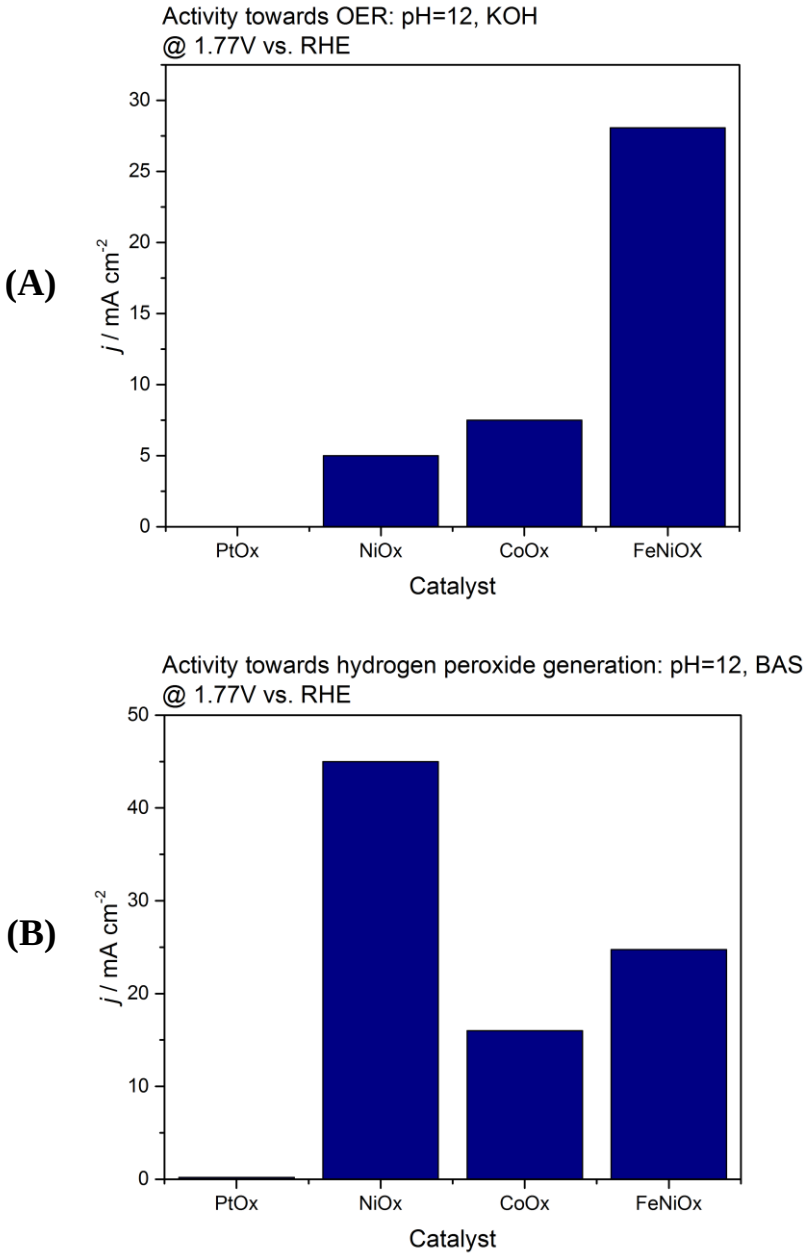

Figure 4.56: Activities of metal-oxide electrodes towards the OER in (A) aqueous 0.4M K_2SO_4 (B) 0.4M BAS. pH=12, set with KOH. The activities are represented as current densities at 1.77V. RDE, 400 r.p.m.

In the aqueous electrolyte, Figure 4.56A, the activities towards OER increase in the order PtO_x < NiO_x < CoO_x < $FeNiO_x$. However, in the presence of the IL (4.56B), the order of activities changes and NiO_x is the most active catalyst, as its activity increases by an order of

magnitude. It is interesting to note that the activity of CoO_x increases as well, but by a much smaller margin, while the activity of the $FeNiO_x$ catalyst remains approximately the same in both electrolytes.

It is interesting to note that it is common that ionic liquids change the OER/ORR selectivity towards peroxide formation. For instance, one if the main ORR products on the cathode in Li-air batteries is superoxide, which is slowly converted to Li_2O_2 in ionic liquids. The accumulation of the product on the electrodes, however, is not desirable.

In acidic aqueous electrolytes, such as H_2SO_4 and $HClO_4$, the ORR mechanism can vary between a two-electron and a four-electron path with hydrogen-peroxide and water as the main products, respectively[365,366]. The effect of the electrolyte composition is even more pronounced in ionic liquids. In certain aprotic, anhydrous ILs the oxygen is reduced *via* a one-electrode process to a superoxide radical, which is readily protonated to H_2O_2 in the presence of protonic impurities[367]. In contrast, in certain protic and wet aprotic ILs the reduction proceeds through two irreversible steps involving the transfer of one electron each. In the first, one superoxide is formed, which is then protonated and subsequently further reduced to HO_2^- [368,369].

These changes between different reaction paths have a direct impact on the kinetic and thermodynamic parameters of the electrocatalytic reactions. It has been shown that the composition of the ILs strongly influences the ORR activation energy, enthalpy of O_2 dissolution, and the activation energy for O_2-diffusion. All these parameters are vital for the real-world applications of ILs, such as PEMFCs or metal-air batteries, and can be used to target the desired reaction path.[370]

A reaction path that entails the formation of water can be problematic in certain cases, as it can alter certain crucial parameters, such as viscosity or proton availability. This can further alter the kinetic and thermodynamic parameters of the system. This might necessitate constant water management to keep the system stable[371,372,373].

A promising approach for the implementation of ILs is their use either as a thin layer (e.g., SCILL - supported catalyst ionic liquid layer[374]) or small droplets at the electrode surface, as this can lead to an increase in electrocatalytic activity. In such cases, the IL film is in direct contact with the aqueous electrolyte as well as the electrode surface, thus creating two new phase boundaries. The new boundaries result in a change of thermodynamic and kinetic parameters[374].

The interface between the IL and the aqueous electrolyte is particularly elaborate, as the different ionicities in the aqueous electrolyte and the IL layer can have a strong influence on the diffusion of different species[375]. Furthermore, the presence of strong electron donors may be in itself sufficient to facilitate the formation of H_2O_2 at the IL/H_2O interface even without the application of potential[376].

While the use of ILs in electrocatalysis holds many promising prospects, it must be recognized that it is still a rather young field and not as developed as one might expect based on the numerous encouraging findings[377,378].

5. Summary and outlook

The focus of this thesis was on elucidating the link between the status of the electrode/electrolyte interface and the electrocatalytic activity, selectivity and stability. In that respect, several methods were developed in which the manipulation of the electrode material, surface structure, or electrolyte composition results in tunable changes in the electrocatalytic properties.

In Section 4.1, the experimental aspects of accurate activity benchmarking were considered. The importance of the establishment of widely accepted experimental protocols, which would allow the more meaningful comparison of data collected by different groups under different conditions, is emphasized. The iR-drop correction, issues arising from the evolution of a non-conducting gas-phase, and the estimation of the real electrode surface area were particularly focused on. It was found that while some authors consider the Ohmic drop negligible, or report erroneous procedures, it has a key impact on the results. EIS is a convenient tool for the implementation of the iR-drop correction. However, the procedure should be performed carefully, taking into account hardware issues, issues related to the electrolyte composition, and emerging gas phase. It was further demonstrated that the fitting of the EIS results to physical models additionally reduces the errors in the determination of the measured resistance. Furthermore, systems with gas evolution present additional challenges for activity benchmarking. For these systems, it is of special importance to perform the iR-drop corrections under conditions as close to real experimental ones as possible, as the uncompensated resistance depends on the applied potential. In the case of gas-evolving electrodes, particularly oxide catalysts for the OER, a rotating microelectrode setup is proposed to assess their activities meaningfully at currents relevant for the real-world applications. Finally, the assessment of the real active surface area of the electrode is another crucial step in the acquisition of accurate experimental results. By choosing the surface limited reaction by which the surface area is determined cautiously, the acquisition of correct data on electrocatalytic activities can be assured and errors due to changes in the electrode/electrolyte interface can be avoided. In order to ensure a precise assessment of the electrocatalytic activity of Pt-alloy electrocatalysts it is proposed to use Cu underpotential deposition instead of hydrogen underpotential deposition and CO-oxidation, which are currently used for these purposes in the literature.

Section 4.2 discusses the effects of the electrode material, and reports the results on the engineering of new active electrocatalytic surfaces and on the understanding of the catalytic trends in Pt-alloy ORR electrocatalysts. While the significance of the electrode composition has been known since the early stages of electrochemistry, the behavior of many materials and the source of their electrocatalytic properties still require elucidation. Section 4.2.2 deals with bulk Pt-alloys with 3d-transtion metals and lanthanides, which are well-known catalysts for the ORR. In the case of such complex surfaces, it is particularly desirable to link the electrocatalytic activity to structural, rather than energetic descriptors. From the literature data that is summarized, it is shown that a variety of experimental findings related to single crystal Pt-alloy electrocatalysts can be explained in the existing theoretical framework. However, this is not the case for polycrystalline and nanoparticulate systems. Nonetheless, it is demonstrated that it possible to define empirical trends, which can be linked to structural variables - namely, the radius of the alloying, “solute”, element that likely statistically determines the maximal lattice

strain introduced to the Pt-rich shell, which in turn determines the electrocatalytic activity. Furthermore, the radius of the "solute" element is suggested as a simple structural descriptor that can be used to explain and, within a certain outline, tentatively predict the behavior of such alloys.

In Section 4.2.3, the activity of surface and near-surface alloys were the focus of the research. Firstly, the effect of Nafion on the performance of model Cu-modified Pt(111) electrocatalysts was investigated (4.2.3.1) by electrochemical techniques in combination with DFT calculations. It was demonstrated that subsurface alloying with Cu not only increases the activity of Pt(111) electrodes towards the ORR, but also prevents catalyst poisoning by electrolyte components relevant for PEMFC applications - the sulfonate groups. The results indicate that the specific adsorption of sulfates and sulfonates on the Pt(111)/Cu NSAs is suppressed, resulting in a significant increase in the ORR activity in 0.05M H_2SO_4, while in 0.1M $HClO_4$ it exhibits the same activity with and without the polymer. Secondly, stability tests of Pt(111)/Cu NSA catalysts were conducted in concord with DFT calculations. It was found that subsurface Cu weakens the binding of the (111) terraces and step-defect sites on Pt-electrodes, resulting in the increased stability of these surfaces against anodic degradation, compared to bulk Pt-Cu alloys and nanostructured materials. After more than 50h of cycling in the potential range of 0.05-1V, around 50% of the initial amount of Cu remained in the subsurface region. The appearance of the "butterfly" voltammetric features after the stability tests suggests the formation of quasi-ordered Pt(111) facets and Cu-Pt(111) NSA during Cu-dissolution.

The focus is the shifted towards the influence of the surface morphology on the electrocatalytic activity in Section 4.3. The generalized coordination number is introduced as a structural activity descriptor and its applicability for a Pt-catalyst design for the ORR is demonstrated. Using the GCN, it is possible to construct "activity-coordination volcano plots" that can be used to predict the optimal geometry of the active sites. The method is then demonstrated on ORR catalyzed by Pt. Sites with the same number of first-nearest neighbors as Pt(111), but an increased number of second-nearest neighbors are predicted to have an enhanced ORR activity. The rationale was then used to create surfaces with such sites on Pt(111) using several electrochemical techniques, such as electrochemical destruction, Pt-Cu NSA dealloying, and galvanic displacement. Curiously, all surfaces with defects introduced in the aforementioned ways displayed an increase in activity towards the ORR. The most active surface, formed by several cycles of electrochemical destruction, showed an activity *ca* 3.5 times in comparison to Pt(111), which cannot be explained by the slight increase in the active surface area (max. 15%), but certainly is the result of defect formation.

Finally, Section 4.4 was dedicated to the elucidation of the electrolyte effect on the electrocatalytic activity and selectivity. While the importance of the electrolyte composition for heterogeneous electrocatalysis has been known for more than seventy years, its modelling and the quantification of its impact is often not trivial. Considering the dynamicity of the electrode/electrolyte interface, it is of great significance to develop both experimental and theoretical methodologies for the description of these systems. The testing and development of existing theories capable of predicting the influence of various species on the activity and selectivity of electrocatalytic centers is also vital for the advancement of electrocatalysis. The

electrolyte composition can be considered an additional degree of freedom in the design of electrocatalytic systems. It was shown that the presence of alkali metals can affect the activities of ORR, HER, HOR, and OER. While the explanation for this phenomenon in certain cases (e.g., ORR in acidic perchloric, or CER in alkaline basic media) seems to be relatively straightforward, employing the suggested formation of the surface complexes (Figure 4.44), in several other cases (e.g., HER or OER in acidic sulfuric electrolyte) the changes in the intermediate binding trends caused by the presence of alkali cations cannot be directly linked to the electrocatalytic activity. This is likely due to the complexity of the interactions taking place at the interface in such system, which prevents the formulation of straightforward explanations. The introduction of ionic liquids likely leads to changes in the selectivity of metal-oxide catalysts towards the ORR. Still, the development of explicit and simple "activity descriptors" is necessary for the rational exploitation of the electrolyte effects. In this work, it has been shown that not only is the effect of the electrolyte not negligible, but in many cases it is an important factor determining the electrocatalytic properties of the system. There are strong indications that the electrolyte composition can change not only the activity, but also the selectivity of the electrocatalytic system (such as in the case of Rb^+ or BAS).

Overall, the experimental results presented in this study show that the modification of the electrode material, surface morphology, and electrolyte composition can be used to manipulate the activity, selectivity, and stability of electrocatalytic systems. However, for the implementation of these effects to their full potential in the rational design of catalysts, further experimental and theoretical efforts are necessary. Primarily, the development of suitable, easily assessable, activity descriptors is of paramount significance. The energetic volcano plots can only identify the surface with ideal energetic properties, however, they can say very little about the exact nature of the sites that would possess such properties. The formulation of structural activity descriptors, instead of energetic ones, would allow the direct definition of the most suitable local compositions and/or geometries of the active sites. Furthermore, the definition of well-defined activity descriptors for the electrolyte is yet to be achieved.

While the formulation of a coherent theoretical framework that would allow the complete rational design of an electrocatalytic system still requires significant advances in both experimental data collection and theoretical understanding, in this work the applicability of catalyst performance modification *via* the manipulation of the electrode/electrolyte interface status is demonstrated for several specific cases. These cases display how the fine-tuning of the electrocatalytic activity, changing of the selectivity, and improvement of the catalyst stability are achievable by the means of changing the electrode material composition, surface morphology of the electrode, and the electrolyte composition.

Appendix A: Symbols and abbreviations

a – activity
ac – alternating current
AFM – atomic force microscopy
AIROF – anodically formed iridium oxide film
aq – aqueous solution
BAS – butylammonium sulfate
BET – Brunauer-Emmett-Teller theory
C – capacitance
C_a – adsorption capacitance
C'_{dl} – factor related to the double-layer capacitance
CA – chronoamperometry
CE – counter electrode
CER – chlorine evolution reaction
cn – coordination number
CNT– carbon nanotubes
CPE – constant phase element
CV – cyclic voltammetry
dc – direct current
DFT – density functional theory
e – elementary charge
E – potential
E_0 – potential at zero current
E_a – anode potential
E_c – cathode potential
E_D – decomposition potential
E_d – disk electrode potential
E_{eq} – equilibrium potential
E_r – ring electrode potential
EEC – equivalent electric circuit
EIS – electrochemical impedance spectroscopy
EQCM – electrochemical quartz-crystal microbalance
F – Faraday constant
f – frequency
FC – fuel cell
fcc – face centered cubic
G – Gibbs free energy
GC – glassy carbon
GCN – generalized coordination number
GD – galvanic displacement
GDL – gas diffusion layer
g – gas
GHG – greenhouse gas
h – Planck constant
hcp – hexagonal close packed crystal structure
$H_{ads./des.}$ – hydrogen adsorption/desorption
HM – hanging meniscus
HOR – hydrogen oxidation reaction
HER – hydrogen evolution reaction
IAEA – International Atomic Energy Agency

IEA – International Energy Agency
I – electric current
i_a – anodic current
i_c – cathodic current
ICE – internal combustion engine
IHP – inner Helmholtz plane
IL – ionic liquid
Im[Z] – imaginary part of the complex number Z
j – current density
j_a – anodic current density
j_c – cathodic current density
L – inductance
l – liquid
m – mass
M – molar mass
MEA – membrane electrode assembly
ML – monolayer
MMS – mercury-mercurous sulfate reference electrode
N_A – Avogadro's number
NASA – National Aeronautics and Space Agency (USA)
NP – nanoparticle
NSA – near-surface alloy
OCP – open circuit potential
OECD – Organization for economic co-operation and development
$OH_{ads./des.}$ – hydroxyl adsorption/desorption
OHP – outer Helmholtz plane
OER – oxygen evolution reaction
ORR – oxygen reduction reaction
pc – polycrystalline
PEM – polymer electrolyte membrane
PEMFC – proton exchange membrane fuel cell
q – electric charge
Q – electric charge
R – universal gas constant
R – resistance
R_a – adsorption resistance
R_{ct} – charge transfer resistance
R_e – external resistance
R_i – internal cell resistance
RDE – rotating disk electrode
RE – reference electrode
Re[Z] – real part of the complex number Z
redox – oxidoreduction
RME – rotating microelectrode
r.p.m. – rotations per minute
RRDE – rotating ring-disk electrode
RHE – reversible hydrogen electrode
SA– surface alloy
SHE – standard hydrogen electrode
SOFC – solid oxide fuel cell
STM – scanning tunneling microscopy

T – temperature
t – time
UPD – underpotential deposition
WE – working electrode
WWS – Water, Wind, Sunlight
XPS – X-ray photoelectron spectroscopy
z – valence number
Z – impedance
α – transfer coefficient
ε – gas phase fraction
η – overpotential
φ – Galvani potential
φ_0 – standard Galvani potential
ϕ_w – work function
μ – chemical potential
$\tilde{\mu}$ – electrochemical potential
υ – stoichiometric coefficient
Θ – surface coverage
ω – angular frequency

Appendix B: Publications

1. V. Čolić, A.S. Bandarenka, *Pt-Alloy Electrocatalysts for the Oxygen Reduction Reaction: From Model Surfaces to Nanostructured Systems,* ACS Catalysis, 2016, 6, 5378-5385. DOI:10.1021/acscatal.6b00997.

2. A. Ganassin, A. Maljusch, V. Čolić, L. Spanier, K. Brandl, W. Schuhmann, A.S Bandarenka, *Benchmarking the performance of thin film oxide electrocatalysts for gas evolution reactions at high current densities*. ACS Catalysis, 2016, 6(5), 3017-3024. DOI: 10.1021/acscatal.6b00455.

3. M. Pohl, V. Čolić, D. Scieszka, A. Bandarenka, *Elucidation of adsorption processes at the surface of Pt(331) model electrocatalysts in acidic aqueous media*. Physical Chemistry Chemical Physics, 2016, 18, 10792-10799. DOI: 10.1039/C5CP08000B.

4. F. Calle-Vallejo, J. Tymoczko, V. Čolić, Q.H. Vu, M.D. Pohl, K. Morgenstern, D. Loffreda, P. Sautet, W. Schuhmann, A.S. Bandarenka, *Finding optimal surface sites on heterogeneous catalysts by counting nearest neighbors*. Science, 2015, 350(6257), 185-189. DOI:10.1126/science.aab3501.

5. V. Čolić, M. Pohl, D. Scieszka, A. Bandarenka, *Influence of the electrolyte composition on the activity and selectivity of electrocatalytic centers*. Catalysis Today, 2015, 262, 24-35. DOI:10.1016/j.cattod.2015.08.003

6. J. Tymoczko, F. Calle-Vallejo, V. Čolić, W. Schuhmann, A.S. Bandarenka, *Evaluation of the Electrochemical Stability of Model Cu-Pt(111) Near-Surface Alloy Catalysts*. Electrochimica Acta, 2015, 179, 469-474. DOI:10.1016/j.electacta.2015.02.110

7. V. Čolić, J. Tymoczko, A. Maljusch, A. Ganassin, W. Schuhmann, A.S. Bandarenka, *Experimental Aspects in Benchmarking of the Electrocatalytic Activity.* ChemElectroChem, 2015, 2, 143-149. DOI: 10.1002/celc.201402295

8. A. Ganassin, V. Čolić, J. Tymoczko, A.S. Bandarenka, W. Schuhmann, *Non-Covalent Interactions in Water Electrolysis: Influence on the Activity of Pt(111) and Iridium Oxide Catalysts in Acidic Media*. Physical Chemistry Chemical Physics, 2015, 17, 8349-8355. DOI: 10.1039/C4CP04791E

9. J. Tymoczko, F. Calle-Vallejo, V. Čolić, M.T.M. Koper, W. Schuhmann, A.S. Bandarenka, *Oxygen Reduction at a Cu-Modified Pt(111) Model Electrocatalyst in Contact with Nafion Polymer.* ACS Catalysis, 2014, 4, 3772-3778. DOI: 10.1021/cs501037y

10. J. Tymoczko, V. Čolić, A. Ganassin, W. Schuhmann, A.S. Bandarenka, *Influence of the Alkali Metal Cations on the Activity of Pt(111) Towards Model Electrocatalytic Reactions in Acidic Sulfuric Media*. Catalysis Today, 2015, 244, 96-102. DOI:10.1016/j.cattod.2014.07.007

11. J. Tymoczko, V. Čolić, A.S. Bandarenka, W. Schuhmann, *Detection of 2D Phase Transitions at the Electrode/Electrolyte Interface Using Electrochemical Impedance Spectroscopy*. Surface Science, 2015, 631, 81-87. DOI:10.1016/j.susc.2014.04.014

Bibliography:

1. M. Wackernagel, N.B. Schultz, D. Deumling, A. Callejas Linares, M. Jenkins, V. Kapos, C. Monfreda, J. Loh, N. Myers, R. Norgaard, J. Randers, PNAS, 2002, 14, 9266.
2. N. Armaroli, V. Balzani, Angew. Chem. Int. Ed., 2007, 46, 52.
3. 2012 Energy Statistics Yearbook, United Nations, New York, 2012.
4. BP Statistical Review of World Energy 2015, Pureprint Group, Ltd., London, 2015.
5. Electricity Information, IEA, 2015.
6. BP Energy Outlook: Outlook to 2035, British Petroleum, BP p.l.c., 2015
7. N.S. Lewis, D.G. Nocera, PNAS, 2006, 103, 15729.
8. Energy and Climate Change, World Energy Outlook special report, IEA, 2015.
9. World Energy Outlook 2015, International Energy Agency, IEA Publications, Paris, France, 2015.
10. N. Armaroli, V. Balzani, Energy for a sustainable world. From the oil age to a sun powered future. Wiley-VCH, Weinheim, 2011.
11. J. O.'M. Bockris, Int. J. Hydrogen Energy, 2002, 27, 731.
12. K. Aleklett, M. Höök, K. Jakobssen, M. Lardelli, S. Snowden, B. Söderbergh, Energy Policy, 2010, 38, 1398-1414.
13. M.Z. Jacobson, M.A., Delucchi, Energy Policy, 2011, 39, 1154.
14. K. Tokimatsu, J. Fujino, S. Konishi, Y. Ogawa, K. Yamaji, Energy Policy, 2003, 31, 775-797.
15. Renewable Energy Sources and Climate Change Mitigation, Intergovernmental Panel on Climate Change, UNEP, 2012.
16. Medium-Term Renewable Energy Market Report 2015, International Energy Agency, IEA Publications, Paris, France, 2015.
17. IPCC 2013, Working Group 1 Contribution to the IPCC Fifth Assessment Report, Climate Change 2013, The physical Science Basis, Summary for Policy Makers, Cambridge University Press. New York, USA.
18. Key Trends in CO_2 Emissions from Fuel Combustion 2015, International Energy Agency, IEA Publications, Paris, France, 2015.
19. E. Dlugokencky, P. Tans, NOAA/ESRL http://www.esrl.noaa.gov/gmd/ccgg/trends/index.htmlf
20. Adoption of the Paris Agreement, UN, Paris, 2015.
http://unfccc.int/resource/docs/2015/cop21/eng/l09r01.pdf
21. Energy Technology Perspectives 2015, International Energy Agency, IEA/OECD, IEA Publications, Paris, France, 2015.
22. State of the World Population 2007, UNFPA 2007. https://www.unfpa.org/sites/default/files/pub-pdf/695_filename_sowp2007_eng.pdf
23. Wind in power, European Statistics 2014, EWEA, 2015.
24. P.C.K. Vesborg, T.F. Jaramillo, RSC Adv., 2012, 2, 7933.
25. R.E. Smalley, MRS Bull., 2005, 30, 412.
26. N. Armaroli, V. Balzani, En. Environ. Sci., 2011, 4, 3193.
27. M.A. Delucchi, M.Z. Jacobson, Energy Policy, 2011, 39, 1170.
28. W.F. Pickard, A.Q. Shen, N.J. Hansing, Renewable Sustainable Energy Rev., 2009, 13, 1934.
29. Y.H. Wan, Long-Term Wind Power Variability, Technical Report TP-5500-53637, NREL, 2012.
30. J. O.'M. Bockris, A.J. Appleby, Environment This Month, 1972, 1, 29.
31. J. O.'M. Bockris, Int. J. Hydrogen Energy, 2013, 38, 2579.
32. S. Singh, S. Jain, V. Ps, A.K. Tiwari, M.R. Nouni, J.K. Pandey, S. Goel, Renewable Sustainable Energy Rev., 2015, 51, 623.
33. N.Z. Muradov NZ, T.N. Verizoglu, J. Hydrogen Energy, 2005, 30(3), 225.
34. G. Marban, T. Valdes-Solis, Int. J. Hydrogen Energy, 2007. 32, 1625.
35. A. Bauen, J. Hart, J.Power Sources, 2000, 86, 482–494.
36. J. Hetland, G. Mulder, Int. j. Hydrogen Energy, 2006, 32, 736.
37. The Hydrogen Economy: Opportunities, Costs, Barriers and R&D Needs, Committee on Alternatives and Strategies for Future Hydrogen Production and Use, The National Academies
Press, Washington, D.C., 2004.

38. S. Dutta, J. Ind. Eng. Chem., 2014, 20, 1148.
39. G. Cipriani, V. Di Dio, F. Genduso, D. La Cascia, R. Liga, R. Miceli and G. R. Galluzzo, Int. J. Hydrogen Energy, 2014, 39, 8482.
40. J.A. Turner, Science, 2004, 305, 972.
41. C. Koroneos, A. Dompros, G. Roumbas, N. Moussipoulos, Int. J. Hydrogen Energy, 2004, 29, 1443.
42. G.F. Naterer, M. Fowler, J. Cotton, K. Gabriel, Int. J. Hydrogen Energy, 2008, 33, 6849.
43. O. Bicakova, P. Straka, Int. J. Hydrogen Energy, 2012, 37, 11563.
44. J.D. Holladay, J. Hu, D.L. King, Y. Wang, Cat. Today, 2009, 139, 244.
45. S. H. Jensen, P. H. Larsen, M. Mogensen, Int. J. Hydrogen Energy, 2007, 32, 3253.
46. J. Yang, A. Sudik, C. Wolverton, D.J. Siegel, 2010, 39, 656.
47. U. Eberle, M. Felderhoff, F. Schüth, Angew. Chem. Int. Ed., 2009, 48, 6608.
48. M. Ball, M. Wietschel, Int. J. Hydrogen Energy, 2009, 34. 615.
49. L. Carrette, K. A. Friedrich, U. Stimming, ChemPhysChem, 2000, 1, 162–163.
50. F.T. Wagner, B. Lakshmanan, M.F. Mathias, J. Phys. Chem. Lett.2010, 1, 2204.
51. H.A. Gasteiger, S.S. Kocha, B. Sompalli, F.T. Wagner, Appl.Catal. B, 2005, 56, 9−35.
52. O.Z. Sharaf, M.F. Orhan, Renewable Sustainable Energy Rev., 2014, 32, 810.
53. Y. Wang, K.S. Chen, J. Mischler, S.C. Cho, X.C. Adroher, Appl. Energy, 2011, 88, 981.
54. A.J. Bard, J. Am. Chem. Soc., 2010, 132, 7559.
55. J. Greeley, N.M. Markovic, Enrgy Environ. Science, 2012, 5, 9246.
56. M. Mavrikakis. Nat. Mat., 2006, 5, 847.
57. A.J. Medford, A. Vojvodic, J.S. Hummelshoy, J. Voss, F. Abild-Pedersen, F. Studt, T. Bligaard, A. Nilsson, J.K. Norskov, J. Catal., 2015, 328, 36-42.
58. N.M. Markovic, P.N. Ross, Surf Sci Rep, 2002, 45, 117.
59. R. Rizo, E. Herrero, J.M. Feliu, Phys.Chem.Chem.Phys., 2013, 15, 15416.
60. A.S. Bandarenka, M.T.M. Koper, J. Cat., 2013, 308, 11.
61. P. Strasser, S. Koh, T. Anniyev, J. Greeley, K. Moore, C. Yu, Z. Liu, S. Kaya, D. Nordlund, H. Ogasawara, M.F. Toney, A. Nilsson, Nat Chem, 2010, 2, 454-460.
62. A.A. Gewirth, M.S. Thorum, Inorg Chem, 2010, 49, 3557.
63. V. Mazudmer, Y. Lee, S. Sun, Adv Funct Mater, 2010, 20(8), 1224.
64. P. Mani, R. Srivastava, P. Strasser, J Phys Chem C, 2008, 112, 2770.
65. M.T.M. Koper, Nanoscale, 2011, 3, 2054.
66. F. Maillard, M. Eikerling, O.V. Cherstiouk, S. Schreier, E. Savinova, U. Stimming, Faraday Discuss., 2004, 125, 357.
67. L. Tiperman, Y.J. Feng, W. Vogel, N. Alonso-Vante, Electrochim Acta, 2010, 55, 7558.
68. T. He, E. Kreidler, L. Xiong, J. Luo, C.J. Zhong, J. Electrochem. Soc., 2006, 153(9), A1637.
69 R.J. Gilliam, D.W. Kirk, S.J. Thorpe, Electrocatal., 2011, 2, 1.
70. A.S. Bandarenka, E. Ventosa, A. Maljusch, J. Masa, W. Schuhmann, Analyst (Cambridge, UK), 2014, 139, 1274.
71. J. Greeley, T. F. Jaramillo, J. Bonde, I. Chorkendorff, J. K. Norskov, Nat. Mater., 2006, 5, 909.
72. .P.P. Lopes, D. Strmcnik, D. Tripkovic, J.G. Connell, V.R.StamenkovicN.M. Markovic, ACS Catal., In press, DOI: 10.1021/acscatal.5b02920
73. A.P. O'Mullane, Nanoscale, 2014, 6, 4012.
74. F. Calle-Vallejo, M.T.M. Koper, A.S. Bandarenka, Chem Soc Rev, 2013, 42, 5210.
75. J. Tymoczko, F. Calle-Vallejo, V. Colic, M.T.M. Koper, W. Schuhmann, A.S.Bandarenka, ACS Catal., 2014, 4, 3772.
76. J.K. Norskov, J. Rossmeisl, A. Logadottir, L. Lindqvist, J.R. Kitchin, T. Bligaard, H. Jonsson, J. Phys. Chem. B, 2004, 108, 17886.
77. T. Zambelli, J. Wintterlin, J. Trost, G. Ertl, Science, 1996, 273, 1688.
78. M. Nesselberger, S. Ashton, J.C. Meier, I. Katsounaros, K.J.J. Mayrhofer, M. Arenz, J. Am. Chem. Soc., 2011, 133, 17428.
79. M.M. Collinson, D.A. Higgins, R. Kommidi, D. Campbell-Rance, Anal. Chem., 2008, 80, 651.
80. I. Heller, S. Chatoor, J. Mannik, M.A.G. Zevenbergen, C. Dekker, S.G. Lemay, J. Am. Chem. Soc., 2010, 132, 17149.

81. W. Yao, Q. Dai, P. Chen, S. Zhong, Z. Yan, RSC Adv., 2015, 5. 19145.
82. A. Ganassin, V. Colic, J. Tymoczko, A.S. Bandarenka, W. Schuhmann, Phys.Chem. Chem. Phys., 2015, 17, 8349.
83. N. Danilovic, R. Subbaraman, D. Strmcnik, A. P. Paulikas, D. Myers, V. R. Stamenkovic, N. M. Markovic, Electrocatalysis, 2012, 3, 221.
84. D. Strmcnik, K. Kodama, D. van der Vliet, J. Greeley, V.R. Stamenkovic, N.M.Markovic, Nat. Chem., 2009, 1, 466.
85. M. Escudero-Escribano, M.E. Zoloff Michoff, E.P.M. Leiva, N.M. Markovic, C.Gutierrez, A. Cuesta, ChemPhysChem, 2011, 12, 2230.
86. M. Nakamura, N. Sato, N. Hoshi, O. Sakata, ChemPhysChem, 2011, 12, 1430.
87. G.A. Ragoisha, T.A. Auchynnikava, E.A. Streltsov, S.M. Rabchynski, Electrochim. Acta, 2014, 122, 218.
88. C. Stoffelsma, P. Rodriguez, G. Garcia, N. Garcia-Araez, D. Strmcnik, N.M.Markovic, M.T.M. Koper, J. Am. Chem. Soc., 2010, 132, 16127.
89. J. Tymoczko, V. Colic, A. Ganassin, W. Schuhmann, A.S. Bandarenka, Catal.Today, 2014, 244, 96.
90. I. Katsounaros, K.J.J. Mayrhofer, Chem. Commun., 2012, 48, 6660.
91. J. Suntivich, E.E. Perry, H.A. Gasteiger, Y. Shao-Horn, Electrocatalysis, 2013, 4, 49.
92. B. B. Berkes, G. Inzelt, W. Schuhmann, A. S. Bondarenko, J. Phys. Chem. C, 2012, 116, 10995.
93. T.H. Silva, V. Garcia-Morales, C. Moura, J.A. Manzanares, F. Silva, Langmuir, 2005, 21, 7461.
94. J. Tymoczko, W. Schuhmann, A.S. Bandarenka, ChemElectroChem, 2014, 1, 213.
95. D. Pillay, M.D. Johannes, Y. Garsany, K.E. Swider-Lyons, J. Phys. Chem. C, 2010, 114, 7822.
96. X.-R. Liu, L. Wang, L.-J. Wan, D. Wang, ACS Appl. Mater. Interfaces, 2015, 7, 9573.
97. J. Sun, C. Zhang, T. Kou, J. Xu, Z. Zhang, ACS Appl. Mater. Interfaces, 2012, 4, 6038.
98. F. Prieto, I. Navarro, M. Rueda, J. Phys. Chem., 1996, 100. 16346.
99. T. Takashima, K. Hashimoto, R. Nakamura, J. Am. Chem. Soc., 2012, 134, 1519.
100. M.R. Tarasevich, O.V. Korchagin, Russ. J. Electrochem., 2013, 49, 600.
101. Compendium of Chemical Terminology, 2nd ed. Eds: A. D. McNaught and A. Wilkinson. IUPAC, Blackwell Scientific Publications, Oxford, 1997.
102. J.J. Berzelius, Ann. Chim. Phys., 1836, 61, 146-151.
103. W. Ostwald, Nature, 1902, 65, 522.
104. G.A. Somorjai, M. Yang, Top. Catal., 2003, 24, 1-4.
105. D.M. Kolb, Angew. Chem. Int. Ed., 2001, 40, 1162.
106. M. Beller, A. Renken, R. van Santen (eds.), Catalysis: From principles to Applications, 2013., Wiley-VCH, Weinheim.
107. P. Sabatier, J.B. Senderens, C.R. Acad. Sci., 1902, 134, 514.
108. Ertl, G. Angew. Chem., Int. Ed. 2008, 47, 3524.
109. H.S. Taylor, Proc. Roy. Soc. (London) A, 1925, 108, 105.
110. M. Boudart, A. Aldag, L.D. Ptak, J.E. Benson, J. Catal., 1968, 11, 35.
111. R.A. van Santen, Acc. Chem. Res., 2009, 42, 57-66.
112. O. Deutschmann, H. Knözinger, K. Kochloefl, T. Turek, Heterogeneous Catalysis and Solid Catalysts, 2009, Wiley-VCH, Weinheim, pp. 8-10.
113. R. Parsons, Trans. Faraday Soc., 1958, 54, 1053.
114. H. Gerischer, Bull. Soc. Chim. Bel., 1958, 67, 506.
115. A.A. Balandin, Adv. Catal. Rel. Subj., 1969, 19, 1.
116. T. Bligaard, J.K. Norskov, S. Dahl, J. Matthiesen, C.H. Christiansen, J. Sehested, J. Catal., 2004, 224, 206.
117. J.K. Norskov, T. Bligaard, A. Logadottir, S. Bahn, L.B. Hansen, M. Bollinger, H. Bengaard, B. Hammer, Z. Sljivancanin, M. Mavrikakis, Y. Xu, S. Dahl, C.J.H. Jacobsen, J. of Catal., 2002, 209, 275.
118. J. Cheng, P. Hu, J. Am. Chem. Soc., 2008, 130, 10868.
119. M.T.M. Koper, J. Electroanal. Chem., 2011, 660, 254.
120. A.B. Anderson, Phys. Chem. Chem Phys., 2012, 14, 1330.
121. F. Abild-Pedersen F, J. Greeley, F. Studt, J. Rossmeisl, T.R. Munter, P.G. Moses, E. Skulason, T. Bligaard, J.K. Norskov, Phys Rev Lett, 2007, 99(1), 016105-1.
122. J. Rossmeisl, A. Logadottir, J.K. Norskov, Chem Phys, 2005, 319, 178.

123. F. Calle-Vallejo, J.I. Martinez, J.M. Garcia-Lastra, J. Rossmeisl, M.T.M. Koper, Phys. Rev. Lett., 2012, 108, 116103.
124. N. Bronsted, Chem. Rev, 1928, 5, 231.
125. M.G. Evans, N.P. Polanyi, Trans. Faraday Soc., 1938, 34, 11.
126. J.K. Norskov, T. Bligaard, J. Rossmeisl, C.H. Christensen, Nat. Chem., 2009, 1, 37.
127. C. Lefrou, P. Fabry, J.-C. Poignet, Electrochemistry: The Basics, with Examples, 2012, Springer-Verlag, Heidelberg.
128. F. Calle-Vallejo, J. Tymoczko, V. Colic, Q.H. Vu, M.D. Pohl, K. Morgenstern, D. Loffreda, P. Sautet, W. Schuhmann, A.S. Bandarenka, Science, 2015, 350, 185.
129. H. Li, Y. Li, M.T.M. Koper, F. Calle-Vallejo, J. Am. Chem. Soc., 2014, 136, 15694.
130. H. Xin, A. Holewinski, N. Schweltzer, E. Nikolla, S. Linic, 2012, 55, 376.
131. F. Maroun, F. Ozanam, O.M. Magnussen, R.J. Behm, Science, 2001, 293, 1811.
132. R. Burch, Acc Chem Res, 1982, 15, 24-31.
133. C.H. Hamann, A. Hamnett, W. Vielstich, Electrochemistry, 2007, Wiley-VCH, Weinheim.
134. A.J. Bard, L.R. Faulkner, Electrochemical Methods: Fundametnals and Applications, 2001, Wiley & Sons, New York.
135. R.L. LeRoy, Int. J. Hydrogen Energy, 1983, 8(6), 401.
136. K. Zeng. D. Zhang, Prog. Energy Combust. Sci., 2010, 36, 307-326.
137. A. Ursua, L.M. Gandia, P. Sanchis, Proc. IEEE, 2012, 100, 410.
138. M. Carmo, D.L. Fritz, J. Mergel, D. Stolten, Int. J. Hydrogen Energy, 2013, 38, 4901.
139. A. Marshall, B. Borresen, G. Hagen, M. Tsypkin, R. Tunold, Energy, 2007, 32, 431–436.
140. F. Babir, Sol. Energy, 2005, 78, 661.
141. J.K. Norskov, T. Bligaard, A. Logadottir, J.R. Kitchin, J.G. Chen, S. Pandelov, U. Stimming, J. Electrochem. Soc., 2005, 152, J23.
142. J. Rossmeisl, Z.-W. Qu, H. Zhu, G.-J. Kroes, J.K. Norskov, J. Electroanal. Chem., 2007, 607, 83.
143. Encyclopedia of electrochemistry, ed. A. J. Bard and M. Stratmann, Wiley-VCH, 2007.
144. M. E. G. Lyons, S. Floquet, Phys. Chem. Chem. Phys., 2011, 13, 5314.
145. T. Reier, M. Oezaslan, P. Strasser, ACS Catal., 2012, 2, 1765.
146. P. Millet, N. Mbemba, S. A. Grigoriev, V. N. Fateev, A. Aukauloo, C. Etievant, Int. J. Hydrogen Energy, 2011, 36, 4134–4142.
147. W. Vielstich, A. Lamm, H.A. Gasteiger, Handbook of Fuel Cells, John Wiley & Sons, Chichester, 2003.
148. J. Greeley, I.E.L. Stephens, A.S. Bondarenko, T.P. Johansson, H.A. Hansen, T.F. Jaramillo, J. Rossmeisl, I. Chorkendorff, J.K. Norskov, Nat. Chem., 2009, 1, 552.
149. M.J. Janik, C.D. Taylor, M. Neurock, J. Electrochem. Soc., 2009, 156, B126.
150. S. Gottesfeld, T.A. Zawodzinski, Polymer electrolyte fuel cells. Advances in Electrochemical Science and Engineering, vol. 5, eds. R.C. Alkire, H. Gerischer, D.M. Kolb, C.W. Tobias, Wiley-VCH, Weinheim, 1997.
151. B. C. H. Steele, A. Heinzel, Nature 2001, 414, 345.
152. V. Mehta, J.S. Cooper, J. Power Sources, 2003, 114, 32.
153. S. Litster, G. McLean, J. Power Sources, 2004, 130, 61.
154. A. Biyikoglu, Int. J. Hydrogen Energy, 2005, 30, 1181.
155. J. Zhang, Z. Xie, J. Zhang, Y. Tang, C. Song, T. Navessin, Z. Shi, D. Song, H. Wang, D.P. Wilkinson, Z.-S. Liu, S. Holdcroft, J. Power Sources, 2006, 160, 872.
156. W. Schmittinger, A. Vahidi, J. Power Sources, 2008, 180, 1.
157. W. Sheng, H.A. Gasteiger, Y. Shao-Horn, J. Electrochem. Soc., 2010, 157, B1529.
158. N.M. Markovic, B.N. Grgur, P.N. Ross, J. Phys. Chem. B, 1997, 101, 5405.
159. J.X. Wang, T.E. Springer, P. Liu, M. Shao, R.R. Adzic, J. Phys. Chem., 2007, 111, 12425-12433.
160. P.J. Rheinländer, J. Herranz, J. Durst, H.A. Gasteiger, J. Electrochem. Soc., 2014, 161, F1448.
161. J. Suntivich, H.A. Gasteiger, N. Yabuuchi, H. Nakanishi, J.B. Goodenough, Y. Shao-Horn, Nat. Chem., 2011, 3, 546.
162. J. Lariminie, A. Dicks, Introduction. Fuel cell systems explained. John Wiley & Sons Ltd., West Sussex, 2003.
163. M. Stratmann, J. Müller, Corros. Sci., 1994, 36, 327.
164. P.G. Bruce, S.A. Freunberger, L.J. Hardwick, J.M. Tarascon, Nat. Mater., 2012, 11, 19.

165. M. Armand, J.M. Tarascon, Building better batteries, Nature, 2008, 451, 652.
166. I.E.L. Stephens, A.S. Bondarenko, U. Gronbjerg, J. Rossmeisl, I. Chorkendorff, En. Environ. Sci., 2012, 5, 6744.
167. A. Panchenko, M.T.M. Koper, T.E. Shubina, S.J. Mitchell, E. Roduner, J. Electrochem Soc., 2004, 151, A2016.
168. Y. Nie, L. Li, Z. Wei, Chem. Soc. Rev., 2015, 44, 2168.
169. J.X. Wang, F.A. Uribe, T.E. Springer, J. Zhang, R.A. Adzic, Faraday Discuss., 2008, 140, 347.
170. S. Siahrostami, A. Verdaguer-Casadevall, M. Karamad, D. Deiana, P. Malacrida, B. Wickman, M. Escudero-Escribano, E.A. Paoli, R. Frydendal, T.W. Hansen, I. Chorkendorff, I.E.L. Stephens, J. Rossmeisl, Nat. Mat., 2013, 12, 1137.
171. G. Goor, J. Glenneberg, S. Jacobi, „Hydrogen peroxide“, Ullmann's Encyclopedia of Industrial Chemistry, Wiley-VCH, Weinheim, 2012.
172. A.A. Topalov, I. Katsounaros, M. Auinger, S. Cherevko, J.C. Meier, S.O. Klemm, K. J.J. Mayrhofer, Angew. Chem. Int. Ed., 2012, 51, 12613.
173. J.C. Meier, I. Katsounaros, C. Galeano, H.J. Bongard, A.A. Topalov, A. Kostka, A. Karschin, F. Schüth, K.J.J. Mayrhofer, Energy Environ. Sci., 2012, 5, 9319.
174. J. Wu, X.Z. Yuan, J.J. Martin, H. Wang, J. Zhang, J. Shen, S. Wu, W. Merida, J. Power Sources, 2008, 184, 104.
175. I.C. Man, H.-Y. Su, F. Calle-Vallejo, H.A. Hansen, J.I. Martinez, N.G. Inoglu, J. Kitchin, T.F. Jaramillo, J.K. Nørskov, J. Rossmeisl, ChemCatChem, 2011, 3, 1159.
176. A.S. Bondarenko, I.E.L. Stephens, I. Chorkendorff, Electrochem. Comm., 2012, 23, 33.
177. J. Tymoczko, W. Schuhmann, A.S. Bandarenka, PCCP, 2013, 15, 12998.
178. A. Berna, V. Climent, J.M. Feliu, Electrochem. Comm., 2007, 9, 2789.
179. J. Tymoczko, F. Calle-Vallejo, V. Colic, W. Schuhmann, A.S. Bandarenka, Electrochim. Acta, 2015, 179, 469.
180. B.S. Yeo, A.T. Bell, J. Am. Chem. Soc. 2011, 133, 5587.
181. B.B. Katemann, W.Schuhmann, Electroanalysis 2002, 14, 22.
182. K.A. Mauritz, R.B. Moore, Chem. Rev., 2004, 104, 4535.
183. J. Rossmeisl, G.S. Karlberg, T. Jaramillo, J.K. Norskov, Faraday Discuss., 2008, 140, 337.
184. A.S: Bandarenka, H.A. Hansen, J. Rossmeisl, I.E.L. Stephens, Phys. Chem. Chem. Phys., 2014, 16, 13625.
185. G. Inzelt, Chronocoulometry in Electroanalytical Methods. Ed.: F. Scholz. Springer-Verlag, Heidelberg, 2010.
186 A.S. Bandarenka, Analyst, 2013, 138, 5540.
187. U. Retter, H. Lohse in Electroanalytical Methods. Ed.: F. Scholz. Springer-Verlag, Heidelberg, 2010.
188. A. Lasia. Electrochemical Impedance Spectroscopy. Springer Science + Business Media, New York, USA, 2014.
189. G.A. Ragoisha, A.S. Bondarenko, 2005, 50, 1553.
190. T. Pajkossy, J. Electroanal. Chem., 1994, 364, 111.
191. A.S. Bondarenko, I.E.L. Stephens, H.A. Hansen, F.J. Perez-Alonso, V. Tripkovic, T.P. Johansson, J. Rossmeisl, J.K. Norskov, I. Chorkendorff, Langmuir, 2011, 27, 2058.
192. G. Sauerbrey, Z Phys 1959, 155, 206
193. G. Inzelt Electrochemical Quartz Crystal Nanobalance in Electroanalytical Methods. Ed.: F. Scholz. Springer-Verlag, Heidelberg, 2010.
194. G. Binnig, C.F. Quate, Phys. Rev. Lett., 1986, 56, 930.
195. P. Schmuki, S. Virtanen, *Electrochemistry at the* Nanoscale, Springer Science + Business Media, New York, USA, 2009.
196. R. Garcia, R. Perez, Surf. Sci. Rep., 2002, 47, 197.
197 S. Hüfner, *Photoelectron spectroscopy*, Springer-Verlag, Heidelberg, Germany, 1996,
198. J. C. Vickerman, I.S. Gilmore, *Surface analysis - The principal techniques*, John Wiley & Sons Ltd., Chichester, UK, 1997.
199. V. Colic, J. Tymoczko, A. Maljusch, A. Ganassin, W. Schuhmann, A.S. Bandarenka, ChemElecroChem, 2015, 2, 143.
200. J. Wojtowicz, L. Laliberte, B. E. Conway, Electrochim. Acta 1968, 13, 361.
201. K.R. Cooper, M. Smith, J. Power Sources, 2006, 160, 1088.

202. I. Epelboin, M. Keddam, H. Takenouti, J. Appl. Electrochem. 1972, 2, 71.
203. F. Mansfeld, Corrosion 1981, 37, 301
204. W. J. Lorenz, F. Mansfeld, Corros. Sci. 1981, 21, 647.
205. Technical note 200m, Subject: Getting to Know your Potentiostat; Potentiostat Stability Considerations, 2010, Princeton Applied Research.
206. Reference Electrodes: Application Note, Rev. 2.0 1/25/2011, 1990–2011,Gamry Instruments.
207. D. van der Vliet, D.S. Strmcnik, C. Wang, V.R. Stamenkovic, N.M. Markovic, M.T.M. Koper, J. Electroanal. Chem., 2010, 647, 29.
208. J. Greeley, J. K. Norskov, L. A. Kibler, A. M. El-Aziz, D. M. Kolb, ChemPhysChem, 2006, 7, 1032.
209. S. Trasatti, J. Electroanal. Chem. 1972, 39, 163.
210. B. E. Conway, J. O'M. Bockris, J. Chem. Phys. 1957, 26, 532.
211. Y. Sun, J. Lu, L. Zhuang, Electrochim. Acta, 2010, 55, 844.
212. M. R. Gennero de Chialvo, A. C. Chialvo, J. Electroanal. Chem., 1996, 415, 97.
213. C.C.L. McCrory, S. Jung, J.C. Peters, T.F. Jaramillo, J. Am. Chem. Soc., 2013, 135, 16977.
214. C.C.L. McCrory, S. Jung, I.M. Ferrer, S.M. Chatman, J.C. Peters, T.F. Jaramillo, J. Am. Chem. Soc., 2015, 37, 4347.
215. M.G. Walter, E.L. Warren, J.R. McKone, S.W. Boettcher, Q. Mi, E.A. Santori, N.S. Lewis, Chem. Rev. 2010, 110, 6446.
216. A. Manabe, M. Kashiwase, T. Hashimoto, T. Hayashida, A. Kato, K. Hirao, K. Shimomura, I. Nagashima, Electrochim. Acta, 2013, 100, 249.
217. S. Trasatti, O. A. Petrii, J. Electroanal. Chem., 1992, 327, 353.
218. G. Jarzabek, Z. Borkowska, Electrochim. Acta, 1997, 42, 2915.
219. T. Binninger, E. Fabbri, R. Kotz, T.J. Schmidt, J. Electrochem. Soc., 2014, 161, H121.
220. S. Rudi, C.H. Cui, L. Gan, P. Strasser, Electrocatalysis, 2014, 5, 408.
221. C.L. Green, A. Kucernak, J. Phys. Chem. B., 2002, 106, 1036.
222. S.W.T. Price, J.D. Speed, P. Kaman, A.E. Russell, J. Am. Chem. Soc., 2011, 133, 19448.
223. L.D. Burke, O.J.J. Murphy, Electroanal Chem., 1980, 112, 39.
224. S.K. Roy, M.E. Orazem, J. Electrochem. Soc., 2009, 156, B203.
225. Z. Kerner, T. Pajkossy, Electrochim. Acta, 2000, 46, 207.
226. T. Pajkossy, Solid State Ionics, 2005, 176, 1997.
227. A. Ganassin, A. Maljusch, V. Colic, L. Spanier, K. Brandl, W. Schuhmann, A.S. Bandarenka, ACS Catalysis, 2016, 6, 3017.
228. J. Tymoczko, F. Calle-Vallejo, W. Schuhmann, A.S. Bandarenka, Nat. Comm., 2016, In Print. DOI: 10.1038/ncomms10990
229. V. Čolić, A.S. Bandarenka, ACS Catalysis.
230. H.A. Gasteiger, N.M. Markovic, Science, 2009, 324, 48.
231. P. Malacrida, H.G. Sanchez Casalongue, F. Masini, S. Kaya, P. Hernandez-Fernandez, D. Deiana, H. Ogasawara, I.E.L. Stephens, A. Nilsson, I. Chorkendorff, Phys. Chem. Chem. Phys. 2015, 17, 28121.
232. C. Wang, N.M. Markovic, V.R. Stamenkovic, ACS Catal. 2012, 2, 891.
233. C. Wang, M. Chi, D. Li, D. van der Vliet, G. Wang, Q. Lin, J.F. Mitchell, K.L. More, N.M. Markovic, V.R. Stamenkovic, ACS Catal., 2011, 1, 1355.
234. U.A.Paulus, A. Wokaun, G.G. Scherer, T.J. Schmidt, V.R. Stamenkovic, N.M. Markovic, R.N. Ross, Electrochim. Acta, 2002, 47, 3787.
235. V. Stamenkovic, T.J. Schmidt, P.N. Ross, N.M- Markovic, J. Phys. Chem. B, 2002, 106, 11970.
236. A.J. Appleby, Catal. Rev., 1970, 4, 221.
237. E. Antolini, J.R.C. Salgado, E.R. Gonzalez, J. Power Sources, 2006, 160, 957.
238. J.L. Zhang, M.B. Vukmirovic, Y. Xu, M. Mavrikakis, R.R. Adzic, Angew. Chem. Int. Ed., 2005, 44, 2132.
239. W.P. Zhou, X.F. Yang, M.B. Vukmirovic, B.E. Koel, J. Jiao, G.W. Peng, M. Mavrikakis, R.R. Adzic, J.. Am. Chem. Soc., 2009, 131, 12755.
240. Y. Takesue, M. Nakamura, N. Hoshi, Phys. Chem. Chem. Phys., 2014, 16, 13774.
241. T. Rurigaki, A. Hitotsuyanagi, M. Nakamura, N. Sakai, N. Hoshi, J. Electroanal. Chem. 2014, 716, 58.
242. V.R. Stamenkovic, B. Fowler, B.S. Mun, G.F. Wang, P.N. Ross, C.A. Lucas, N.M- Markovic, Science 2007, 315, 493.

243. Y. Bando, Y. Takahashi, E. Ueta, N. Todoroki, T. Wadayama, J. Electrochem. Soc., 2015, 162, F463.
244. I.E.L. Stephens, A.S. Bondarenko, F.J. Perez-Alonso, F. Calle-Vallejo, L. Bech, T.P. Johansson, A.K. Jepsen, R. Frydendal, B.P. Knudsen, J. Rossmeisl, I. Chorkendorff, J. Am. Chem. Soc., 2011, 133, 5485.
245. A. Kuzume, E. Herrero, J.M. Feliu, J. Electroanal. Chem., 2007, 599, 333.
246. A. Hitotsuyanagi, M. Nakamura, N. Hoshi, Electrochim. Acta 2012, 82, 512.
247. M.D. Macia, J.M. Campina, E. Herrero, J.M. Feliu, J. Electroanal. Chem., 2004, 564, 141.
248. N.M. Markovic, R.R. Adzic, B.D. Cahan, E.B. Yeager, J. Electroanal. Chem., 1994, 377, 249.
249. N. Hoshi, M. Nakamura, A. Hitotsuyanagi, Electrochim. Acta, 2013, 112, 899.
250. M.J.T.C. van der Niet, N. Garcia-Araez, J. Hernandez, J.M. Feliu, M.T.M. Koper, Catal. Today 2013, 202 105.
251. G.A. Tritsaris, J. Greeley, J. Rossmeisl, J.K. Norskov, Catal. Lett., 2011, 141, 909.
252. V. Stamenkovic, B.S. Mun, J.J. Mayrhofer, P.N. Ross, N.M. Markovic, J. Rossmeisl, J. Greeley, J.K. Norskov, Angew. Chem. Int. Ed., 2006, 45, 2897.
253. B.D.B. Aaronson, C.-H. Chen, H. Li, M.T.M. Koper, S.C.S. Lai, P.R. Unwin, J. Am. Chem. Soc., 2013, 135, 3873.
254. F.J. Perez-Alonso, D.N. McCarthy, A. Nierhoff, P. Fernandez-Hernandez, C. Strebel, I.E.L. Stephens, J.H. Nielsen, I. Chorkendorff, Angew. Chem. Int. Ed., 2012, 51, 4641.
255. C. Zhang, S.Y. Hwang, Z.J. Peng, J. Mat. Chem. A, 2014, 2, 19778.
256. P. Hernandez-Fernandez, F. Masini, D.N. McCarthy, S.E. Strebel, D. Friebel, D. Deiana, P. Malacrida, A. Nierhoff, A. Bodin, A.M. Wise, J.H. Nielsen, T.W. Hansen, A. Nilsson, I.E.L. Stephens, I. Chorkendorff, Nat. Chem., 2014, 6, 732.
257. M. Escudero-Escribano, P. Malacrida, M.H. Hansen, U.G. Vej-Hansen, A. Velázquez-Palenzuela, V. Tripkovic, J. Schiøtz, J. Rossmeisl, I.E.L. Stephens, I. Chorkendorff, Science, 2016, 352, 73.
258. J. Erlebacher, M.J. Aziz, A. Karma, N. Dimitrov, K. Sieradzki, Nature, 2001, 410, 450.
259. F.U. Renner, A. Stierle, H. Dosch, D.M. Kold, T.-L. Lee, J. Zegenhagen, Nature, 2006, 439, 707.
260. T.P. Moffat, F.-R. Fan, A.J.J. Bard, Electrochem. Soc., 1991, 138, 3224.
261. V. Stamenkovic, T.J. Schmidt, P.N. Ross, N.M. Markovic, J. Electroanal. Chem. 2003, 554-555, 191.
262. V.R. Stamenkovic, B.S. Mun, M. Arenz, K.J.J. Mayrhofer, C.A. Lucas, G.F. Wang, P.N. Ross, N.M. Markovic, Nat. Mater., 2007, 6, 241.
263. V.R. Stamenkovic, B.S. Mun, K.J.J. Mayrhofer, P.N. Ross, N.M. Markovic, J. of Am. Chem. Soc., 2006, 128, 8813.
264. A.V. Ruban, H.L. Skriver, J.K. Norskov, Phys. Rev. B, 1999, 59, 15990.
265. C. Wang, M. Chi, D. Li, D. Strmcnik, D. van der Vliet, G. Wang, V. Komanicky, K.-C. Chang, A.P. Paulikas, D. Tripkovic, J. Pearson, K.L. More, N.M. Markovic, V.R. Stamenkovic, J. Am. Chem. Soc. 2011, 133, 14396.
266. C. Wang, M. Chi, G. Wang, D. van der Vliet, D. Li, K. More, H.-H. Wang, J.A. Schlueter, N.M. Markovic, V.R. Stamenkovic, Adv. Funct. Mater. 2011, 21, 147.
267. M. Mavrikakis, B. Hammer, J.K. Norskov, Phys. Rev. Lett., 1998, 81, 2819.
268. M. Lischka, C. Mosch, A. Gross, Electrochim. Acta, 2007, 52, 2219.
269. A. Schlapka, M. Lischka, A. Groß, U. Käsberger, P. Jakob,. Phys. Rev. Letts. 2003, 91, 016101.
270. D. van der Vliet, C. Wang, M. Debe, R. Atanasoski, N.M. Markovic, V.R. Stamenkovic, Electrochim. Acta, 2011, 56, 8695.
271. D. Wang, H.L. Xin, R. Hovden, H. Wang, Y. Yu, D.A. Muller, F.J. DiSalvo, H.D. Abruna, Nat. Mater. 2012, 12, 81.
272. S. Mukerjee, S. Srinavasan, M.P. Soriaga, J.J. McBreen, Electrochem. Soc., 1995, 142, 1409.
273. I.E.L. Stephens, A.S. Bondarenko, L. Bech, I. Chorkendorff, ChemCatChem 2012, 4, 341.
274. S. Beyhan, N.E. Sahin, S. Pronier, J.-M. Leger, F. Kadirgan, Electrochim. Acta, 2015, 151, 565.
275. M. Escudero-Escribano, P. Malacrida, A.A. Velazquez-Palenzuela, A.F. Pedersen, D. Friebel, A. Nilsson, I.E.L. Stephens, I. Chorkendorff, What Is the Optimum Strain for Pt Alloys for Oxygen Electroreduction? ECS Meeting. Chicago, USA, May 25, 2015. MA2015-01:1820. ECS Meeting Abstracts. http://ma.ecsdl.org/content/MA2015-01/32/1820.short (accessed 03/05/2016)
276. M. Escudero-Escribano, P. Malacrida, U.G. Vej-Hansen, V. Tripkovic, J. Rossmeisl, I.E.L. Stephens, I. Chorkendorff, Engineering the Activity and Stability of Pt-Alloy Cathode Fuel-Cell Electrocatalysts by Tuning

the Pt-Pt Distance. ECS and SMEQ Joint International Meeting. Cancun, Mexico, Oct 5, 2014. MA2014-02:1038. ECS Meeting Abstracts. http://ma.ecsdl.org/content/MA2014-02/21/1038.short (accessed 01/12/2015)
277. M. Escudero-Escribano, A. Verdaguer-Casadevall, P. Malacrida, U. Gronbjerg, B.P. Knudsen, A.K. Jepsen, J. Rossmeisl, I.E.L. Stephens, I. Chorkendorff, J. Am. Chem. Soc. 2012, 134, 16476.
278. E. Teatum, K. Gschneider, J. Waber, In Report NoLA-2345; U.S. Dept. of Commerce: Washington, D.C., 1960; p 45.
279. U. Simon, In Nanoparticles: From Theory to Application; Schmid, G., Ed. Wiley-VCH: Weinheim, 2004; p 328.
280. A.S. Bandarenka, A.S. Varela, M. Karamad, F. Calle-Vallejo, L. Bech, F.J. Perez-Alonso, J. Rossmeisl, I.E.L. Stephens, I. Chorkendorff, Angew. Chem. Int. Ed., 2012, 51, 11845.
281. T. Wadayama, N. Todoroki, Y. Yamada, T. Sugawara, K. Miyamoto, Y. Iijama, Electrochem. Commun. 12, 2010, 1112.
282. E.A. Ticianelli, C.R. Derouin, S. Srinivasan, J. Electroanal. Chem. 1988, 251, 275.
283. R. Subbaraman, D. Strmcnik, V. Stamenkovic, N.M. Markovic, J. Phys. Chem. C, 2010, 114, 8414.
284. R. Subbaraman, D. Strmcnik, A.P. Paulikas, V. Stamenkovic, N.M. Markovic, ChemPhysChem, 2010, 11, 2825.
285. J. Tymoczko, F. Calle-Vallejo, V. Čolić, M.T.M. Koper, W. Schuhmann, A.S. Bandarenka, ACS Catal., 2014, 4, 3772.
286. B. Braunschweig, W. Daum, Langmuir, 2009, 25, 11112.
287. D.S. Strmcnik, D.V. Tripkovic, D. van der Vliet, K.C. Chang, V. Komanicky, H. You, G. Karapetrov, J. Greeley, V.R. Stamenkovic, N.M. Markovic, J. Am. Chem. Soc., 2008, 130, 15332.
288. D, Strmcnik, M. Escudero-Escribano, K. Kodama, V.R. Stamenkovic, A. Cuesta, N.M. Markovic, Nat. Chem. 2010, 2, 880.
289. J.A. Herron, M. Mavrikakis, Catal. Commun. 2014,52, 65.
290. J. Greeley, J.K. Nøskov, Electrochim. Acta, 2007, 52, 5829.
291. X. Zhang, S. Yu, W. Zheng, P. Liu, Phys. Chem. Chem. Phys., 2014, 16, 16615.
292. P. Strasser, S. Koh, J. Greeley, Phys. Chem. Chem. Phys., 2008, 10, 3670.
293. K.J. Andersson, F. Calle-Vallejo, J. Rossmeisl, I. Chorkendorff, J. Am. Chem. Soc., 2009, 131, 2404.
294. J. Knudsen, A.U. Nilekar, R.T. Vang, J. Schnadt, E.L. Kunkes, J.A. Dumesic, M. Mavrikakis, F. Besenbacher, J. Am. Chem. Soc., 2007, 129, 6485.
295. A.K. Schuppert, A. Savan, A. Ludwig, K.J.J. Mayrhofer, Electrochim. Acta, 2014, 144, 332.
296. F. Viñes, J.R.B. Gomes, F. Illas, Chem. Soc. Rev., 2014, 43, 4922.
297. J. Kleis, J. Greeley, N.A. Romero, V.A. Morozov, H. Falsig, A.H. Larsen, J. Lu, J.J. Mortensen, M. Dulak, K.S. Thygesen, J.K. Norskov, K.W. Jacobsen, Catal. Lett., 2011, 141, 1067.
298. G. Mpourmpakis, A. N. Andriotis, D. G. Vlachos, Nano Lett., 2010, 10, 1041.
299. F. Calle-Vallejo, J.I. Martinez, J.M. Garcia-Lastra, P. Sautet, D. Loffreda, Angew. Chem. Int. Ed., 2014, 53, 8316.
300. G. A. Somorjai, J. Carrazza, Ind. Eng. Chem. Fundam., 1986, 25, 63.
301. D. C. Johnson, D. T. Napp, S. Bruckenstein, Electrochim. Acta, 1970, 15, 1493.
302. L. Dubau, M. Lopez-Haro, J. Durst, L. Guetaz, Bayle-Guillermaud, M. Chatenet, F. Maillard, J. Mater. Chem. A, 2014, 2, 18947.
303. L. Liu, J. Hu, J. Zhang, C. Cao, Anal. Chem., 2009, 81, 3199.
304. R. Matthessem, J. Fransaer, K. Binnemansc, D.E. De Vos, RSC Adv., 2013, 3, 4634.
305. S. Santi, A. Bisello, R. Cardenaa, A. Donoli, Dalton Trans., 2015, 44, 5234.
306. R. Naegeli, J. Redepenning, F.C. Anson, J. Phys. Chem., 1986, 90, 6227.
307. M. Grotheer, R. Alkire, R. Varjian, Electrochem. Sco. Interface, 2006, 15, 52.
308. P. Herasymenko, I. Slednyk, Z. Phys. Chem. A, 1930, 149, 230.
309. M. Tokuoka, Collect. Czech. Chem. Commun., 1932, 4, 444.
310. M. Tokuoka, J. Ruzicka, Collect. Czech. Chem. Commun., 1934, 6, 339.
311. J. Heyrovsky, Actualites Sci. et Ind., 1933, 90, 4, Paris.
312. A.N. Frumkin, Trans. Farady Soc., 1959, 55, 156.
313. V.E. Kazarinov, O.A. Petrii, J. Electroanal. Chem., 1970, 27, App.1 – App. 2.
314. G. Lamoureux, B. Roux, J. Phys. Chem. B, 2006, 110, 3308.
315. L.M.C. Pinto, P. Quaino, M.D. Arce, E. Santos, W. Schmickler, Chem. Phys. Chem., 2014, 15, 2003
316. D. Strmcnik, D.F. van der Vliet, K.-C. Chang, V. Komanicky, K. Kodama, H. You, V.R. Stamenkovic, N.M. Markovic, Phys. Chem. Lett., 2011, 2, 2733.

317. D. Crihan, M. Knapp, S. Zweidinger, E. Lundgren, C.J. Westrate, J.N. Andersen, A.P. Seitsonen, H. Over, Angew. Chem., 2008, 120, 2161.
318. N. Lopez, J. Gomez-Segura, R.P. Marin, J. Perez-Ramirez, J. Catal. 2008. 255, 29.
319. S. Zweidinger, D. Crihan, M. Knapp, J.P. Hofmann, A.P. Seitsonen, C.J.Westrate, E. Lundgren, J.N. Andersen, H. Over, J. Phys. Chem. C, 2008, 112, 9966.
320. D. Teschner, R. Farra, L. Yao, R. Schogl, H. Soerijanto, R. Schomacker, T.Schmid, L. Szentmiklosi, A.P. Amrute, C. Mondelli, J. Perez-Ramirez, G.Novell-Leruth, N. Lopez, J. Catal., 2012, 285, 273.
321. A.P. Amrute, C. Mondelli, M. Moser, G. Novell-Leruth, N. Lopez, D. Rosenthal,R. Farra, M.E. Schuster, D. Teschner, T. Schmidt, J. Perez-Ramirez, J. Catal., 2010, 286, 287.
322. H.A. Hansen, I.C. Man, F. Studt, F. Abild-Pedersen, T. Bligaard, J. Rossmeisl, Phys. Chem. Chem. Phys., 2010, 12, 283.
323. A.R. Zeradjanin, N. Menzel, P. Strasser, W. Schumann, Chem. Sustain. Chem., 2012, 5, 1897.
324. G. Cabello, E.P.M. Leiva, C. Gutierrez, A. Cuesta, Phys. Chem. Chem. Phys., 2014, 16, 14281.
325. N. Garcia, V. Climent, J.M. Orts, J.M. Feliu, A. Aldaz, ChemPhysChem, 2004, 5, 1221.
326. J.M. Feliu, M.J. Valls, A. Aldaz, J. Electroanal. Chem., 1993, 345, 471.
327. M. Wasisaka, H. Suzuki, S. Mitsui, H. Uchida, M. Watanabe, Langmuir, 2009, 25, 1897.
328. E. Skulason, V. Tripkovic, M. E. Björketun, S. Gudmundsdottir, G. Karlberg, J. Rossmeisl, T. Bligaard, H. Jonsson and J. K. Norskov, J. Phys. Chem. C, 2010, 114, 18182.
329. M. Neurock, M. Janik, A. Wieckovski, Faraday Discuss., 2008, 140, 363.
330. G. Garcia, M.T.M. Koper, Phys. Chem. Chem. Phys., 2008, 10, 3802.
331. D.F. van der Vliet, M.T.M. Koper, Surf. Sci., 2010, 604, 1912.
332. I. Kastounaros, W.B. Schneider, J.C. Meier, U. Benedikt, P.U. Biedermann, A.A.Auer, K.J.J. Mayrhofer, Phys. Chem. Chem. Phys., 2012, 14, 7384.
333. E.M. Aran-Ais, M.C. Figueiredo, F.J. Vidal-Iglesias, V. Climent, E. Herrero, J.M.Feliu, Electrochim. Acta, 2011, 58, 184.
334. N. Garcia-Araez, V. Climent, P. Rodriguez, J.M. Feliu, Phys. Chem. Chem. Phys., 2010, 12, 12146.
335. V. Climent, N. Garcia-Araez, J.M. Feliu, Electrochem. Commun., 2006, 8, 1577.
336. M.A. Omole, V.A. Okello, V. Lee, L. Zhou, O.A. Sadik, ACS Catal., 2011, 1, 139.
337. J.D. Froehlich, C.P. Kubiak, J. Am. Chem. Soc., 137, 2015, 3565.
338. J.D. Froehlich, C.P. Kubiak, J. Am. Chem. Soc., 2015, 2015, 3565.
339. J. Rodriguez-Lopez, A.J. Bard, J. Am. Chem. Soc. 2010, 132, 5121.
340. R.E. Rettew, N.K. Allam, F.M. Alamgir, ACS Appl. Mater. Interfaces, 2011, 3, 147.
341. H.N. Sharma, V. Sharma, A.B. Mhadeshwar, R. Ramprasad, J. Phys. Chem.Lett., 2015, 6, 1140.
342. Y. Zhong, K. Ueno, Y. Mori, T. Oshikiri, H. Misawa, J. Phys. Chem. C, 2015, 119, 8889.
343. J.O'M. Rockris, R. Parso, Trans. Faraday Soc., 1949, 45, 916.
344. B.J. Murphy, F. Sargent, F.A. Armstrong, Energy Environ. Sci., 2014, 7, 1426.
345. C. Wildi, G. Cabello, M.E. Zoloff Mischoff, P. Velez, E.P.M. Leiva, J.J. Calvente, R. Andreu, A. Cuesta, J. Phys. Chem. C, in print, DOI: 10.1021/acs.jpcc.5b04560.
346. B.B. Blizanac, C.A. Lucas, M.E. Gallagher, M. Arenz, P.N. Ross, N.M. Markovic,,J. Phys. Chem. B, 2004, 108, 625.
347. J. Durst, A. Siebel, C. Simon, F. Hasché, J. Herranz, H.A. Gasteiger, EnergyEnviron. Sci., 2014, 7, 2255.
348. J. Durst, C. Simona, A. Siebel, P.J. Rheinländer, T. Schuler, M. Hanzlik, J.Herran, F. Hasché, H.A. Gasteiger, ECS Trans., 2014, 64, 1069.
349. P. Rheinländer, S. Henning, J. Herranz, H.A. Gasteiger, ECS Trans., 2013, 50, 2163.
350. J.H. Barber, B.E. Conway, J. Electroanal. Chem., 1999, 461, 80.
351. W. Sheng, Z. Zhuang, M. Gao, J. Zheng, J.G. Chen, Y. Yan, Nat. Commun., 2015, 6, 5848.
352. D. Strmcnik, M. Uchimura, C. Wang, R. Subbaraman, N. Danilovic, D. van der Vliet, A.P. Paulikas, V.R. Stamenkovic, N.M. Markovic, Nat. Chem., 2013, 5, 300.
353. R. Subbaraman, D. Tripkovic, D. Strmcnik, K.-C. Chang, M. Uchimura, A.P.Paulikas, V. Stamenkovic, N.M. Markovic, Science, 2011, 334, 1256.
354. B.B. Blizanac, P.N. Ross, N.M. Markovic, Electrochim. Acta, 2007, 52, 2264.
355. A.M. Gómez-Marín, R. Rizoa, J.M. Feliu, Catal. Sci. Technol., 2014, 4, 1685.
356. P. Walden, Bull. Acad. Sci. St. Petersburg, 1914, 8, 405.
357. H. Ohno (Ed.), Electrochemical Aspects of Ionic Liquids, John Wiley & Sons,Inc., Hoboken, 2005.
358. M.V. Fedorov, A.A. Kornyshev, Chem. Rev., 2014, 114, 2978.
359. J.B. Rollins, J.C. Conboy, J. Electrochem. Soc., 2009, 156, B943.
360. A.S. Barnes, E.I. Rogers, I. Streeter, L. Aldous, C. Hardacre, G.G. Wildgoose,R.G. Compton, J. Phys. Chem. C, 2008, 112, 13709.
361. M.M. Islam, T. Ohsaka, J. Phys. Chem. C, 2008, 112, 1269.
362. J.T. Frith, A.E. Russell, N. Garcia-Araez, J.R. Owen, Electrochem. Commun., 2014, 46, 33.
363. D.R. MacFarlane, J.M. Pringle, Energy Environ. Sci., 2014, 7, 232.

364. A. Izgorodin, E. Izgorodina, D.R. MacFarlane, Energy Environ. Sci., 2012, 5, 9496.
365. D.H. Chin, G. Chiericato Jr., E.J. Nanni Jr., D.T. Sawyer, J. Am. Chem. Soc., 1982, 104, 1296.
366. E. Yeager, Electrochim. Acta, 1984, 29, 1527.
367. R.G. Evans, O.V. Klymenko, S.A. Saddoughi, C. Hardacre, R.G. Compton, J.Phys. Chem. B, 2004, 108, 7878.
368. D. Zhang, T. Okajima, F. Matsumoto, T. Ohsaka, J. Electrochem. Soc., 2004, 151, D31.
369. E.E. Switzer, R. Zeller, Q. Chen, K. Sieradzki, D.A. Buttry, C. Friesen, J. Phys.Chem. C, 2013, 117, 8683.
370. A. Khan, X. Lu, L. Aldous, C. Zhao, J. Phys. Chem. C, 2013, 117, 18334.
371. D.A. Walsh, A. Ejigu, J. Smith, P. Licence, Phys. Chem. Chem. Phys., 2013, 15, 7548.
372. X.-Z. Yuan, V. Alzate, Z. Xie, D.G. Ivey, W. Qu, J. Electrochem. Soc., 2014, 161, A451.
373. G. Feng, X. Jiang, R. Qiao, A.A. Kornyshev, ACS Nano, 2014, 8, 11685.
374. G.-R. Zhang, M. Munoz, B.J.M. Etzold, ACS Appl. Mater. Interfaces, 2015, 7, 3562.
375. D. Zigah, A. Wang, C. Lagrost, P. Hapiot, J. Phys. Chem. B, 113, 2019.
376. J. Jedraszko, W. Nogala, W. Adamiak, S. Dongmo, G. Wittstock, H.H. Girault, M. Opallo, Chem. Commun., 2015, 51, 6851.
377. T. Welton, Coord. Chem. Rev., 2004, 248, 2459.
378. H. Olivier-Bourbigou, L. Magna, D. Morvan, Appl. Catal. A, 373, 2010, 1.

Acknowledgments

The completion of this thesis would not have been possible without the help and support of many people.

Firstly, I would like to thank my academic supervisor Prof. Dr. Aliaksandr Bandarenka for giving me the opportunity to work in his group and for his guidance throughout my thesis. I am especially thankful for all the help he offered me, both scientific and non-scientific.

I wish to express my gratitude to Prof. Dr. Wolfgang Schumann, for giving me the opportunity to work in his group and for the numerous helpful discussions.

Special thanks to Dr. Jakub Tymoczko for introducing me to single crystal electrochemistry methods and the encouragement in the early stages of my PhD studies.

I am thankful to Alberto Ganassin and Marcus Pohl for the fruitful collaboration and discussions in the lab.

I wish to thank Dr. Federico Calle-Vallejo for conducting the DFT calculations used in this work. I would also like to thank Prof. Dr. Karina Morgenstern for her help in obtaining AFM images.

I also want to thank Dr. Faheem Butt, Bianca Paulitsch, Albrecht Dorsel, Armin Lang, David Reinisch, Sebastian Watzele, Daniel Scieszka, Jeongsik Yun, Yunchang Liang, Philipp Marzak, and Lakshmi Swaroopa Ganti for their help and support during the completion of this thesis.

I want to thank the former students in the group, Lukas Spanier, Kurt Brandl, and Umair ul-Hassan, for conducting OER measurements.

I am grateful to all the members of the Analytical Chemistry—Center for Electrochemical Sciences (CES) group at Ruhr-Universität Bochum and the Physics of Energy Conversion and Storage group at Technische Universität München for their support, interesting discussions, and fun times.

I wish to express my deepest gratitude to my family, without which none of this would have been possible, for all the support and encouragement I received from them my entire life.

Finally, yet importantly, I would like to thank my partner, Irene, for all her support, understanding, and patience.